**Title**

One- and two-dimensional infrared spectroscopic studies of solution-phase homogeneous catalysis and spin-forbidden reactions

**Permalink**

https://escholarship.org/uc/item/7zq1s4wv

**Author**

Sawyer, Karma Rae

**Publication Date**

2010-01-13

# One- and two-dimensional infrared spectroscopic studies of solution-phase homogeneous catalysis and spin-forbidden reactions.

by

Karma Rae Sawyer

B.S. (Syracuse University) 2003

A dissertation submitted in partial satisfaction of the
requirements for the degree of
Doctor of Philosophy

in

Chemistry

in the

GRADUATE DIVISION
of the
UNIVERSITY OF CALIFORNIA, BERKELEY

Committee in charge:
Professor Charles B. Harris, Chair
Professor Daniel Neumark
Professor Alexis Bell

Fall 2008

The dissertation of Karma Rae Sawyer is approved:

Chair Date

Date

Date

University of California, Berkeley

Fall 2008

# One- and two-dimensional infrared spectroscopic studies of solution-phase homogeneous catalysis and spin-forbidden reactions.

by

Karma Rae Sawyer

# Abstract

One- and two-dimensional infrared spectroscopic studies of solution-phase
homogeneous catalysis and spin-forbidden reactions.

by

Karma Rae Sawyer
Doctor of Philosophy in Chemistry

University of California, Berkeley

Professor Charles B. Harris, Chair

Understanding chemical reactions requires the knowledge of the elementary steps of breaking and making bonds, and often a variety of experimental techniques are needed to achieve this goal. The initial steps occur on the femto- through picosecond time-scales, requiring the use of ultrafast spectroscopic methods, while the rate-limiting steps often occur more slowly, requiring alternative techniques. Ultrafast one and two-dimensional infrared and step-scan FTIR spectroscopies are used to investigate the photochemical reactions of four organometallic complexes. The analysis leads to a detailed understanding of mechanisms that are general in nature and may be applicable to a variety of reactions.

Professor Charles B. Harris
Dissertation Committee Chair

Dedicated to my husband, Mike.

Thank you.

# Contents

# List of Figures

# List of Tables

## Acknowledgments

I have learned more in grad school than I ever thought I could and I attribute that to the incredible people in my life. Some challenged me intellectually, some cheered me on as I struggled and many did both. None of this work would have been possible without them.

First, I would like to acknowledge my advisor, Charles Harris. Looking back, I realize that when I started grad school, I relied on my professors and older grad students to guide me. Thanks to Charles, I got over that fast. He forced me to be an independent scientist and it was exactly what I needed. I wasn't tough enough when I started, and I still have a long way to go in that regard, but I am so much more confident than I was before. Charles taught me that when I am faced with a scientific problem, it is my responsibility to dive right in, solve it and do it well. No questions asked.

I would also like to acknowledge Vijaya Narasimhan, the Harris group administrative assistant. Vijaya works endlessly to ensure that the group runs smoothly. I hope that she realizes how much we appreciate it. She provided me with so much support, making sure that we didn't go over budget and that I was paid on time every month. More importantly though, Vijaya is an incredibly sweet and bright woman. I really enjoyed spending time with her.

The people that deserve the biggest thank you, though, are my coworkers in the Harris group. As a member of the Liquid Side, I have had the privilege of working with many talented scientists. Most notably, though, are James Cahoon and Jacob Schlegel. I will never able to think of grad school without thinking of them and I am really going to miss them. James is the most talented scientist I know. He has taught me more than anyone else at Berkeley and is very supportive of my work. He has gone through every paper I've written with a fine-toothed comb because he's just that type of guy. I cannot wait to see what happens to James in the future. He is going to become one of those really big names. I can't wait to tell people that I knew him way back when he was drinking chicken-water and perfecting the James-pour. Jacob is the best friend that I made at Berkeley. During the first few weeks getting him to open up was like pulling teeth, but I'm so glad that I stuck it out. Whenever I'm looking for a good conversation and some dry humor, I turn to Jacob. I never have to worry about making a fool of myself, asking stupid questions in lab or even having an emotional breakdown. He may not enjoy dealing with my antics, but he's a good friend and he'll do what needs to be done. Sometimes he even brings in baked goods. Even when we were working on that consistently misaligned delay stage, Jacob made me smile, a lot. He also taught me so much about subjects from monkey trivia to nonlinear optics. I hope that Jacob and I stay friends for a very long time.

Libby Glascoe and Matthias Kling were my mentors when I started in the Harris group. Matthias was ever-present in lab during my first year. He helped me run my first experiment and was always happy to answer my questions. Libby guided me through my first 3 years. We shared an office and there was a time that I spent more time with Libby than anyone else. She spent hours teaching me how to align the OPA, and she cheered me up as I cried about my qualifying exam. Most importantly though, Libby became a very good friend, and I can still call her if I need someone to talk to. Matt Zoerb joined the Harris group at the beginning of my fourth year. He is hilarious and so much fun to work with. He turns even the most mundane days in lab into a good time. Over the past two years, I've been able to watch him mature into a talented scientist. He's a fighter and has an incredible work ethic. He's going to do great things professionally and I feel very comfortable leaving the Liquid Side in his hands. Dan Lucas joined the group in the beginning of my fifth year. He was a very good scientist-to-be and I wish he would have been more confident in his abilities. He is warmly remembered and deeply missed. I also really enjoyed the time I spent with the Surface Side members of the group, Paul Szymanski, Steve Shipman, Sean Garrett-Roe, Aram Yang, Matt Strader, James Johns and Eric Muller. These guys were a constant source of beer, silly jokes and solid professional advice. Grad school would not have been the same without them; they have been good friends to me. Anne Perring, Idalia Perez and Nandini Ananth are also wonderful friends. They always made time to go to Strada or the gym with me. It was great to have these strong, brilliant and inspiring women in my life; their friendship made this whole process a lot more interesting.

I couldn't have finished this work with the help of my collaborators. I worked very closely with Ryan Steele, who recently graduated from the Head-Gordon group, on my first project in grad school. Without Ryan's help I never would have been able to finish that work. He is very bright and enthusiastic and I wish him the best. I also worked with C. Edwin Webster, a professor at the University of Memphis, on the transition-metal–boryl project. He performed an incredible number of calculations, as a result, the project has finally been completed. Finally, I would like to acknowledge Dr. Heinz Frei in the Physical Biosciences Division at LBNL, who gave me the chance to use his step-scan FTIR spectrometer. I learned a lot from him and I appreciate the opportunity he gave me.

This work was supported by the NSF's Divisions of Inorganic and Physical Chemistry. I also acknowledge some specialized equipment supported by the U.S. Department of Energy Office of Basic Energy Sciences, Chemical Sciences Division, under contract DE-AC02-05CH11231 and contractor supported research (CSR). The National Energy Research Scientific Computing Center is acknowledged for computational time.

I am also grateful to a number of people outside of the College of Chemistry. Liz Vivirito, Stephan Hutter, Jess Eastman and Jon Stewart probably don't know what a huge effect they had on my professional life. Of course, it was great to be able to go out with them and put all of my lab worries behind me, but they also reminded me to work towards the greater good. Their friendship means a lot to me. My family, Mom, Dad and Andrew, stood by me through my entire education and have been my loudest cheerleaders. They wholeheartedly celebrate my successes, and they are always there when I need some words of encouragement. Similarly, my family-in-law has been encouraging me since they came out to California and helped me move to Berkeley over 5 years ago. I also have two wonderful dogs, Benny and Hope, who always sit next to me and keep me company as I debug code or edit papers. I am incredibly lucky to have all of these people (and dogs) in my life. Most importantly, though, my husband Mike has been by my side, tirelessly supporting me, for almost 12 years. He is the most loyal and sincere person that I have ever known, and his unconditional love and wonderful sense of humor makes everything I do a lot easier and a lot more fun.

# Chapter 1

# Introduction

Organometallic chemistry is the study of compounds containing a metal bound to a nonmetal. The field is at the intersection of inorganic and organic chemistry, and its growth has lead to significant scientific advances. [1,2] For example, the use of organometallic compounds as homogeneous catalysts has become an invaluable technique in synthetic chemistry. The manipulation of alkene functionalized organic compounds is of great use in the synthesis of fine chemicals and is only feasible using the Grubbs catalyst ($RuCl_2(=CHPh)(PCy_3)_2$ ($Cy=C_6H_{11}$)). [3] Organometallic compounds also boost the efficiency of the hydrogenation of alkene bonds, a process that is assisted by Wilkinson's catalyst ($RhCl(PPh_3)_3$ ($Ph=C_6H_6$)). [4] Additionally, organometallic complexes are found in biological systems. [5] Hemoglobin and myoglobin have iron atoms at the center of a porphyrin ring. In hemoglobin, iron binds to $O_2$ and transports it throughout the body, and unfortunately, other small organic molecules, such as CO, NO and Cl, can bind competitively to the iron, preventing $O_2$ transport. [6]

While organometallic chemistry clearly encompasses a wide range of interesting and important scientific questions, it is also a somewhat limited field that is typically investigated from a synthetic chemistry perspective. [1, 2] The approach taken in this work is quite different. As a physical chemist, I have investigated fundamental trends in the reactivity of organometallic complexes using step-scan, ultrafast UV-pump, IR-probe and transient two-dimensional infrared (T2D-IR) and spectroscopies in order to better understand reactivity trends in organometallic systems. All of my experimental investigations have been supplemented with density functional theory (DFT) modeling, which has been used to investigate the details of the reactions that are not apparent based on experiments alone.

Figure 1.1 shows a summary of the reactions that have been investigated in this work. Chapter 3 shows an investigation of the process of alkene isomerization by photoactivated $Fe(CO)_5$ (see Figure 1.1a) studied using a model system, $Fe(CO)_4(\eta^2$-1-hexene) in neat 1-hexene solution. This catalytic reaction is one of the most prevalent in organometallic chemistry and is regularly utilized by synthetic chemists. [2, 7–12] I have monitored the dynamics of the isomerization reaction on the nano- through microsecond time-scales and present the first direct evidence for its mechanism in solution. [13, 14] The second reaction (see Figure 1.1b) is discussed in Chapter 4. This is a combined experimental and computational investigation that I performed in collaboration with Ryan Steele and Martin Head-Gordon in the Department of Chemistry at the University of California, Berkeley. This work shows the first direct observation of photoinduced transition-metal–bent nitrosyl excited state complexes, a class of molecules that are thought to be important as signalling

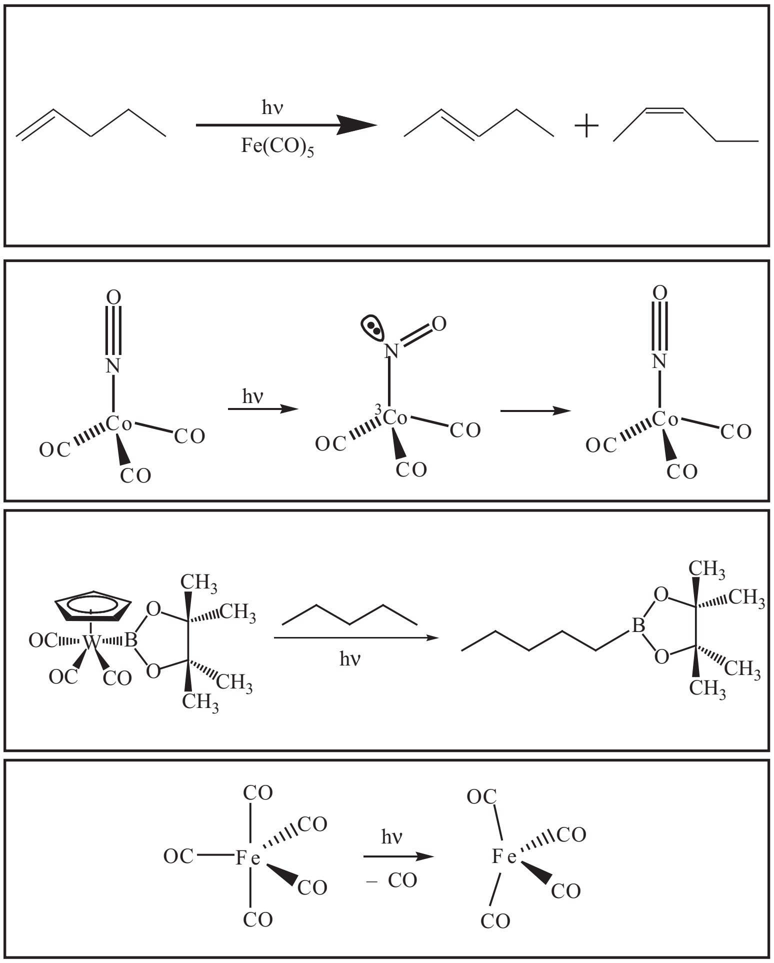

Figure 1.1: Summary of reactions discussed in this work. (a) Chapter 3: Iron-catalyzed alkene isomerization, (b) Chapter 4: Photochemical formation of excited state transition-metal–bent nitrosyl complexes, (c) Chapter 5: Selective C–H bond activation catalyzed by transition-metal–boryl complexes, (d) Chapter 6: CO photodissociation from $Fe(CO)_5$

molecules in biological systems [5, 15–18] and for optical data storage applications. [19–22] In Chapter 5, I present an investigation of selective C–H bond activation reaction by novel transition-metal–boryl complexes. The activation of the strong C–H bonds in saturated alkanes presents enormous challenges to chemists and has been the focus of numerous research efforts. Recently, Hartwig et al. reported on transition-metal–boryl complexes that selectively activate C–H bonds in high yields. [23–27] I present the first experimental evidence for the reaction, including the observation of side-reactions that are expected to affect the final yield of bond-activation. Lastly, I present an experimental technique, transient two-dimensional infrared spectroscopy (T2D-IR) that can be used to track vibrational energy during the process of ligand dissociation from a prototypical transition-metal complex $Fe(CO)_5$. $Fe(CO)_5$ possesses both axial and equitorial CO ligands, but there is currently no experimental method capable of determining which CO is photodissociated from the complex in solution. In Chapter 6, I present an analysis of T2D-IR spectroscopy in light of DFT calculations and recent 2D-IR experiments performed in the Harris group [28] that reveals the power of T2D-IR in answering these fundamental questions that can not be answered by more traditional spectroscopic techniques.

## 1.1 Photochemistry

All of the reactions in Figure 1.1 begin by irradiating the sample with UV (266 or 400 nm) light. I have investigated two types of photochemical reactions, dissociative (Chapters 3, 5 and 6) and nondissociative (Chapter 4).

Figure 1.2a shows a sketch of the potential energy landscape of a simplified disso-

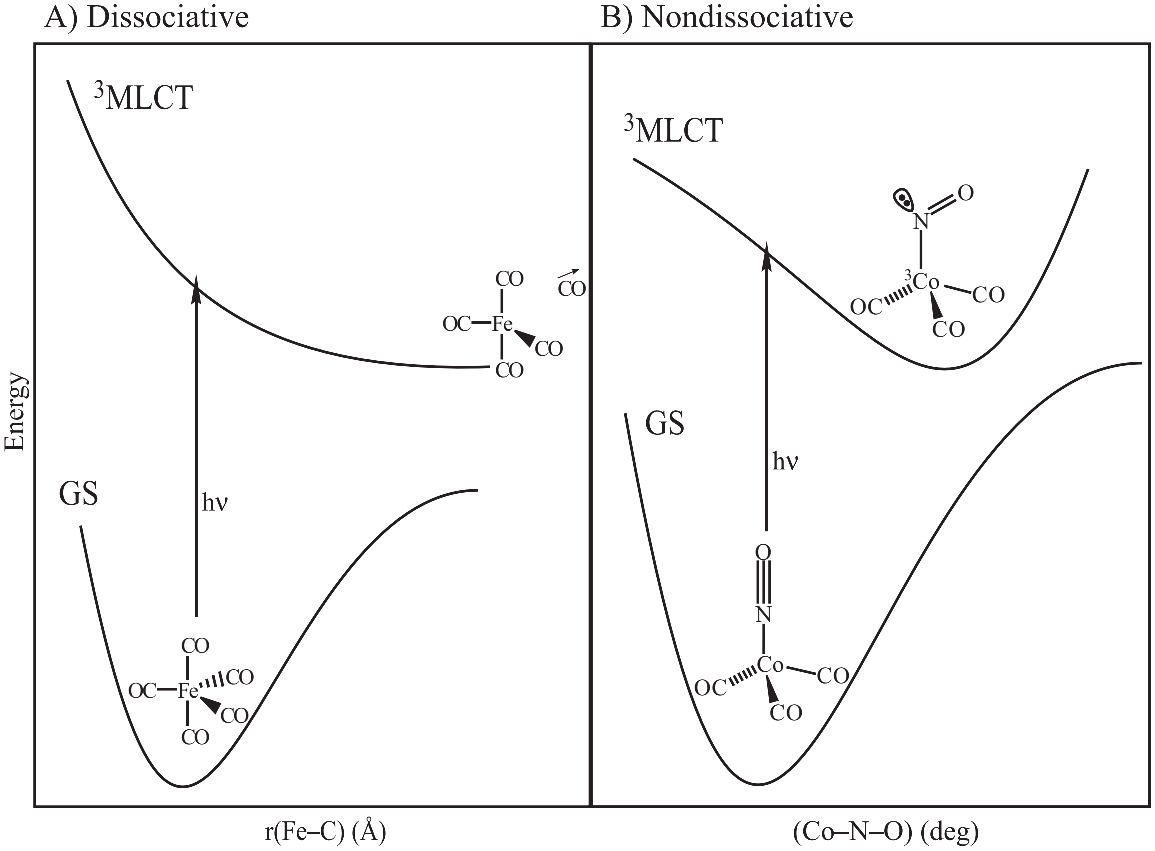

Figure 1.2: Sketch of potential energy curves involved in example **A**) dissociative and (**B**) nondissociative photochemical reactions. Note that the potential energy landscapes presented in this figure are greatly simplified for pedagogical purposes.

ciative photochemical reaction, CO photodissociation from $Fe(CO)_5$. This reaction will be discussed in detail in Chapter 6. When a UV photon (266 nm) is incident on $Fe(CO)_5$ in its ground state, the molecule is promoted into an excited metal-to-ligand charge transfer (MLCT) state that is unbound along the Fe–C geometric coordinate. Once the complex is in this excited state, it relaxes to its lowest energy structure by increasing the Fe–C bond distance until the CO is no longer bound to the metal. [29] The photochemical cleavage of a metal–ligand bond typically occurs in ca. 100 femtoseconds, leaving a coordinatively unsaturated complex. [30] [1] Since the metal is electron deficient, the system, consisting of the metal complex and the surrounding solvent bath, rearranges to lower its energy. [2,31–33]

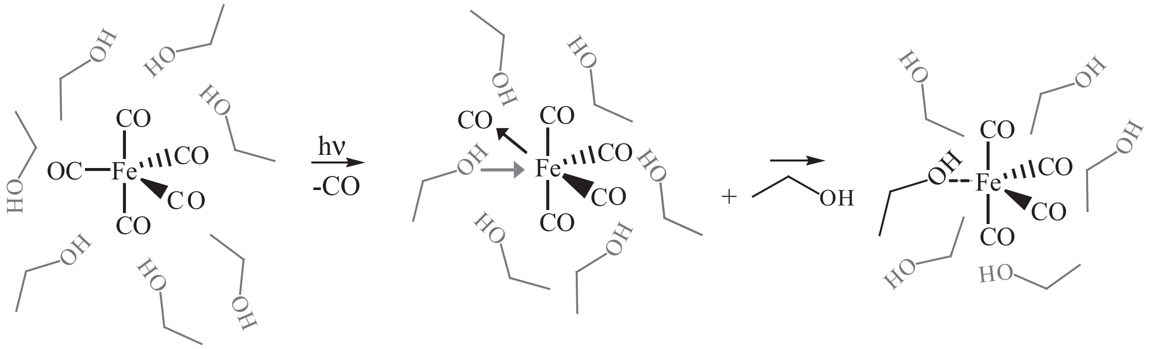

Figure 1.3: Mechanism for solvation following CO photodissociation from $Fe(CO)_5$ in ethanol solution.

In solution phase, there are two common ways for a system to lower its energy after ligand photodissociation, solvation and internal rearrangement. [34,35] In this work, solvation is defined as the coordination of a molecule from the bath to the electron deficient metal center. This process, shown schematically in Figure 1.3 for CO photodissociation from $Fe(CO)_5$, typically occurs in 1–2 ps after photolysis. [34] Solvent moieties, such as carbon-

---

[1] In solution phase, the dissociated CO ligand may collide with the solvent shell and rebind to the metal center. This process is called primary geminate recombination and typically occurs on the femto- through picosecond time-scale. [30] The coordinatively unsaturated complexes observed on the picosecond time-scale correspond to systems in which the CO escaped from the solvent shell. [30]

carbon double and triple bonds, –OH ligands or Lewis bases, form strong interactions with the metal center, [32, 36] creating complexes that are stable on a time-scale of milliseconds or longer. [13] On the other hand, weakly polarizable solvents, such as the C–H bonds in saturated alkanes, interact weakly with the metal centers. [31, 33, 37] These metal complexes are stable on the pico- through microsecond time-scales, depending on the system. [31–33, 38, 39] In fact, the interaction between the metal and the solvent in these complexes may be so weak that the solvents are considered to be token ligands, i.e., the solvent molecule bound to the metal is exchanged with other solvent molecules on a picosecond time-scale. [35]

Internal rearrangement is another common method to stabilize an electron deficient metal complex. [31, 36, 39] In this process, shown schematically in Figure 1.4, ligands rearrange so that additional electron density is donated towards the metal. This process has been studied extensively, including recent work by Elizabeth Glascoe et al., and can occur in less than 1 ps, or on a much longer (ns-$\mu$s) time-scale. [31, 39] The lifetimes of internally stablized complexes also vary significantly depending on the amount of electron density that is donated to the metal center. [31, 36, 39]

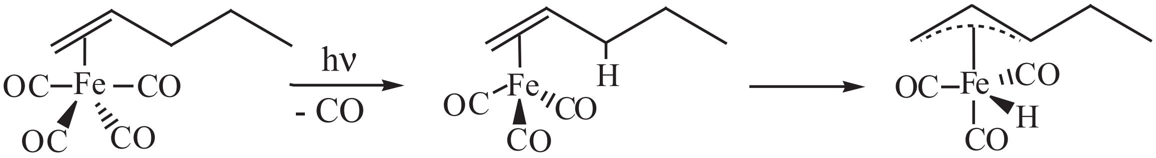

Figure 1.4: Schematic illustration of internal rearrangement following CO photodissociation from Fe(CO)$_4$($\eta^2$-1-hexene).

While coordinatively unsaturated metal complexes are inherently energetically unstable, there are systems in which it is not thermodynamically and/or kinetically favorable to solvate the coordinatively unsaturated complexes. This type of reactivity is most common for coordinatively unsaturated complexes in the ground triplet electronic state in solution with non-coordinating solvents. Preston Snee investigated the solvation of triplet transients in detail and found that in neat alkane solution they are often stable on the nano- through microsecond time-scales. [33, 37, 38]

My doctoral research also includes the investigation of non-dissociative photochemical reactions. Figure 1.2b shows the potential energy landscape for an example non-dissociative photochemical reaction, [20, 40, 41] which is discussed in detail in Chapter 4. The absorption of 400-nm photon excites the ground state complex into an MLCT excited state with a minimum energy structure on the excited state surface. [40] When the complex is excited to this MLCT state, its geometry changes until it relaxes to the minimum energy structure. Since non-dissociative reactions do not involve the cleavage of a bond, the excited state structure will ultimately relax back down to the ground state. The process of excited state relaxation is quite complicated. Typically, high energy excited states relax to the ground state of a femtosecond time-scale, however, there are some examples of excited state complexes that are stable on the pico- through microsecond time-scales. [40]

## 1.2 Spectroscopic Methods

Photoproducts stabilize on time-scales as short as 100 femtoseconds, and thus, to get a detailed picture of the reaction dynamics, it is necessary to monitor the reactions on the ultrafast time-scale. In this work, one- and two-dimensional time-resolved IR spectroscopy is used to monitor the dynamics of photoproducts on the picosecond time-scale. The experiments are performed using the ultrafast laser system discussed Chapter 2. The original UV-pump, IR-probe experimental apparatus was constructed by Elizabeth Glascoe, Matthias Kling and Jennifer Shanoski. Since then, the system has been upgraded significantly by my coworkers, James Cahoon and Jacob Schlegel, and me. Figure 1.5 shows the four pulse sequences that are accessible using the ultrafast laser system. Each of these pulse sequences and the corresponding experiments are discussed below. In order to monitor dynamics on the nano- through microsecond time-scales, I performed step-scan FTIR spectroscopy experiments in collaboration with Dr. Heinz Frei and his research group in the Physical Biosciences Division of Lawrence Berkeley National Laboratory. The step-scan FTIR experimental apparatus is discussed in section 2.3.

### 1.2.1 UV-pump, IR-probe Spectroscopy

UV-pump, IR-probe spectroscopy is a simple 2-pulse experiment, shown in Figure 1.2. The UV pump pulse starts the reaction by promoting the system into an excited electronic state, and the IR probe pulse follows in time inducing a $v = 0 \rightarrow 1$ transition for each IR-active CO or NO stretching mode. In other words, any IR light is absorbed if it has the same frequency as one of the CO and/or NO modes for the reactant, intermediate and product species in the photochemical reaction present at the time delay between the UV pump and IR probe pulses. The IR probe pulse ranges in energy from 1650 to 2100 cm$^{-1}$, which corresponds to the typical frequency range of metal bound CO and NO stretching modes.

Figure 1.6 shows an illustration of the bond between a transition-metal and a terminal CO ligand in a transition-metal. There are two types of interactions in this geometry. The first is a $\sigma$ bond in which electron density from the carbon is donated into the $d_{z^2}$

(a) UV-pump, IR-probe Spectroscopy

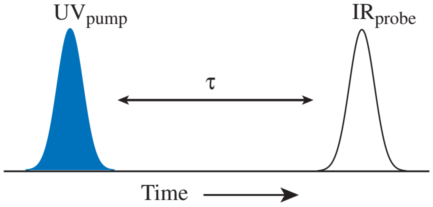

(b) Two-dimensional infrared (2D-IR) Spectroscopy

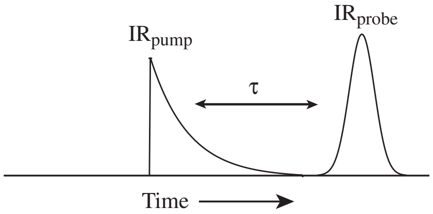

(c) Transient two-dimensional infrared (T2D-IR) Spectroscopy

UV-pump, 2D-IR-probe pulse sequence

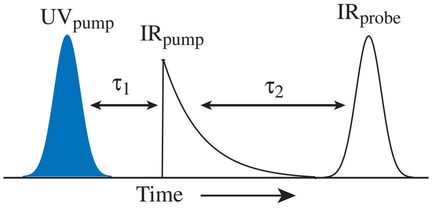

Vibrational labeling pulse sequence

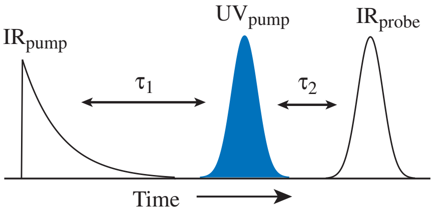

Figure 1.5: Pulse sequences utilized in UV-pump, IR-probe, 2D-IR and transient 2D-IR spectroscopy.

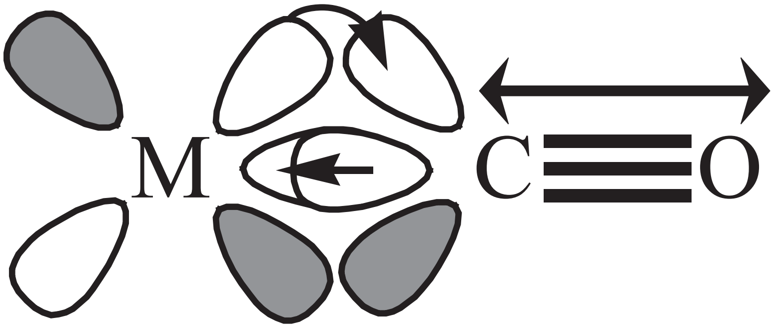

Figure 1.6: Illustration of binding between a transition metal and a carbonyl ligand.

orbital of the metal. The second is a $\pi$ back bond in which the metal $d_{xz}$ and $d_{yz}$ orbitals donate electron density into the empty $\pi^*$ orbitals of the CO. The $\pi$ back bond strengthens the bond between the metal and the carbon, and weakens the bond between the carbon and oxygen. Thus, the frequency of the CO stretch is sensitive to the amount of electron density at the metal center. This bond is nearly identical to the linear transition-metal–NO bond, however there are other types of transition-metal–nitrosyl bonds that are quite different. Transition-metal–nitrosyl complexes are discussed in detail in Chapter 4.

The relationship between the frequency ($\omega$) of the stretch of a bond and the force constant ($k$) of that bond is

$$\omega = \sqrt{\frac{k}{\mu}} \tag{1.1}$$

where $\mu$ is the reduced mass of the two bonded atoms. As the metal complex undergoes a chemical reaction, the amount of electron density at the metal center changes. This results in a change in the amount of electron density donated to the CO, and a change in the force constant ($k$) and, thus, the frequency ($\omega$) of the CO bond. As a result, the reactants, intermediates and products of a reaction will have a unique set of CO stretching modes, allowing us to directly observe the sequential steps in its mechanism.

All of the IR spectra presented here are plotted as difference spectra. Figure 1.7 shows a UV-pump, IR-probe spectrum for the photochemical reaction, $R \xrightarrow{h\nu} P$. This is presented to familiarize the reader with difference spectra. A more detailed discussion of the collection and analysis of difference spectra is presented in section 2.2.5. In brief, to generate difference spectrum, the IR spectrum of the UV-pumped sample is subtracted from the IR spectrum of the sample that has not been UV-pumped. As a result, the negative features correspond to the reactant (the species that have been depleted by the UV pump pulse) and the positive features correspond to the intermediates and products (the species that have been formed from the UV pump pulse).

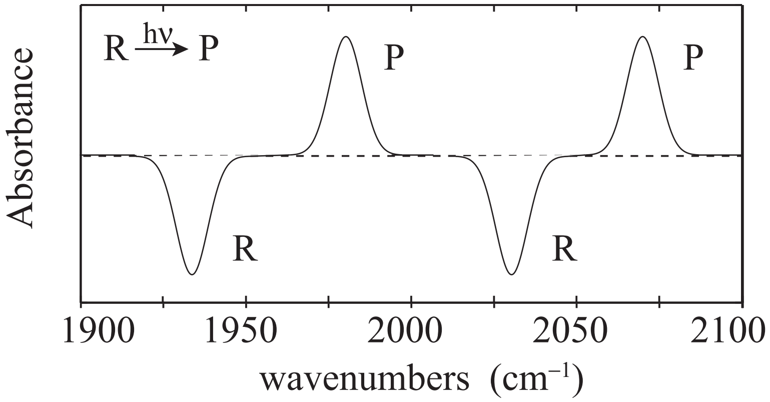

Figure 1.7: Illustration of a UV-pump, IR-probe spectrum for the $R \xrightarrow{h\nu} P$ reaction.

### 1.2.2 Two-Dimensional IR Spectroscopy

The pulse sequence in Figure 1.5b describes a two-dimensional infrared (2D-IR) spectroscopy experiment. 2D-IR spectroscopy is a relatively new technique in which the contributions to a standard IR spectrum are separated into two frequency dimensions to reveal more detailed information about the system, such as molecular anharmonicities, molecular structure and local environments. 2D-IR spectroscopy has been employed by a number of research groups over the past decade to study systems ranging from large proteins to liquid water. [28,42–49] Recently, the Harris Group has used 2D-IR to determine the structure of transition states in a chemical reaction. [28] None of the projects in this work employ the 2D-IR pulse technique, as it is used to investigate systems at equilibrium and the work presented here focuses exclusively on photochemical reactions. It is, however, instructive to discuss 2D-IR here because it is the basis of transient two-dimensional infrared (T2D-IR) spectroscopy discussed in Chapter 6. A more detailed discussion of this method is presented in James Cahoon's thesis and his recent *Science* paper. [28]

Two experimental approaches are used to collect 2D-IR spectra, double-resonance and pulsed Fourier-transform experiments. [50] Each has advantages and disadvantages, but ultimately, the techniques give nearly identical results. [50] The pulsed Fourier transform 2D-IR experiment provides better spectral and temporal resolution than the double resonance 2D-IR experiment, but is also a much more complicated experiment. [50] Data collection and analysis are significantly easier with the double resonance 2D-IR experiment. A key advantage of the technique is that, unlike the pulsed Fourier transform technique, it is possible to use the double resonance 2D-IR methods to quantitatively monitor the kinetics of any spectral feature. Since we generally monitor picosecond, my coworkers and I built an experimental appartus that uses the relatively simple double resonance pulse sequence (refer to Figure 1.5b). [28]

The double resonance 2D-IR experiment is a pump-probe technique in which the

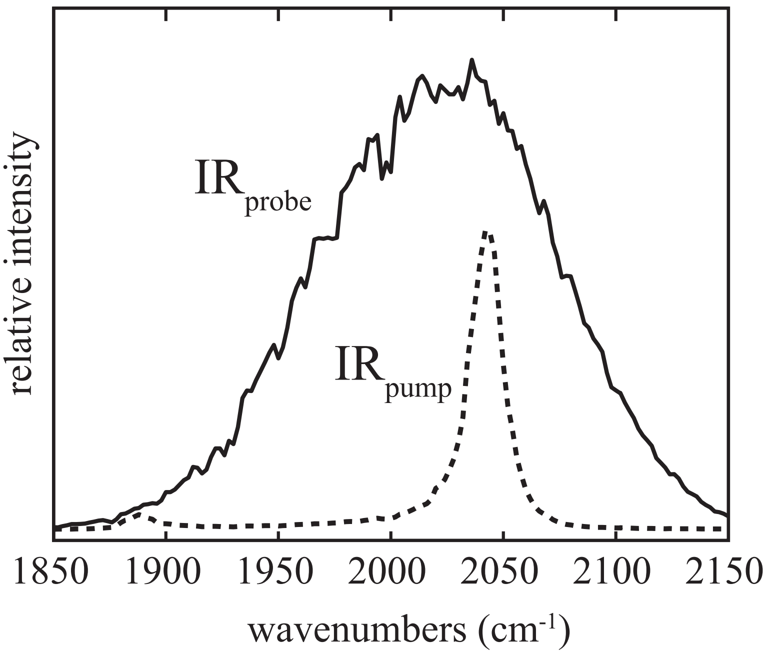

Figure 1.8: Spectral profile of the IR-pump and IR-probe pulses for 2D-IR and T2D-IR experiments.

pump is a narrowband IR pulse, with an exponential pulse profile, and the probe is the same broadband IR pulse described in section 1.2.1. The spectral profile of the two IR pulses are shown in Figure 1.8. The IR probe pulse has a spectral width of ca. 150 cm$^{-1}$ and is ca. 100 fs long. In contrast, the IR pump pulse has a spectral width of 10-13 cm$^{-1}$ and is ca. 1 ps long. Because the IR pump pulse is spectrally narrow, it is used to deposit energy into a specific vibrational mode of a sample, resulting in a vibrational coherence between the $v = 0$ and $v = 1$ vibrational levels. The IR probe pulse then follows the IR pump pulse in time and is used to monitor the changes in absorbance in the system. The energy level scheme for this process is shown in Figure 1.9a. The IR pump pulse (blue arrow) is used to excite population from the v=0 to v=1 levels and the IR probe pulse then either transfers that population to higher vibrational levels (red arrow) or stimulates emission from v = 1 to v = 0 (dashed blue arrow). An illustration of the 2D-IR spectrum that would result from this pulse sequence with two IR pump pulses with frequencies of $\omega_1$ and $\omega_2$ is presented in Figure 1.9b. The negative (blue) features in the spectra result from the blue arrows in Figure 1.9a and the positive (red) features result from the red arrows. The negative peaks along the diagonal in 2D-IR spectra are identical to the peaks that would be measured in an FTIR spectrum, the $v = 0 \rightarrow 1$ transitions for each modes. The positive features that are red shifted from the diagonal features correspond to the $v = 1 \rightarrow 2$ transitions, and thus, the spacing between the negative and positive features corresponds to the anharmonicity of the vibrational potential.

The features in the 2D-IR spectrum that contain the most unique information are the off-diagonal peaks, also called cross peaks. Cross peaks show the correlations between the different vibrational modes in the system. They result from the interaction of two vibrational eigenstates, and they appear at the intersection of the frequencies of the two vibrational modes, depicted by the dashed line in Figure 1.9b. The dynamics and positions of the cross peaks give information about the flow of vibrational energy throughout a system. More specifically, monitoring the change in the specific cross peak intensity as a function of the time delay between the IR pump and IR probe pulses gives detailed kinetic information about energy flow between modes.

Often 2D-IR is presented as the vibrational spectroscopy analogue to 2D-NMR spectroscopy and is used to investigate the structure and local environments of protein systems. [28,42–49] However, recently more attention has been paid to 2D-IR spectroscopy as a technique for investigating reactions and chemical exchange on the ultrafast time-

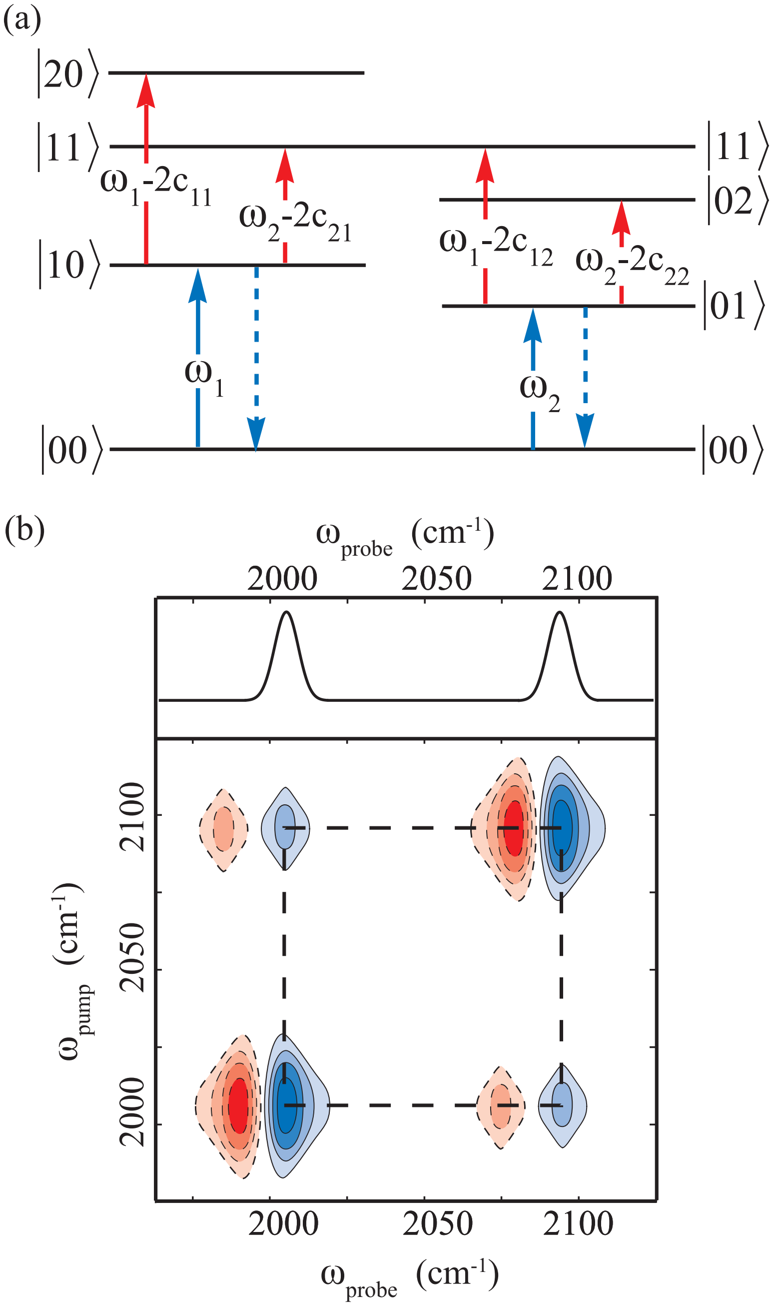

Figure 1.9: Illustration of the (a) energy level diagram for $|01\rangle$ and $|10\rangle$ normal modes and (b) the resulting 2D-IR spectrum.

scale. [28,51–54] The transient 2D-IR (T2D-IR) spectroscopy work presented here represents preliminary attempts to extend this work to photochemical investigations.

### 1.2.3 Transient Two-Dimensional IR Spectroscopy

Hamm et al. recently developed a new technique for the extension of 2D-IR spectroscopy from systems at equilibrium to photochemical reactions, transient 2D-IR (T2D-IR) spectroscopy. [50, 55] While Hamm and coworkers have investigated the details and theoretical framework of the T2D-IR experiment at length, [50, 55] the technique has not yet been applied to complex chemical reactions. Figure 1.5c shows the two different pulse sequences that can be used for T2D-IR experiments: UV-pump, 2D-IR probe and vibrational labeling T2D-IR. Figures 1.10 and 1.11 shows illustrations of the UV-pump, 2D-IR probe and vibrational labeling spectra (and the corresponding UV-pump, IR probe spectra) for the photochemical reaction, $R \xrightarrow{h\nu} P$.

The UV-pump, 2D-IR probe experiment is most the intuitive way of combining the UV-pump and 2D-IR experiments. Just as in the UV-pump, IR-probe experiment, the UV pump pulse begins a photochemical reaction by promoting the system into an excited electronic state. The UV pump pulse is followed in time ($\tau_1$) by a IR pump and IR probe pulse, which are separated in time by $\tau_2$ in Figure 1.5c. The resulting data gives 2D-IR spectra of the nonequilibrium ensemble at $\tau_1$. In this experiment, $\tau_2$ is held constant and small relative to $\tau_1$ to minimize the effects on the spectrum from intramolecular vibrational relaxation (IVR) resulting from the preceding UV pump pulse. The data from this experiment (refer to Figure 1.10) are plotted as a double difference spectrum where the positive 2D-IR spectrum (solid square in Figure 1.10) corresponds to the 2D-IR spectrum of intermediate and prod-

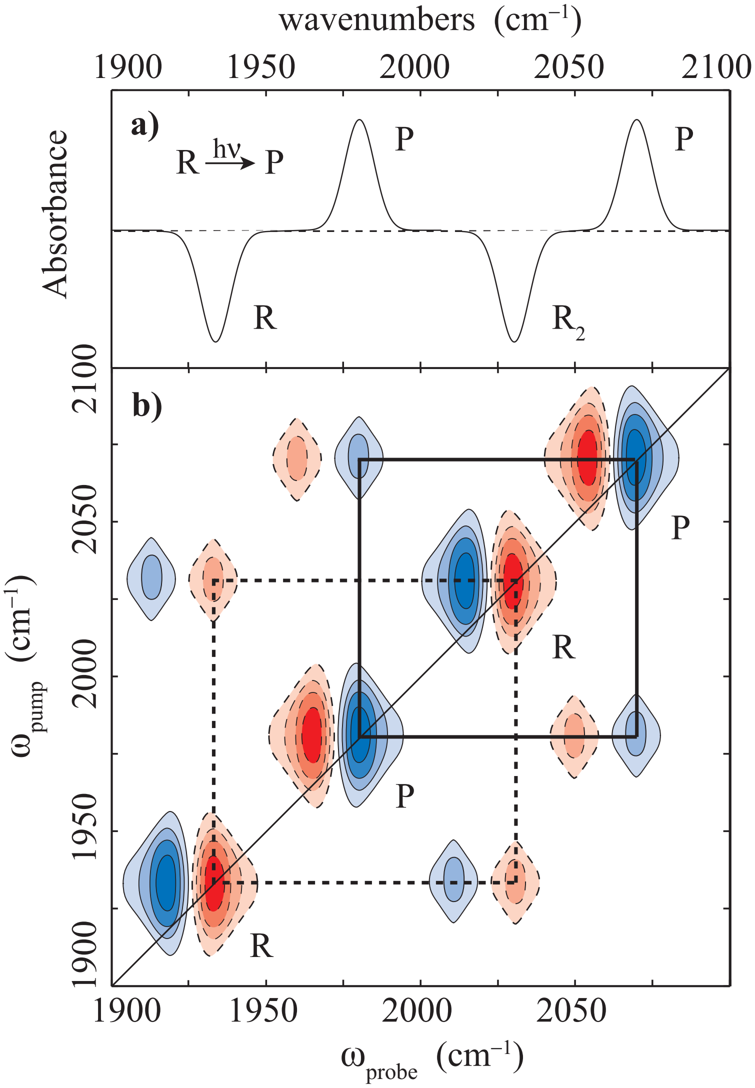

Figure 1.10: Illustration of UV-pump, IR-probe and UV-pump, 2D-IR probe spectra for the $R \xrightarrow{h\nu} P$ reaction.

uct species and the negative 2D-IR spectrum (dashed square in Figure 1.10) corresponds to the 2D-IR spectrum of the reactant. This method allows us to measure characteristics about chemical reactions that are not accessible using standard spectroscopic techniques, such as molecular structure of short-lived transient species, anharmonicity and the rates and mechanisms for energy flow throughout chemical reactions.

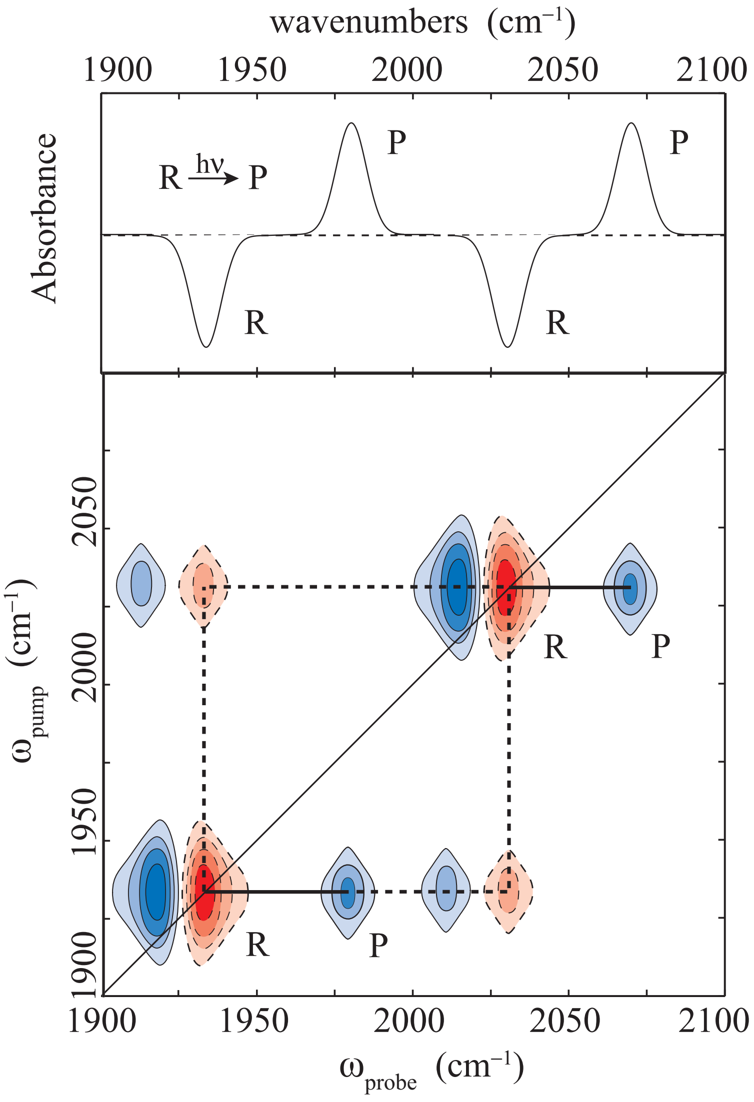

Figure 1.11: Illustration of UV-pump, IR-probe and vibrational labeling T2D-IR spectra for the $R \xrightarrow{h\nu} P$ reaction.

The vibrational labeling experiment is a more unusual pulse sequence in which the UV pump pulse is situated between the IR pump and IR probe pulses (refer to Figure 1.5c). In this experiment, the narrowband IR pump pulse labels a specific vibrational mode in the reactant by transferring population from the $v = 0$ to the $v = 1$ vibrational level. After the $\tau_1$ time delay, the UV pump pulse initiates the chemical reaction by promoting population into an excited electronic state. The vibrational coherence created by the IR pump pulse is preserved through the electronic excitation and can be tracked from the reactant, through any intermediates that exist within the vibrational coherence lifetime, to the product. The UV pump pulse is followed by an IR probe pulse that is used to measure the absorption spectrum of the system. Figure 1.11 shows an illustration of an example vibrational labeling T2D-IR spectrum of the photochemical reaction, $R \xrightarrow{h\nu} P$. Again, the data are plotted as double difference spectrum. Along the x-axis the product peaks are at the same position as they are in the UV pump, IR probe spectrum. However, since the IR pump only interacts with the reactant species, the location of the product peaks along the y-axis does not change. Therefore, the spectrum shows correlations between the vibrations in the reactant and the vibrations in the product. In this example spectrum, the vibrational mode in the lowest energy reactant mode (1940 $\text{cm}^{-1}$) is transferred to the lowest energy vibrational mode in product (1980 $\text{cm}^{-1}$). By monitoring the correlation between the reactant and product vibrational modes, it is possible to identify intermediates species that are too short-lived to be directly observed. Both T2D-IR experiments will be discussed in more detail in Chapter 6.

## 1.3 Density Functional Theory (DFT) Modeling

Throughout this work, reaction mechanisms and transient intermediates are identified by comparing experimental results to computational results from density functional theory (DFT) modeling. DFT calculations have been shown to be reliable for calculating energies, structures and frequencies for transition-metal complexes and transition states. [28, 31–33, 56] These calculations provide molecular structures, vibrational frequencies and relative thermodynamic stabilities of reactant, intermediate and product species and their interconnecting transition state structures. These results are used to assign spectral features and to determine the details of chemicals reactions that are cannot be determined based on only experimental results. In Chapters 3 and 4, DFT calculations are also used to determine the topology of a one-dimensional slice of relevant ground and excited state potentials. These results provide a qualitative picture of the nonadiabatic transitions between states, and when they are compared to experiment results give considerable insight into excited state dynamics. The details of the DFT modeling for each project are presented in the relevant chapters.

# Chapter 2

# Methods

## 2.1 Introduction

The investigations presented here were performed using a variety of experimental and theoretical techniques. The primary technique utilized is time-resolved IR spectroscopy which was used to monitor photochemical reactions on the pico- through microsecond time-scales. Three different forms of time-resolved IR experiments are presented: UV-pump, IR-probe, transient two-dimensional infrared (T2D-IR) and step-scan FTIR spectroscopies. Each technique provides different information about chemical reactions (as discussed in Chapter 1). The UV-pump, IR-probe and the T2D-IR experiments were performed using the ultrafast time-resolved infrared laser system in D93 Hildebrand Hall at the University of California, Berkeley. The step-scan FTIR experiments were performed in collaboration with Dr. Heinz Frei in the Physical Biosciences Division of Lawrence Berkeley National Laboratory. All of the experimental work presented herein was supplemented with density functional theory (DFT) calculations which were used to identify transient structures and to provide insight into spin-forbidden dynamics. The DFT modeling presented in Chapter 4 and 5 was performed in collaboration with Ryan Steele and Martin Head-Gordon at the University of California, Berkeley and C. Edwin Webster at the University of Memphis, respectively. The details of the ultrafast laser system, DFT modeling, data-analysis and sample handling are discussed below.

| **Label** | **Description** | **Manufacturer** |
|---|---|---|
| L1 | BK7 quartz<br>FL=20 cm d=1.0 in | unknown |
| L2 | BK7 or quartz<br>FL=-5 cm d=1.0 in | unknown |
| L3 | BK7 or quartz<br>FL=25 cm | unknown |
| L4 | UV-grade fused silica<br>FL=30 cm<br>(AR coating for 266 and 400 nm) | Newport<br>SPX030AR.10 |
| L5 | BK7<br>FL=100 mm, d=30 mm | Photonics Components<br>01LDK168 |
| L6 | BK7<br>FL=30 mm, d=30 mm | Photonics Components<br>01LDX057 |
| L7 | BK7<br>FL=500 mm, d=42 mm | Photonics Components<br>01LDX247 |
| L8 | BK7<br>FL=200 mm, d=30 mm | Photonics Components<br>01LDX218 |
| L9 | BK7<br>FL=-50 mm, d=-50 mm | Photonics Components<br>01LDX247 |
| L10 | $CaF_2$<br>FL=50 cm | unknown |
| L11 | $CaF_2$<br>FL=30 cm | unknown |
| L12 | $CaF_2$<br>FL=35 cm | unknown |
| L13 | $CaF_2$<br>FL=15 cm | unknown |

Table 2.1: List of lenses used in the home built portion of the ultrafast laser system. Refer to Figures 2.1 – 2.4 for the placement in the experimental setup.

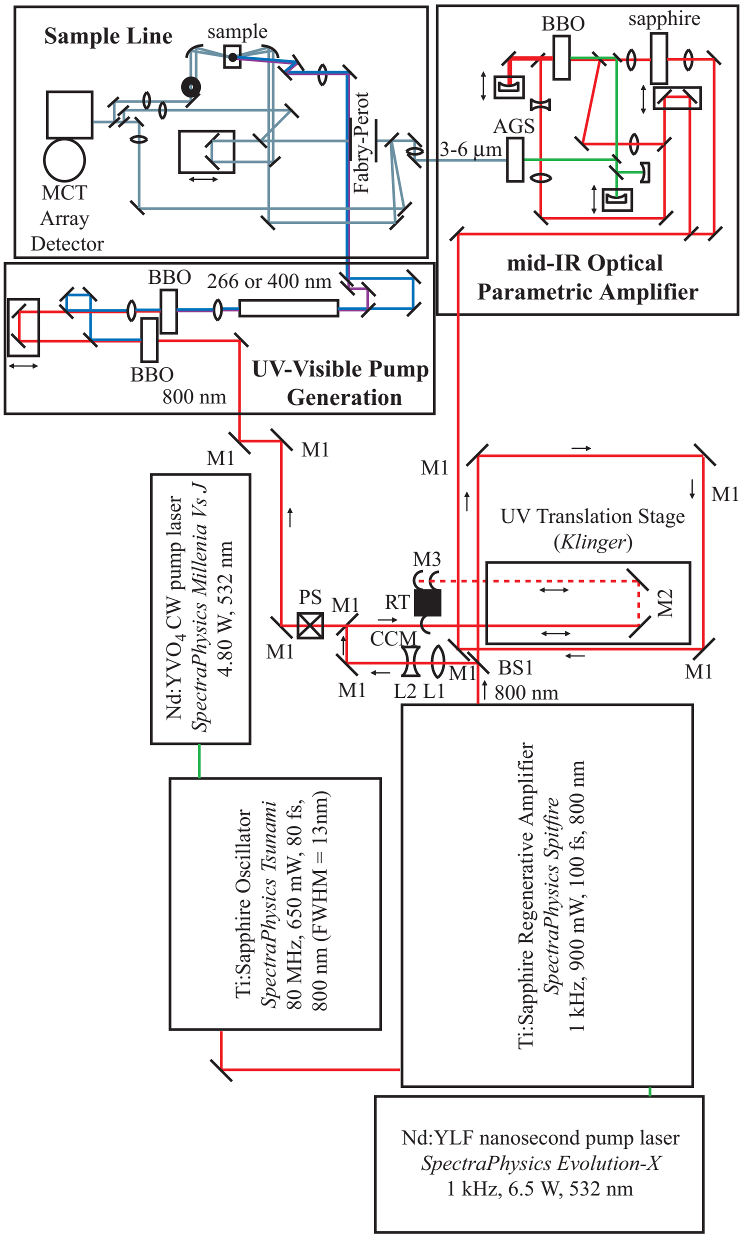

Figure 2.1: Schematic illustration of the ultrafast time-resolved infrared laser. Optics and equipment are listed in Tables 2.3 – 2.4. Detailed schematics of the UV pump generation, the mid-IR OPA and the sample line are included in Figures 2.2 – 2.4

| Label | Description | Manufacturer |
|---|---|---|
| BS1 | 70/30 Beam Splitter | unknown |
| BS2 | Fused Silica Window<br>d=1.0 in, 1.0 mm thick | unknown |
| HS | Harmonic Separator 400/800 nm<br>R 99% at 400 nm, T 90% at 800 nm | CVI Laser<br>BSR-48-1025 |
| ZnSe | ZnSe wedge cut at 3° | RMI Co. |
| $SiO_2$ | Q0 fused silica rod<br>25mm x 250mm with polished ends | SCHOTT North American |
| WP1 | Zero Order Half Waveplate<br>800 nm | CVI Laser<br>W1-PW1-10045-UV-800-45UNP |
| WP2 | Zero Order Half Waveplate<br>266 or 400 nm | CVI Laser<br>QWPO-266-10-2-R15<br>QWPO-400-10-2-R15 |
| WP3 | Dual Element (CdS/CdSe)<br>180° retardance from 4.5–6.0$\mu$m | Cleveland Crystals |

Table 2.2: List of other optics used in the home built portion of the ultrafast laser system. Refer to Figure 2.1 – 2.4 for the placement in the experimental setup.

## 2.2 Ultrafast Time-Resolved Infrared Laser

Figure 2.1 shows a diagram of the ultrafast time-resolved infrared laser system used to perform the UV-pump, IR-probe and the T2D-IR experiments. The optics and equipment utilized in these experiments are listed in Tables 2.2 and 2.4. In brief, the setup consists of a regeneratively amplified commercial Ti:sapphire oscillator. Seventy percent of regenerative amplifier output is used to pump a two-pass $\beta$-$BaB_2O_4$-based (BBO = $\beta$-$BaB_2O_4$) mid-IR optical parametric amplifier (OPA) based on a design by Peter Hamm. [57] The mid-IR OPA generates 100-fs pulses tunable from 3.0 to 6.0 $\mu$m with a spectral width of 150 $cm^{-1}$. A small fraction of the output of the OPA is reflected off of the surfaces of a ZnSe wedge to create the signal (IR probe) and reference lines. The remainder of the OPA output passes through the wedge and is used as an IR pump pulse. The remaining thirty

| **Label** | **Description** | **Manufacturer** |
|---|---|---|
| M1 | 800-nm High Reflector<br>(R> 99.4%) d=1.0 in | RMI Co. |
| M2 | 800-nm High Reflector<br>(R> 99.4%) d=0.5 in | RMI Co. |
| M3 | 800-nm Rectangular High Reflector<br>(R> 99.4%) | RMI Co. |
| M4 | 400-nm High Reflector<br>(R>99%) | CVI Laser<br>TLM1-400-45-UNP-1025 |
| M5 | 266-nm High Reflector<br>(R>99%) | CVI Laser<br>Y4-1025-45-UNP |
| M6 | Protected Aluminum Mirror<br>(R>85% for 0.2–1.0$\mu$m) | Newport<br>AL.2 |
| M7 | Broadband Low GVD Ultrafast Mirror<br>(700-825 nm) d=1.0 in. | unknown |
| M8 | Protected Gold Mirror<br>(R>95% for 0.6–10.0$\mu$m) | unknown |
| M9 | Protected Silver Mirror<br>(R>95% for 0.6–10.0$\mu$m) | CVI Laser<br>PS-PM-1037 |
| CM1 | Protected Silver Concave Mirror<br>FL=25 cm, d=1.0 in | unknown |
| CM2 | Protected Silver Concave Mirror<br>FL=50 cm, d=1.0 in. | unknown |
| DM1 | Dichroic Mirror $\mu$m<br>R at 800 nm and T at 1.2–2.2 | RMI Co. |
| DM2 | Dichroic Mirror $\mu$m<br>R at 1.2–1.7 $\mu$m and T at 1.7–2.2 | RMI Co. |
| PM | Off-axis Gold-coated Parabolic Mirror<br>FL= 10 cm | Janos Tech. |

Table 2.3: List of mirrors used in the home built portion of the ultrafast laser system. Refer to Figures 2.1 – 2.4 for the placement in the experimental setup.

| **Label** | **Description** | **Manufacturer** |
|---|---|---|
| BBO 1 | type I BBO crystal<br>5x5x0.7mm<br>$\theta$=29.2°, $\phi$=0°<br>p-coated at 800 nm | Photox Optical Systems |
| BBO 2 | type I BBO crystal<br>5x5x0.2mm<br>$\theta$=44.3°, $\phi$=0°<br>p-coated at 800 nm | Photox Optical Systems |
| BBO 3 | type II BBO crystal, | Photox Optical Systems |
| AGS | $AgGaS_2$ crystal, | Photox Optical Systems |
| sapphire | C-axis cut sapphire window | Int. Sci. Prod. |
| RM | Rotation Stage | Newport<br>Model RGV100 |
| CCM | Motorized Stability Mount | NewFocus<br>Model 8816-6 |
| PS | Periscope Assembly | Thorlabs<br>Model RS99 |
| WGP | Wire Grid Polarizer | Thorlabs<br>Model WP50H |
| Fabry Perot | Piezo-Electric<br>Kinetic Mounts and System | Thorlabs<br>Model KC1-T-PZ |

Table 2.4: List of crystals and other equipment used in home built portion of the ultrafast laser system. Refer to Figure 2.1 – 2.4 for the placement of the optics in the experimental setup.

percent of amplifier output is used for the generation of 400- or 266-nm UV pump pulses via a pair of type-I BBO crystals. The IR pump and IR probe pulses are focused onto the sample cell and spatially overlapped with the focused UV pump pulse. Reference and IR probe beams are detected by a 2x32 element MCT (mercury cadmium telluride) array IR detector (InfraRed Associates, Inc.) with a resolution of ca. 3 $\text{cm}^{-1}$ and a high speed signal acquisition system and data acquisition software (Infrared Systems Development Corp.). The details of this experimental apparatus are presented in the subsequent sections.

### 2.2.1 Ultrafast Ti:Sapphire Oscillator and Regenerative Amplifier

The experimental apparatus begins with a diode-pumped Nd:$YVO_4$ CW laser (CW = continuous wave) (*SpectraPhysics: Millenia Vs J*) with a 4.80-W output centered at 532 nm. This laser pumps a mode-locked Ti:sapphire oscillator (*SpectraPhysics: Tsunami*) to produce a 80 MHz pulse train of <80-fs pulses centered at 800 nm (FWHM = 11–14 nm). Under standard operating procedures, the oscillator produces a 650-mW output that is used to seed a regenerative amplifier (*SpectraPhysics: Spitfire*). Before amplification the pulses are stretched using a grating pair in order to avoid unwanted self-focusing and damage to optics during amplification. A Ti:sapphire rod is initially excited with a 6.5-W nanosecond pulsed Nd:YLF pump laser at 527 nm (*SpectraPhysics: Evolution-X*), and amplification occurs when the stretched pulses are introduced into the cavity. A pair of Pockels cells are used to confine the pulses until they complete ca. 20 round trips through the cavity (ca. 200 ns) so that the pulse power is 1.3–1.4 W. The pulses are then compressed via four grating interactions producing a 1-kHz train of <90-fs pulses centered at 800 nm with an average pulse power of 0.9 mW.

### 2.2.2 UV Light Generation

The output of the regenerative amplifier is split by 70:30 beam splitter (BS1). The strong arm is directed into the mid-IR OPA which is discussed in more detail in the subsequent section. The weak arm is telescoped to $\frac{1}{3}$ of its original size (ca. 3 mm diameter) and is directed into the UV translation stage (*Klinger:MT-160*: length = 250 mm and step increment = 1 $\mu$m) using a computer controller mirror (CCM). The UV translation stage is used to vary the path length of the UV pump beam relative to the IR probe beam, generating a time delay between them. The CCM is used in conjunction with a custom Labview program and position detector (*NewFocus Quadrant Photoreceiver*: Model 2921) to ensure that the beam is properly aligned into the translation stage. From the CCM the beam is directed onto a retroreflector built from the M2 mirrors on the translation stage. The beam passes between the M2 mirrors and a series of three retroreflectors mounted vertically so that the beam completes four round trips of the translation stage length in which each trip is about one inch higher than the preceeding trip. Since the 800-nm beam traverses the translation stage four times, it covers a maximum of one meter in 8 $\mu$m step increments. As a result, a complete translation of the stage results in a 6.7-ns delay of the beam path, leading to a stage resolution of 24 fs per step.

Generation of UV (266 and 400 nm) light is achieved via second and third harmonic generation (SHG and THG) of the 800-nm pulses from the regenerative amplifier. This process is well understand and is discussed in detail in Elizabeth Glascoe's Ph.D. thesis. A schematic of the UV and visible pump generation in this experimental setup is included in Figure 2.2.

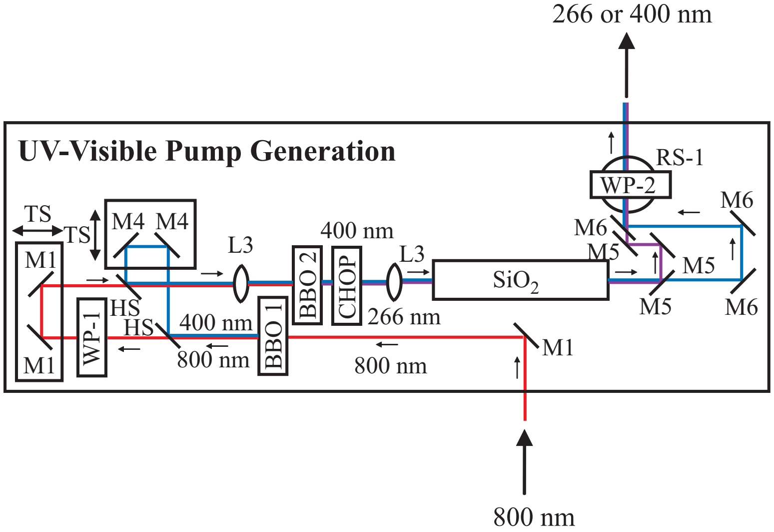

Figure 2.2: Schematic illustration of the UV pump generation. The optics and equipments are listed in Tables 2.3 – 2.4. TS corresponds to manually controlled translation stages.

In brief, approximately 30% of the output of the regenerative amplifier is aligned through a type-I BBO crystal ($\beta$-$BaB_2O_4$), BBO 1 in Figure 2.2, to generate 400 nm light via second harmonic generation (SHG). When the 800-nm beam is incident on a material with a nonzero second-order susceptibility, $\chi^{(2)}$, the polarization that is created in the crystal is

$$P(2\omega_1) = 2\chi^{(2)}E_1^2 \tag{2.1}$$

where $2\omega_1$ corresponds to the frequency of the newly generated 400-nm light and $E_1$ correspondelectric field amplitude of the 800-nm light. Under normal operating conditions, ca. 45 $\mu$J of 400-nm light is generated.

The conversion efficiency of BBO 1 is only ca. 20%, so there is still 800 nm light available for generation of the third harmonic (266 nm). BBO 1 is a type 1 crystal, and as a result, the 400-nm light has a polarization that is orthogonal to the polarization of the 800-nm light. These two colors are separated using a harmonic separator (HS in

Figure 2.2) and the polarization of the 800 nm light is rotated using a half-waveplate so that its polarization is parallel to the polarization of the 400-nm light. The 400- and 800-nm beams are recombined using another harmonic separator and are spatially and temporally overlapped onto a second type I BBO crystal to generate 266-nm light via sum frequency generation (SFG). SFG is similar to SHG described in equation 2.1 except that the input fields have different frequencies (800 and 400 nm). In this case the polarization created in the crystal is

$$P(\omega_1 + \omega_2) = 2\chi^{(2)} E_1 E_2 \tag{2.2}$$

where $E_1$ and $E_2$ correspond to the electric field amplitudes of the 800- and 400-nm light. Similarly, $\omega_1$ and $\omega_2$ correspond to the 800- and 400-nm light and $\omega_1 + \omega_2$ corresponds to the 266-nm light. [58] Under normal operating conditions, 5–7 $\mu$J of 266-nm light is generated.

After the BBO 2 crystal, the 400- and 266-nm pulses pass through a fused silica rod (*Schott Glass North America*: 25 mm x 250 mm Q0 fused silica with polished ends), which temporally stretches the pulses to give a 1.1-ps cross correlation of the mid IR and 400 nm pulses at the sample. The stretched pulses are necessary in order to achieve high pump powers and low signal-to-noise without generating products due to multi-photon excitation. The stretched pulses also prevent artifacts from nonlinear optical effects in the sample cell windows. A high pump power is particularly advantageous for investigating photochemical pathways with low quantum yields or complexes with low oscillator strengths modes.

### 2.2.3 Mid-IR Light Generation

Generation of mid-IR light is achieved via a two-pass BBO-based optical parametric amplifier. The mid-IR OPA is based on a design by Peter Hamm. [57] The theory behind the OPA and the deviations from Peter Hamm's design are discussed in detail in Jennifer Shanoski's Ph.D. thesis. A schematic of the mid-IR OPA is included in Figure 2.3. In brief, 600-mW of the 800-nm beam from the regenerative amplifer is directed into the mid-IR OPA. Approximately 10-mW of the light is split off from the main beam using a fused silica window (BS2) creating the first-pass seed beam and ca. 25-mW is split off using a second fused silica window (BS2) to create the first-pass pump beam. The remaining 580-mW is used as the second-pass pump. These pathways are labeled in Figure 2.3.

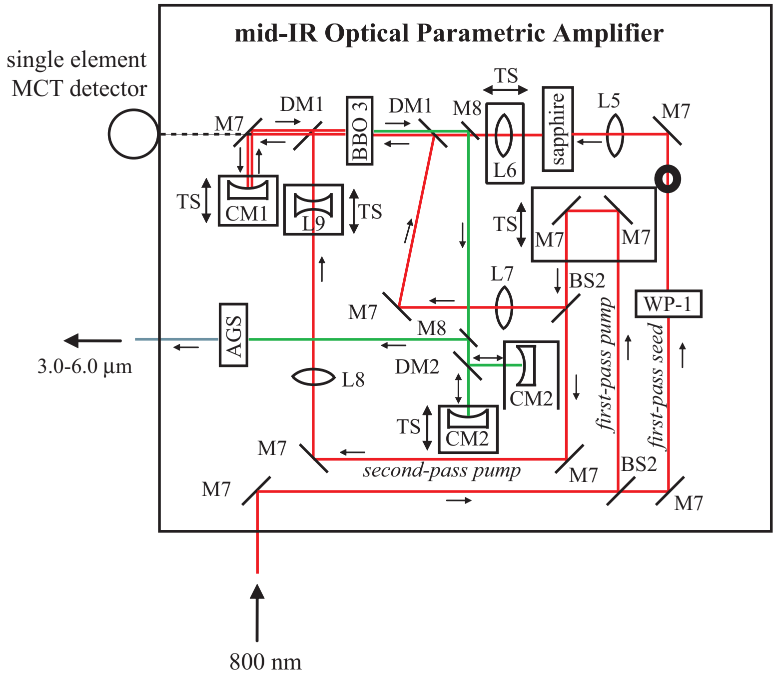

Figure 2.3: Schematic illustration of the mid-IR optical parametric parametric amplifier. The optics and equipments are listed in Tables 2.3 – 2.4. TS corresponds to manually controlled translation stages.

The polarization of the first-pass seed beam is rotated using a half waveplate so that it is orthogonal to the polarization of the first-pass pump and is spatially filtered through a small iris. The beam is then focused onto a thin sapphire window to create a white-light continuum. In order to generate stable white light, the length of the 800-nm pulses and the focus of the first-pass seed onto the sapphire is adjusted until the beam directly after L6 is stable and white in the center with a symmetric red ring at the perimeter.[1] This first-pass seed (now a white light continuum) is aligned through the top half of BBO 3 and onto the center of CM1 (Figure 2.3). The first-pass pump beam is directed into a retroreflector on a manual translation stage and is focused onto the top half of the BBO 3 crystal.[2] The first-pass seed and the first-pass pump are temporally and spatially overlapped on BBO 3 so that the seed beam is amplified via a process called optical parametric amplification. Optical parametric amplification is a specific type of difference frequency generation (DFG). DFG is described by the following form of the nonlinear polarization

$$P(\omega_1 - \omega_2) = 2\chi^{(2)} E_1 E_2^* \tag{2.3}$$

During this process, a photon at the higher frequency ($\omega_1$) is destroyed and two photons at the lower frequencies are created ($\omega_2$ and $\omega_3$).

$$\omega_3 = \omega_1 - \omega_2 \tag{2.4}$$

This process is referred to as optical parametric amplification when the $\omega_2$ and $\omega_3$ fields are amplified because the presence of these fields stimulates the additional emission of photons

---

[1] In the event that the white-light continuum is not observable, the compression of the regenerative amplifier can be adjusted to maximize the power of the 400-nm pulses. This will ensure that the pulses are sufficiently short to create a white light continuum at the sapphire window.

[2] In practice, the first-pass pump beam is not focused directly onto the crystal because it will burn the crystal and create white light. Instead, the first-pass pump beam is focused before the crystal so that it as close as possible to the crystal without generating white light.

at these frequencies. Conventionally, $\omega_1$, $\omega_2$ and $\omega_3$ corresponds to the pump frequency ($\omega_{pump}$ = 800-nm), the signal frequency ($\omega_{signal}$ = 1.2–1.7$\mu$m) and the idler frequency ($\omega_{idler}$ = 1.8–2.2$\mu$m), respectively. [58] In this case, the first-pass seed corresponds to the signal beam, and it is amplified in this OPA design. After DFG occurs at BBO 3, the the idler passes through DM1 and DM2 and its intensity is monitored at the single element MCT detector to verify that the first-pass through BBO 3 is properly aligned. The signal beam, on the other hand, passes through DM1, is reflected off of DM2 and is aligned onto the center of CM1. CM1 collimates the signal beam and directs it towards the bottom half of BBO 3 where it is amplified a second time. The second-pass pump is telescoped and spatially overlapped with the signal beam. The timing between the second-pass pump and the signal beams is adjusted using the translation stage holding CM1 until they are temporally overlapped. When the beams are overlapped, bright green light is observable after BBO 3. The signal and idler beams are separated using a dichroic mirror (DM2) and are aligned onto separate curved mirrors with 50 cm focal lengths (CM2). The signal and idler beams are spatially and temporally recombined onto a $AgGaS_2$ crystal (AGS) to generate broadband mid-IR light (ca. 150 cm$^{-1}$ spectral width and pulse duration of ca. 100 fs) that is tunable from 3.0 to 6.0 $\mu$m.

### 2.2.4 Sample Line

After the $AgGaS_2$ crystal in Figure 2.3, the mid IR light is collimated using a 50-cm focal length lens (L10). A small fraction of the output of the OPA is reflected off of the surface of a ZnSe wedge cut at 3° to create the signal (IR probe) and reference lines. The remainder of the OPA output passes through the wedge and is used as an IR pump pulse. For 2D-IR experiments, after the ZnSe wedge, the IR pump beam passes through a computer-controlled Fabry-Perot interferometer based on a design by Peter Hamm and coworkers. [28, 55] The interferometer narrows the spectral width of the mid-IR light from 150 cm$^{-1}$ to ca. 11 cm$^{-1}$ and stretches the pulse in time from ca. 100 fs to ca. 1 ps. The intensity profile of the beam also changes from a Gaussian to a Lorentzian shape during this process. A Fabry-Perot interferometer consists of two plane parallel partially reflective mirrors (ca. 85 % reflectivity here). When the interferometer is illuminated by a broadband source, the light is reflected between the parallel surfaces so that the transmission spectrum of a Fabry-Perot interferometer shows peaks corresponding to the resonances of the interferometer. The transmission spectrum is caused by the interference of the reflections of light between the mirrors; transmission maxima correspond to the beams that are in phase and transmission minima correspond to beams that are out of phase. The center frequency of the peaks in the Fabry-Perot spectrum is adjusted by mechanically changing the distance between the mirrors. [59] Note that the Fabry-Perot interferometer is removed for broadband IR pump, IR probe experiments (refer to Chapter 5). Two computer controlled translation stages (Figure 2.4; *Newport Corp.: XM-160* and Figure 2.1: *Klinger*) are used to create time delays between the IR pump and IR probe pulses (up to ca. 300 ps) and the UV pump and IR probe pulses (up to ca. 3 ns). The polarizations of the UV pump and IR pump pulses are set relative to the polarization of the IR probe using zero-order half-wave plates mounted in computer controlled rotation stages (*Newport Corp.: RGV100*). The IR pump and IR probe pulses are overlapped and focused (ca. 200 $\mu$m) onto the sample using a gold parabolic mirror and are spatially overlapped with the focused (ca.

400 $\mu$m) UV pump pulse. An iris is used to block the IR pump beam after the sample and the IR probe and reference beams are focused into the spectrograph with the slit opening set at 35–50 $\mu$m. The grating in the spectrograph has 150 grooves/mm and is blazed for 2000 cm$^{-1}$. The IR spectrum is measured with a custom built 32x2 element MCT (mercury cadmium telluride) array detector by InfraRed Associates Inc. and a high speed signal acquisition system and data acquisition software by Infrared Systems Development Corp. At the 2000 cm$^{-1}$ the spectral resolution of the detector is 2.3 cm$^{-1}$.

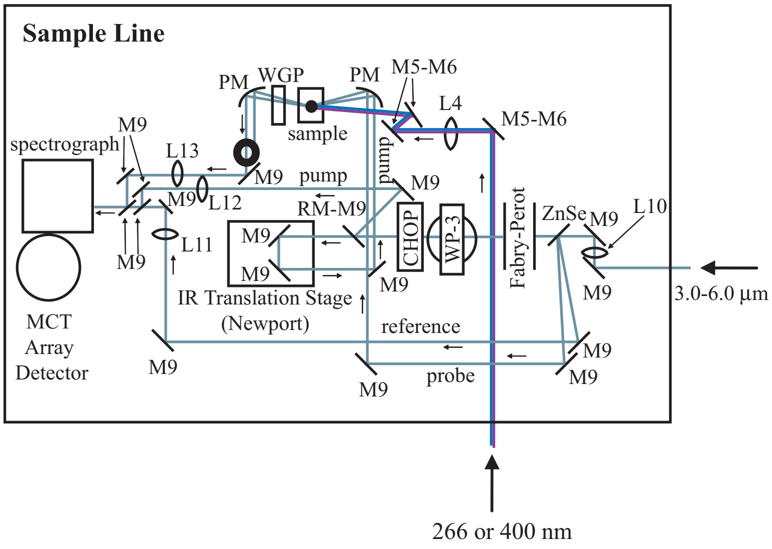

Figure 2.4: Schematic illustration of the sample line of the ultrafast time-resolved infrared laser. The optics and equipments shown are listed in Tables 2.3 – 2.4.

## Sample Handling

For the UV-pump, IR-probe and transient 2D-IR experiments, the sample is flowed using a mechanical pump through a stainless steel cell (Harrick Scientific) fitted with 2.0-mm-thick $CaF_2$ or $MgF_2$ windows.[3] The optical path length ranges from 250 $\mu$m to 1 mm

---

[3] UV grade, Crystran LTD, Poole, England

depending on the experiment. The sample cell is moved normal to the incident beams by computer controlled translational stages (Standa) after each measured spectrum to ensure that absorptions are not masked or enhanced due to photoproducts accumulating on the sample cell windows. The sample concentrations are generally 1–2 mM but are significantly higher (up to 20 mM) for the experiments presented in Chapter 4. The sample cell used in the IR-pump, IR-probe and 2D-IR experiments is identical to the one used in the photochemical experiments except that the sample is held stationary and is not flowed.

### 2.2.5 Data Collection and Analysis

The array detector measures two different IR spectra, the signal (IR probe) and reference spectra. These two spectra are divided to account for the fluctuations in the mid-IR light. Additionally, the UV and IR pump beams are chopped in order to collect spectra of the pumped and unpumped sample. For the 2D-IR; UV-pump, IR-probe; and IR-pump, IR-probe experiments, the pump beams are chopped at a frequency of 500 Hz so that half of data is spectra of the pumped sample and the other half is spectra of the unpumped sample. Difference spectra are calculated by subtracting the absorbance spectrum of the pumped sample from the absorbance spectrum of the unpumped sample.

$$A_{difference} = A_{unpumped} - A_{pumped} \tag{2.5}$$

For the transient 2D-IR experiments, the UV-pump is chopped at a frequency of 250 Hz and the IR-pump is chopped at a frequency of 500 Hz so that four different types of spectra are measured—$A_{UV_{on}IR_{on}}$ (UV and IR pump hit the sample), $A_{UV_{on}IR_{off}}$ (only UV pump hits the sample), $A_{UV_{off}IR_{on}}$ (only IR pump hits the sample) and $A_{UV_{off}IR_{off}}$ (neither UV nor IR pump hit the sample).

The 2D-IR spectrum of the sample that has not been photolyzed by the UV-pump is

$$A_{UV_{off_{difference}}} = A_{UV_{off}IR_{off}} - A_{UV_{off}IR_{on}}. \tag{2.6}$$

Similarly, the 2D-IR spectrum of the sample that has been photolyzed by the UV-pump is

$$A_{UV_{on_{difference}}} = A_{UV_{on}IR_{off}} - A_{UV_{on}IR_{on}}. \tag{2.7}$$

The transient 2D-IR spectra is calculated by substracting the 2D-IR spectra of the pumped sample (equation 2.7) from the 2D-IR spectra of the unpumped sample (equation 2.6).

$$A_{T2D-IR} = A_{UV_{off}IR_{off}} - A_{UV_{off}IR_{on}} - A_{UV_{on}IR_{off}} + A_{UV_{on}IR_{on}}. \tag{2.8}$$

In a typical experiment, 2000 difference spectra are measured at each time position, which is divided into 10 sets and averaged. The dynamics of the features in the spectra are determined by fitting the peak area, plotted as a function of time, to a sum of exponentials with the Levenberg-Marquardt method. All errors correspond to a 95% confidence interval.

## 2.3 Step-scan FTIR Spectroscopy

Step-scan FTIR spectroscopy experiments were performed for the studies presented in Chapters 3 and 5 in order to investigate the dynamics on the nano- through microsecond time-scales. These studies were done in collaboration with Dr. Heinz Frei and Dr. Lars K. Anderson in the Physical Biosciences Division at Lawrence Berkeley National Laboratory.

The experimental setup of the step-scan FTIR apparatus has been described in detail elsewhere. [60, 61] For experiments in the 1700–2100 $\text{cm}^{-1}$ region with a spectral resolution of ca. 4 $\text{cm}^{-1}$, an MCT PV detector KMPV8-1-J2 (fwhm = 37 ns, RC decay of AC amplifier = 1.4 ms) was employed. AC-coupled and DC-coupled interferometric signals were simultaneously acquired by a 40-MHz, 12-bit digitizer (model PAD 1232). Samples were photolyzed with 25-ns pulses of the fourth harmonic of a Nd:YAG laser (DCR2A, GCR-3 optics) at 266-nm. Photolysis light was aligned in a nearly collinear geometry (10°) with the infrared beam. To prevent scattered 266 nm light from reaching the interferometer and detector optics, antireflection-coated Ge plates (International Scientific, 95% transmittance) were placed in the openings of the interferometer and detector compartments. Data acquisition was triggered by a small fraction of the photolysis laser pulse detected with an EG&G Silicon photodiode (SGD-444). A similar sample cell that was employed in the ultrafast UV-pump, IR-probe experiments was used here. Data was typically averaged over 15 laser-induced decays recorded for each mirror position of the step-scan apparatus and 5–10 full time-resolved step-scan experiments were performed on each sample to ensure reproducibility and allow for statistical analysis of data. Typically, changes in optical density of $5\text{x}10^{-5}$ were resolvable in these experiments. Again, time constants for chemical reactions were determined by fitting the kinetics to a sum of exponentials using the Levenberg–Marquardt method. All errors correspond to a 95% confidence interval.

## 2.4 DFT Modeling

Density functional theory (DFT) calculations have been used to model all of the photochemical reactions in this work because they have been shown to be reliable for calculating energies, structures and frequencies for transition-metal complexes and transition states. [28, 31–33, 56] However, the DFT calculations done for Chapters 3, 4 and 5 are very different. Most notably, the DFT calculations for Chaper 4 were done in collaboration with Ryan Steele and Prof. Martin Head-Gordon at the University of California, Berkeley and the DFT calculations presented in Chapter 5 were done in collaboration with Prof. C. Edwin Webster at the University of Memphis. Because the calculations vary significantly, the details of the computational work are presented in the individual chapters.

# Chapter 3

# The mechanism for iron-catalyzed alkene isomerization

This chapter has been reproduced with permission from K.R. Sawyer, E.A. Glascoe, J.F. Cahoon, J.P. Schlegel and C.B. Harris, *Organometallics*, 27(17), 4370–4379 (2008).

## 3.1 Introduction

One of the most important roles of organometallic complexes is their frequent use as homogeneous catalysts in organic reactions. [2] Photoactivated $Fe(CO)_5$, which is used to catalyze alkene isomerization, is a particularly efficient catalyst, and as a result, it has been used by synthetic chemists for decades. [2,7–12] Numerous mechanistic studies have resolved the key intermediates in the isomerization reaction under a variety of conditions (gas- and solution-phase and low temperature matrices), [8, 9, 11–14, 36, 62–68] yet many questions remain about the mechanism in room-temperature solution, particularly concerning the role of high spin intermediates. Here I report on time-resolved infrared (IR) experiments performed on the nano- through the microsecond time-scales that answer the remaining questions and conclusively determine the mechanism in solution. I have also performed a computational investigation using density functional theory (DFT) modeling to explore steps in the reaction that are not experimentally observable. The experimental results, coupled with the DFT analysis, give reason for a significant revision of the currently accepted mechanism. [13, 14]

The most detailed mechanism for this reaction currently presented in the literature is based on time-resolved IR studies in the gas phase and is summarized in Figure 3.1. [13,14] In the gas phase, UV-irradiation of $Fe(CO)_5$ leads to the dissociation of two CO ligands to form $^3Fe(CO)_3$. [36, 63, 69–71] It is hypothesized that $^3Fe(CO)_3$ coordinates a single 1-pentene molecule via a spin-allowed process to form $Fe(CO)_3$(1-pentene) ($\mathbf{B}_1$). [13, 14] The efficiency of the isomerization reaction may be due to the proposed triplet spin state of $\mathbf{B}_1$; however, no study has explored how or why the high spin state accelerates the reaction. [36, 63, 69–71] Species $\mathbf{B}_1$ was not directly observed in the gas phase experiments but was assumed to undergo an intramolecular C–H bond-cleavage reaction to form the allyl hydride species, $HFe(CO)_3(\eta^3\text{-}C_5H_9)$ (**C**), faster than the time resolution of the experiments (70 ns). [13, 14] The authors propose that, in addition to the $\mathbf{B}_1 \rightarrow \mathbf{C}$ intramolecular rearrangement, $\mathbf{B}_1$ and its 2-pentene analog, $\mathbf{B}_2$, react via a collision with a gaseous 1-pentene molecule to form a singlet bisalkene species (**D**), either $Fe(CO)_3(\text{1-pentene})_2$ ($\mathbf{D}_1$) or $Fe(CO)_3$(1-pentene)(2-pentene) ($\mathbf{D}_2$). [13, 14] Again, the authors were unable to observe the $\mathbf{B}_1 \rightarrow \mathbf{D}$

reaction because, at the experimentally accessible pressures of 1-pentene, this reaction is slow relative to the $\mathbf{B}_1 \rightarrow \mathbf{C}$ reaction. However, the rate of the $\mathbf{B}_1 \rightarrow \mathbf{D}$ reaction in solution may be as fast, if not faster, than the internal rearrangement reaction to form **C**. Since neither of the key steps has been observed experimentally, significant questions remain about the mechanism. [13, 14]

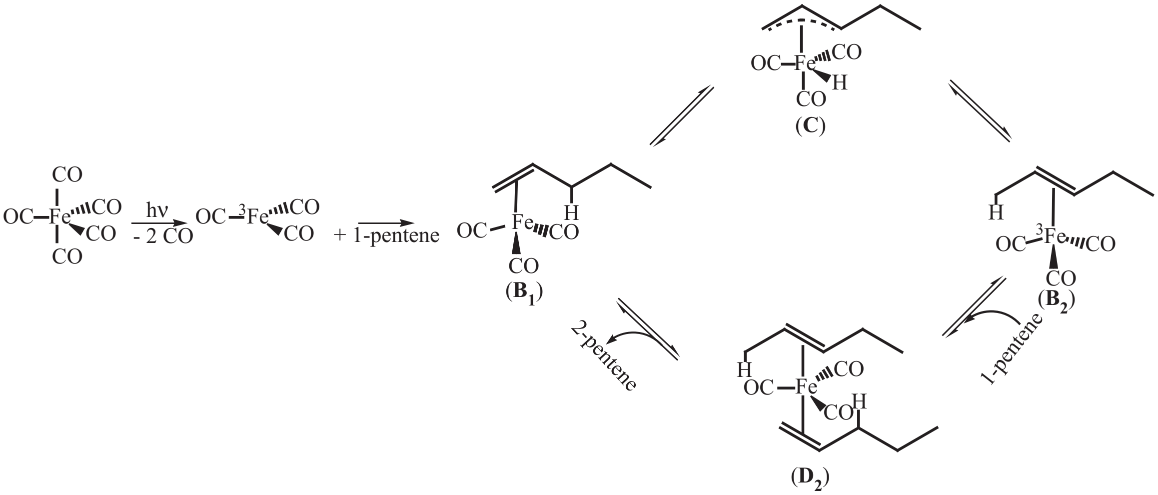

Figure 3.1: Proposed mechanism for pentene isomerization catalyzed by photoactivated $Fe(CO)_5$ based on time-resolved studies performed in the gas phase. Note that previous studies have been performed with complexes with a pentene ligand, but the experiments herein have been performed with complexes with a hexene ligand. [13]

Here I investigate the mechanism for iron-catalyzed alkene isomerization in room-temperature solution. I could not study the isomerization reaction directly with photoactivated $Fe(CO)_5$ because in solution irradiation of this complex with a single pulse of UV light leads to the dissociation of a single CO to form $Fe(CO)_4$ and not the active metal catalyst, $^3Fe(CO)_3$. [38] I circumvented this challenge by using $Fe(CO)_4(\eta^2\text{-1-hexene})$ (**A**) as a model system. Irradiation of this complex with a single 266-nm laser pulse leads to the dissociation of a single CO to form $Fe(CO)_3(\eta^2\text{-1-hexene})$ ($\mathbf{B}_1$), the first intermediate in the isomerization reaction (Figure 3.1). [13, 14, 36, 72] I have investigated the reactivity of $\mathbf{B}_1$ in neat 1-hexene solution in order to directly monitor the rates and mechanism for the formation of **C** and **D**.

Recently, Glascoe et al. performed a similar experiment on a picosecond time-scale and found that after 266-nm excitation of **A** a single CO is dissociated to form $\mathbf{B}_1$ within a few ps. [36] Species $\mathbf{B}_1$ does not react on the time-scale of the ultrafast experiments ($\tau \leq$ 5 ns), and neither **C** nor **D** was observed, presumably because the $\mathbf{B}_1 \rightarrow \mathbf{C}$ and $\mathbf{B}_1 \rightarrow \mathbf{D}$ reactions occur on a longer time-scale. [36] I have monitored this reaction using nano- through microsecond time-resolved IR spectroscopy in order to observe these key steps.

## 3.2 Methods

### 3.2.1 Sample preparation: Synthesis of $Fe(CO)_4(\eta^2$-1-hexene)

$Fe(CO)_4(\eta^2$-1-hexene) (**A**) was prepared by a modified version of a published procedure. [36, 73] A 1.7-g (0.0045 mol) portion of $Fe_2(CO)_9$ (Sigma-Aldrich) and 10 mL (0.08 mol) of 1-hexene (Sigma-Aldrich) were combined and stirred in the dark under a $N_2$ atmosphere for 20 hours. This mixture was distilled and fractionally condensed for 30 hours. The identity of the sample was verified with static FTIR spectroscopy. The sample was diluted in a small excess of 1-hexene and stored at –80 °C. Dilute solutions were prepared in 1-hexene. Because the contaminants precipitate out of solution at low temperature, solutions were prepared by decanting a small aliquot of the sample while it was held in dry ice. For experiments, a 0.5-mL aliquot of **A** was diluted to 75 mL with 1-hexene (Sigma-Aldrich) to give a final sample concentration of a few millimolar. Static FTIR spectra were taken prior to experiments to ensure sample purity. The sample is stable when exposed to air under ambient conditions for ca. 24 hours.

### 3.2.2 DFT Modeling

Density functional theory (DFT) calculations have been used to model the isomerization reaction because they have been shown to be reliable for calculating energies, structures and frequencies for transition-metal complexes. [32,33,35,38,39,56,74] Whenever possible the shortest-chain alkene was used in order to minimize computational expense. The same species labels (**A**–**D**) were used for both experiment and theory regardless of whether the alkene chain was hexene or a shorter alkene (butene or ethene), respectively. For example, species **C** corresponds to $HFe(CO)_3(\eta^3\text{-}C_6H_9)$ in the experiments but corresponds to $HFe(CO)_3(\eta^3\text{-}C_4H_7)$ in the DFT calculations. Shortening the alkene ligand to reduce computational expense has been done in studies of similar systems and is not expected to effect the mechanistic results. [13, 14, 36, 75]

All calculations were performed with Gaussian03 program package [76] and utilized Becke's 1988 exchange functional together with the Perdew 1986 correlation functional (BP86). [77, 78] The 6-31+g* basis set was used for carbon and oxygen atoms; the 6-31+g** basis set was used for hydrogen atoms; and the LANL2DZ basis set was used for iron atoms. [79–81] The LANL2DZ effective core potential were used for iron atoms to account for relativistic effects. [82] Transition states were calculated using the combined synchronous transit-guided and quasi-Newton (STQN) method. [83,84] All transition states were verified by following the appropriate eigenvectors, i.e., those eigenvectors corresponding to the imaginary frequency, to their interconnected stationary points. The reported energies for fully optimized molecular structures correspond to zero-point corrected electronic energies. The Cartesian coordinates for all fully optimized molecular geometries are provided in Appendix B. Frequency calculations were done for all local minima and saddle points and have not been scaled. [72]

Since species $\mathbf{B}_1$ has been proposed to be most stable in the triplet spin state, I have modeled the formation of **C** from the triplet potential of $Fe(CO)_3(\eta^2$-1-butene) ($\mathbf{B}_1$). One-dimensional slices of ground singlet ($S_0$) and triplet ($T_1$) potential energy surfaces were calculated by performing successive partial geometry optimizations and energy calculations in the triplet and singlet spin states of $\mathbf{B}_1$ at fixed distances between the iron and the $\gamma$-hydrogen (ca. 1.5 to 4 Å). This method is qualitatively effective at describing the dynamics of spin-forbidden reactions in transition-metal compounds, but the one-dimensional slices of the potential energy surfaces calculated using this method are approximate since the true reaction pathways have high dimensionality in phase space. [38,85] The partial optimization calculations were also performed using the B3LYP [86–88] functional to test their accuracy in comparison to experiment, [56,75,89–91] and these results are presented in Appendix A. I have also performed the calculations of slightly different starting geometries of $\mathbf{B}_1$ to verify the location of the crossing point. These calculations are discussed further in the Appendix A. Transition state calculations were performed to identify the barriers to forming all **C** isomers identified by Cedeno et al. from the singlet forms of **B** and from the isomers of **C** identified by Cedeno et al. [75]

## 3.3 Experimental Results: Nano- through microsecond time-resolved IR spectroscopy of $Fe(CO)_4(\eta^2\text{-1-hexene})$ in 1-hexene solution

Nano- and microsecond time-resolved IR spectra of **A** in neat 1-hexene solution after laser irradiation at 266 nm are presented in Figure 3.2a and 3.2b, respectively. Table 3.1 shows peak assignments and the dynamics of all features. There are six features observed in Figure 3.2a, three negative peaks, assigned to **A** (1977, 2000 and 2078 $cm^{-1}$), two strong positive peaks centered at 1990 and 2058 $cm^{-1}$ and a small positive peak centered at 1930 $cm^{-1}$. All of the positive features are discernible at 25 ns and do not have dynamics between 25 ns and 1 $\mu$s. The large positive peaks at 1990 and 2058 $cm^{-1}$ are assigned to the anti-symmetric and symmetric carbonyl stretches of **C**, respectively. The peak assignments are made on the basis of literature assignments and DFT-calculated CO stretching frequencies (Table 3.1). [36, 67] The spectra in Figure 3.2a are noticeably different from the spectra of the same system measured by Glascoe et al. on the picosecond time-scale, which showed intense $\mathbf{B}_1$ absorptions (1931 and 2031 $cm^{-1}$), but no peaks corresponding to **C**. [36] By 25 ns the features assigned to $\mathbf{B}_1$ are no longer observable; instead, the **C** peaks have grown in, showing that $\mathbf{B}_1$ has rearranged to form **C** on a time-scale of 5–25 ns. [36] Assuming that the oscillator strengths of the analogous CO stretching modes of $\mathbf{B}_1$ and **C** are similar, the absence of $\mathbf{B}_1$ peaks indicates that the equilibrium between $\mathbf{B}_1$ and **C** favors species **C**.

In the spectra measured on a microsecond time-scale (Figure 3.2b), a new absorption at 1969 $cm^{-1}$ is observed and assigned to either $Fe(CO)_3(\eta^2\text{-1-hexene})_2$ ($\mathbf{D}_1$) or

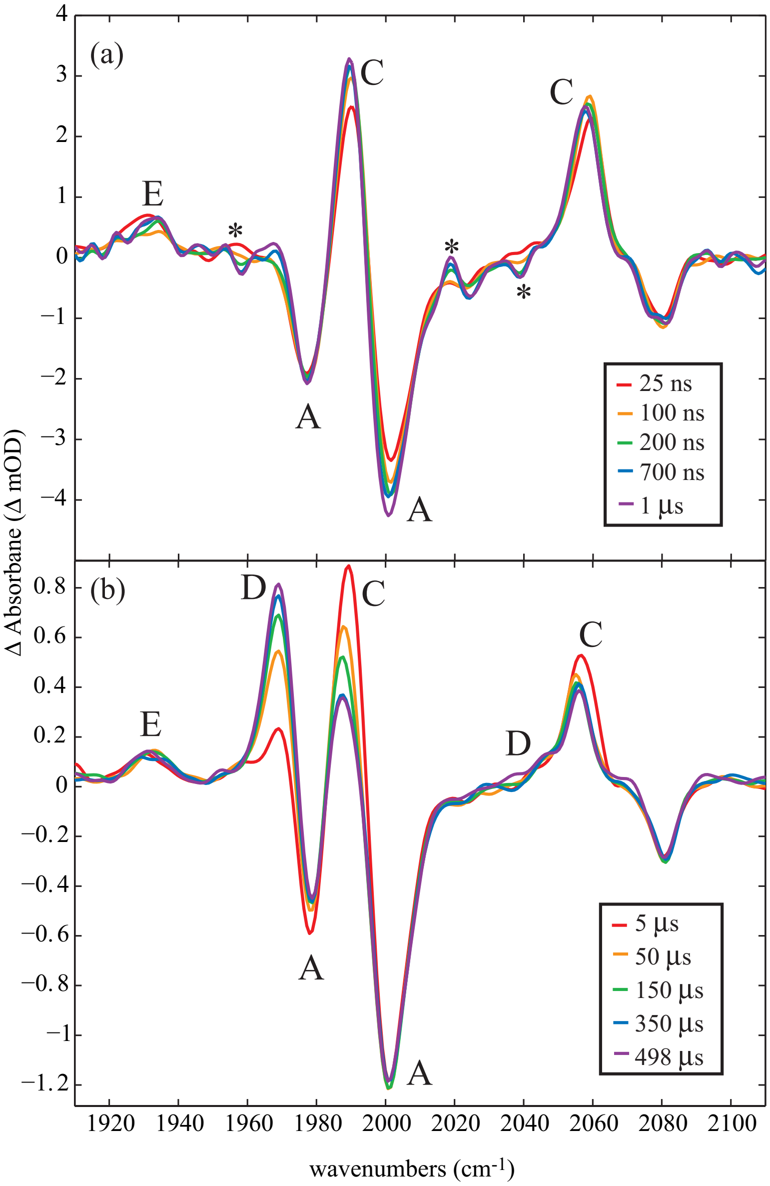

Figure 3.2: Transient IR spectra of $Fe(CO)_4(\eta^2$-1-hexene) (**A**) in solution with neat 1-hexene on the (a) nanosecond and (b) microsecond time-scales. The oscillations marked with '*' are experimental artifacts and are discussed further in Appendix A.

| **Species** | **Frequency ($\mathbf{cm^{-1}}$)** | | | $\tau$ (**$\mu$s**) | **Trend** |
|---|---|---|---|---|---|
| | **Exp.** | **Lit.** | **DFT** | | |
| $Fe(CO)_4(\eta^2$-1-hexene) | 1977 | 1981 | 1986 | 28±6 | rise |
| (**A**) [36] | | | | 170±45 | rise |
| | 2000 | 2002 | 1996 | no change | |
| | 2078 | 2083 | 2003 | no change | |
| $Fe(CO)_3(\eta^2$-1-hexene) | N/A | 1932 | 1960/72 ($S_0$) | no change | |
| (**B**$_1$) [36] | | | 1946/51 ($T_1$) | no change | |
| | N/A | 2031 | 2029 ($S_0$) | no change | |
| | | | 2009 ($T_1$) | no change | |
| $HFe(CO)_3(\eta^3$-$C_6H_9)$ | 1990 | 1994 | 1988 | 19±2 | decay |
| (**C**) [36] | | | | 145±4 | decay |
| | obscured | 2003 | 1991 | N/A | |
| | 2058 | 2060 | 2045 | 12±2 | decay |
| | | | | 130±10 | decay |
| $Fe(CO)_3(\eta^2$-hexene$)_2$ | 1969 | 1972 | 1963/60 | 20±2 | rise |
| (**D**) [67] | | | | 141±5 | rise |
| | obscured | 1977 | 1974/1975 | refer to **A** | |
| | 2045 | 2048 | 2033/30 | obscured | |
| $Fe(CO)_3(\eta^2$-1-hexene)(alkyl) (**E**) | 1930 | N/A | N/A | no change | |

Table 3.1: Dynamics of photoproducts of $Fe(CO)_4(\eta^2$-1-hexene) (**A**) in neat 1-hexene solution observed by time-resolved IR spectroscopy. [36, 67] The literature frequencies of **A** and **D** are estimated from $Fe(CO)_4(\eta^2$-1-pentene) and $Fe(CO)_3$(pentene$)_2$, respectively. The DFT calculated CO stretching modes of $HFe(CO)_3(\eta^3$-$C_6H_9)$ correspond to the $\mathbf{C}_{endo}$ isomer. The DFT calculated CO stretching modes for the $\mathbf{C}_{exo}$ isomer are at 1987, 1993 and 2046 $cm^{-1}$. The analogous modes for the $\mathbf{C}_{mer}$ isomer are at 1978, 1983 and 2042 $cm^{-1}$. The dynamics of the 1977 $cm^{-1}$ bleach are attributed to an overlapping **D** peak centered at 1977 $cm^{-1}$. The first set of DFT calculated CO stretching frequencies correspond to the $\mathbf{D}_1$ isomer and the second set correspond to the $\mathbf{D}_2$ isomer.

$Fe(CO)_3(\eta^2$-1-hexene$)(\eta^2$-2-hexene) ($\mathbf{D}_2$) on the basis of the literature values and DFT-calculated CO stretching frequencies (Table 3.1). [36, 67, 68, 92] Additionally, the peaks labeled **C** decay on the microsecond time-scale. Kinetics plots for the **C** and **D** peaks are displayed in Figure 3.3 and are both well fit to a biexponential function (solid red line). Figure 3.3 also shows a single exponential fit to the data (dashed blue line). The single exponential does not fit the data adequately as it is not able to capture the early time dynamics. The biexponential fit to the data shows that the **D** peak grows in with fast rise time of 22 ± 2 $\mu$s and a slow rise time of 158 ± 5 $\mu$s. Similarly, the intensities of **C** peaks decay with an average fast decay time of 16 ± 2 $\mu$s and average slow decay time of 138 ± 7 $\mu$s. The biexponential dynamics of the **C** and **D** peaks suggest that **C** is reacting to form both isomers of **D**, i.e., $Fe(CO)_3(\eta^2$-1-hexene$)_2$ ($\mathbf{D}_1$) and $Fe(CO)_3(\eta^2$-1-hexene$)(\eta^2$-2-hexene) ($\mathbf{D}_2$). However, I do not expect to be able to distinguish between species $\mathbf{D}_1$ and $\mathbf{D}_2$ by IR spectroscopy since the CO modes are expected to be nearly identical for the two isomers (Table 3.1). Species **D** is predicted to have two additional peaks at 2048 $cm^{-1}$ and 1977 $cm^{-1}$. The former is a small shoulder of the 2058 $cm^{-1}$ peak centered at 2045 $cm^{-1}$, and the latter is masked by the parent bleach at 1977 $cm^{-1}$.[1] The intensity of the bleach at 1977 $cm^{-1}$ decreases with a fast time constant of 28 ± 6 $\mu$s and a slow time constant of 170 ± 45 $\mu$s, but the other parent bleaches (2078 and 2000 $cm^{-1}$) do not have dynamics on the microsecond time-scale. Therefore, I attribute the dynamics of the parent bleach at 1977 $cm^{-1}$ to the dynamics of an overlapping peak assigned to **D**.

The small peak centered at 1930 $cm^{-1}$ is assigned to an alkyl-solvated form of

---

[1] The dynamics of the shoulder at 2045 $cm^{-1}$ are masked by the dynamics of the neighboring peak at 2058 $cm^{-1}$.

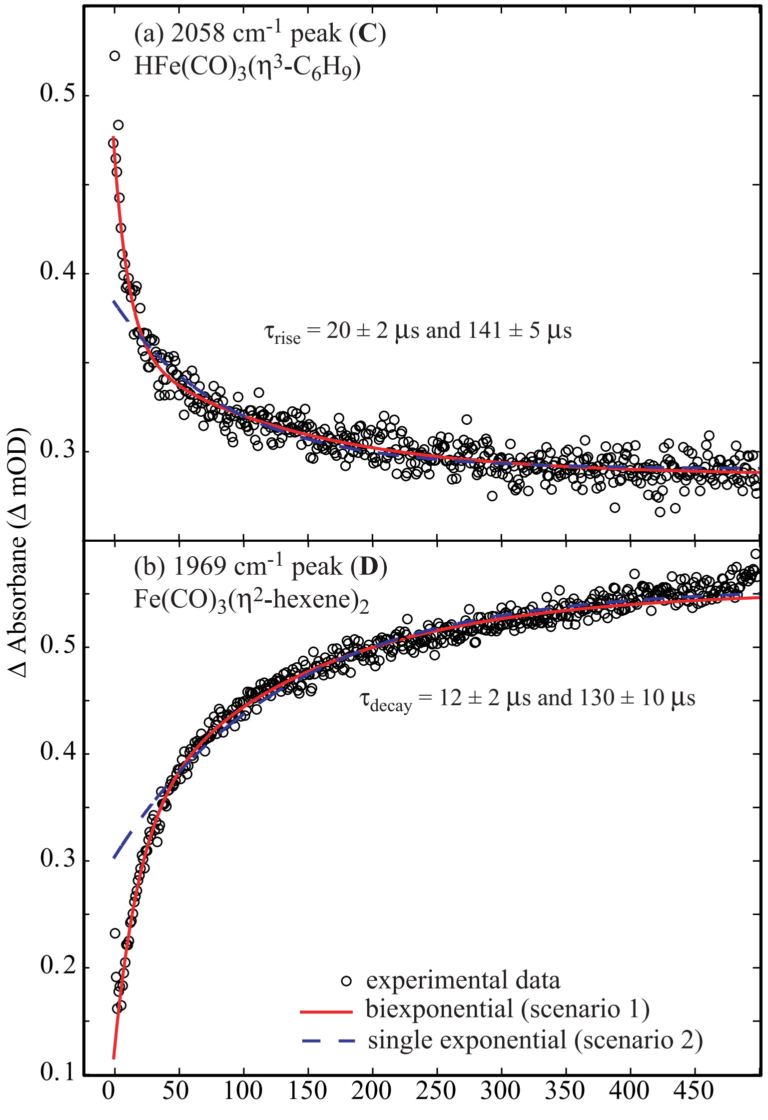

Figure 3.3: Kinetic traces of the 1990 and 1969 cm$^{-1}$ peaks (**C** and **D**). Note that The time constants reported in the text are average values, while the time constants in the figure are for the specific **C** and **D** peaks displayed.

$Fe(CO)_3(\eta^2$-1-hexene)(alkyl) (**E**), solvated either by the alkyl portion of the 1-hexene ligand or the alkyl portion of a token ligand from the bath. I have performed control experiments of **A** in solution with neat cyclohexane and found a similar species. The **E** peak does not have dynamics out to 500 $\mu$s indicating that it is a side-product to the iron-assisted alkene-isomerization reaction. Species **E** is not expected to be stable since alkane ligands generally interact weakly with coordinatively unsaturated transition-metal complexes. Ultimately, **E** will either reform **A** by collision with a carbonyl group, dimerize after collision with another metal complex or enter the catalytic cycle via rearrangement to **C** or **D**.[2] The lifetime of **E** is limited by the rate of diffusion and weak binding strength of the saturated alkane, and so **E** is expected to decay on the micro- through millisecond time-scale. [35, 93]

The high selectivity to form **D** from **C** rather than from $\mathbf{B}_1$ shows that the barrier of the $\mathbf{B}_1 \rightarrow \mathbf{D}$ reaction is significantly greater than barrier to the $\mathbf{B}_1 \rightarrow \mathbf{C}$ reaction, implying that the $\mathbf{C} \rightarrow \mathbf{D}$ reaction does not proceed through a $\mathbf{B}_1$ intermediate as predicted by past gas phase work (Figure 3.1). This is further supported by the correlation between the dynamics of the **C** and **D** peaks. Moreover, the results suggest that **C** is the key intermediate in the isomerization reaction. If the reaction proceeds through **C**, shifting the location of the double bond to form either isomer of **D** is expected to be facile since the $\eta^3$-bound ligand on **C** is a transitional structure between a 1-hexene and a 2-hexene ligand. [14, 68, 73]

---

[2] Based on the amplitude of the 1930 cm$^{-1}$ peak, which is expected to be the largest peak in the **E**, I expect the population of **E** to be small. Therefore, the contribution to the catalytic cycle will be small and not detectable

## 3.4 Results and Discussion

The experimental results presented above have been analyzed in the context of DFT calculations to elucidate the details of the isomerization mechanism that are not apparent from the experiments alone. This section is divided into two parts. In section 3.4.1, I present the details of the $\mathbf{B}_1$→**C** reaction, specifically the role of the transients in the $T_1$ state; in section 3.4.2, I discuss the mechanism for the formation of $\mathbf{D}_1$ and $\mathbf{D}_2$ in light of the biexponential dynamics of the **C** and **D** peaks and the high barrier to the $\mathbf{B}_1$→**D** reaction. On the basis of this combined experimental and computational study, I present a novel mechanism for iron-catalyzed alkene isomerization in Figure 3.8.

### 3.4.1 Mechanism for the formation of $\mathbf{HFe(CO)_3(\eta^3\text{-}C_6H_9)}$

The experimental results imply an isomerization mechanism that is different from the mechanism presented in the literature (Figure 3.1). [13] In solution, $\mathbf{B}_1$ undergoes an internal C–H bond activation reaction to form **C** on an early nanosecond time-scale, but does not coordinate a second alkene from the bath to form **D**. It has been proposed that this selectivity is due to the high spin state of $\mathbf{B}_1$. [36] Additionally, many authors have proposed that the triplet spin state of $\mathbf{B}_1$ contributes to the extraordinary efficiency of the isomerization reaction. [63, 69, 71, 86, 94] I have performed detailed DFT calculations to test this hypothesis and to identify the role of the ground triplet state in the formation of **C**. Unfortunately, an explicit, time-dependent simulation of the system is not computationally feasible because the dynamics following photolysis involve multiple potentials. Furthermore, a precise calculation of spin-orbit coupling is necessary to accurately assess the spin-forbidden dynamics. Instead, one-dimensional sections of the relevant potential energy surfaces have been used to offer a qualitative picture for the dynamics of the system. These results lend considerable insight to the isomerization mechanism when they are analyzed in the context of the experimental results.

Figure 3.4 shows the energy of the both the ground singlet ($S_0$) and triplet ($T_1$) potential energy surfaces plotted as a function of the Fe–$\gamma$H distance, shown in red and blue, respectively. These potentials were calculated by fixing the Fe–$\gamma$H distance and allowing the remaining degrees of freedom in the system to fully optimize. Identical calculations were performed with a B3LYP functional to determine if the BP86 functional led to artificially stable singlet states. The calculations performed with the B3LYP functional (refer to Appendix A) do not agree with the experimental results or previously published experimental work because the calculations predict that the allyl hydride complex (**C**) is less energetically stable than the lowest energy form of the CO-loss complex (**B**). [13,14,36,62,63,67,68,75]

The triplet curve in Figure 3.4 shows that $^3\mathbf{B}_1$ is most stable with a Fe–$\gamma$H distance of ca. 3.3 Å and that increasing or decreasing that bond distance results in a rise in energy. The singlet curve shows two local minima along the Fe–$\gamma$H coordinate at Fe–$\gamma$H distances of 3.4 Å and 1.8 Å: $\mathbf{B}_1$* and $\mathbf{B}_1$, respectively. The fully optimized structures for these local minima are shown in Figure 3.5. The structures of $^3\mathbf{B}_1$ and $\mathbf{B}_1$* (Figures 3.5a- 3.5b) are nearly identical; the $\gamma$H in $^3\mathbf{B}_1$ and $\mathbf{B}_1$* does not interact with the metal center and is bound only to the alkene moiety. Furthermore, these structures are significantly different from the $\mathbf{B}_1$ structure in Figure 3.5c that is discussed in detail below.

Figure 3.4 shows that the $S_0$ and $T_1$ surfaces are nearly isoenergetic in the vicinity

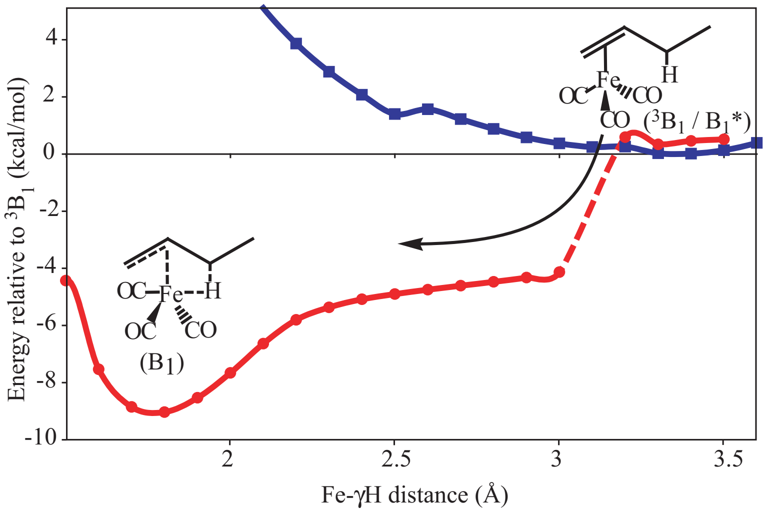

Figure 3.4: DFT calculated one-dimensional potential energy surfaces of the ground singlet and triplet spin states ($S_0$ and $T_1$) of Fe(CO)$_3$(1-butene) along the Fe–$\gamma$H bond. The curves are generated by performing successive partial geometry optimizations at fixed values of the Fe–$\gamma$H distance. The lines that connect the data points are guides to the eye. The dashed line on the $S_0$ potential at 3 Å corresponds to a small shift in the position of the CO ligands and is not physically meaningful.

| **Species** | **Energy** | **Enthalpy** |
|---|---|---|
| $\mathbf{B}_1$* | 0.880 | -0.156 |
| $\mathbf{B}_2$ | -8.82 | -9.68 |
| $\mathbf{B}_1$ | -8.25 | -9.21 |
| $\mathbf{D}_1$ | -9.15 | -10.5 |
| $\mathbf{C}_{endo}$ | -11.2 | -12.8 |
| $\mathbf{C}_{exo}$ | -12.2 | -13.2 |
| $\mathbf{C}_{mer}$ | -8.86 | -9.73 |
| $\mathbf{D}_2$ | -21.3 | -22.7 |
| $\mathbf{B}_1\rightarrow\mathbf{C}_{exo}$ **TS** | 8.69 | 7.44 |
| $\mathbf{B}_2\rightarrow\mathbf{C}_{exo}$ **TS** | 8.39 | 6.90 |
| $\mathbf{B}_2\rightarrow\mathbf{C}_{mer}$ **TS** | -0.34 | -1.37 |
| $\mathbf{C}_{endo}\rightarrow\mathbf{C}_{mer}$ **TS** | -0.73 | -1.71 |
| $\mathbf{C}_{mer}\rightarrow\mathbf{C}_{exo}$ **TS** | -0.52 | -1.72 |
| $\mathbf{B}_1\rightarrow\mathbf{C}_{endo}$ **TS** | -4.58 | -5.74 |
| $\mathbf{B}_2\rightarrow\mathbf{C}_{endo}$ **TS** | 8.28 | -5.99 |

Table 3.2: Relative energy and enthalpy (kcal/mol) of the key intermediates in the iron-assisted alkene isomerization reaction scaled relative to lowest energy isomer of $^3\mathbf{B}_1$.

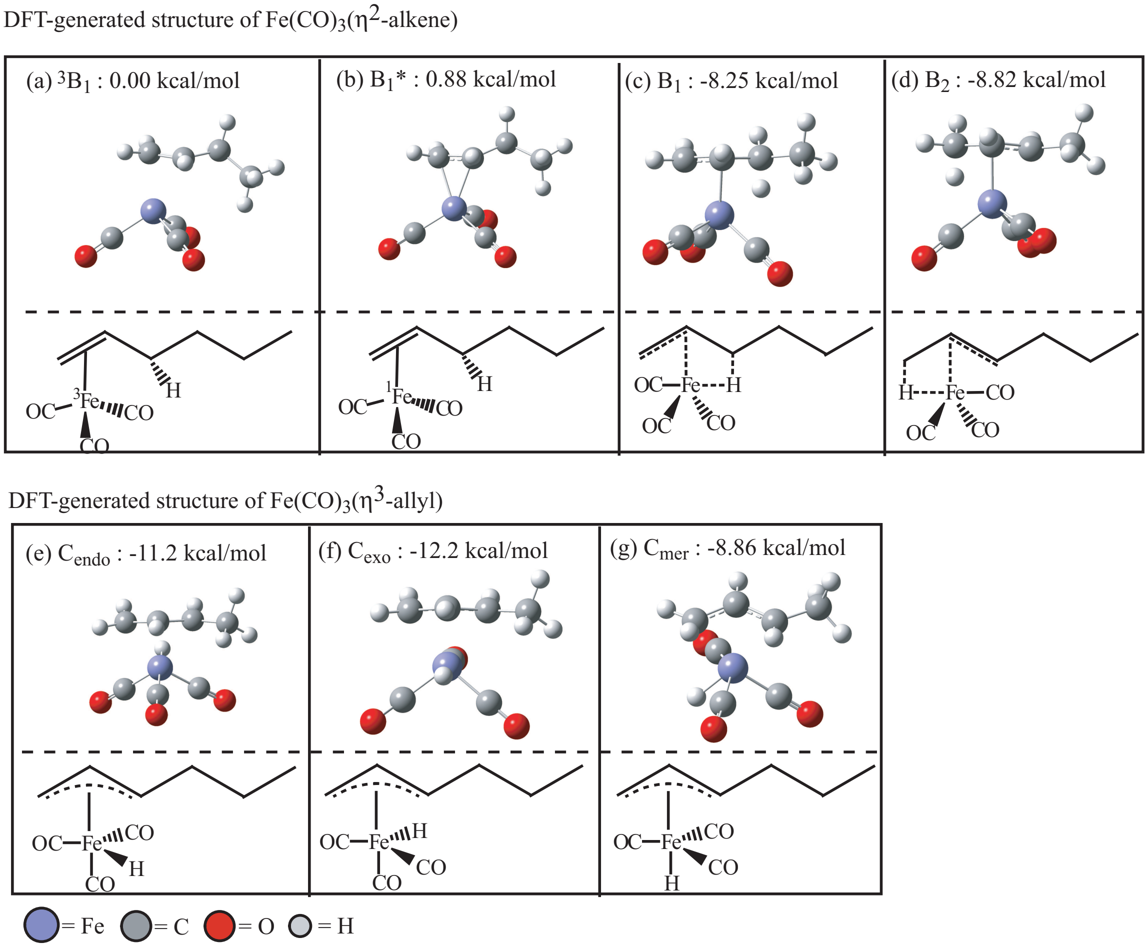

Figure 3.5: Calculated structures of (a) $^3$Fe(CO)$_3$($\eta^2$-1-butene) ($^3\mathbf{B}_1$), (b) $^1$Fe(CO)$_3$($\eta^2$-1-butene) ($\mathbf{B}_1$*****), (c) $^1$Fe(CO)$_3$($\eta^2$-1-butene) with a M–$\gamma$H–C agostic interaction ($\mathbf{B}_1$), (d) $^1$Fe(CO)$_3$($\eta^2$-2-butene) with a M–$\gamma$H–C agostic interaction ($\mathbf{B}_2$), (e) facial-endo HFe(CO)$_3$($\eta^3$-C$_4$H$_7$) ($\mathbf{C}_{endo}$), (f) facial-exo HFe(CO)$_3$($\eta^3$-C$_4$H$_7$) ($\mathbf{C}_{exo}$), (g) meridional HFe(CO)$_3$($eta^3$-C$_4$H$_7$) ($\mathbf{C}_{mer}$). The energies listed are relative to the lowest energy structure of $^3\mathbf{B}_1$. Below each DFT structure is the analogous structure observed in the experiments (i.e., with a hexene ligand).

| Species | Fe–$\alpha$C | Fe–$\beta$C | Fe–$\gamma$C | Fe–$\gamma$H | Fe–$\alpha$H |
|---|---|---|---|---|---|
| $^3\mathbf{B}_1$ | 2.15 | 2.37 | 3.29 | 3.35 | 2.63 |
| $\mathbf{B}_1$* | 2.04 | 2.04 | 3.16 | 3.35 | 2.71 |
| $\mathbf{B}_1$ | 2.11 | 1.98 | 2.28 | 1.77 | 2.68 |
| $\mathbf{B}_2$ | 2.25 | 1.99 | 2.17 | 2.67 | 1.78 |
| $\mathbf{C}_{endo}$ | 2.15 | 2.09 | 2.22 | 1.52 | 2.65 |
| $\mathbf{C}_{exo}$ | 2.15 | 2.08 | 2.22 | 1.52 | 2.68 |
| $\mathbf{C}_{mer}$ | 2.14 | 2.08 | 2.25 | 2.65 | 1.50 |
| $\mathbf{D}_1$ | 2.14 | 2.18 | 3.22 | 3.35 | 2.74 |
| $\mathbf{D}_1$ | 3.17 | 2.18 | 2.17 | 2.70 | 3.43 |

Table 3.3: Calculated structural parameters for key intermediates in the iron-assisted alkene isomerization reaction.

of the $^3\mathbf{B}_1$ and $\mathbf{B}_1$* local minima. Since the $^3\mathbf{B}_1$ and $\mathbf{B}_1$* are energetically and structurally similar, I expect that there is crossing point in the vicinity of these minima and that $^3\mathbf{B}_1$ is a short-lived structure. While $S_0$ and $T_1$ are close in energy at long Fe–$\gamma$H distances, when the distance decreases to less than 3 Å, the $S_0$ potential is lower in energy, suggesting that a spin-crossover to $S_0$ is thermodynamically favorable. These calculations are in agreement with past experimental work that showed that the allyl hydride complexes are more thermodynamically stable than the CO loss structures. [13,14,36,62,63,67,68,75] Species $^3\mathbf{B}_1$ undergoes a spin crossover from $T_1$ to $S_0$ to form $\mathbf{B}_1$*, [85,95] which is able to form a complex with an M–H–C agostic bond between the Fe atom and the $\gamma$H on the alkene moiety, species $\mathbf{B}_1$ (Figure 4c). The M–H–C agostic interaction stabilizes the complex by more than 8 kcal/mol. Species $\mathbf{B}_1$ is distinctly different from **C**, the allyl hydride complex, and can be thought of as an internally solvated form of the CO loss complex. Because this agostic interaction stabilizes the coordinatively unsaturated metal center, $\mathbf{B}_1$ is the most thermodynamically stable structure of $Fe(CO)_3(\eta^2$-1-butene). Agostic M–H–C bonds are common in organometallic complexes and have been proposed to stabilize coordinatively unsaturated transients to such an extent that further solvent coordination is not necessary. [39, 96] I was not able to identify a triplet structure with an agostic M–H–C, most likely because coordinatively unsaturated triplet metal centers do not interact favorably with saturated C–H bonds. [37, 38, 74] The other singlet forms of $Fe(CO)_3(\eta^2$-1-alkene), such as $\mathbf{B}_1$*****, are higher in energy than $^3\mathbf{B}_1$, and therefore, it is only thermodynamically favorable to form $\mathbf{B}_1$. Figure 3.5 also shows the 2-alkene isomer, $Fe(CO)_3(\eta^2$-2-butene) ($\mathbf{B}_2$), in which there is an agostic interaction between the $\alpha$C–H bond and the iron atom. Species $\mathbf{B}_2$ is nearly isoenergetic with $\mathbf{B}_1$.

Many authors argue that $Fe(CO)_3(\eta^2$-alkene) is most stable in the triplet spin state. [36, 62, 63, 67, 68] DFT calculations are in good agreement with this prediction; $^3\mathbf{B}_1$ is more energetically stable than the analogous singlet complex, $\mathbf{B}_1$***** (see Table 3.2 and Figure 3.4). However, the calculations also show evidence for a self-solvated form of $Fe(CO)_3(\eta^2$-alkene) ($\mathbf{B}_1$), which is structurally different and more thermodynamically stable than $^3\mathbf{B}_1$. The calculated CO modes for $\mathbf{B}_1$ and $^3\mathbf{B}_1$ (Table 3.1) are both in reasonable agreement with experiment, [36] given the accuracy of DFT calculations. [85] As a result, I cannot distinguish between the structures using their calculated CO stretching frequencies alone. Transition state calculations, discussed below, show that $\mathbf{B}_1$ will react to form **C** on a nanosecond time-scale, in agreement with experiment. In light of these results, I expect that the peaks assigned to $Fe(CO)_3(\eta^2$-1-hexene) ($\mathbf{B}_1$) observed on the picosecond time-scale are due to the singlet species ($\mathbf{B}_1$) and not the triplet ($^3\mathbf{B}_1$). [36]

Species $\mathbf{B}_1$ is structurally similar to the facial-endo isomer of **C** ($\mathbf{C}_{endo}$) (Figure 3.5), though the Fe–$\gamma$H bond distance is slightly shorter in $\mathbf{C}_{endo}$ and the hydrogen is not coordinated to the alkene ligand, suggesting that $\mathbf{B}_1$ is an intermediate structure between $^3\mathbf{B}_1$ and $\mathbf{C}_{endo}$. I have performed a fully optimized transition state calculation for the $\mathbf{B}_1 \rightarrow \mathbf{C}_{endo}$ reaction and found that the barrier is 3.7 kcal/mol and the reverse reaction barrier is 6.6 kcal/mol (Table 3.2). The calculated barrier for the $\mathbf{B}_2 \rightarrow \mathbf{C}_{endo}$ reaction is 4.5 kcal/mol. These barriers correspond to a time-scale of pico- to nanoseconds for the formation of $\mathbf{C}_{endo}$ from $\mathbf{B}_1$, in agreement with the experimental results. [97]

I have also performed transition state calculations to determine the barrier to $\mathbf{B}_1 \rightarrow \mathbf{C}$ reaction for the other isomers of $\mathbf{C}$ (i.e. $\mathbf{C}_{endo}$ and $\mathbf{C}_{mer}$; see Figure 3.5f- 3.5g), that have been identified by Cedeno et al. (Figure 3.6 and Table 3.2). In agreement with Cedeno's work, I found that the $\mathbf{C}_{endo}$ and $\mathbf{C}_{exo}$ structures are more thermodynamically stable than the $\mathbf{C}_{mer}$ structure. [75] However, while $\mathbf{C}_{exo}$ is the most thermodynamically stable isomer, the barrier to the $\mathbf{B}_1 \rightarrow \mathbf{C}_{exo}$ reaction is nearly an order of magnitude higher than the barrier to the $\mathbf{B}_1 \rightarrow \mathbf{C}_{endo}$ reaction, indicating that only the $\mathbf{C}_{endo}$ isomer is formed directly from $\mathbf{B}_1$ on the early nanosecond time-scale. On a longer time-scale (ca. 500 nanoseconds), $\mathbf{C}_{endo}$ isomerizes to $\mathbf{C}_{exo}$ via $\mathbf{C}_{mer}$ or $\mathbf{B}_2$, as shown in Figure 3.6. On this longer time-scale, all of the $\mathbf{B}$ and $\mathbf{C}$ isomers on the $S_0$ potential will be in equilibrium,[3] but since the $\mathbf{C}_{exo}$ and $\mathbf{C}_{endo}$ structures are the most thermodynamically stable, I expect that the equilibrium favors them, in agreement with previous DFT work and the spectra in Figure 3.2. [75] Note that the spectral resolution of the experiments does not allow us to distinguish between the CO stretching modes of the different $\mathbf{C}$ isomers, These results are also in qualitative agreement with low temperature studies of $Fe(CO)_4(\eta^2$-propene) that

---

[3] By simple transition state theory I estimate that the barriers to forming $\mathbf{C}_{mer}$ and $\mathbf{C}_{exo}$ isomers from $\mathbf{B}_2$ and $\mathbf{C}_{mer}$, respectively, correspond to a time constant of 200 ns.

found that $\mathbf{B}_1$ thermally converts to one of the **C** isomers at 5 K and the other at 50 K. [63]

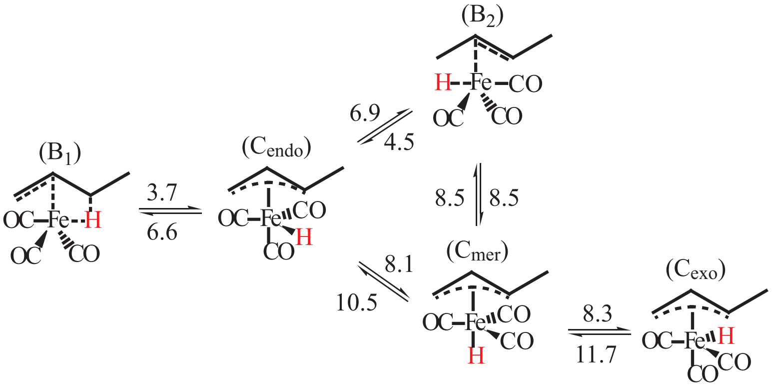

Figure 3.6: 1,3-hydrogen migration in Fe(CO)$_3$($\eta^2$-alkene) (**B**) through allyl hydride intermediates (**C**). The barrier to each step is listed in units of kcal/mol. The $\mathbf{B}\rightarrow\mathbf{C}_{endo}$ reactions ($\mathbf{B} = \mathbf{B}_1$ and/or $\mathbf{B}_2$) are not expected to be relevant since the barriers to these reactions are an order of magnitude higher than the barriers to the reactions shown here.

Figure 3.6 shows the equilibrium between the different isomers of **B** and **C**, in which the hydrogen (red) is migrating between the $\alpha$- and $\gamma$-carbons on the alkene ligand and the double bond is moving between 2-butene and 1-butene locations. Previous low-temperature $^1$H-NMR studies of the $\eta^3$-propyl analog of **C** provide further support for this type of reversible 1,3-hydrogen migration in the system. Moreover, the study suggests the existence of agostic structures, akin to $\mathbf{B}_1$ and $\mathbf{B}_2$. [63] The DFT results illustrate that the only agostic structures are in the singlet spin state ($\mathbf{B}_1$ and $\mathbf{B}_2$), providing further evidence that $^3\mathbf{B}_1$ is not directly involved in the isomerization process. For clarity, hereafter the **C** label corresponds to the facial-endo isomer.

### 3.4.2 Mechanism for the formation of Fe(CO)$_3$($\eta^2$-hexene)

I hypothesize that species **C** is the key intermediate in the isomerization mechanism. [14, 36, 68, 73] In the following section, I use DFT modeling and basic kinetic analysis to elucidate the reactivity of **C** on the microsecond time-scale.

### Analysis of biexponential dynamics

The spectra in Figure 3.2b show that **C** decays to form **D** on a microsecond time-scale. The kinetic traces of the **C** and **D** peaks, shown in Figure 3.3, are well fit to biexponential functions giving an average fast time constant of 20 $\mu$s and an average slow time constant of 150 $\mu$s. These biexponential kinetics imply that **C** reacts to form to two isomers of **D** via two different pathways, $\mathbf{C}\rightarrow\mathbf{D}_1$ and $\mathbf{C}\rightarrow\mathbf{D}_2$. However, on the basis of the experiments alone I cannot determine which of these pathways has the lower barrier. I have used basic kinetic analysis of the parallel $\mathbf{C}\rightarrow\mathbf{D}_1$ and $\mathbf{C}\rightarrow\mathbf{D}_2$ pathways coupled with DFT calculated energies of **C** and **D** to elucidate the details of the reactions.

Figure 3.7 shows the DFT-calculated structures of $\mathbf{D}_1$ and $\mathbf{D}_2$ and the relative structural parameters for both complexes are presented in Table 3.3. Structurally, the only significant difference between $\mathbf{D}_1$ and $\mathbf{D}_2$ is the location of the double bond on the alkene ligand. Similarly, the calculated CO stretching modes of $\mathbf{D}_1$ and $\mathbf{D}_2$ are nearly identical and are in excellent agreement with the experimentally observed peaks (Table 3.1). Despite the structural similarities between $\mathbf{D}_1$ and $\mathbf{D}_2$, DFT calculations indicate that there is a significant energetic difference between them (Table 3.2).[4] Most notably, species $\mathbf{D}_2$ is ca. 10 kcal/mol lower in energy than **C**, while species $\mathbf{D}_1$ is slightly higher in energy than **C**.

These results suggest that there should be an equilibrium between $\mathbf{D}_1$ and **C**, and that the $\mathbf{C}\rightarrow\mathbf{D}_2$ reaction is irreversible ($\Delta$E = 12.2 kcal/mol):

---

[4] DFT geometry optimization and energy calculations have been performed for the *cis*-isomer of $\mathbf{D}_2$ and indicated that this isomer is isoenergetic with the *trans*-isomer

$$\mathbf{C} + \text{alkene} \underset{k_{-1}}{\overset{k_1}{\rightleftharpoons}} \mathbf{D}_1$$

and

$$\mathbf{C} + \text{alkene} \xrightarrow{k_2} \mathbf{D}_2$$

The rate equations for **C** and **D** for these parallel reactions are

$$\frac{d[\mathbf{C}]}{dt} = k_1[\mathbf{D}_1] - k[\mathbf{C}] \tag{3.1}$$

and

$$\frac{d[\mathbf{D}]}{dt} = -k_1[\mathbf{D}_1] + k[\mathbf{C}] \tag{3.2}$$

where $\mathrm{k} = (\mathrm{k}_{-1} + \mathrm{k}_2)$ and $[\mathbf{D}] = [\mathbf{D}_1] + [\mathbf{D}_2]$.

According to equations 3.1 and 3.2, I would expect to observe a biexponential decay of the **C** peaks and a corresponding biexponential rise of the **D** peaks, assuming that the CO stretching modes of the **D** peaks are identical within the spectral resolution of the experiment. This prediction is in excellent agreement with the observed kinetics. The fast rate constant corresponds to the time it takes to establish an equilibrium between **C** and $\mathbf{D}_1$ ($k_1$) and the slow rate constant corresponds to the irreversible $\mathbf{C}\rightarrow\mathbf{D}_2$ reaction ($k = k_{-1} + k_2$). In other words, the equilibrium between **C** and $\mathbf{D}_1$ is established in 20 $\mu$s, but because **C** and $\mathbf{D}_1$ are nearly isoenergetic, once the equilibrium has been established, there is still population of **C** available to react via the slow pathway to form $\mathbf{D}_2$. This mechanism is presented in Figure 3.7. [97] Note that if I neglect the $\mathbf{D}_1\rightarrow\mathbf{C}$ back reaction, I would expect to observe a single exponential decay of the **C** and a corresponding single exponential rise of the **D** peaks with rate constants of $(k_1 + k_2)$.

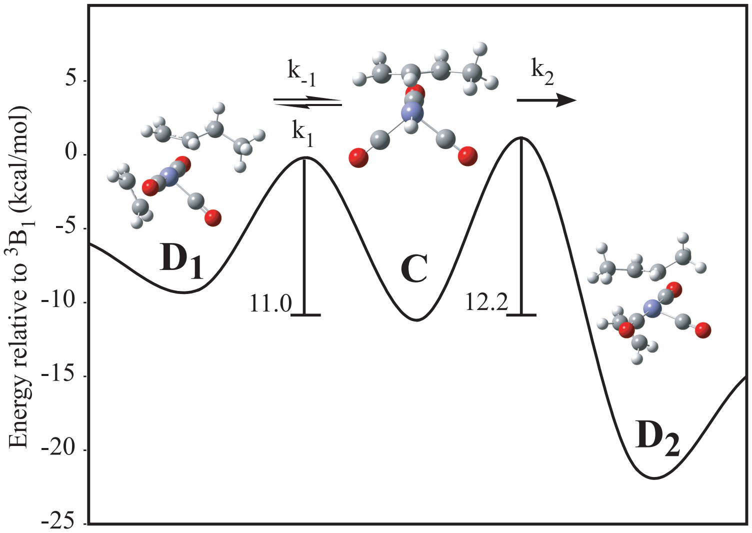

Figure 3.7: DFT calculated relative energies of species **C**, $\mathbf{D}_1$ and $\mathbf{D}_2$ and the energetic barriers that connect them as determined by the time-resolved IR experiments. The energies of all minima and transition states are scaled relative to the lowest energy structure of $^3\mathbf{B}_1$.

If $\mathbf{D}_2$ is formed via the fast pathway, so that $k_2 > k_1$, the decay of **C** will be a single exponential because the $\mathbf{C}\rightarrow\mathbf{D}_2$ reaction will be completed before the $\mathbf{C}\rightarrow\mathbf{D}_1$ occurs.[5] The $\mathbf{C}\rightarrow\mathbf{D}_2$ reaction would be ca. 90% complete within 45 $\mu$s, [97] and there would be no substantial back reaction since $\mathbf{D}_2$ is considerably more stable than **C**. As a result, there would not be a significant population of **C** remaining to react via slower pathway to form $\mathbf{D}_1$. Therefore, if the $\mathbf{C}\rightarrow\mathbf{D}_2$ reaction is faster than the $\mathbf{C}\rightarrow\mathbf{D}_1$ reaction, I would expect to observe a single exponential decay of the **C** peaks and a corresponding single exponential rise of the **D** peak due to species $\mathbf{D}_2$, but no observable formation of species $\mathbf{D}_1$. [97] The

---

[5] If $\mathbf{D}_2$ is formed via the fast pathway, rate equations can be simplified to

$$\frac{d[\mathbf{C}]}{dt} = -k_2[\mathbf{C}] \tag{3.3}$$

and

$$\frac{d[\mathbf{D}]}{dt} = k_2[\mathbf{C}] \tag{3.4}$$

Here the $\mathbf{D}_1$ and **C** back reaction can be neglected because $k_2 >> k_{-1}$ according to the DFT results summarized in Table 3.2.

dashed blue line Figure 3.3 shows a single exponential fit to the experimental data. The single exponential function gives a poor fit to the data since it does not capture the dynamics before ca. 50 $\mu$s.

Using generalized transition state theory to estimate the barriers from the experimentally observed time constants, I find that the barrier for the $\mathbf{C}\rightarrow\mathbf{D}_1$ pathway is 1.2 kcal/mol lower in energy than the barrier to the $\mathbf{C}\rightarrow\mathbf{D}_2$ pathway. The DFT calculated molecular structure of **C** gives qualitative insight into the reason for the difference between the barriers (Table 3.2). The $\gamma$C on the alkene ligand is slightly closer than the $\gamma$C to the metal center in **C**. The minor asymmetry in the allyl hydride structure, which is observed for all of the **C** isomers (Table 3.3), suggests that there is a slightly lower barrier to forming a structure with 1-alkene ligand compared to the 2-alkene species. Note that I cannot distinguish which **C** isomer reacts to form **D** or if the **C** isomers react differently in the $\mathbf{C}\rightarrow\mathbf{D}$ reaction. The DFT calculated barriers (Figure 3.6) indicate that conversion between the **C** isomers occurs on a nanosecond time-scale, and thus I do not expect to be able to observe any of the related dynamics on the time-scale of the $\mathbf{C}\rightarrow\mathbf{D}$ reaction. Furthermore, I am unable to distinguish between the CO stretching modes of the different **C** isomers by IR spectroscopy (Table 3.1).

### $\mathbf{HFe(CO)_3(\eta^3\text{-}C_6H_9)\rightarrow Fe(CO)_3(\eta^2\text{-}C_6H_{10})_2}$: Associative vs. Dissociative

One of primary goals of this work was to experimentally determine the mechanism for forming **D** in solution phase. The $\mathbf{C}\rightarrow\mathbf{D}$ reaction can be thought of as an intramolecular ligand substitution reaction in which the hydrogen bound to the metal center in **C** is replaced by an alkene ligand from the bath to form **D**. Ligand substitution reactions are generally described using either associative or dissociative mechanisms. In the context of this work, a dissociative mechanism does not correspond to the full dissociation of the hydrogen from the metal complex but instead corresponds to a step-wise mechanism in which the hydrogen is dissociated from the metal center in **C** and re-coordinates to the alkene moiety to form $\mathbf{B}_1$. Species $\mathbf{B}_1$ is then solvated by an alkene molecule from the bath to form **D**. In contrast, the associative mechanism corresponds to a direct solvation of **C** by an alkene to form **D**, so that the transfer of the hydrogen from the metal to the alkene and the solvation of the metal center happens concomittantly. [1] Previous gas phase studies have proposed a dissociative mechanism in which the triplet form of $\mathbf{B}_1$ ($^3\mathbf{B}_1$) is an intermediate in the $\mathbf{C}\rightarrow\mathbf{D}$ reaction. [13, 14] However, the authors were not able to observe the $\mathbf{B}_1\rightarrow\mathbf{D}$ reaction and, therefore, were not able to rule out an associative mechanism. [13, 14] I have already established that $^3\mathbf{B}_1$ is extremely short-lived, if it is formed at all (Figure 3.4), and thus, $^3\mathbf{B}_1$ cannot be solvated to form $\mathbf{D}_1$ as is predicted in Figure 3.1. [34] However, the singlet form of $\mathbf{B}_1$ that is stabilized by a M–H–C agostic interaction is observable on the pico- through early nanosecond time-scales, and questions still remain about whether this singlet transient is an intermediate in the $\mathbf{C}\rightarrow\mathbf{D}$ reaction. [36]

This work provides direct experimental evidence that $\mathbf{B}_1$ is not an intermediate in the $\mathbf{C}\rightarrow\mathbf{D}$ reaction. The $\mathbf{B}_1\rightarrow\mathbf{D}$ reaction is not observable on a pico- through microsecond time-scales, [36] indicating that the barrier to this reaction is considerably higher than the barrier to the $\mathbf{B}_1\rightarrow\mathbf{C}$ reaction. If the barrier to the $\mathbf{B}_1\rightarrow\mathbf{D}$ reaction were lower, I would observe **D** peaks on the pico- through the nanosecond time-scales since both **D** isomers are thermodynamically stable. Additionally, I see no evidence for $\mathbf{B}_1$ peaks past 25 ns

(Figure 3.2). Thus, if $\mathbf{B}_1$ were an intermediate in the $\mathbf{C}\rightarrow\mathbf{D}$ rearrangement, it would have to be under steady-state conditions, i.e., the concentration of $\mathbf{B}_1$ would have to remain sufficiently low so that its dynamics are not observable. In order for $\mathbf{B}_1$ to be under steady-state conditions, the $\mathbf{B}_1\rightarrow\mathbf{D}$ reaction would have to be fast relative to the $\mathbf{B}_1\rightarrow\mathbf{C}$ reaction. [97] The experiments show the opposite trend, providing direct experimental evidence that $\mathbf{B}_1$ is not an intermediate in the $\mathbf{C}\rightarrow\mathbf{D}$ reaction. However, I cannot exclude the possibility that there is a different short-lived intermediate in the reaction that is so short-lived that it is not observable.

This mechanism, summarized in Figure 3.8, is different from the gas phase mechanism in Figure 3.1. The most notable difference between the mechanisms is that in Scheme 3 $\mathbf{B}_1$ is not an intermediate in the $\mathbf{C}\rightarrow\mathbf{D}$ rearrangement. While this mechanism is markedly different from the gas phase mechanism, the data presented in the gas phase studies do not preclude the mechanism that I propose. The dynamics of $\mathbf{B}_1$ were not observed in that work, and thus their data supports either mechanism. In contrast, this data provide the first direct experimental evidence that in the solution phase $\mathbf{B}_1$ is not an intermediate in the $\mathbf{C}\rightarrow\mathbf{D}$ reaction. [13, 14]

## 3.5 Conclusion

On the basis of this analysis, I present a novel mechanism for iron-catalyzed alkene isomerization, shown in Figure 3.8. UV irradiation of $Fe(CO)_4(\eta^2\text{-1-hexene})$ (**A**) leads to the dissociation of a single CO to form $^3Fe(CO)_3(\eta^2\text{-1-hexene})$ ($^3\mathbf{B}_1$), which undergoes a spin-crossover process on the sub-picosecond time-scale to form $Fe(CO)_3(\eta^2\text{-1-hexene})$ ($\mathbf{B}_1$).

The $\mathbf{B}_1 \rightarrow \mathbf{D}_1$ reaction does not occur, and instead $\mathbf{B}_1$ reacts to form **C** via an internal C–H bond cleavage process in 5–25 ns. Species **C** is solvated by a 1-hexene molecule from the bath to form $\mathrm{Fe(CO)_3(\eta^2\text{-1-hexene})_2}$ ($\mathbf{D}_1$) in ca. 20 $\mu$s. Species **C** and $\mathbf{D}_1$ are nearly isoenergetic and, as a result, are in equilibrium. In this step, **C** is solvated by the 1-hexene bath, and the hydrogen atom that is bound to the metal center moves to the $\alpha$-carbon on the 1-hexene. After equilibrium has been established between **C** and $\mathbf{D}_1$, **C** is again solvated by a 1-hexene molecule in ca. 150 $\mu$s. In this step, species **C** reacts to form $\mathrm{Fe(CO)_3(\eta^2\text{-1-hexene})(\eta^2\text{-2-hexene})}$ ($\mathbf{D}_2$)—the hydrogen atom that is bound to the metal center moves to the $\gamma$-carbon and the double bond migrates to the secondary position. Species $\mathbf{D}_2$ is 10 kcal/mol more stable than **C**, and therefore, the $\mathbf{C} \rightarrow \mathbf{D}_2$ reaction is irreversible, heavily favoring $\mathbf{D}_2$. To complete the catalytic cycle, the 2-hexene ligand is dissociated from $\mathbf{D}_2$ to form either $\mathbf{B}_1$ or **C**; however, I do not observe this step since it is expected to occur on a longer time-scale than I can investigate with this experiment. [13, 14]

The motivation for this work was to determine why photoactivated iron–carbonyl complexes are such extraordinary alkene-isomerization catalysts. Many authors have proposed that the efficiency of the reaction is linked to the high spin state of $\mathbf{B}_1$ since the turnover rate for the reaction catalyzed with photoactivated $\mathrm{Ru(CO)_5}$, a complex with only singlet transient species in the catalytic cycle, is much less efficient. [36, 62, 67, 68, 70, 98] However, this work indicates that the triplet form of $\mathbf{B}_1$ does not play a significant role in the isomerization reaction since it reacts to form a singlet form of $\mathbf{B}_1$ on a sub-picosecond time-scale. The singlet form of $\mathbf{B}_1$ is a internally solvated structure with an agostic M–H–C bond that stabilizes the structure so that it is stable on the pico- through early nanosecond

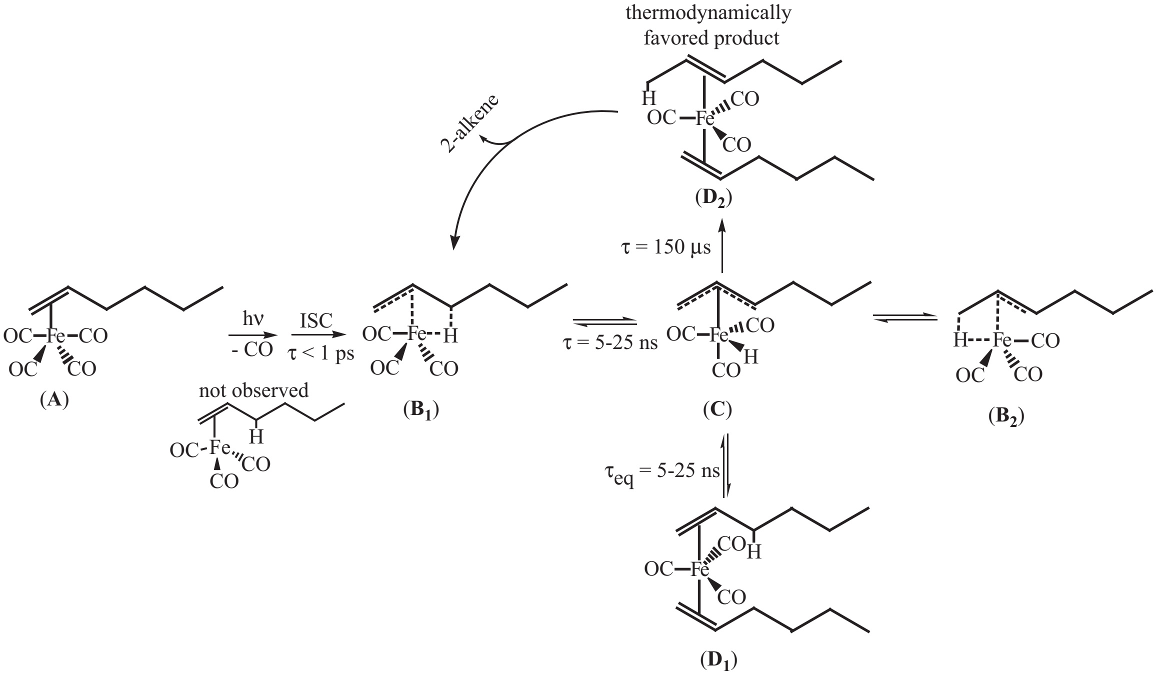

Figure 3.8: Summary of time-resolved IR studies of $Fe(CO)_4(\eta^2\text{-1-hexene})$ in neat 1-hexene solution on the pico- through the microsecond time-scales. Note that I cannot rule out the possibility that there are short-lived intermediates to the **C**→**D** reactions and cannot establish the role of the different **C** isomers in the **C**→**D** reaction.

time-scale. [36] As a result, $\mathbf{B}_1$ selectively reacts to form **C** and is not solvated to form $\mathbf{D}_1$. This selectivity allows the alkene-isomerization reaction to proceed through **C** so that both bisalkene isomers, $\mathbf{D}_1$ and $\mathbf{D}_2$, are formed. Species $\mathbf{D}_1$ is not thermodynamically stable, and, as a result, is a side-product in the reaction. On the other hand, the desired product, $\mathbf{D}_2$, is thermodynamically stable, and, as a result, the majority of the population of species **C** will ultimately react to form $\mathbf{D}_2$. When the system comes to equilibrium, nearly 100% of the alkene population will be 2-hexene. [8]

# Chapter 4

# Direct observation of photoinduced bent nitrosyl excited-state complexes

This chapter has been reproduced with permission from K.R. Sawyer, R.P. Steele, E.A. Glascoe, J.F. Cahoon, J.P. Schlegel, M. Head-Gordon and C.B. Harris, *The Journal of Physical Chemistry A*, 112(37),8505–8514 (2008). Copyright 2008 American Chemical Society.

## 4.1 Introduction

The reactivity of transition-metal-NO complexes is different than the reactivity of isoelectronic transition-metal–CO complexes, [2, 5, 15, 99] and there is interest in the chemistry of these molecules because NO is an important signaling molecule in biological systems. [5, 15] Recent work has shown that irradiation of some transition-metal-NO complexes leads to structural isomers that may be involved in neurotransmission and cancer reduction. [16–18] The photophysical properties of transition-metal–NO complexes, such as $[Fe(CN)_5(NO)]^{2-}$, are also of interest because of long-lived metastable states that are promising for optical data storage. [19–22]

The unusual reactivity of transition-metal–NO complexes is attributed to the unpaired electron on the NO radical. [2, 100–105] The NO ligand usually binds to transition metals with a linear MNO bond angle, yet it may also bind in a bent geometry ($\angle$ MNO = 120–170°). In a linear MNO geometry, the $\sigma$(NO) orbital is bound to the metal $d_{z^2}$ orbital, and the $\pi^*$(NO) orbital participates in $\pi$ back-bonding with the metal. Conversely, in a bent MNO geometry, the N is $sp^2$ hybridized and there is a $\sigma$-donation between the $d_{z^2}$ orbital on the metal and an $sp^2$ orbital on the NO. There is lone pair on the NO ligand in this geometry, and the amount of $\pi$ back-bonding with the metal center is reduced. [2,99] A shift from a linear to bent geometry is accompanied by a shift in electron spin density from the metal to the NO ligand. This unusual characteristic is regularly cited in inorganic chemistry textbooks and is key to the thermal and photochemical reactivity of transition-metal–NO compounds. [2, 106–108] Recent work has also shown that at least 80 transition-metal–NO complexes possess ground state structural isomers with isonitrosyl (M–ON) or side-on nitrosyl ligands ($\eta^2$-NO). The isonitrosyl binding mode is nearly identical to the linear MNO binding mode, except that there is less back-bonding with the metal because of the smaller lobes of the oxygen $\pi^*$ orbitals. The side-on NO binding mode, on the other hand, is quite different; the metal is bound in a $\sigma$-fashion to the NO bond rather than either the N or

O atoms. [20] Figure 4.1 shows the differences in geometry, back-bonding and MNO angle between the structures.

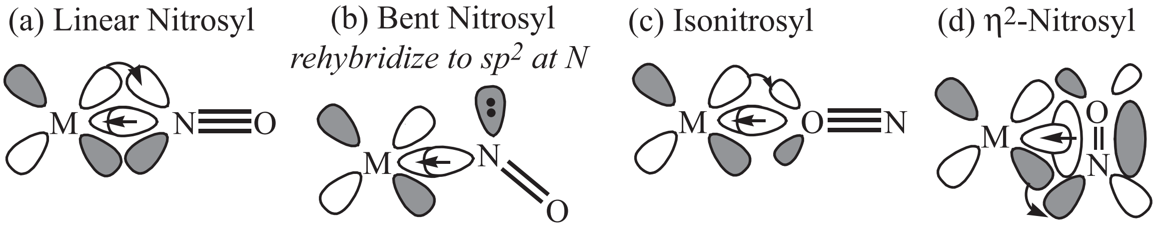

Figure 4.1: Binding modes of a nitrosyl ligand to a transition metal where the nitrosyl ligands are lying in the same plane as the metal atom. a) Linear M–NO b) Bent M–NO: Note that the amount of $\pi$ back-bonding with the metal center is reduced in this geometry because there is no longer an interaction between the $\pi^*$(NO) orbital and the d-orbitals in the plane of the paper; however, there is $\pi$ back-bonding between $\pi^*$(NO) orbital and the d-orbitals that are perpendicular to the page. c) M–ON d) M–($\eta^2$-NO)

Stable transition-metal-NO complexes have either linear- or bent-NO ligands, whereas ON and $\eta^2$-NO metastable structures are formed by visible irradiation of stable compounds. The photochemical formation of ON and $\eta^2$-NO complexes is well-established. [19–22, 109, 110] It has also been suggested that visible irradiation of linear-NO complexes leads to the formation of a triplet bent-NO excited state, [41, 111] but a bent-NO excited state has never been directly observed. [20] In this study, I use ultrafast time-resolved infrared (IR) spectroscopy to examine the excited state structures and dynamics of a model transition-metal-NO complex, $Co(CO)_3(NO)$. I observe two bent-NO excited state complexes and their dynamics for the first time but find no evidence for either the ON or $\eta^2$-NO isomers. I have worked in collaboration with Ryan Steele using density functional theory (DFT) modeling to calculate the structures, frequencies and energetics of the ground and excited state complexes. DFT analysis indicates that 400-nm irradiation of $Co(CO)_3(NO)$ leads to the formation of a triplet excited state with a bent-NO ligand which decays in ca.

350 ps to form a bent-NO complex in the ground triplet state. This work provides the first direct evidence for photochemically induced bent-NO transition-metal complexes.

$Co(CO)_3(NO)$, a model transition-metal-NO complex, has a linear Co–N–O bond in the electronic ground state ($S_0$). [41,99,106,111,112] The electronic absorption spectrum of $Co(CO)_3(NO)$ (Figure 4.2) shows two bands between 200 and 400 nm. The strong band centered at 200 nm is assigned to an excitation that leads to cleavage of either a Co–CO or the Co–NO bond. [113] The weak band, centered at 380 nm ($\sigma_{380}$ = 1.8 x $10^-18$ cm$^2$), is attributed to a cobalt-to-nitrosyl (Co→NO) charge-transfer transition. Photochemical excitation into this band is proposed to lead to a geometry change to a bent-NO complex. [41] The relatively low intensity of the 380-nm band illustrates that the Co→NO charge-transfer transition is a minor photochemical pathway. [112,114]

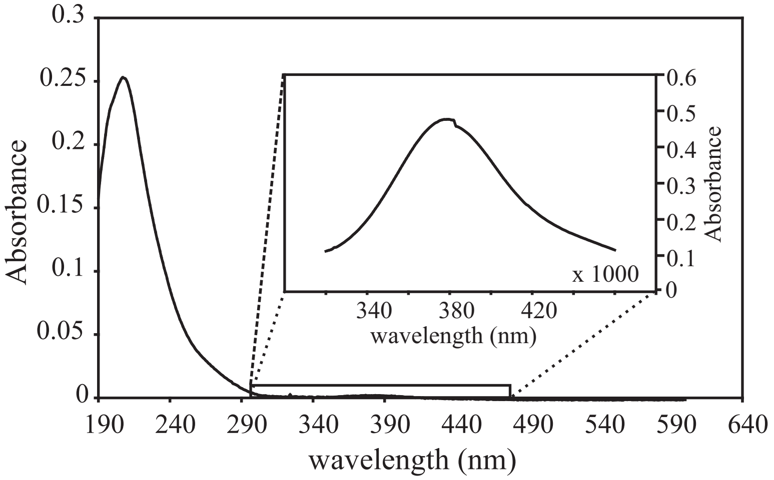

Figure 4.2: Electronic absorption spectrum of $Co(CO)_3(NO)$ in a neat hexane solution.

The differences between the linear- and bent-NO bonding modes of $Co(CO)_3(NO)$ are shown in the molecular orbital correlation diagram of the $\{CoNO\}^{10}$ structural unit predicted by Enemark and Feltham (Figure 4.3). [41, 111] In the ground electronic state, the HOMO is the $4a_1$ orbital, comprising primarily a cobalt $d_{z^2}$ and the $\sigma$(NO) orbital. The LUMO is the 4e orbital, the totally anti-bonding $\pi$-type molecular orbital that is primarily the cobalt $d_{xz}$ and $d_{yz}$ orbitals and the $\pi^*$(NO) orbitals. Irradiating $Co(CO)_3(NO)$ with 400-nm light corresponds to a $4a_1 \rightarrow 4e$ transition, and upon promoting an electron to the 4e orbital, the relative energies of the 4e and 3e orbitals shift. The molecule then rearranges to lower the orbital energies and forms a triplet complex with a bent Co–N–O bond angle. Note that this picture also predicts a change in the geometry of the entire structure from tetrahedral to pseudo-square planar. [41]

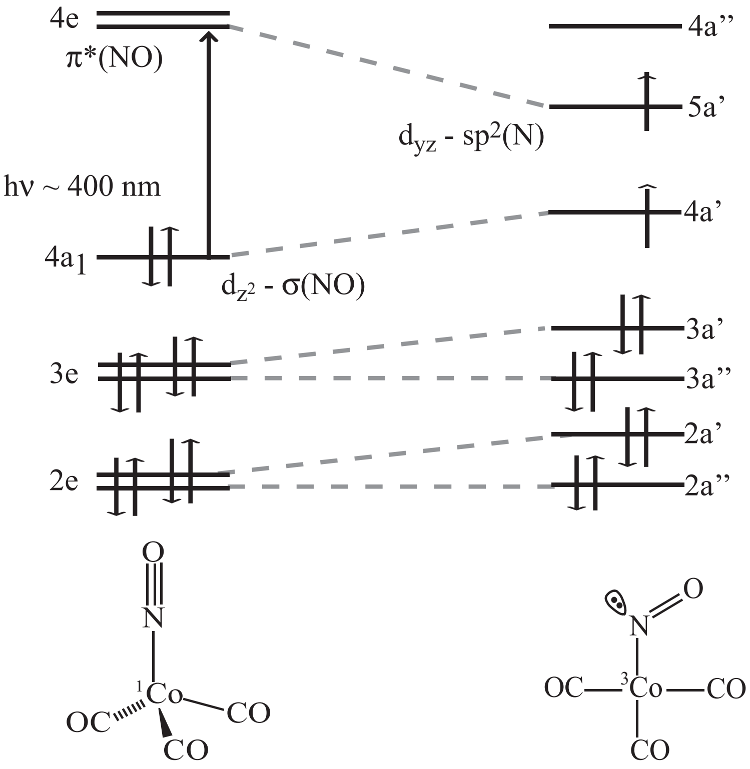

Figure 4.3: The molecular orbital correlation diagram of the $\{CoNO\}^{10}$ structural unit in the linear-NO and bent-NO forms of $Co(CO)_3(NO)$, predicted by Enemark and Feltham.

Despite the molecular orbital arguments that photolysis of $Co(CO)_3(NO)$ results in the formation of a triplet bent-NO complex, there is debate in the literature regarding this mechanism. [41, 112, 114–116] Gas phase studies suggest that visible photolysis of $Co(CO)_3(NO)$ results in the formation of an excited state of $Co(CO)_3(NO)$ with a bent Co–N–O bond and a negatively charged NO ligand. [41] These authors also showed that visible irradiation of $Co(CO)_3(NO)$ in Lewis base solution (e.g. $PPh_3$, $AsPh_3$ and pyridine) results in associative photochemical substitution of a single CO, providing indirect evidence for a coordinatively unsaturated bent-NO complex. [41] However, the only photochemical reaction observed via IR studies of $Co(CO)_3(NO)$ in frozen matrices and in the gas phase is the dissociation of a CO or NO ligand. [112, 113, 116] The goal of this study is to determine whether a bent-NO complex is formed from visible photolysis of $Co(CO)_3(NO)$, and if it is formed, to determine the mechanism for its formation.

## 4.2 Methods

### 4.2.1 Sample Preparation

$Co(CO)_3(NO)$ and spectroscopic grade hexane were purchased from Strem Chemicals, Inc. and EMD Chemicals Inc., respectively. All samples were used without further purification. Dilute solutions of $Co(CO)_3(NO)$ in hexane were stable when exposed to air under ambient conditions.

### 4.2.2 DFT Modeling

The DFT modeling performed for this project was done by Ryan P. Steele, a former graduate student in Martin Head-Gordon's research group in the Chemistry Department at the University of California, Berkeley. His description of the computational methods used are included below.

Kohn-Sham Density Functional Theory (DFT) [117] calculations were performed with a development version of Q-Chem 3.1. [118] The BP86 functional [77,78] was employed, as it generally gives satisfactory results for transition-metal systems. [56] The agreement between the calculated NO stretching frequency for $Co(CO)_3(NO)$ (1842 $cm^{-1}$) is in reasonable agreement with the known experimental values (1808 $cm^{-1}$) and is typical of the observed accuracy for this functional.[1] [72] Furthermore, initial tests verified that the calculations adequately predict vibrational frequencies for $Co(CO)_3(NO)$ without empirical scaling. [72,119] An analysis of basis set and functional dependence of frequencies is provided in reference [120]. All calculations are reported using the 6-311+G(3df) [119,121,122] basis set for the ligands and 6-31G* for the metal center. Cartesian d functions were used for both basis sets. Though the 6-311G basis does not exist for Co, further extension of the basis set to cc-pVTZ [123, 124] produced only marginal (1–9 $cm^{-1}$) changes in reported frequencies at significantly increased computational expense. No pseudopotentials were employed for the metal center. Initial testing indicated that a pseudopotential (LANL2DZ) [82] led to relatively insignificant (less than 5 $cm^{-1}$) changes in the CO and NO stretching frequencies. Additionally, omitting the core potential simplified analysis of basis set effects. All calculations were performed with the SG-1 integration grid. [125] The self-consistent field was converged to $10^{-8}$ a.u., using integral thresholds of $10^{-12}$ a.u. Geometry optimizations were converged to the Q-Chem default tolerances of $3x10^{-4}$ a.u. (maximum gradient) and

---

[1] The calculated CO stretches of $Co(CO)_3(NO)$ are only 20 $cm^{-1}$ different from the experimental CO stretches.

either 1.2x$10^{-3}$ a.u. (displacement) or 1x$10^{-6}$ a.u. (energy). No symmetry constraints were applied, and initial structures were perturbed to check for structures of lower symmetry.

Excited state single-point energies were obtained with time-dependent DFT (TD-DFT) [126–129] within the Tamm-Dancoff approximation, [130] using the parameters described above. The structure and frequency of the first excited singlet ($S_1$) were obtained with a spin-corrected single-reference method using the Maximum Overlap Method to produce the excited configuration.[2]

## 4.3 Results and Discussion

### 4.3.1 Ultrafast visible-pump, IR-probe spectroscopy of $Co(CO)_3(NO)$ in hexane solution

Figure 4.4 shows the ultrafast visible-pump, IR-probe spectra of $Co(CO)_3(NO)$ (**A**) in neat hexane solution. Peak dynamics and assignments are listed in Table 4.1. Peak assignments are based on the observed kinetics and peak positions and the DFT analysis discussed in below. Figures 4.4a and 4.4b show peaks in the NO stretching region, and Figure 4.4c shows peaks in the CO stretching region. Features attributed to parent molecules (**A**) (1807, 2037 and 2100 cm$^{-1}$) and $^1Co(CO)_2(NO)$(hexane) and $Co(CO)_3$, are not shown here for clarity but are presented in the Appendix A.2. [112,116,131]

The spectra in Figure 4.4 show peaks that are not attributable to either of the CO-

---

[2] The Maximum Overlap Method is a recently-developed (and unpublished) feature of Q-Chem 3.1, implemented by P. Gill. Originally designed to force oscillating SCF calculations to choose a configuration, MOM occupies SCF orbitals by maximum overlap with the previous set of occupied orbitals, instead of the usual occupation of the lowest orbitals. By choosing a configuration in which electrons are promoted to higher orbitals, excited state configurations can be converged, using MOM from the initial SCF guess.

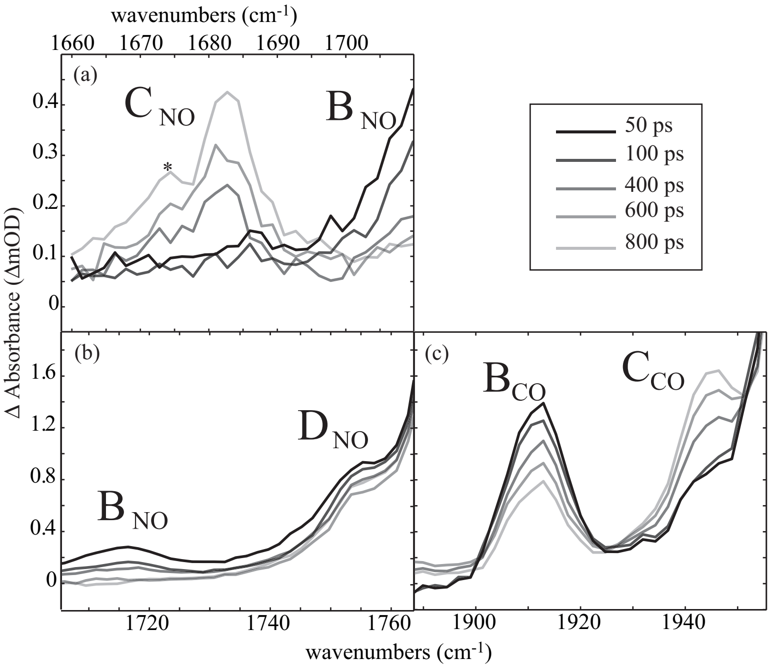

Figure 4.4: Ultrafast time-resolved visible-pump, mid-IR probe spectra of the (a) NO stretching region of ca. 20 mM $Co(CO)_3(NO)$, (b) NO stretching region of ca. 5 mM $Co(CO)_3(NO)$ and (c) CO stretching region of ca. 5 mM $Co(CO)_3(NO)$ in neat hexane solution. * corresponds to a feature discussed in Appendix A.2.

or NO-loss pathways that have been observed in past studies, [112,116] confirming that there are intermediates formed via non-dissociative photochemical pathways. The experimental results for these pathways are discussed herein. Figures 4.4a and 4.4b show peaks centered at 1684, 1715 and 1755 cm$^{-1}$, respectively. The relatively low stretching frequencies of the peaks indicate that they correspond to NO stretching modes. The DFT calculations presented in section 4.3.2 indicate that CO ligands of all of the possible intermediates are terminally bound, and consequently, it is unlikely that their stretching frequencies will be more than 100 cm$^{-1}$ lower than the antisymmetric CO stretch of **A** (2037 cm$^{-1}$). [31,92, 132,133] This is further supported by past studies, [112,113,116] which indicate that none of the CO- and NO-loss intermediates possess a CO stretching mode below ca. 1980 cm$^{-1}$. Thus, I assign the 1684, 1715 and 1755 cm$^{-1}$ peaks (labeled $\mathbf{C}_{NO}$, $\mathbf{B}_{NO}$, $\mathbf{D}_{NO}$) to the stretching frequency of the NO ligand in three distinct complexes: **C**, **B** and **D**.

| **Peak** | **Species** | **Exp. Freq (cm$^{-1}$)** | **$\tau$ (ps)** | **Trend** |
|---|---|---|---|---|
| **B** | $^3$Co(CO)$_3$(NO) | 1715 (NO) | 9.4 ± 2 | decay |
| | (T$_2$ or T$_3$) | | 350 ± 150 | decay |
| | | 1913 (CO) | 5.1 ± 2 | rise |
| | | | 209 ± 78 | decay |
| **C** | $^3$Co(CO)$_3$(NO) | 1684 (NO) | 12 ± 3 | decay |
| | (T$_1$) | | 350 ± 100 | rise |
| | | 1949 (CO) | 8.1 ± 3 | decay |
| | | | 297 ± 18 | rise |
| **D** | $^3$Co(CO)$_2$(NO) | 1755 (NO) | 11 ± 1 | decay |
| | (T$_1$) | | | |

Table 4.1: Peak assignments and dynamics for the features shown in Figure 4.4. The electronic state and the nature of the stretching modes is listed in parentheses. These assignments are based on the frequencies of the modes compared to literature values complexes and the DFT calculations.

The peak labeled $\mathbf{D}_{NO}$ partially decays with a time constant of $\tau$ = 11 ± 1 ps

(Table 4.1) and is stable for the duration of the experiment. The fast decay of this peak is similar to the recovery of the NO stretch of **A** (23 ± 1 ps) and the decay of the NO stretch of the vibrationally hot parent molecules (17 ± 2 ps) (refer to Appendix A.2). Therefore, the decay of $\mathbf{D}_{NO}$ is assigned to vibrational cooling of the NO ligand and not to CO loss reactive dynamics. The peaks labeled $\mathbf{B}_{NO}$ and $\mathbf{C}_{NO}$ do have dynamics that are separate from vibrational cooling. Neglecting the vibrational cooling dynamics, the $\mathbf{B}_{NO}$ peak decays with a time constant of $\tau = 359 \pm 150$ ps and $\mathbf{C}_{NO}$ rises with a time constant of $\tau = 350 \pm 100$ ps (Figure 4.5). The agreement of the time constants suggest that species **B** converts to species **C** in approximately 350 ps.

Figure 4.4c shows two peaks centered at 1913 and 1949 $\text{cm}^{-1}$. Neglecting vibrational cooling dynamics, exponential fits to these peaks yield a decay time of 209 ± 78 ps and a rise time of 297 ± 18 ps, respectively (Figure 4.6). Since these time constants are similar to the time constants obtained for peaks $\mathbf{B}_{NO}$ and $\mathbf{C}_{NO}$, I propose that they correspond to the CO stretching modes of species **B** and **C**. [31, 92, 132, 133] The CO stretching frequencies of species **D** ($\mathbf{D}_{CO}$) were not observed experimentally, most likely because the CO stretch of **D** was hidden by the larger peaks from the CO- and NO-loss pathways.

The shifts in the frequency of the $\mathbf{B}_{NO}$, $\mathbf{C}_{NO}$ and $\mathbf{D}_{NO}$ peaks relative to the NO stretch of **A** provide clues to their structures. [2, 20, 99] Within a given complex, the stretching frequencies of the bent-NO, ON and $\eta^2$-NO ligands are red-shifted relative to the stretching frequency of the linear-NO ligand. The $\eta^2$-NO stretching mode is generally 400 $\text{cm}^{-1}$ lower in energy than the linear-NO mode (1807 $\text{cm}^{-1}$ for **A**). [112] Consequently, if a complex with an $\eta^2$-NO ligand was formed from visible irradiation of $\text{Co(CO)}_3\text{(NO)}$, I would

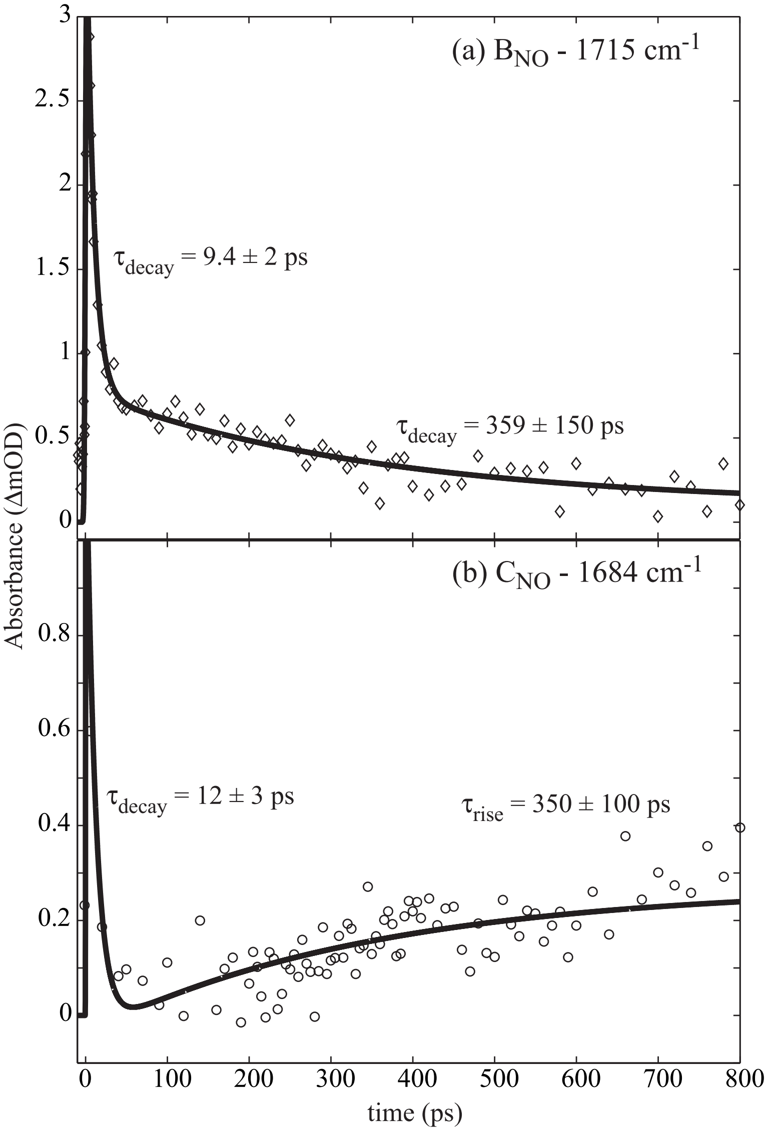

Figure 4.5: Kinetic plots of the peaks at (a) 1715 cm$^{-1}$ ($\mathbf{B}_{NO}$) and (b) 1684 cm$^{-1}$ ($\mathbf{C}_{NO}$) in hexane solution.

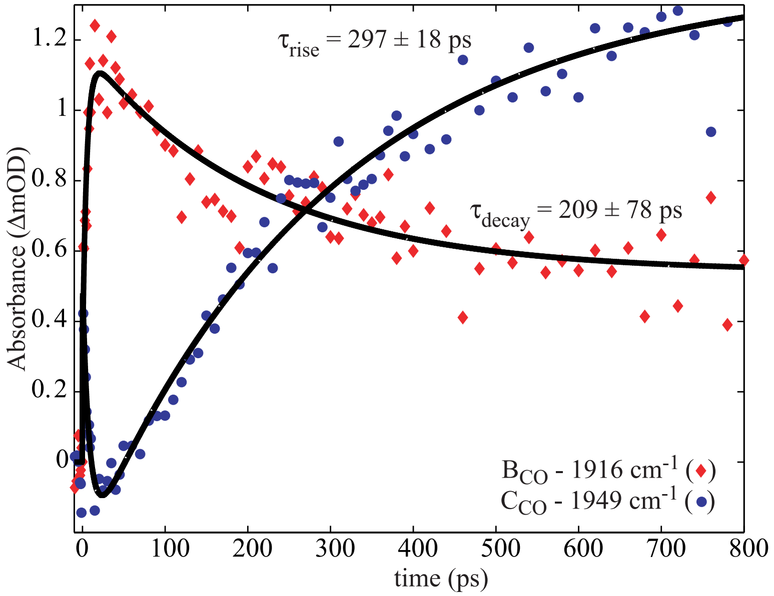

Figure 4.6: Kinetic plots of the carbonyl stretches of peaks at 1917 cm$^{-1}$ ($\mathbf{B}_{CO}$) and 1949 cm$^{-1}$ ($\mathbf{C}_{CO}$) in solution.

not be able to observe the $\eta^2$-NO stretch because the experimental setup does not permit us to monitor absorptions below 1650 cm$^{-1}$. Similarly, an ON stretching mode is generally 100 cm$^{-1}$ lower in energy than the corresponding linear-NO mode. [20,134] However, I do not expect to observe an ON complex since past studies indicate that they are typically formed via multi-photon processes. [109,110,134] The stretching frequency of bent-NO ligands is also approximately 100 cm$^{-1}$ lower in energy than the frequency of linear-NO stretches. Linear-to-bent NO conversion can be thought of as rehybridization of nitrogen from sp to sp$^2$, corresponding to a weakening of the NO bond, thus decreasing the frequency of the NO stretch. [2,41,99,106,107]

Species **B**, **C** and **D** have lower energy stretching frequencies than species **A** by 92, 113 and 52 cm$^{-1}$, respectively. Thus, any of these species could correspond to either a complex with an ON or a bent-NO ligand. [20,99] Since none of these species have been observed in past studies, we have utilized DFT quantum chemical modeling to determine their structures, electronic states, energies and harmonic frequencies.

### 4.3.2 DFT modeling of $Co(CO)_3(NO)$ and its photoproducts

DFT calculations were used to identify species **B**, **C** and **D**, and to determine the mechanism that was observed experimentally. The analysis presented herein focuses on static structures and the topography of relevant potential energy surfaces. An explicit, time-dependent simulation of the excited state dynamics following photoexcitation is not feasible because the dynamics are relatively slow (pico- through early nanosecond time-scales) and involve multiple excited states. Furthermore, some of the key processes are spin-forbidden, and an explicit simulation would require the calculation of spin-orbit coupling [135,136] to an accuracy commensurate with the energies and couplings. Relevant potential energy surfaces will be used to offer qualitative arguments for the dynamics of the system. The resulting picture, when compared to the experimental results presented above, lends considerable insight to the photochemical mechanism.

#### Molecular orbital diagram of $Co(CO)_3(NO)$

Figure 4.7 shows a partial Kohn-Sham orbital diagram for **A**. It has a linear NO group and a tetrahedral ($C_{3v}$) geometry, as expected. Both the HOMO and LUMO of **A** are of e symmetry and are doubly degenerate. The HOMO contains contributions from the overlap of metal $d_{xz}/d_{yz}$ orbitals with $\pi^*$(NO) orbitals, whereas the LUMO is primarily composed of $\pi^*$(NO) ligand orbitals. Note that the HOMO–LUMO gap (68 kcal/mol) almost perfectly matches the energy of the 400 nm pump pulse used in the experiment (400 nm = 71 kcal/mol). It is possible that a 400 nm excitation corresponds to the $2a_1 \rightarrow 4e$ electronic transition; DFT predicts that these orbitals are 76 kcal/mol apart (ca. 375 nm). However, the TD-DFT calculations presented below show that, while both transitions are weak, the transition moment for the $2a_1 \rightarrow 4e$ transition is half as intense as the transition moment for the $3e \rightarrow 4e$ transition. Ultimately, I expect that both transitions will result in the same dynamics on the picosecond time-scale, provided that the former transition is not dissociative. Note that this diagram is different from the MO diagram in Figure 4.3, since DFT predicts the $a_1$ orbital is 8.2 kcal/mol below the HOMO. [111]

The two pairs of degenerate frontier orbitals lead to four single-excitation excited states, discussed further below. Figure 4.8 shows that as the Co–N–O angle decreases into $C_s$ symmetry, the 3e and 4e orbitals split into non-degenerate pairs, labeled a' and a". In this staggered geometry the three CO groups are not arranged symmetrically; the angle between two of the CO ligands is slightly wider, creating a gap into which the NO can bend. Optimization of a structure in which the NO bends into the smaller gap between CO ligands was attempted but was unsuccessful as this structure is simply a distorted form of the structure in which the NO is bent into the larger gap. The convention throughout this work is that the positive bending coordinate signifies an NO that is bent so that it bisects the angle between the neighboring CO ligands and the negative bending coordinate denotes an NO ligand bent directly toward the third CO. The a' orbital stemming from the original 3e HOMO (blue) rises in energy, due to diminished $\pi$ back-bonding. The a' and a" orbitals stemming from the LUMO (red) decrease in energy as the Co–N–O angle decreases, suggesting that the lowest-lying singlet and triplet excited states ($S_1$ and $T_1$) will

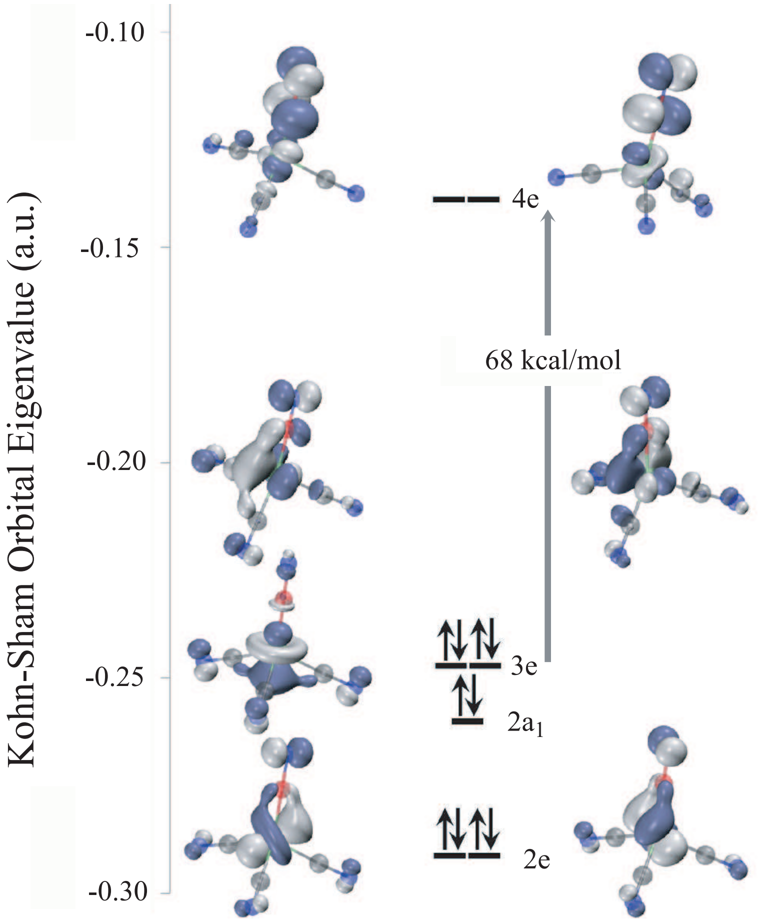

Figure 4.7: Calculated Kohn-Sham orbital diagram for Co(CO)$_3$(NO). Plots of orbitals are generated by VMD [137] from Q-Chem outputs. In all cases, the NO is pointing up.

have distinctly different structures than the ground state ($S_0$).

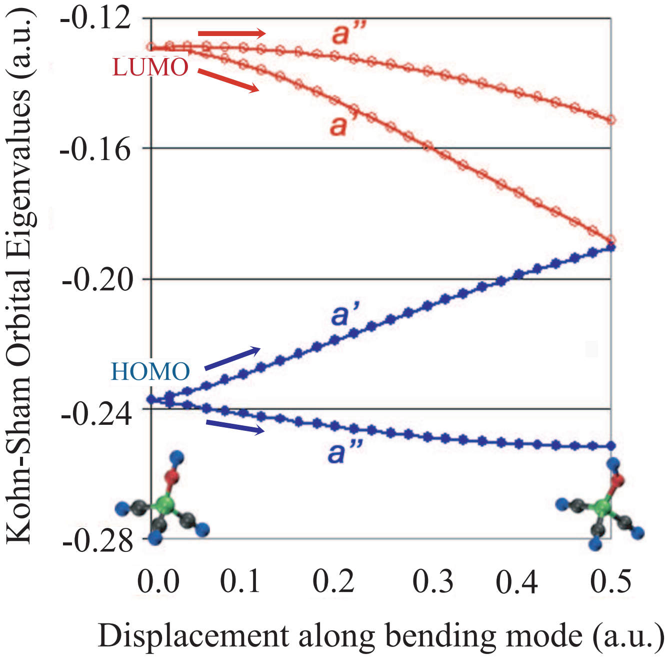

Figure 4.8: Frontier orbitals (occupied: closed blue circles, unoccupied: open red circles) along the positive half of the NO bending mode (588 cm$^{-1}$).

### Structures and Harmonic Frequencies

Optimized molecular structures and harmonic frequencies were obtained for structural isomers of the parent compound (**A**) on the ground state potential, the lowest energy structures on the lowest-lying triplet ($T_1$) and singlet ($S_1$) excited state potentials and the singlet and triplet CO-loss complexes. Figure 4.9 shows the optimized molecular geometries, and the key structural parameters, harmonic frequencies and relative energies are listed in Table 4.2.

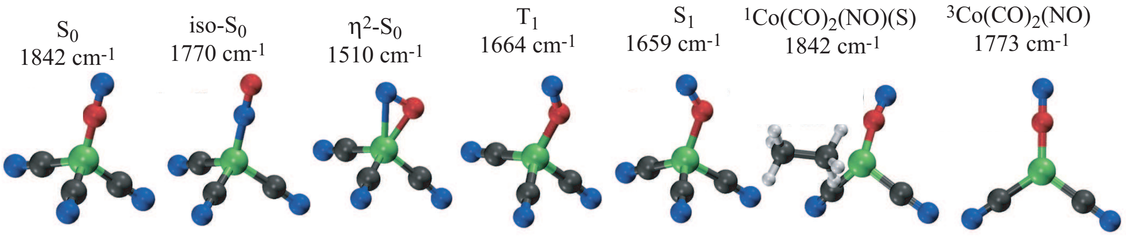

Figure 4.9: Optimized molecular geometries and harmonic NO stretching frequencies for ground and excited structures of $Co(CO)_3(NO)$ and the associated CO-loss species.

| | **Energy** | **Bond Length** | | | | **Bond Angle** | | **Mode** | |
|---|---|---|---|---|---|---|---|---|---|
| | (kcal/mol) | NO | CoN | CO | CoC | CoNO | CoCO | NO | CO |
| $S_0$ (**A**) | 0.0 | 1.162 | 1.661 | 1.151 | 1.799 | 180.0 | 178.5[c] | 1842 | 2015 |
| | | | | | 1.800 | | 178.4 | | 2016 |
| | | | | | | | | | 2075 |
| $\eta^2$-$S_0$ | 27.9 | 1.203 | 1.781 | 1.150[c] | 1.827 | 85.0 | 174.8[c] | 1510 | 2011 |
| | | | | 1.152 | 1.781 | | 174.9 | | 2014 |
| | | | | | | | | | 2070 |
| $T_1$ (**C**) | 38.4 | 1.184 | 1.808 | 1.152[c] | 1.812[c] | 137.1 | 176.8 | 1664 | 1998 |
| | | | | 1.151 | 1.819 | | | | 2004 |
| | | | | | | | | | 2058 |
| $S_1$ | 40.4 | 1.186 | 1.830 | 1.182 | 1.815 | 128.7 | 178.6[c] | 1659 | 1998 |
| | | | | 1.151 | 1.817 | | 178.5 | | 2040 |
| | | | | | | | | | 2067 |
| iso-$S_0$ | 42.1 | 1.161 | 1.745[a] | 1.153 | 1.792 | 179.9[a] | 178.0[c] | 1770 | 1999 |
| | | | | | 1.793 | | 178.1 | | 2002 |
| | | | | | | | | | 2060 |

Table 4.2: DFT calculated geometric and energetic parameters of relevant structures in the photochemistry of $Co(CO)_3NO$, optimized with BP86/6-311+G(3df) (6-31G* on Co). [a] In the iso-$S_0$ structure the Co is bound to the O, not the N. As a result, the values listed for the Co–N bond length corresponds to the Co–O bond length and the Co–N–O bond angle corresponds to the Co–O–N bond angle.; [b] The energy of $^1Co(CO)_2(NO)$(ethane) and $^3Co(CO)_2(NO)$ includes the energy of the dissociated CO ligand.; [c] Geometric parameter for the two identical CO ligands.

**CO-loss structures** Past studies have indicated that the highest yield pathway upon 400 nm photolysis of $Co(CO)_3(NO)$ is CO dissociation. [112, 113, 116] $^1Co(CO)_2(NO)(hexane)$ was observed in the experiments discussed above ($\nu$(NO) = 1775 cm$^{-1}$). [112,113,116] DFT predicts that the NO ligand is slightly bent (Table 4.2, Figure 4.9) and has a stretching frequency (1803 cm$^{-1}$) that is only 39 cm$^{-1}$ lower in energy than the NO stretch of $S_0$.[3] In addition to $^1Co(CO)_2(NO)(hexane)$, a triplet CO-loss complex, $^3Co(CO)_2(NO)$, is accessible with a 400 nm photon.[4] DFT predicts that $^3Co(CO)_2(NO)$ has a linear NO ligand and a stretching frequency of 1773 cm$^{-1}$. Peak **D**, which shows no reactive dynamics on the time-scale of the experiment, is assigned to be $^3Co(CO)_2NO$ since the calculated frequency agrees well with the **D** peak (1755 cm$^{-1}$). Note that based on the absolute DFT calculated frequencies, I cannot distinguish between the singlet and triplet forms of $Co(CO)_2(NO)$. However, the DFT calculated frequencies indicate that the NO stretch of the singlet (1803 cm$^{-1}$) will be higher in energy than the NO stretch of the triplet (1773 cm$^{-1}$). Thus, I assign the higher energy peak (1775 cm$^{-1}$) to the singlet $Co(CO)_2(NO)(hexane)$ and the lower energy peak (1755 cm$^{-1}$) to the triplet $Co(CO)_2(NO)$. Additionally, the singlet–triplet gap (20 kcal/mol)[5] for the CO-loss complexes is large enough that coupling between the states should be small so that $^3Co(CO)_2(NO)$ is long-lived, in good agreement with experimentally observed dynamics for **D**. Past studies indicate that triplet coordinatively unsaturated complexes, like $^3Co(CO)_2(NO)$, do not interact strongly with non-polarizable solvents, such as saturated alkanes, and are, therefore, unreactive on a picosecond time-scale.

---

[3] The coordinatively unsaturated singlet was found to bind a solvent molecule, although the Co–N–O bond angle decreased by only 1° and shifted the frequency by 2 cm$^{-1}$.

[4] The CO bond dissociation energy of **A** was calculated to be 43.0 kcal/mol, easily accessible with a 400 nm photon (ca. 71 kcal/mol). The triplet CO loss intermediate is calculated to be 20.6 kcal/mol above the singlet CO loss intermediate.

[5] The singlet–triplet gap in the singlet geometry is calculated to be 32 kcal/mol.

DFT calculations confirm these predictions since attempts to coordinate a hydrocarbon to $^3$Co(CO)$_2$(NO) were unsuccessful. On the other hand, $^1$Co(CO)$_2$(NO) does coordinate to a saturated hydrocarbon, but the experiments indicate that the singlet-triplet energy gap is still high enough in solution that the $^3$Co(CO)$_2$(NO) to $^1$Co(CO)$_2$(NO)(hexane) spin-crossover reaction does not occur on a picosecond time-scale. [33, 138]

**Ground State Structural Isomers and Lowest Excited State Structures** Figure 4.9 shows the optimized geometries of the three ground state structural isomers linear-NO, $\eta^2$-NO and ON complexes, hereafter referred to as $S_0$, $\eta^2$-$S_0$, and iso-$S_0$, respectively. Both $S_0$ and iso-$S_0$ contain a linear (iso)nitrosyl group, whereas the Co–N–O bond angle in the $\eta^2$-$S_0$ complex is strongly bent (85°) so that it bisects two of the CO ligands. The iso-$S_0$ and $\eta^2$-$S_0$ structures are 42.0 and 38.4 kcal/mol, respectively, higher in energy than $S_0$. The NO stretching frequencies of both isomers are red-shifted from the corresponding stretch of $S_0$: $\nu(\mathrm{NO}) = 1509\ \mathrm{cm}^{-1}$ for $\eta^2$-$S_0$ and $1770\ \mathrm{cm}^{-1}$ for iso-$S_0$.

Figure 4.9 also shows the optimized molecular structures on the first excited triplet and singlet potentials ($T_1$ and $S_1$). Both $T_1$ and $S_1$ have bent-NO ligands, with bond angles of 137° and 129°, respectively. Once again, the bond is bent so that it bisects two of the CO ligands, resulting in a pseudo-tetrahedral $C_s$ structure. [111] Both of the structures have NO bond lengths that are more than 0.02 Å longer than the NO bond in $S_0$ due to the decrease in the bond order. Additionally, the Co–N bonds are longer by 0.15 Å ($T_1$) and 0.17 Å ($S_1$), due to reduced back-bonding.[6] Accordingly, the NO stretching frequency of

---

[6] The differences in the CO bond parameters are insignificant, and are limited to a minor ($\leq 5°$) bending of the carbonyl bonds and breaking of symmetry due to the presence of the bent nitrosyl ligand. Additionally, no significant changes were observed in the carbonyl frequencies of the different isomers on the ground or excited potentials.

the $T_1$ and $S_1$ structures are red-shifted relative to $S_0$: $\nu(\mathrm{NO}) = 1664\ \mathrm{cm}^{-1}$ for $T_1$ and $1659\ \mathrm{cm}^{-1}$ for $S_1$. The calculated NO stretching frequencies for these complexes reflect the differences in their geometries. The red-shifting of the NO stretching modes of the bent-NO ligands confirms that the NO bond is weaker when bound to the metal center in a bent configuration compared to a linear configuration.

The DFT calculations indicate that the experimentally observed peaks cannot be assigned to $\eta^2$-$S_0$ because the frequency of its NO stretch is outside of the experimentally observable range, however, I cannot rule out the possibility that this $\eta^2$-$S_0$ isomer is formed by the UV pump pulse. On the other hand, the calculated NO modes of the iso-$S_0$, $S_1$ and $T_1$ structures are all within error of the experimentally observed peaks, and thus, they are all candidates for both **B** and **C**. The calculated frequencies do not provide any information about the dynamics of these complexes; their energies and the barriers connecting them provide the crucial remaining evidence.

### Potential Energy Surfaces

One-dimensional slices of the ground and two lowest excited potential energy surfaces ($S_0$, $T_1$ and $S_1$) of $\mathrm{Co(CO)_3(NO)}$ were calculated to aid in the identification of **B** and **C**. Since the Co–N–O bond angle appears roughly to be the relevant reaction coordinate, a constrained potential energy scan was calculated while fixing this parameter at successive bond angles ranging between 80° and 180°. The remaining 3N–7 degrees of freedom were fully optimized at each point. The results of these calculations are presented in Figure 4.10a.

Figure 4.10a confirms that the global minimum on the $S_0$ potential has a linear-NO structure and predicts that a ca. 28 kcal/mol barrier connects $S_0$ to $\eta^2$-$S_0$. The reverse barrier is only ca. 3 kcal/mol, suggesting that even if $\eta^2$-S$_0$ were formed, it would quickly isomerize back to S$_0$.[7] [19] Iso-S$_0$ is less stable than S$_1$ and T$_1$ (Table 4.2), and a significant barrier exists to accessing it from either state. Thus, neither **B** nor **C** is due to iso-S$_0$. This is consistent with previous studies that have shown that multiple photons are needed to form iso-S$_0$ from S$_0$ and that the formation of iso-S$_0$ relies upon the presence of a stable, photochemically accessible $\eta^2$-S$_0$ intermediate. [19, 109, 110]

Since neither species **B** nor **C** can be assigned to $\eta^2$-S$_0$ or iso-S$_0$, the unassigned peaks must be due to excited state bent-NO complexes. The calculated NO stretching frequencies for both T$_1$ (1664 cm$^{-1}$) and S$_1$ (1659 cm$^{-1}$) agree best with the NO stretching mode of **C** (1685 cm$^{-1}$). Anharmonic corrections to the T$_1$ frequency via vibrational perturbation theory [139] bring the calculated frequency to 1692 cm$^{-1}$, even closer to the observed value.

Since the calculated NO stretching frequencies of S$_1$ and T$_1$ are indistinguishable given the accuracy of DFT calculations, [72] I have used the calculated potentials in Figures 4.10b and 4.10c to further differentiate between them. Figures 4.10b and 4.10c show the vertical energies of S$_0$, single-point energy calculations that were performed at the optimized structures of the paired opt state. Figure 4.10c shows that S$_1$ and S$_0$ are close in energy in the vicinity of the minimum on the S$_1$ potential.[8] [22, 140] I estimate that there is a ca. 2 kcal/mol energetic barrier to accessing the point of closest approach from the minimum energy structure of S$_1$. However, in the case of the S$_1$→S$_0$ transition, the coupling between the states is strong and thus the nonadiabatic transition may occur before

---

[7] The calculated barrier to the $\eta^2$-S$_0$ isomerization is much smaller than the corresponding barrier for $[Fe(CN)_5(NO)]^{2-}$ (12 kcal/mol).

[8] I expect that the close approach between S$_0$ and S$_1$ enables the formation of $\eta^2$ complexes in other transition-metal–NO complexes.

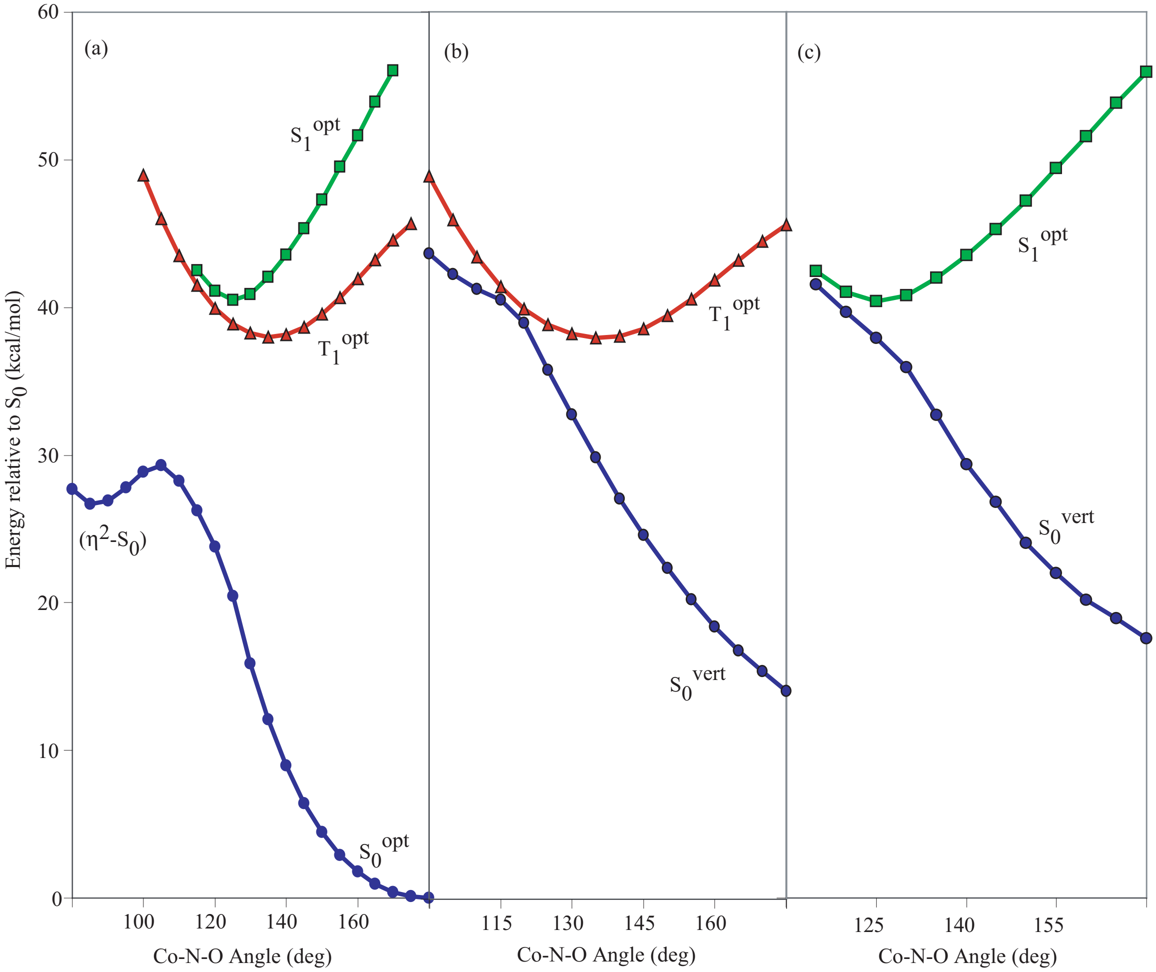

Figure 4.10: $S_0$, $T_1$ and $S_1$ potential energy surfaces along the Co–N–O bending angle of $Co(CO)_3(NO)$, calculated with BP86/6-31G*: (a) a constrained potential energy scan calculated while fixing the Co–N–O bending angle at successive values ranging between 80° and 180°; (b) single-point energy calculation of $S_0^{vert}$ performed at the optimized structures on the $T_1^{opt}$ state; (c) single-point energy calculation of $S_0^{vert}$ performed at the optimized structures on the $S_1^{opt}$ state The opt superscript denotes constrained optimization at a given bending angle. The vert superscript signifies a single-point energy calculation on a different potential energy surface, with the same molecular structure as the paired opt state.

the classical barrier is crossed. [141] Therefore, $S_1$ must be short-lived (i.e., less than 1 ps) and cannot be assigned to **C**, which exists for at least 700 ps.

Figure 4.10b shows also shows a close approach between $T_1$ and $S_0$ along the Co–N–O angle. However, because $T_1$ is a high-spin state, it is reasonable that it is long-lived. The magnitude of spin-orbit coupling in this vicinity—not calculated for these species but typically on the order of 20–200 $cm^{-1}$—would lower the nonadiabatic transition probability for $T_1 \rightarrow S_0$ transition as compared to the $S_1 \rightarrow S_0$ transition. [33, 142, 143] Further, there is a small classical barrier (ca. 3 kcal/mol) to accessing the point of closest approach between $T_1$ and $S_0$ from the minimum energy $T_1$ structure, akin to the inverted region of Marcus theory. [144, 145] In other words, because the $T_1 \rightarrow S_0$ transition is spin-forbidden, the coupling between the states is weak in all regions except for the crossing point between the states. Thus, before the system can undergo the nonadiabatic transition to ground state, it must pass over the classical barrier to access the crossing point. [144,145] As a result, it is reasonable to expect the bent-NO complex in the $T_1$ to be long-lived. Moreover, since $T_1$ is a coordinatively unsaturated species in the ground triplet state, it is expected to be unreactive on the picosecond time-scale when in solution with saturated alkanes. [33,36,38,138] Since the calculated NO stretching frequency of $T_1$ is in good agreement with the experimentally observed **C** peak and since the calculated potentials suggest that $T_1$ would be a stable on the picosecond time-scale, I assign species **C** to the bent-NO complex in the ground triplet state, $T_1$.

The identification of the short-lived species, **B**, remains. Given that the NO stretch of **B** is red-shifted relative to **A** and slightly blue-shifted relative to **C**, I expect that **B** should be assigned to a complex with a NO ligand that is less bent than the NO ligand in **C**. The $S_1$ complex has a bent-NO ligand, but the $S_1$ NO stretch is slightly red-shifted, not blue-shifted, from the corresponding mode of **C**. Further, the nonadiabatic $S_1 \rightarrow S_0$ transition is also more plausible than the spin-forbidden $S_1 \rightarrow T_1$ transition, so that if the bent-NO $S_1$ complex were formed, it would quickly isomerize to the parent rather than decaying to form **C** ($T_1$).

Since no evidence exists for a bent-NO complex that is less bent than **C** on the ground state ($S_0$) or either of the two lowest excited states ($S_1$ or $T_1$), I expect that **B** corresponds to a complex on a higher excited state. **B** must correspond to an excited state complex that decays to form $T_1$ with a time constant of 350 ps that is either due to a classical barrier or low nonadiabatic coupling between the states. To further explore this possibility, I have investigated the TD-DFT vertical excitation energies of the higher excited singlet and triplet states along the 588 $cm^{-1}$ NO bending mode (the same coordinate as Figure 4.8). Figure 4.11 shows four states that arise from the original, doubly degenerate HOMO and LUMO of **A**. The singlet states are shown in green (circles), and the triplet states are shown in red (triangles). As mentioned earlier, in the positive bending mode (right side of Figure 4.11), the NO ligand bends so that it bisects two of the CO ligands, whereas in the negative bending mode (left side), the structure is eclipsed so that the NO is bent directly towards the third CO group. Optimization of these states would lead to more pronounced minima and shift of the Co–N–O angle, as has been observed for $T_1$ and $S_1$. All but one of the states in Figure 4.11 have at least one local minimum that corresponds to a structure with a bent-NO group, and all of the bent-NO structures on the higher states have

NO ligands that are less bent than $T_1$ (**C**).[9] Therefore, based on the bond angles alone, I cannot determine which of the higher excited states corresponds to **B**.

The relative energies and topographies of the excited states in Figure 4.11 provide the additional information necessary to identify **B**. Three singlet states labeled $S_1$, $S_2$ and $S_3$ are in the vicinity of the photon energy shown in Figure 4.11 (dashed line at 71 kcal/mol). TD-DFT calculated transition dipole moments predict that only the degenerate $S_1$ and $S_3$ states have non-zero oscillator strengths, suggesting that 400-nm photolysis leads to the population of these states, both of which have minimum energy structures with bent-NO ligands. However, all of the singlet excited states with bent-NO ligands intersect with another excited state, typically in the vicinity of local minima. As a result, any population in the excited singlet states will rapidly relax to the lowest energy singlet state, $S_0$. These dynamics are all expected to occur more quickly than I can observe experimentally; [40] thus, none of the excited singlet states are expected to be involved in the experimentally observed dynamics. It is possible that this pathway occurs and may contribute to the low quantum yield of the pathway involved in the formation of **B** and **C**.

The topography of the excited triplet states is quite different and suggests that **B** corresponds to either the $T_2$ or $T_3$ excited triplet states in Figure 4.11. A relatively large energy gap separates the ground triplet state ($T_1$) and the higher triplet states ($T_2$ and $T_3$), suggesting that the higher triplet states will be relatively long-lived. The point of closest approach between $T_1$ and the higher triplet states ($T_2$ and $T_3$) along this coordinate occurs when the Co–N–O bond is bent into an eclipsed structure, at which point $T_1$ is ca.

---

[9] In the plot, $S_3$ does not show a minimum; along a similar coordinate in which the NO bond angle is the only degree of freedom, a shallow minimum as is seen for $T_4$.

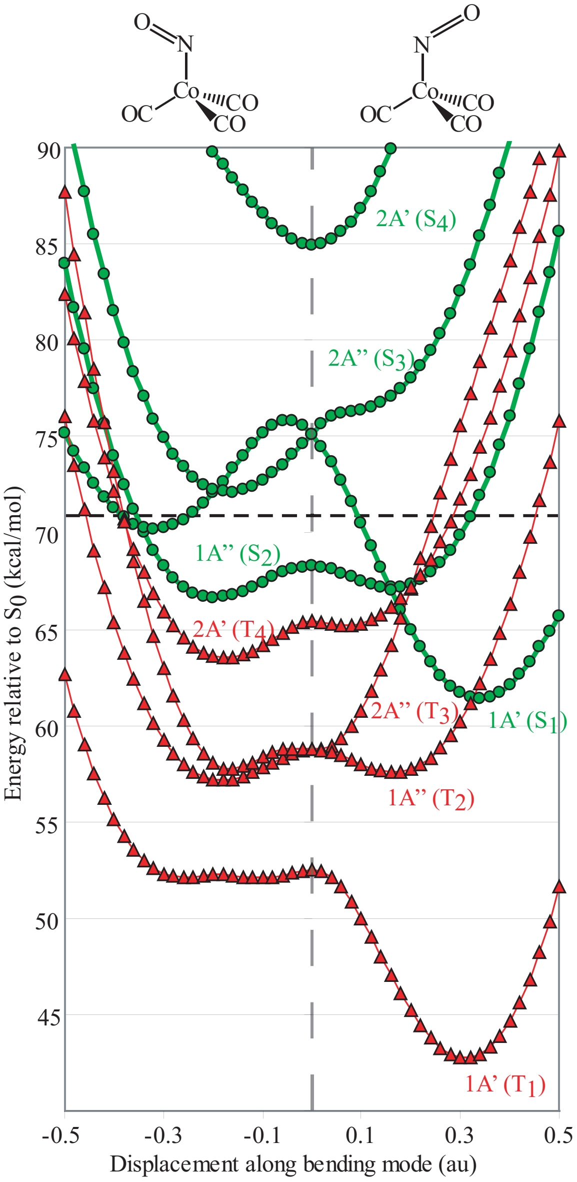

Figure 4.11: TD-DFT vertical excited states along the bending mode of Co(CO)$_3$(NO). Shown are the four single-excitation states of each spin symmetry arising from the original doubly degenerate HOMO and LUMO. Singlet states are shown in green (circles), and the triplet states are shown in red (triangles). The symmetries (A' and A") correspond to the symmetries for the individual states with positive bending modes, and the numbering of the states is based on the energy ordering of the states when the complex has a bent-NO geometry. The horizontal dashed line (71 kcal/mol) corresponds to the 400-nm photon energy.

5 kcal/mol lower in energy than the higher states. Significant distortion of this structure would be required for favorable coupling to $T_1$. Since the staggered and eclipsed minima in the $T_2$ state and the eclipsed $T_3$ minimum are nearly isoenergetic and connected by small barriers (ca. 3 kcal/mol), I cannot determine which structure (staggered or eclipsed) or which electronic state ($T_2$ or $T_3$) corresponds to **B**. Intuitively, one would expect that the eclipsed structure would be more stable. However, since a full optimization of the excited state structures is not computationally feasible, I cannot rigorously rule out the possibility that **B** corresponds to the staggered structure. A reasonable conjecture is that the excited state structure would have to access the small, but non-zero, barrier connecting the staggered and eclipsed structures in Figure 4.11 multiple times before transition to $T_1$ occurs. In other words, the molecule may switch back and forth between the staggered and eclipsed structures on either the $T_2$ and the $T_3$ surfaces before relaxing to $T_1$. While some ambiguity remains in assigning **B** to either $T_2$ or $T_3$,[10] it is clear from this analysis that **B** is an excited state triplet complex with a bent-NO ligand. Species **B** is stable for ca. 350 ps before relaxing to form species **C**, a bent-NO complex in the ground triplet state ($T_1$).

## 4.4 Discussion and Conclusions

Using time-resolved infrared spectroscopy and DFT modeling performed by Ryan Steele, I have, for the first time, directly observed a photoinduced linear-to-bent NO geometry change in a transition-metal complex. Excited states with bent-NO ligands in transition-metal–NO complexes have been proposed in the literature for 40 years, but the

---

[10] While the highest lying triplet state in Figure 4.11, also has an NO ligand that is less bent than the NO in $T_1$, I do not expect it to be long-lived. Figure 4.11 suggests that $T_4$ will rapidly relax to a lower lying state on a femtosecond time-scale.

formation of these excited states has never been directly observed. [41, 111–115] I have observed two kinetically correlated, excited triplet bent-NO complexes that exist on the picosecond time-scale. I propose the mechanism shown in Figure 4.12 for the photochemical formation of these bent-NO complexes. Photolysis of $Co(CO)_3(NO)$ with a single pulse of 400-nm light leads to population of a manifold of short-lived excited states which decay to an excited triplet state (either $T_2$ or $T_3$ in Figure 4.11) in less than one picosecond. The excited triplet structure has a bent NO ligand with a Co–N–O bond angle predicted to be roughly 155°-166°.[11] This structure is stable for 350 ps before nonadiabatic coupling induces a transition to the ground triplet state ($T_1$). The most stable structure in $T_1$ also has a bent NO ligand with a Co–N–O bond angle of 137°. The bent-NO complex in $T_1$ is observable throughout the remainder of the experiment. $T_1$ is expected to ultimately decay back to the parent, but I do not observe these dynamics on the picosecond time-scale.

The UV-visible absorption spectrum in Figure 4.2 indicates that the formation of the bent-NO complexes is a minor photochemical pathway, [112, 114] which is further verified by the low intensity of the **B** and **C** peaks in Figure 4.4. I expect that the triplet bent-NO complexes were not observed in past studies of $Co(CO)_3(NO)$ because the quantum yield for this pathway is so low. [112] It is possible that this pathway is more significant in other systems, but since the bent-NO complexes are excited state structures, they may be too short-lived to be observed by conventional methods. [40] Further experimental and theoretical investigations are suggested to determine the generality of this mechanism and to determine the effect that this pathway has on the photophysical properties of other

---

[11] The Co–N–O bond angle in the excited triplet structures in estimated based on the TD-DFT calculated presented in Figure 4.11 and is not based on fully optimized structures.

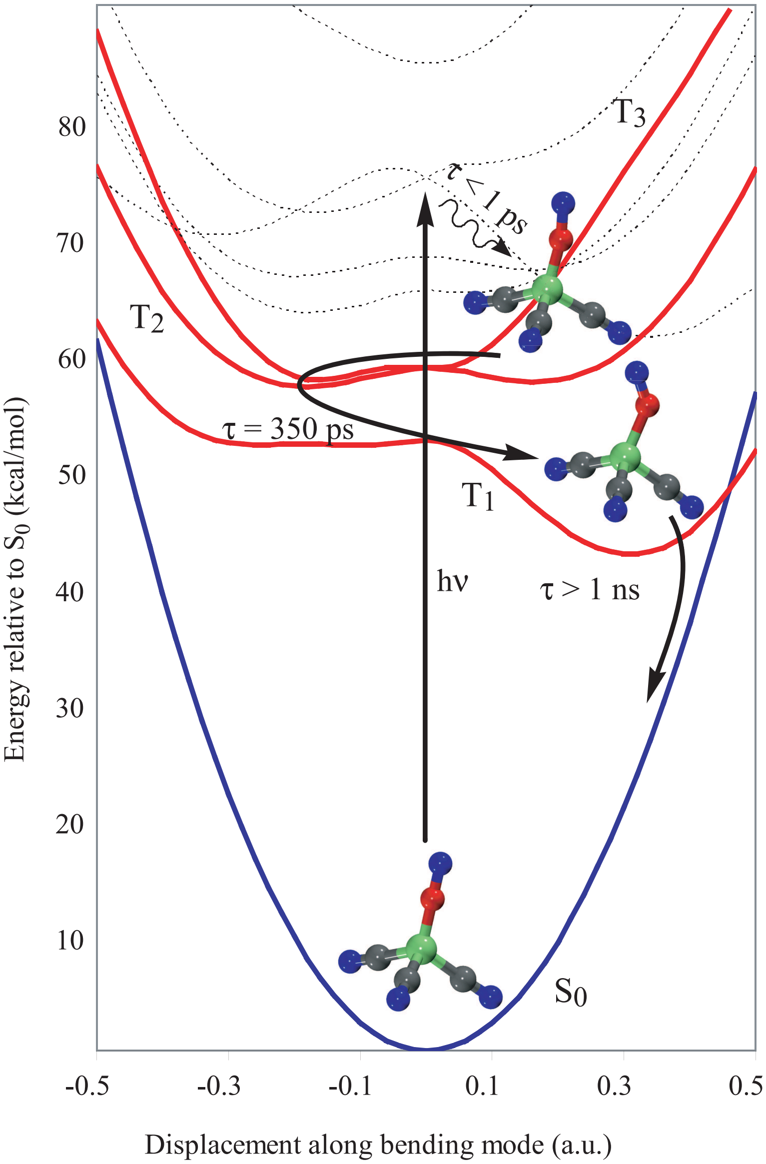

Figure 4.12: Photochemical mechanism for the formation of excited state bent-NO complexes of $Co(CO)_3(NO)$. While it is clear that **B** corresponds to a triplet excited state complex with a bent-NO ligand, I cannot definitively say which state ($T_2$ or $T_3$ in Figure 4.11) is populated.

transition-metal–NO compounds.

Questions remain concerning the generality of this mechanism. Numerous studies have proposed that $[Fe(CN)_5(NO)]^{2-}$ is particularly promising for optical data storage because visible photolysis of this compound leads to formation of Fe–ON and Fe–$\eta^2$-NO metastable states. The photochemical formation of these metastable states is extremely common in transition-metal–nitrosyl complexes; it has been observed in 80 compounds, including $Na_2[Fe(CN)_5(NO)]$, Cp*NiNO, $K_2[RuCl_5NO]$ and $[CpRe(CO)_2(NO)]BF_4$. However, the work presented herein indicates that there are additional photochemical pathways that may decrease the quantum yield for forming the metastable states. [19,20,22] Previous studies have ruled out stable triplet states with bent-NO ligands using ESR spectroscopy of complexes such as $[Fe(CN)_5(NO)]^{2-}$ and Cp*Ni(NO). [19] There are two possible reasons why the bent-NO complexes were not observed in those studies: (1) the excited state complexes are too short lived or (2) the $T_1$ bent-NO complex is formed in low yield. Even if the latter option is true, any small loss to $T_1$ may hold significant consequences for accurate and reliable data storage.

In addition, there is interest in transition-metal–NO complexes because they are important in medical applications that rely on the controlled release of NO from metal complexes. [5,15–18] The $\eta^2$-NO and ON structural isomers are proposed to be important to these processes because the metal–NO bond is weaker in these structures compared to complexes with linear-NO ligands. [17] Similarly, the metal–NO bond is weaker in bent-NO complexes compared to linear-NO structures. [2] This work suggests that bent-NO complexes may also be used to control NO signaling in biological systems. However, this study is the first to report the photochemical formation bent-NO complexes, and it is still unclear if there are similar mechanisms for more biologically relevant transition-metal–NO complexes.

# Chapter 5

# UV-pump, IR-probe investigation of selective C–H bond activation by transition-metal–boryl catalysts in solution

## 5.1 Introduction

The activation of the strong C–H bonds in saturated alkanes presents an enormous challenge which has been the focus of numerous research efforts over the past fifty years. [2,23,27,146,147] It has long been known that transition-metal complexes can catalyze C–H bond activation in room temperature alkane solutions, but the reactions are generally not selective for a specific type of C–H bond. [148] Recently, however, Hartwig and coworkers discovered transition-metal–boryl complexes that selectively [23,25–27,149] activate primary C–H bonds via both thermal [26,27] and photochemical [23,25,25] reactions with yields as high as 92%. The mechanism for bond activation by these compounds has been investigated experimentally [23–27] and theoretically, [26, 149, 150] but intermediates have not been observed by spectroscopic methods. In this study, I use pico- through the microsecond time-resolved IR spectroscopy and density functional theory calculations (DFT), in collaboration with C. Edwin Webster from the University of Memphis, to determine the sequential steps in the mechanism for C–H bond activation by photoactivated $Cp^*W(CO)_3(Bpin)$ ($Cp^* = C_5(CH_3)_5$; pin = 1,2-$O_2C_2$-$(CH_3)_4$), a compound that activates the primary C–H bonds of saturated alkanes in 72% yield. [23, 25, 26]

Figure 5.1 shows two mechanisms that have been proposed for this reaction. [24, 26, 149, 150] Both pathways begin with CO photodissociation from the reactant to form $Cp^*W(CO)_2(Bpin)$, which is solvated by a pentane molecule from the bath. In the $\sigma$-bond metathesis mechanism, the solvated complex forms a $\sigma$-borane intermediate, $Cp^*W(CO)_2(H\text{–}Bpin)(C_5H_{11})$ which has isomers with the H or B of the borane ligand adjacent to the $C_5H_{11}$ group. In the oxidative addition mechanism, on the other hand, the alkane is oxidatively added to the metal center to form $Cp^*W(CO)_2(Bpin)(H)(C_5H_{11})$. In both pathways, the next step is the formation of a strong B–C bond between a carbon on the $C_5H_{11}$ ligand and the boron on the Bpin ligand, forming a metal hydride bound to an alkylboronate ester, $Cp^*W(CO)_2(H)(H_{11}C_5\text{–}Bpin)$. The final step is the elimination of the ester to form a metal hydride, $Cp^*W(CO)_2(H)$.

The mechanisms for both pathways have been investigated in previous DFT stud-

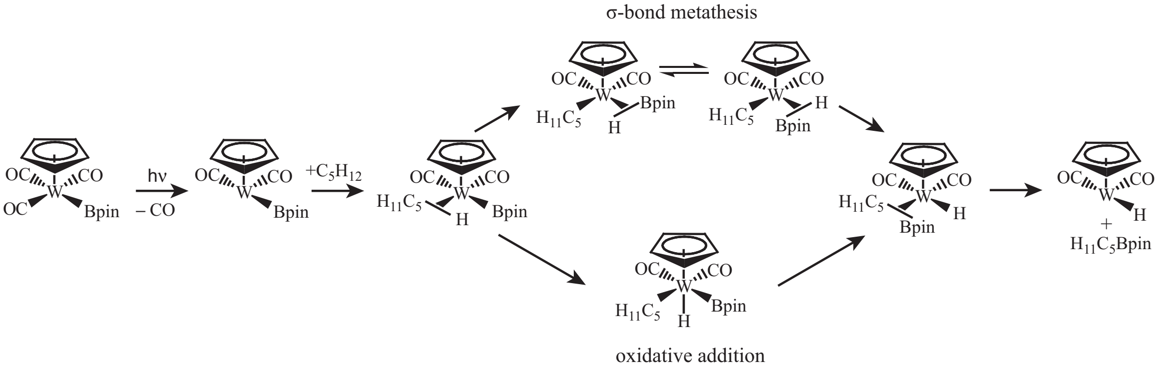

Figure 5.1: Proposed mechanisms for the C–H bond activation by photoactivated tungsten–boryl complexes in neat pentane solution: $\sigma$-bond metathesis and oxidative addition. [23,24] Note that the methyl groups on the Cp* rings are not shown here for clarity of presentation.

ies and both have been found reasonable in room temperature solution. [149, 150] Initially, the oxidative addition mechanism was considered more favorable because it is a common mechanism for C–H bond activation by mid- to late-transition-metal catalysts, such as $[\mathrm{Cp^*Ir(PMe_3)(CH_3)}]^+$ and $\mathrm{Tp^*Rh(CO)_2}$ ($\mathrm{Tp^*}$ = HB–$\mathrm{Pz_3}^*$ where Pz* = 3,5-dimethylpyrazolyl). [146, 151] Along the same lines, the $\sigma$-bond metathesis mechanism was initially considered less favorable because the mechanism generally only occurs for early transition-metal complexes, whereas tungsten–boryl complexes produced the highest yields of C–H bond activation. [23, 24, 150] Nevertheless, the most recent DFT studies predict that the $\sigma$-bond metathesis mechanism is more energetically favorable than the oxidative addition mechanism. [26, 149, 150]

The goal of this study is to use a combination of the results from time-resolved IR spectroscopy and DFT calculations to conclusively determine the mechanism for C–H bond activation by photoactivated transition-metal–boryl compounds. These techniques have been shown to be effective for determining the bond activation mechanisms of transition-metal catalysts. [33, 36, 74, 146, 151, 152] I have been able to confirm that the reaction proceeds via a $\sigma$-bond metathesis mechanism, and I have identified two side reactions that limit the yield of bond-activation products.

## 5.2 Methods

### 5.2.1 Synthesis of Cp*W(CO)$_3$(Bpin) and Sample Preparation

Cp*W(CO)$_3$(Bpin)(Cp* = $C_5(CH_3)_5$; pin = 1,2-$O_2C_2$-$(CH_3)_4$) was synthesized, following a published procedure, [23–25] by Dr. Marko Hapke, a postdoctoral researcher in Prof. John Hartwig's group at Yale University. The compound was stored and handled under nitrogen atmosphere in a glove-box (Vacuum Atmospheres Company). For the experiments, dilute solutions were prepared in neat pentane and the air-sensitive solutions were held under a positive pressure of argon.

### 5.2.2 Density Functional Theory (DFT) Calculations

The DFT Modeling performed for this project was done by Prof. C. Edwin Webster at the University of Memphis. His description of the computational methods used are included below.

The theoretical calculations have been carried out using the Gaussian03 [76] implementation of B3LYP (the B3 exchange functional [77] and LYP correlation functional) [86] and BVP86 (the Becke exchange functional (B) [77] and the Perdew correlation functional (VP86)) [78, 153] density functional theories [154] using the default pruned fine grids for energies (75, 302), default pruned course grids for gradients and Hessians (35, 110) (neither grid is pruned for tungsten), and default SCF convergence for geometry optimizations

($10^{-8}$). BVP86 will hereafter be referred to as BP86. To ease computational expense, a methane molecule was used in place of the pentane ligand used experimentally. Shortening alkane ligands is a common method for reducing computational expense and is not expected to significantly change the mechanistic results. [33, 39, 74, 75, 149, 150]

All calculations used the same basis set combination. The basis set for tungsten (341/341/21) was the Hay and Wadt basis set and effective core potential (ECP) combination (LANL2DZ) [82, 155] as modified by Couty and Hall, where the two outermost p functions have been replaced by a (41) split of the optimized tungsten 6p function. [156] All metal-ligated atoms, borons and oxygens utilized the cc-pVDZ basis sets. [124,157] Each cc-pVDZ basis set has had the redundant functions removed and has been linearly transformed, as suggested by Davidson. [158] All other atoms utilized the D95 basis sets. [159] The density fitting approximation [160–164] for the fitting of the Coulomb potential was used for all BP86 calculations; auxiliary density-fitting basis functions were generated automatically (by the procedure implemented in Gaussian 03) for the specified AO basis set. Spherical harmonic d functions were used throughout, i.e., there are five angular basis functions per d function. Full ligands (except pentane for which methane was substituted) were used in all computations. All structures were fully optimized, and analytical frequency calculations were performed on all structures to ensure either a zeroth-order saddle point (a local minimum) or a first-order saddle point (transition state: TS) was achieved. All energies, enthalpies and free energies reported have been calculated using the B3LYP functional, and the vibrational frequencies reported have been calculated using the BP86 functional and have not been scaled. [39, 72, 75, 120, 165, 166]

## 5.3 Experimental Results

### 5.3.1 Picosecond dynamics

Figure 5.2 shows UV-pump, IR-probe spectra of Cp*W$(CO)_3$(Bpin) in neat pentane solution measured at time delays ranging from 5 ps to 3 ns. The three negative features (referred to as parent bleaches) are centered at 1899, 1914 and 2000 $cm^{-1}$ and are due to the depletion of the reactant by the UV-pump pulse. The positive features are due to species formed as a result of the UV-pump pulse. Peak assignments are based on observed dynamics, literature [24, 167] and calculated CO vibrational frequencies. The intensities of the parent bleaches in Figure 5.2 rise on two time-scales, an average fast time-scale of 35 ± 11 ps and an average slow time-scale of 222 ± 80 ps, as shown in a kinetic plot of the 2000 $cm^{-1}$ bleach in Figure 5.3 (refer to Table 5.1 for dynamics of the individual spectral features). The fast recovery of the bleach is due to vibrational cooling of reactant molecules which have been left vibrationally excited by the UV-pump pulse. This explanation is confirmed by ultrafast IR-pump, IR-probe measurements of the reactant (refer to Appendix A.3) which confirm that this molecule undergoes vibrational relaxation in ca. 35 ps.

The 1888 and 1978 $cm^{-1}$ peaks are assigned to the Cp*W$(CO)_3^{\bullet}$ radical which is produced by photodissociation of $Bpin^{\bullet}$ from the reactant. [167] These peaks decay on a time-scale of 229 ± 8 ps, in agreement with the slow rise of the bleaches (Figure 5.3), indicating that Cp*W$(CO)_3^{\bullet}$ recombines with $Bpin^{\bullet}$ in ca. 200 ps. The radical recombination is remarkably efficient—Cp*W$(CO)_3^{\bullet}$ peaks to decay to zero within experimental noise. Thus, neither Cp*W$(CO)_3^{\bullet}$ or $Bpin^{\bullet}$ are involved in C–H bond activation, in agreement with past investigations which provide no evidence for radical involvement in bond activation. [23–25, 149]

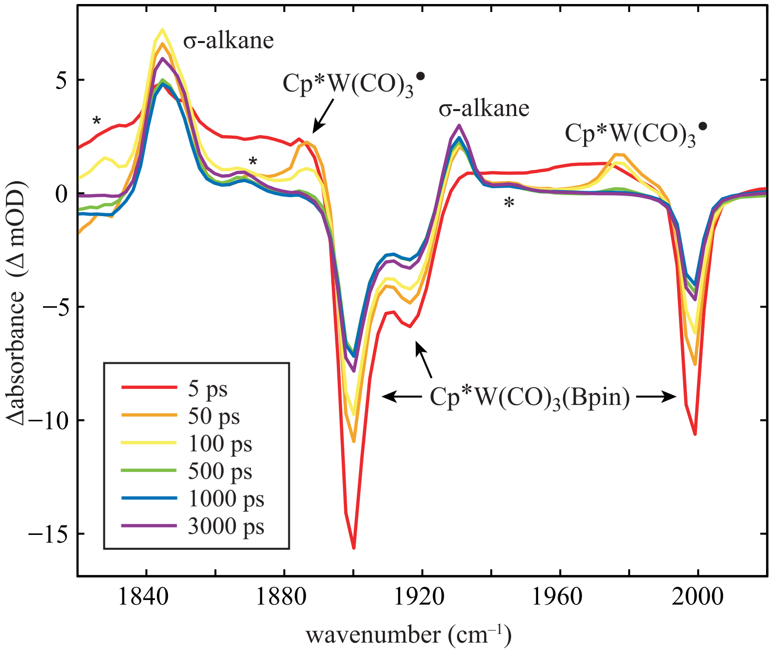

Figure 5.2: Picosecond UV-pump, IR-probe spectra of Cp*W(CO)$_3$(Bpin) in neat pentane solution. The features marked with * are minor side products that are discussed in the Appendix A.3.

Instead, previous experimental and computational studies show that bond activation begins with the photodissociation of a CO from the reactant and subsequent solvation of the coordinatively unsaturated complex with an alkane molecule from the bath. [23–25, 149, 150] Generally, CO photodissocation occurs in less than 200 fs and solvation occurs in 1–2 ps. [29, 30, 168–170] Therefore, I assign the remaining features centered at 1844 cm and 1931 cm$^{-1}$ to the $\sigma$-alkane complex, Cp*W(CO)$_2$(Bpin)(C$_5$H$_{12}$). Upon close examination of the 1844 cm$^{-1}$ feature, however, it appears that there are actually two overlapping peaks in this region. Figures 5.4a and 5.4b show an enlargement of the feature at 2 ps and 1000 ps, respectively, along with a fit of the feature to Lorentzian functions. The data and fits clearly show a large peak at 1844 cm$^{-1}$ and a shoulder at 1852 cm$^{-1}$. I pro-

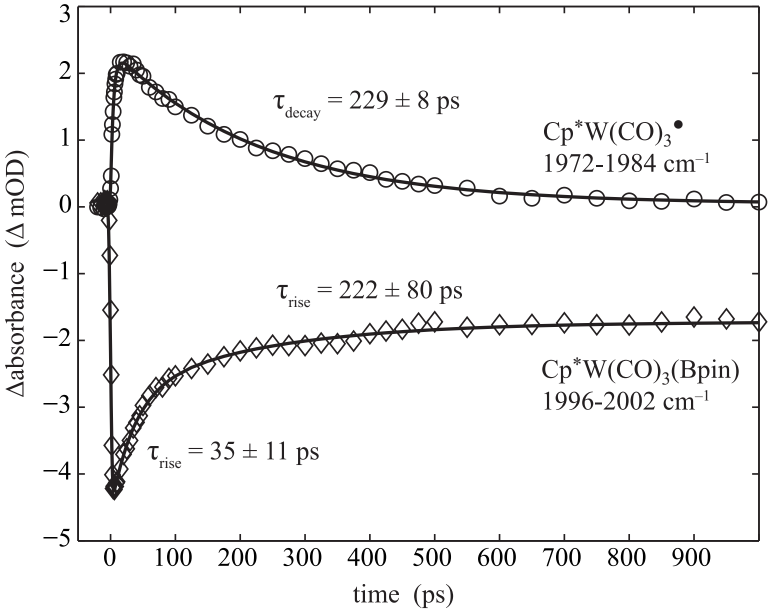

Figure 5.3: Kinetic plots for Cp*W(CO)$_3$(Bpin) and Cp*W(CO)$_3$$^\bullet$.

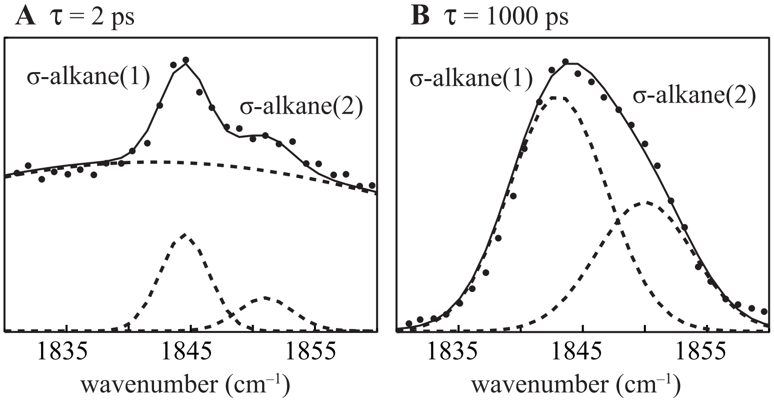

Figure 5.4: Enlargement of the feature attributed to Cp*W(CO)$_2$(Bpin)(C$_5$H$_{12}$) at time delays of (**A**) 2 ps and (**B**) 1000 ps. The solid line corresponds to a fit of the data to multiple Lorentzian functions which are shown individually as dashed lines. The broad Lorentzian in (A) is an adjustment to the baseline to account for vibrationally excited $\sigma$-alkane population and is not needed for spectra measured at time delays ($\tau$) greater than ca. 30 ps.

pose that the two peaks correspond to two different isomers of Cp*W(CO)$_2$(Bpin)(C$_5$H$_{12}$), denoted $\sigma$-alkane(1) and $\sigma$-alkane(2) for convenience. The two peaks show similar dynamics on the picosecond time-scale, an average fast rise of 24 ± 11 ps and an average slow decay of 219 ± 59 ps (refer to Table 5.1 for the dynamics of the individual features). The fast rise is due to vibrational cooling, and the slow decay, which is in good agreement with the rise of the parent bleaches, is assigned to geminate recombination between the coordinatively unsaturated metal complex and the CO ligand. The peak intensities do not change further between 500 ps and 3 ns.

The $\sigma$-alkane isomers have never before been observed experimentally. However, past DFT studies have indicated that the *cis*-$\sigma$-alkane isomer is the first intermediate in bond activation, [26, 149, 150] suggesting that one of these structures is due to *cis*-Cp*W(CO)$_2$(Bpin)(C$_5$H$_{12}$) and the other is a different isomer possibly involved in a side-reaction. The reactions of these species occur on the nano- through microsecond time-scales, as described in the following sections.

### 5.3.2 Nanosecond and microsecond dynamics

Figure 5.5 shows step-scan FTIR spectra of Cp*W(CO)$_3$(Bpin) in neat pentane solution measured on the nano- through microsecond time-scales. The spectra at time delays between 25 ns and 200 ns are displayed in Figure 5.5a. The $\sigma$-alkane peaks are the only observable features in the spectra, and they exhibit no dynamics on this time-scale. Figure 5.5b, on the other hand, shows data collected from 1 $\mu$s through 40 $\mu$s, and the $\sigma$-alkane peaks do decay on this time-scale. Again, the $\sigma$-alkane feature in the spectra is asymmetric, a clear indication that it consists of two peaks. Figure 5.6a and 5.6b shows an enlargement of this feature at two distinct time delays, 1 μs and 5 μs, respectively, along with a fit of the feature to two Lorentzian functions. The 1 μs spectra clearly show an asymmetric line-shape that is the result of a large feature at 1844 $cm^{-1}$ and a shoulder at 1852 $cm^{-1}$. However, the asymmetric line-shape changes as a function of time. The asymmetry is no longer observable in the 5 μs spectra because the $\sigma$-alkane(2) peak on the blue side of the feature (1852 $cm^{-1}$) has decayed, leaving only the $\sigma$-alkane(1) peak (1844 $cm^{-1}$). Kinetic plots on the red and blue sides of the feature are shown in Figure 5.7a and 5.7b, respectively. The $\sigma$-alkane(1) peak on the red side at 1844 $cm^{-1}$ decays in 13 ± 2 μs (Figure 5.7a), and the $\sigma$-alkane(2) peak on the blue side at 1852 $cm^{-1}$ decays in 7 ± 2 μs (Figure 5.7b).[1] The different time constants suggest that the two $\sigma$-alkane isomers undergo different chemical reactions.

Figure 5.5b also shows three new peaks at 1828, 1859 and 1942 $cm^{-1}$, which grow in on the early microsecond time-scale. The peaks at 1859 and 1942 $cm^{-1}$, denoted Int(1), grow in with time constants of 20 ± 3 μs and 21 ± 4 μs, respectively, in agreement with the decay time constants of the $\sigma$-alkane(1) peak. A third peak, centered at 1828 $cm^{-1}$ and denoted Int(2), grows in on a shorter time-scale of 6 ± 2 μs, in agreement with the decay of the $\sigma$-alkane(2) peak. The kinetic plots for these species are displayed in Figures 5.7a and b. Based on the dynamics, it appears that $\sigma$-alkane(1) forms Int(1) in ca. 15 μs whereas $\sigma$-alkane(2) reacts to form Int(2) in approximately 7 μs. One of these pathways corresponds to the bond activation reaction, and the other corresponds to a side-reaction, as will be

---

[1] The kinetic traces for the both $\sigma$-alkane isomers were determined by fitting a narrow peak area ($\sigma$-alkane(1): 1844–1845 $cm^{-1}$ and $\sigma$-alkane(2): 1851–1852 $cm^{-1}$) plotted as a function of time to a single exponential function in order to extract separate time constants for the $\sigma$-alkane(1) and (2) isomers. The peak area of the entire feature, encompassing both the $\sigma$-alkane(1) and (2) peaks, plotted as a function of time is best fit to a biexponential function, indicating that the decays of the $\sigma$-alkane(1) and (2) peaks are separate kinetic events.

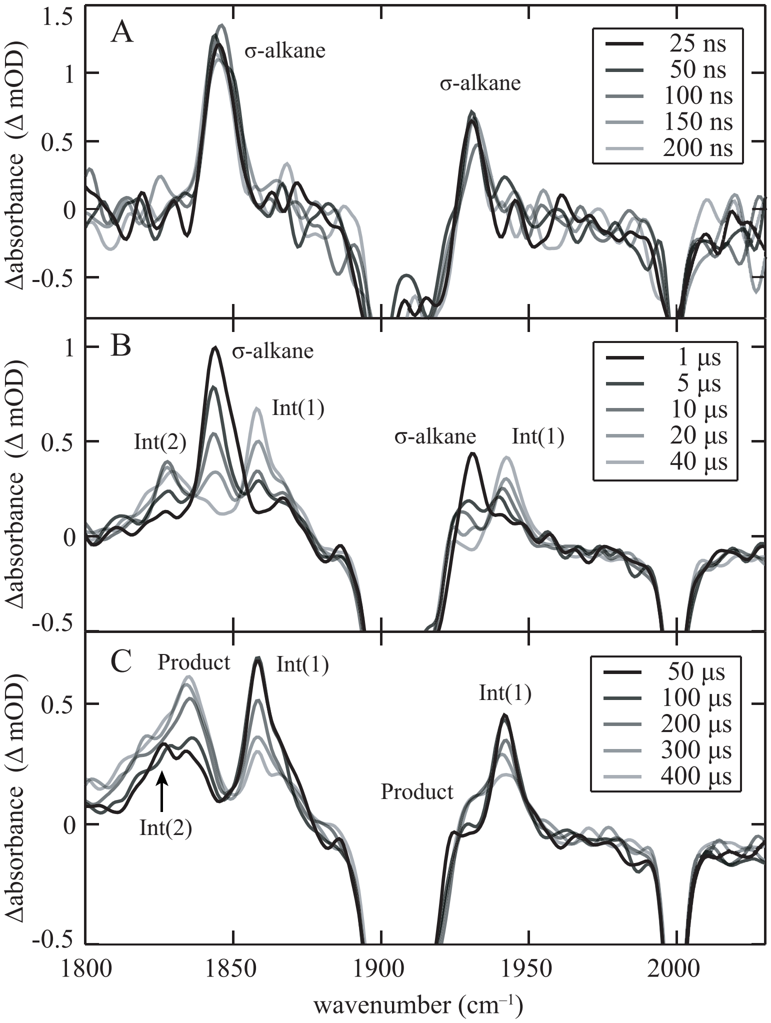

Figure 5.5: Nano- through microsecond step-scan FTIR spectra of Cp*W(CO)$_3$(Bpin) in neat pentane solution with time delays between (A) 25 ns and 200 ns, (B) 1 $\mu$s and 40 $\mu$s, and (C) 50 $\mu$s and 400 $\mu$s. The parent bleaches have been omitted since they do not have dynamics on these time-scales.

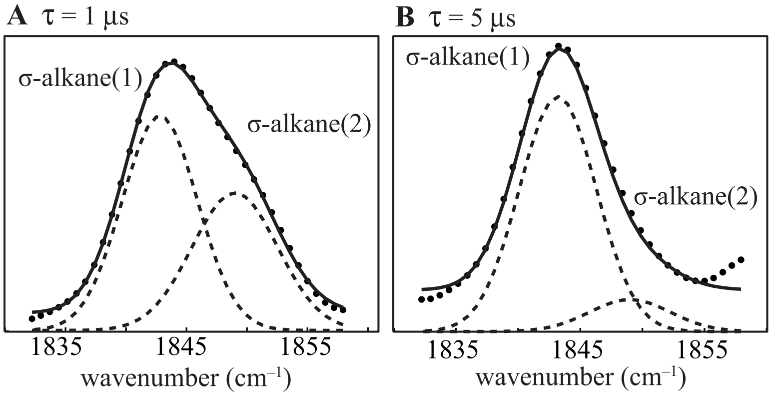

Figure 5.6: Enlargement of the feature attributed to Cp*W(CO)$_2$(Bpin)(pentane) at time delays of (**A**) 1 $\mu$s, (**B**) 5 $\mu$s. The solid line corresponds to a fit of the data to multiple Lorentzian functions which are shown individually as dashed lines.

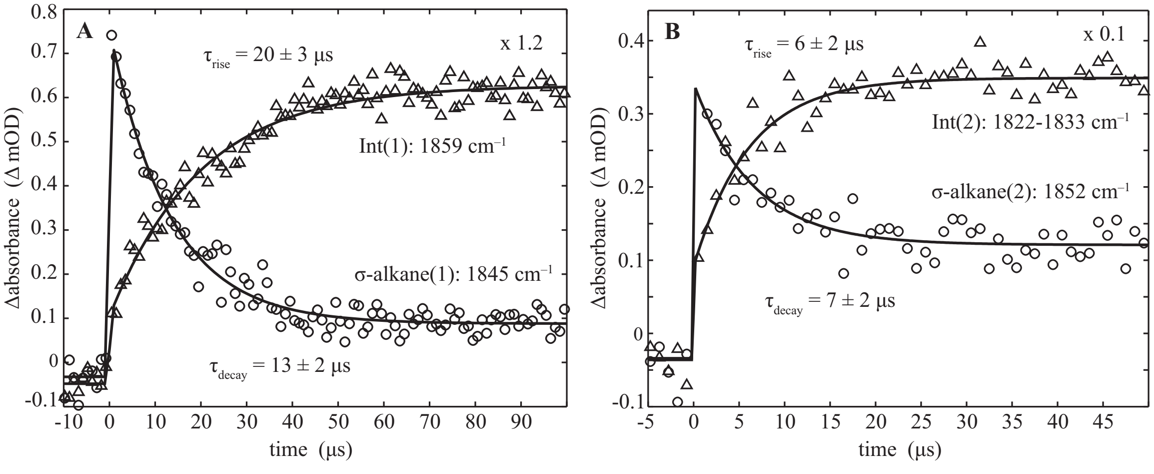

Figure 5.7: Kinetic plots for (**A**) the decay of the $\sigma$-alkane(1) peak (1845 cm$^{-1}$) and the rise of the Int(1) peak (1859 cm$^{-1}$) and (**B**) the decay of the $\sigma$-alkane(2) peak (1852 cm$^{-1}$) and the rise of the Int(2) peak (1828 cm$^{-1}$). The kinetics of Int(1) and Int(2) are scaled by 1.2 and 0.1, respectively, for clarity of presentation.

discussed in Section 5.4.

Figure 5.5c shows spectra between 50 and 400 $\mu$s. Two new features appearing at 1835 and 1932 cm$^{-1}$ are labeled Product because they persist throughout the remainder of the experiment. Kinetic plots of the Product and Int(1) peaks are shown in Figure 5.8. The Int(1) peak at 1859 cm$^{-1}$ decays with a time constant of 191 ± 39 $\mu$s, and similarly, the Product features grow in average time-scale of 149 ± 25 $\mu$s. The agreement of the time constants indicates that Int(1) forms the Product in 150–200 $\mu$s. Conversely, Int(2) has no discernable dynamics, suggesting that it participates in a slower side reaction discussed in Section 5.4.3. In the following sections, I turn to DFT calculations to conclusively understand all peaks and dynamics observed experimentally.

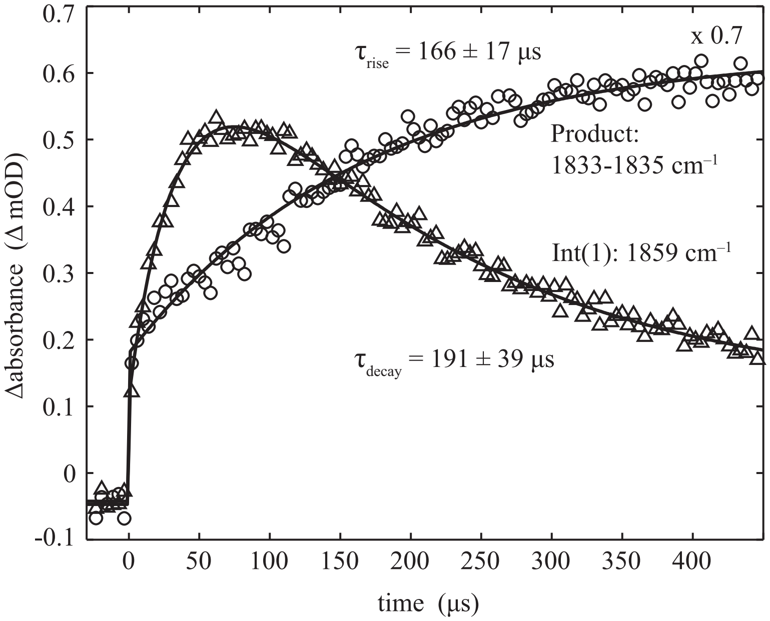

Figure 5.8: Kinetic plots for the decay of the Int(1) peak (1859 cm$^{-1}$) and the rise of the Product peak (1835 cm$^{-1}$). The kinetics of the product are scaled by 0.7 for clarity of presentation.

| **Species** | **Freq. ($cm^{-1}$)** | | | $\tau$ | **Trend** |
|---|---|---|---|---|---|
| | **DFT** | **Lit.** | **Exp.** | | |
| Cp*W$(CO)_3$(Bpin) [25] | 1899(1.0) | 1900 | 1899(s) | 29 ± 12 ps | rise[c] |
| | | | | 213 ± 71 ps | rise[d] |
| | 1917(0.69) | 1916 | 1914(m) | not observable | |
| | 1978(0.67) | 1999 | 2000(s) | 36 ± 12 ps | rise[c] |
| | | | | 222 ± 80 ps | rise[c] |
| *cis*-Cp*W$(CO)_2$(Bpin)$(C_5H_{12})$ | 1863(0.93) | N/A | 1844(s) | 21 ± 8.4 ps | rise[c] |
| (*cis*-$\sigma$-alkane) | | | | 247 ± 62 ps | rise[d] |
| | | | | 13 ± 2 $\mu$s | rise |
| | 1921(1.0) | N/A | | not observable | |
| Cp*W$(CO)_2$(HBpin)$(C_5H_{11})$ | 1775(0.12)[a] | N/A | | not observable | |
| (Int(1)/Bpin-back) | 1865(0.91) | | 1859(s) | 20 ± 3 $\mu$s | rise |
| | | | | 191 ± 39 $\mu$s | decay |
| | 1941(1.0) | | 1942(m) | 21 ± 4 $\mu$s | rise |
| | | | | 196 ± 41 $\mu$s | decay |
| Cp*W$(CO)_2$(H) | 1841(0.2)[a] | N/A | 1820(w) | not observable | |
| (Product) | 1877(1.0) | | 1835(s) | 166 ± 17 $\mu$s | rise |
| | 1931(1.0)[b] | | 1932(w)[b] | 131 ± 33 $\mu$s | rise |
| $\sigma$-alkane(2) | 1856(1.0)[e] | N/A | 1852(m) | 26 ± 13 ps | rise[c] |
| | 1867(1.0)[f] | | | 190 ± 56 ps | decay[d] |
| | | | | 7 ± 2 $\mu$s | decay |
| | 1917(0.45)[e] | NA | 1931(m) | | |
| | 1926(0.87)[f] | | | 5 ± 1 $\mu$s | decay |
| Int(2) | N/A | N/A | 1828(m) | 6 ± 2 $\mu$s | rise |
| Cp*W$(CO)_3^\bullet$ [167] | 1895(1.0) | 1887 | 1888(m) | 147 ± 14 ps | decay |
| | 1900(0.66) | | | | |
| | 1965(0.63) | 1984 | 1978(m) | 4.5 ± 1 ps | rise |
| | | | | 229 ± 8.3 ps | decay |

Table 5.1: Peak assignments and dynamics for experimentally observed species with relative intensities given in parentheses. DFT results correspond to complexes with methane substituted for pentane. [a] W–H stretch; b peak is partially obscured by the neighboring bleach (1914 $cm^{-1}$); [c] dynamics due to vibrational cooling; [d] dynamics due to geminate recombination; [e] *trans*-Cp*W$(CO)_2$(Bpin)$(CH_4)$ DFT calculated CO stretching modes; [f] Cp*W$(CO)_2$($\eta^2$-Bpin)$(CH_4)$ DFT calculated modes

## 5.4 DFT calculations of C–H bond activation catalyzed by $\mathrm{Cp^*W(CO)_2(Bpin)}$

I have utilized DFT calculations to identify the peaks described in section 5.3 and to interpret the experimental data in terms of a C–H bond activation mechanism. The analysis herein focuses on the two mechanisms that have been proposed for transition-metal–boryl catalysts, $\sigma$-bond metathesis and oxidative addition (refer to Figure 5.1). [23, 25] C. Edwin Webster, a professor at the University of Memphis, has calculated multiple $\sigma$-bond metathesis and oxidative addition pathways, and here I present the most energetically favorable (i.e., lowest reaction barriers) $\sigma$-bond metathesis and oxidative addition mechanisms. Note that all calculations use methane rather than pentane as the solvent for computational efficiency. For both mechanisms, the lowest energy pathways exclusively involve transient species with the CO ligands in the *cis* geometry. I present an analysis of the experimental data in light of the free energies and CO vibrational frequencies of the intermediates and transition states for both mechanisms. The resulting picture, when compared to the experiment, lends considerable insight into the bond activation mechanism. The computational work shows that the reaction pathways in which transient species have CO ligands in a *trans* geometry are 5–15 kcal/mol higher in energy than the most energetically favorable mechanism. These higher barriers are most likely the result of the geometric changes that must occur in order to bring the B and C in proximity in the *trans* geometry.

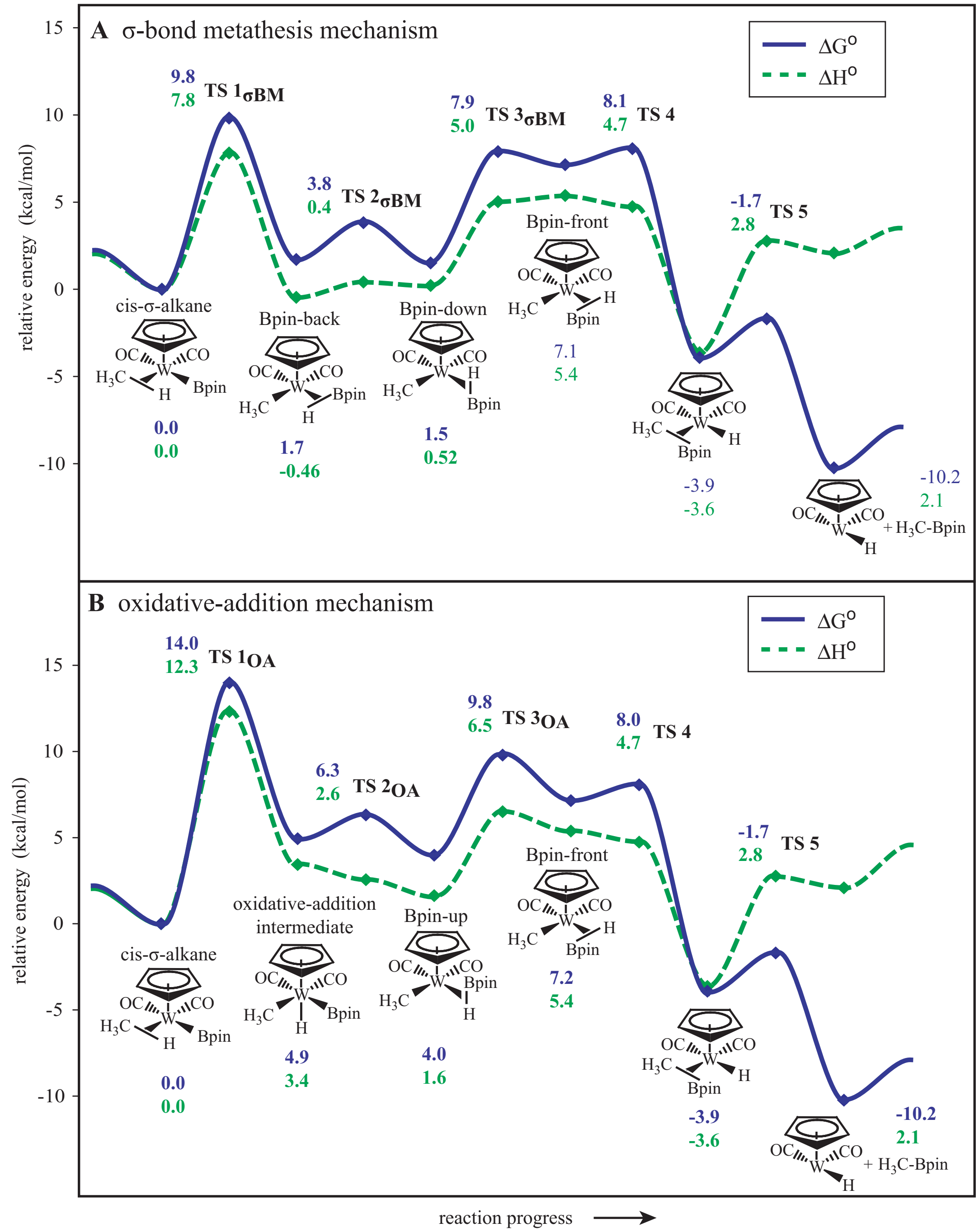

Figure 5.9: Lowest energy reaction mechanisms for (**A**) $\sigma$-bond metathesis and (**B**) oxidative addition pathways as calculated by DFT. Enthalpies and free energies (kcal/mol) are relative to *cis*-Cp*W(CO)$_2$(Bpin)(CH$_4$). Note that for clarity of presentation, the methyl groups on the Cp* rings are not shown.

### 5.4.1 $\sigma$-bond metathesis

The lowest energy pathway for bond activation that we have found is the $\sigma$-bond metathesis pathway depicted in Figure 5.9a. In agreement with past DFT studies, [149] the first key intermediate in the mechanism is the *cis*-$\sigma$-alkane complex, *cis*-Cp*W(CO)$_2$(Bpin)(pentane). Because the dynamics described in section 5.3 indicate that the $\sigma$-alkane(1) peak corresponds to the first species involved in the bond-activation reaction, we have assigned $\sigma$-alkane(1) to this *cis* isomer ($\sigma$-alkane(1) will now be referred to as *cis*-$\sigma$-alkane). The kinetics in Figure 5.7 show that *cis*-$\sigma$-alkane reacts to form Int(1) in ca. 15 $\mu$s. As depicted in Figure 5.9a, the most likely reaction for *cis*-$\sigma$-alkane is the cleavage of a saturated C–H bond on the alkane ligand and the shift of the H to the Bpin ligand, generating a $\sigma$-borane complex with the H atom adjacent to the CH$_3$ ligand (hereafter referred to as Bpin-back). The calculated free energy of activation ($\Delta G^{\ddagger}$) to this reaction (TS1$_{\sigma BM}$) is 9.8 kcal/mol, which corresponds to a 2.5 $\mu$s time constant by generalized transition state theory. [97] This time constant is in good agreement (within an order of magnitude) of the 15 $\mu$s decay of *cis*-$\sigma$-alkane. The calculated CO stretching modes of Bpin-back (1865 and 1941 cm$^{-1}$) are also in excellent agreement with the Int(1) peaks (1859 and 1942 cm$^{-1}$). The agreement of both the calculated frequencies and time constants with the experimental values strongly supports the assignment of Int(1) to Bpin-back.

Past experimental studies show that alkylboronate ester (alkyl–Bpin) is the final product of the bond activation reaction. [23–26] It is not possible to form the ester from Bpin-back because the B atom is not adjacent to the alkyl ligand. [26, 149] Thus, the next step in the reaction involves rotation of the borane ligand to bring the B and C into close proximity, as depicted in Figure 5.9a. The first rotation moves the borane ligand so that it is pointing down (refer to Figure 5.9 for the meaning of down). This $\sigma$-borane structure, denoted Bpin-down, is nearly isoenergetic with Bpin-back ($\Delta G^{\circ}_{back}$ = 1.7 kcal/mol; $\Delta G^{\circ}_{down}$ = 1.5 kcal/mol). Thus, based on the energetics we cannot determine if one or both isomers contribute to the Int(1) peaks in Figure 5.5b. However, the calculated CO stretching modes of Bpin-back agree better with the experimentally observed Int(1) peaks suggesting that they are due to Bpin-back. Thus, while Bpin-back and Bpin-down are most likely in equilibrium, the DFT calculated CO stretching modes of the two species suggest that the equilibrium favors Bpin-back. From Bpin-down, the borane ligand rotates a second time so that the Bpin ligand is adjacent to the $CH_3$ group (Bpin-front). Because the B and C atoms are in close proximity in Bpin-front (B–C = 2.47 Å), the creation of a B–C bond is facile, and the alkylboronate metal complex, $Cp^*W(CO)_2(H)(H_3C\text{–}Bpin)$, is readily formed. We do not expect to observe this alkylboronate complex in the experiment, though, because the interaction between the tungsten and the alkyl–Bpin ligand is weak and the alkyl–Bpin ligand should be quickly eliminated.

A course-grained look at Figure 5.9a shows that there are two significant barriers in the $\sigma$-bond metathesis mechanism. The first barrier, as discussed earlier, corresponds to the reaction from *cis*-$\sigma$-alkane to Bpin-back on a time-scale of 15 $\mu$s, and I propose that the second large barrier, between Bpin-down and Bpin-front ($TS3_{\sigma BM}$), corresponds to the 170 $\mu$s Int(1)$\rightarrow$Product reaction observed experimentally. By generalized transition state theory, a 170 $\mu$s time constant corresponds to a free energy difference ($\Delta G^{\ddagger o}$) of at least 12.3 kcal/mol, however, the DFT value for the free energy of activation from Bpin-down to Bpin-front ($TS3_{\sigma BM}$) is only 6.4 kcal/mol. This discrepancy is likely an artifact in the DFT results caused by the use of methane rather than pentane as the alkane in the bond activation reaction. The pentyl groups should experience greater steric interaction with the boryl ligand compared to the methyl groups used in the calculations, possibly explaining the discrepancy. Under this interpretation, the Product peaks in Figure 5.5c (1835 and 1932 $cm^{-1}$) correspond to $Cp^{*}W(CO)_2(H)$, which are in fair agreement with the calculated CO stretching modes for this complex (1877 and 1931 $cm^{-1}$). $Cp^{*}W(CO)_2(H)$ will eventually react to form either $Cp^{*}W(CO)_3(H)$ or $[Cp^{*}W(CO)_3]_2$ by collision with free CO or a $Cp^{*}W(CO)_2(H)$ fragment, respectively. [23–25] While we do not observe the formation of these complexes on the microsecond time-scale, they have been observed as final products by Hartwig and coworkers. [23–26]

These results are in agreement with past experimental and computational studies of tungsten–, iron– and rhodium–boryl complexes that have suggested the $\sigma$-bond metathesis mechanism is the most energetically feasible reaction. [26, 149] The mechanism in Figure 5.9a is, however, slightly different from the $\sigma$-bond metathesis mechanism presented in the literature for the related tungsten–boryl complex, $CpW(CO)_2(B(OCH_2)_2)$. [149] In our DFT calculations, the methyl groups on the Bpin and Cp* ligands were included in order to improve the agreement between calculated and observed CO stretching modes. Including these groups also led to a slight change in the $\sigma$-bond metathesis mechanism, presumably because the larger ligands introduce greater steric interactions in the system. Specifically, there are three stable $\sigma$-borane intermediates in the $Cp^{*}W(CO)_3(Bpin)$ reaction but only two with $CpW(CO)_3(B(OCH_2)_2)$. These differences suggest that although variations in the boryl ligands lead to slight changes in the mechanism, the overall the reaction still proceeds by $\sigma$-bond metathesis.

### 5.4.2 Oxidative addition

Although the evidence for the $\sigma$-bond metathesis mechanism as outlined above is compelling, I have also considered the alternative oxidative addition mechanism. Oxidative addition processes are more common for C–H bond activation by transition-metal catalysts, especially for compounds with mid-to-late transition-metals. [146, 151] In the case of transition-metal–boryl compounds, the most efficient catalysts have tungsten and rhodium metal centers, and for this reason, the oxidative addition mechanism was originally favored. [25]

Prof. C. Edwin Webster has modeled an oxidative addition mechanism for C–H bond activation of $CH_4$ by *cis*-Cp*W$(CO)_2$(Bpin) using DFT, and the lowest oxidative addition energy pathway is depicted in Figure 5.9b. The reaction begins with the familiar *cis*-$\sigma$-alkane complex, but in this case, the first step is insertion of W into a C–H bond of $CH_4$, forming the oxidative addition intermediate, Cp*W$(CO)_2$(Bpin)(H)$(CH_3)$. The free energy of activation to this process ($TS1_{OA}$) is 4.2 kcal/mol higher than the corresponding step ($TS1_{\sigma BM}$) in the $\sigma$-bond metathesis mechanism. The time constant for the reaction as predicted by generalized transition state theory is 3 ms, in poor agreement with the 15 $\mu$s time constant observed experimentally. The next step is the formation of a B–H bond between the Bpin and the hydride ligand, creating a $\sigma$-borane complex with Bpin ligand pointing up (Bpin-up). Similar to the mechanism in Figure 5.9a, the borane ligand rotates so that the B and C atoms are close enough to form a bond. From this point forward

(TS3-TS5) the mechanisms in Figure 5.9a and 5.9b are identical.

If the oxidative addition mechanism is correct, the intermediate labeled Int(1) in the spectra would correspond to the oxidative addition intermediate or Bpin-up. The calculated CO stretching frequencies of neither Bpin-up (1917 and 1964 $\text{cm}^{-1}$) nor the oxidative addition intermediate (1927 and 1974 $\text{cm}^{-1}$) agrees with experiment (1859 and 1942 $\text{cm}^{-1}$). The large discrepancies between the observed and calculated frequencies (ca. 60 and ca. 30 $\text{cm}^{-1}$ for the antisymmetric and symmetric modes, respectively) and the high energy of $\text{TS1}_{OA}$ clearly provide no support for this mechanism.

### 5.4.3 Side-reactions

The preceding analysis provides compelling evidence for the $\sigma$-bond metathesis mechanism in Figure 5.9a. However, the data also provides evidence for a side-reaction involving $\sigma$-alkane(2) and Int(2) (refer to section 5.3.2). Unlike the radical side reaction discussed in section 5.3.1, this side-reaction yields long-lived products that influence the final bond activation yield. Species $\sigma$-alkane(2) is discernible within 2 ps after photolysis and is predicted to be an isomer of $\text{Cp*W(CO)}_2\text{(Bpin)(C}_5\text{H}_{12})$. Unlike the *cis*-$\sigma$-alkane isomer, $\sigma$-alkane(2) is not involved in the primary bond activation reaction and, instead, decays to form Int(2) in 7 $\mu$s. Int(2) is unreactive on the time-scale of the experiment (500 $\mu$s).

All of the intermediates discussed up to this point have CO ligands in a *cis* geometry. We believe, however, that $\sigma$-alkane(2) has CO ligands in a different geometry. Figure 5.10 shows two other isomers of $\text{Cp*W(CO)}_2\text{(Bpin)(CH}_4)$. The simplest explanation for $\sigma$-alkane(2) is that it corresponds to the *trans*-$\sigma$-alkane isomer, *trans*-

| **Species** | | **B3LYP** | | **BP86** |
|---|---|---|---|---|
| | $\Delta$E | $\Delta$H° | $\Delta$G° | Freq. (cm$^{-1}$) |
| Cp*W(CO)$_2$(Bpin)(CH$_4$)<br>*cis*-$\sigma$-alkane | 0 | 0 | 0 | 1863 (0.93)<br>1921 (1.0) |
| *cis*-$\sigma$-alkane→Bpin-back<br>TS1$_{\sigma BM}$ | 10.2 | 7.82 | 9.82 | N/A |
| Cp*W(CO)$_2$(HBpin)(CH$_3$) | 0.11 | -0.46 | 1.71 | 1775 (0.12)$^a$<br>1865 (0.92)<br>1941 (1.0) |
| Bpin-back→Bpin-down<br>TS2$_{\sigma BM}$ | 2.00 | 0.42 | 3.82 | N/A |
| Cp*W(CO)$_2$(HBpin)(CH$_3$)<br>Bpin-down | 1.51 | 0.52 | 1.51 | 1771 (0.18)$^a$<br>1891 (1.0)<br>1951 (0.95) |
| Bpin-down→Bpin-front<br>TS3$_{\sigma BM}$ | 6.26 | 5.03 | 7.90 | N/A |
| Cp*W(CO)$_2$(HBpin)(CH$_3$)<br>Bpin-front | 5.83 | 5.38 | 7.15 | 1840 (0.10)$^a$<br>1891 (0.72)<br>1945 (1.0) |
| Bpin-front→Cp*W(CO)$_2$(H)(H$_3$C–Bpin)<br>TS4 | 6.18 | 4.74 | 8.06 | N/A |
| Cp*W(CO)$_2$(H)(H$_3$C–Bpin) | -2.11 | -3.64 | -3.91 | 1842 (0.13)$^a$<br>1884 (0.81)<br>1935 (1.0) |
| Cp*W(CO)$_2$(H)(H$_3$C–Bpin)→Cp*W(CO)$_2$(H)<br>TS5 | 4.85 | 2.77 | -1.69 | N/A |

Table 5.2: B3LYP energies, enthalpies and free energies of the intermediates, transition states and products and BP86 frequencies of the intermediates and products in the lowest energy $\sigma$-bond metathesis reaction of Cp*W(CO)$_2$(Bpin) in alkane solution. Energy, enthalpy and free energies (kcal/mol) are relative to *cis*-Cp*W(CO)$_2$(Bpin)(CH$_4$), and the CO ligands are oriented in a cis geometry. Calculated intensities are given in parentheses. $^a$ W–H stretch

| **Species** | **B3LYP** | | | **BP86** |
|---|---|---|---|---|
| | $\Delta$E | $\Delta$H° | $\Delta$G° | Freq. (cm$^{-1}$) |
| Cp*W(CO)$_2$($\eta^2$-Bpin)(CH$_4$) | 1.58 | 1.05 | -2.5 | 1867 (1.0)<br>1926 (0.87) |
| *trans*-Cp*W(CO)$_2$(Bpin)(CH$_4$) | 1.11 | 0.43 | 3.0 | 1856 (1.0)<br>1917 (0.45) |
| *cis*-$\sigma$-alkane→Ox-Add<br>TS1$_{OA}$ | 14.9 | 12.3 | 14.0 | N/A |
| Cp*W(CO)$_2$(Bpin)(H)(CH$_3$)<br>Ox-Add | 4.98 | 3.44 | 4.94 | 1922 (0.08)[a]<br>1927 (1.0)<br>1974 (0.8) |
| Ox-Add→Bpin-up<br>TS2$_{OA}$ | 4.95 | 2.56 | 6.32 | N/A |
| Cp*W(CO)$_2$(HBpin)(CH$_3$)<br>Bpin-up | 2.85 | 1.63 | 3.98 | 1791(0.05)[a]<br>1917 (0.97)<br>1964 (1.0) |
| Bpin-up→Cp*W(CO)$_2$(HBpin)(CH$_3$)<br>TS3$_{OA}$ | 7.69 | 6.51 | 9.79 | N/A |
| Cp*W(CO)(Bpin)(CH$_4$)[b] | 0.0 | 0.0 | 0.0 | 1835 |
| Cp*W(CO)(Bpin)(CH$_3$)(H)[b] | -5.30 | -7.03 | -6.12 | 1926 |
| Cp*W(CO)(HBpin)(CH$_3$)[b] | -12.5 | -14.7 | -13.9 | 1840 |

Table 5.3: B3LYP energies, enthalpies and free energies of the intermediates, transition states and products and BP86 frequencies of the intermediates and products in the lowest energy oxidative addition of of Cp*W(CO)$_2$(Bpin) in alkane solution and the possible side-reactions. Unless otherwise noted, energy values (kcal/mol) are relative to *cis*-Cp*W(CO)$_2$(Bpin)(CH$_4$), and the CO ligands are oriented in a cis geometry. Calculated intensities are given in parentheses. [a] W–H stretch; [b] Energies, enthalpies, and free energies set relative to Cp*W(CO)(Bpin)(CH$_4$)

$Cp^*W(CO)_2(Bpin)(C_5H_{12})$ (Figure 5.10a). The vibrational frequency of this complex (1856 $cm^{-1}$) is in good agreement with the $\sigma$-alkane(2) peak (1852 $cm^{-1}$). I have also identified a different isomer with the Bpin ligand bound in an $\eta^2$ fashion to the metal through the B–O bond. This structure has the two CO ligands and the Bpin ligand in a three-legged piano stool orientation (Figure 5.10b). The $\eta^2$-bound structure is slightly more stable than the *trans*-$\sigma$-bonded complex, and the vibrational frequency (1866 $cm^{-1}$) is also in good agreement with experiment (1852 $cm^{-1}$). Thus, I cannot conclusively determine which of the two structures in Figure 5.10 corresponds to the $\sigma$-alkane(2) peak, and since the complexes have nearly overlapping CO stretching modes and are similar in energy, we cannot rule out the possibility that both contribute to the feature. However, our DFT modeling indicates that the $\eta^2$-Bpin structure (Figure 5.10b) cannot directly activate a C–H bond; instead, it must first rearrange to either the *cis*- or the *trans*-$\sigma$-alkane, both of which are capable of catalyzing bond activation.

The experimental data shows that $\sigma$-alkane(2) decays into Int(2) on a time-scale of 7 $\mu$s. We observe a single feature for Int(2) at 1828 $cm^{-1}$. Intuitively, one expects that $\sigma$-alkane(2) will react through a $\sigma$-bond metathesis mechanism like the one presented in Figure 5.9a except with intermediates that have CO ligands in a *trans* geometry. In spite of this, our DFT calculations indicate that there cannot be a $\sigma$-bond metathesis reaction for *trans*-$\sigma$-alkane because it is not possible to form a $\sigma$-borane complex in this geometry since the B and H atoms are too far apart to interact with one another (4.2 Å).[2] Thus, we do

---

[2] Note that DFT calculations indicate that *trans*-$\sigma$-borane has a W–H stretching mode of 1827 $cm^{-1}$, nearly identical to observed Int(2) peak (1828 $cm^{-1}$), but the calculated intensity of this mode is only 12% of the intensity of the most intense CO stretch. The calculated trans-$\sigma$-borane complex has two CO stretching modes, 1880 and 1958 $cm^{-1}$, but we do not observe Int(2) features at these frequencies. One could argue that the 1880 $cm^{-1}$ peak overlaps with the bleach at 1900 $cm^{-1}$, but we do not observe any dynamics of the bleach on the microsecond time-scale, suggesting otherwise. There is also no evidence for

A trans-Cp*W(CO)$_2$(Bpin)(CH$_4$)

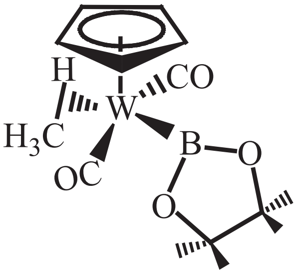

1856 cm$^{-1}$ (1.0)
1917 cm$^{-1}$ (0.45)
$\Delta H^o$ = 0.43 kcal/mol
$\Delta G^o$ = 2.96 kcal/mol

B Cp*W(CO)$_2$($\eta^2$-Bpin)(CH$_4$)

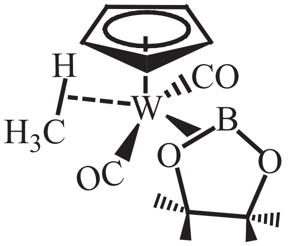

1866 cm$^{-1}$ (1.0)
1926 cm$^{-1}$ (0.45)
$\Delta H^o$ = 1.05 kcal/mol
$\Delta G^{\ddagger/o}$ = -2.51 kcal/mol

Figure 5.10: DFT calculated structures of (**A**) *trans*-Cp*W(CO)$_2$(Bpin)(CH$_4$) and (**B**) Cp*W(CO)$_2$($\eta^2$-Bpin)(CH$_4$). ΔH° and ΔG° are relative to *cis*-Cp*W(CO)$_2$(Bpin)(CH$_4$). Note that the methyl groups on the Cp* ligands are not shown for clarity of presentation.

not expect that the $\sigma$-alkane(2)→Int(2) rearrangement corresponds to a $\sigma$-bond metathesis reaction.

We have, however, found an oxidative addition pathway in which the intermediates have CO ligands arranged in the *trans* geometry, shown in Figure 5.11a. If $\sigma$-alkane(2) reacts via this mechanism, we would expect that Int(2) would be due to the first oxidative addition intermediate since the first step in the mechanism has a free energy of activation of only 9.7 kcal/mol, corresponding to a time constant of 2.5 $\mu$s by generalized transition state theory, in good agreement with the observed 7 $\mu$s time constant for the $\sigma$-alkane(2)→Int(2) reaction. However, CO stretching modes of the first oxidative addition intermediate (1885 and 1961 $\mathrm{cm}^{-1}$) have poor agreement with the observed Int(2) peak. The lowest energy calculated CO stretch (1885 $\mathrm{cm}^{-1}$) is nearly 60 $\mathrm{cm}^{-1}$ higher than the Int(2) peak, and there is no evidence for any Int(2) feature in the vicinity of the higher energy 1961 $\mathrm{cm}^{-1}$ mode. Thus, we cannot assign Int(2) to be an intermediate in a *trans* oxidative addition bond activation reaction.

Since the DFT calculations suggest that the $\sigma$-alkane(2)→Int(2) reaction does not correspond to any bond activation reaction with CO intermediates in a *trans* geometry, we have investigated some ligand dissociation reactions of the $\sigma$-alkane complexes in an attempt to find a stable complex with a CO stretch near 1828 $\mathrm{cm}^{-1}$. Unfortunately, we are still unable to conclusively assign Int(2). We have considered the possibility that Int(2) is due to $\mathrm{Cp^*W(CO)_2^\bullet}$ which is formed after the dissociation of $\mathrm{Bpin^\bullet}$ from *trans*-$\sigma$-alkane, but the DFT calculated $\mathrm{Bpin^\bullet}$ bond dissociation energy is ca. 71.0 kcal/mol and the calculated

---

the 1958 $\mathrm{cm}^{-1}$ peak in the spectra. The discrepancies between the observed and calculated CO stretching modes suggest that Int(2) does not correspond to *trans*-$\sigma$-borane.

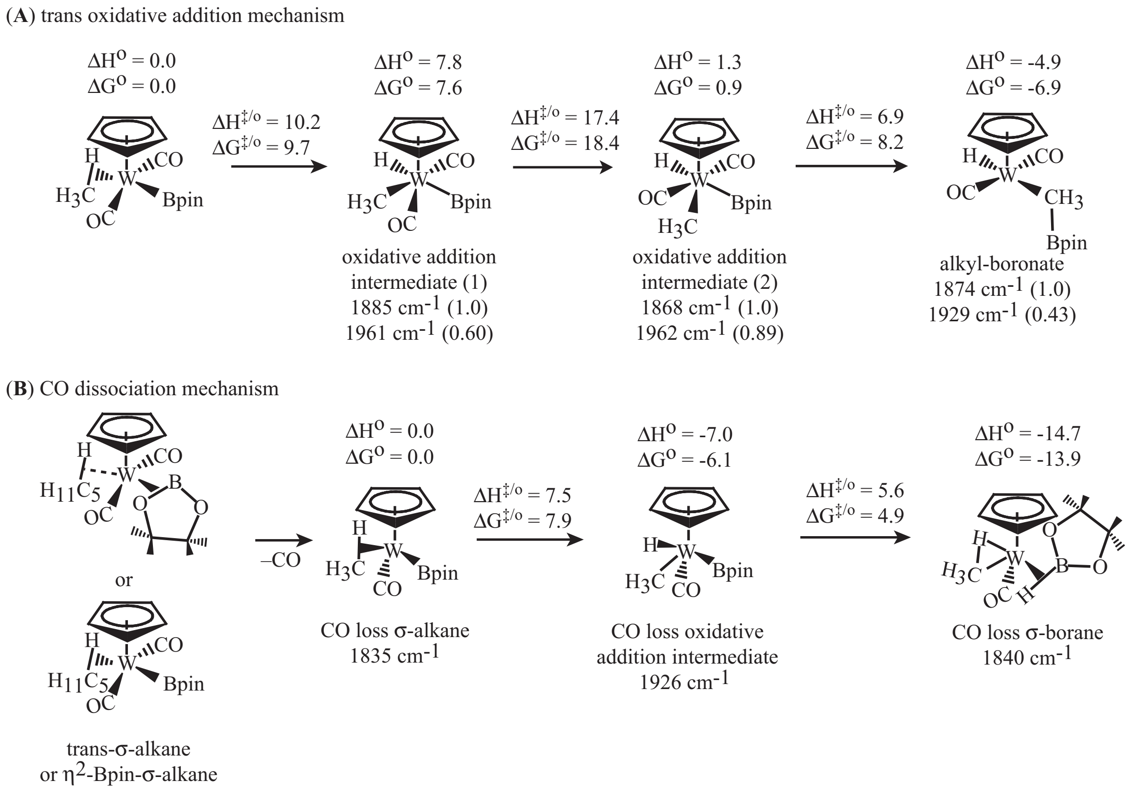

Figure 5.11: DFT calculated mechanisms for (**A**) the oxidative addition bond activation reaction of *trans*-$\sigma$-alkane and (**B**) the stabilization of Cp*W(CO)(Bpin)($CH_4$), the intermediate formed after CO dissociation for one of the $\sigma$-alkane complexes. Again, reported enthalpies and free energies (kcal/mol) are calculated with BP3LYP functional, and vibrational frequencies are calculated with the BP86 functional. Note that the methyl groups on the Cp* ligands are not shown for clarity of presentation.

CO stretching modes (1851 and 1908 $\mathrm{cm}^{-1}$) have poor agreement with experiment. Another possibility is that Int(2) is a complex that is formed after a CO photodissociated from a $\sigma$-alkane complex. Admittedly, it seems unlikely that any $\sigma$-alkane isomer would lose a ligand since they are formally 16-electron complexes. However, the only species that we found with a CO stretching mode in the vicinity of 1828 $\mathrm{cm}^{-1}$ have only one CO ligand. DFT calculations indicate that the dissociation of a CO from a $\sigma$-alkane complex leads to the formation of Cp*W(CO)(Bpin)($CH_4$), a $\sigma$-alkane complex in which the $CH_4$ is coordinated via an $\eta^3$ interaction involving the C and two H atoms. Dissociation of a CO ligand from any of the $\sigma$-alkane structures, *cis*-$\sigma$-alkane, *trans*-$\sigma$-alkane or Cp*W$(CO)_2$($\eta^2$-Bpin)($CH_4$) ultimately leads to the formation of this single CO $\sigma$-alkane complex. However, we do not expect *cis*-$\sigma$-alkane to lose a CO since the DFT analysis presented above indicates that it follows the more energetically favorable reaction in Figure 5.9a. On the other hand, we find no evidence for an analogous *trans* bond activation reaction, suggesting that the it may react via alternative route.[3]

The most energetically favorable pathway for the stabilization of the single CO $\sigma$-alkane complex, Cp*W(CO)(Bpin)($CH_4$), is shown in Figure 5.11b. The first step is the oxidative addition of the W into one of the C–H bonds to form Cp*W(CO)(Bpin)($CH_3$)(H). The next step is the formation of a B–H bond between the Bpin and $CH_4$ ligands to create a $\sigma$-borane complex, Cp*W(CO)(H–Bpin)($CH_3$). This structure is more thermodynamically stable than the other intermediates because of an agostic interaction between the W and

---

[3] We have been unable to identify a direct reactive pathway for Cp*W(CO)($\eta^2$-Bpin)($CH_4$), so we propose that any *trans* bond activation reaction proceeds through Cp*W(CO)(Bpin)($CH_4$). However, the $\eta^2$-Bpin ligand only destablizes Cp*W(CO)(Bpin)($CH_4$) by 2.6 kcal/mol, and the free energy of activation to the Cp*W(CO)($\eta^2$-Bpin)($CH_4$)$\rightarrow$Cp*W(CO)(Bpin)($CH_4$) reaction is only 6.2 kcal/mol, suggesting that the two are in equilibrium on the microsecond time-scale.

the $CH_3$ group. The free energies of activation to these two steps are 7.9 and 4.9 kcal/mol, corresponding to time constants of ca. 100 ns and 650 ps, respectively, by generalized transition state theory. Both time constants are much lower than the 7 $\mu$s observed time constant for the $\sigma$-alkane(2)$\rightarrow$Int(2) reaction, and thus, if the $\sigma$-alkane(2) loses a CO group, the 7 $\mu$s time constant likely corresponds to the rate of CO dissociation. In this scenario, we would observe $\sigma$-alkane(2) decaying to form the $\sigma$-borane complex, Cp*W(CO)(H–Bpin)($CH_3$). In other words, the Int(2) peak would correspond to Cp*W(CO)(H–Bpin)($CH_3$) since the other intermediates are too short-lived to be observable on the microsecond time-scale.[4] DFT calculations support this assignment—the calculated CO stretch of Cp*W(CO)(H–Bpin)($CH_3$) is 1840 $cm^{-1}$, in good agreement with experiment (1828 $cm^{-1}$). We do not observe any further reaction of Int(2) out to 500 $\mu$s, and similarly, the DFT results predict a high free energy of activation to forming the desired B–C bond from Cp*W(CO)(H–Bpin)($CH_3$) because of the agostic interaction between the $CH_3$ and W. Note that none of the single CO complexes that we have investigated are stabilized by the addition of a second $CH_4$ solvent molecule; the second $CH_4$ molecule interacts weakly with the metal (the W–C bond distances are ca. 3.4 and 3.6 Å in Cp*W(CO)(Bpin)($CH_4$)$_2$).

While the calculated CO stretch of Cp*W(CO)(H–Bpin)($CH_3$) agree well with the Int(2) peak, it still seems unlikely that a CO ligand would be dissociated from $\sigma$-alkane(2) in only 7 $\mu$s since DFT calculations predict that the $\sigma$-alkane CO bond dissociation energy is 54.2 kcal/mol.[5] It is possible that the CO dissociation occurs via a concerted solvent-assisted mechanism, but this mechanism seems improbable since a second $CH_4$ molecule

---

[4] We also found direct rearrangement mechanism from Cp*W(CO)(Bpin)($CH_4$) to Cp*W(CO)(H–Bpin)($CH_3$), but this pathway is significantly higher in energy than the step-wise mechanism.

[5] This energy is similar to the CO bond dissociation energy for Cp*W$(CO)_3$(Bpin) which is calculated to be 53.2 kcal/mol.

does not stabilize Cp*W(CO)(Bpin)($CH_4$). Thus, we cannot conclusively assign Int(2) to Cp*W(CO)(H–Bpin)($CH_3$). Nonetheless, based on the experimentally observed peak intensities and the calculated oscillator strengths of the $\sigma$-alkane complexes, we can calculate the effect of the $\sigma$-alkane(2) side-reaction on the total bond activation yield. We estimate that 35% of the reactant molecules which lose a CO after photoexcitation form $\sigma$-alkane(2). This complex reacts to form Int(2) in ca. 7 $\mu$s, and this pathway does not contribute to the final C–H bond activation yield. The other 65% of the reactant molecules form *cis*-$\sigma$-alkane. This complex follows the more favorable bond activation mechanism depicted in Figure 5.9a, resulting in the formation of the final bond activation product, $H_{11}C_5$–Bpin.[6] This prediction is in accord with past studies on this complex, which report a C–H bond activation yield of 72%. [23–25] Thus, the imperfect yield is likely the result of an alternative $\sigma$-alkane structure formed within only 2 ps after photolysis.

## 5.5 Conclusion

The results of these time-resolved IR studies are summarized in Figure 5.12. The primary reaction pathway, shown in the center row, begins with the photodissociation of a CO from Cp*W($CO)_3$(Bpin) and solvation of the metal complex by a pentane molecule, forming *cis*-$\sigma$-alkane within 2 ps. *Cis*-$\sigma$-alkane undergoes a $\sigma$-bond metathesis reaction to cleave a C–H bond on the pentane ligand in favor of a B–H bond. To ultimately form a B–C bond, it is necessary for the borane ligand to rotate twice so that the B on the borane is adja-

---

[6] The branching ratio is estimated by analyzing the relative peak amplitudes of the antisymmetric CO stretching modes of *cis*-Cp*W($CO)_2$(Bpin)($C_5H_{12}$) and *trans*-Cp*W($CO)_2$($\eta^2$-Bpin)($C_5H_{12}$), the 1844 and 1852 $cm^{-1}$ peaks in Figure 5.4, respectively. The Lorentzian fit to these peaks indicates that the 1852 $cm^{-1}$ peak is 54% as intense as the 1844 $cm^{-1}$ peak. Throughout this analysis, we weight the branching ratio by the calculated oscillator strengths of the antisymmetric CO stretching modes for the two complexes.

cent to the $C_5H_{11}$ ligand. From this configuration, the B–C bond is readily formed, creating a metal-hydride bound to an alkylboronate metal complex, Cp*W$(CO)_2$(H)($H_{11}C_5$–Bpin). The $H_{11}C_5$–Bpin group is weakly bound to the metal and is readily eliminated to form Cp*W$(CO)_2$(H) and the desired free product $H_{11}C_5$–Bpin. The rate-limiting step, occurring in 170 $\mu$s, is the rotation of the borane ligand from pointing down to being oriented adjacent to the $C_5H_{11}$ ligand.

In addition to the desired bond activation reaction, we have observed two side reactions. UV photoexcitation leads to the photodissociation of the Bpin$^\bullet$ radical to form CpW$(CO)_3^\bullet$ (refer to the bottom pathway in Figure 5.12). This radical pathway is of relatively minor importance because Cp*W$(CO)_3^\bullet$ is produced in low yield and efficiently recombines with Bpin$^\bullet$ to reform the reactant within 200 ps. The second side reaction is more important to the product yield. The molecules involved in the side reaction are similar to those involved in bond activation except that the CO ligands are arranged in a different manner, either in a *trans* or three-legged piano-stool structure. In these structures, the boryl and alkyl ligands are ca. 4.2 and 6.0 Å apart for the *trans* and piano-stool geometries, respectively, increasing the barrier to forming the B–C or B–H bonds necessary for bond activation. Unfortunately, we cannot conclusively determine the nature of the $\sigma$-alkane(2)$\rightarrow$Int(2) side-reaction.

This work represents the first direct observation of a $\sigma$-bond metathesis mechanism for C–H bond activation by tungsten–boryl complexes, a mechanism that is notably different from the bond activation mechanisms for other late transition-metal compounds. [146–148, 151] $\sigma$-bond metathesis mechanisms are usually only observed for early

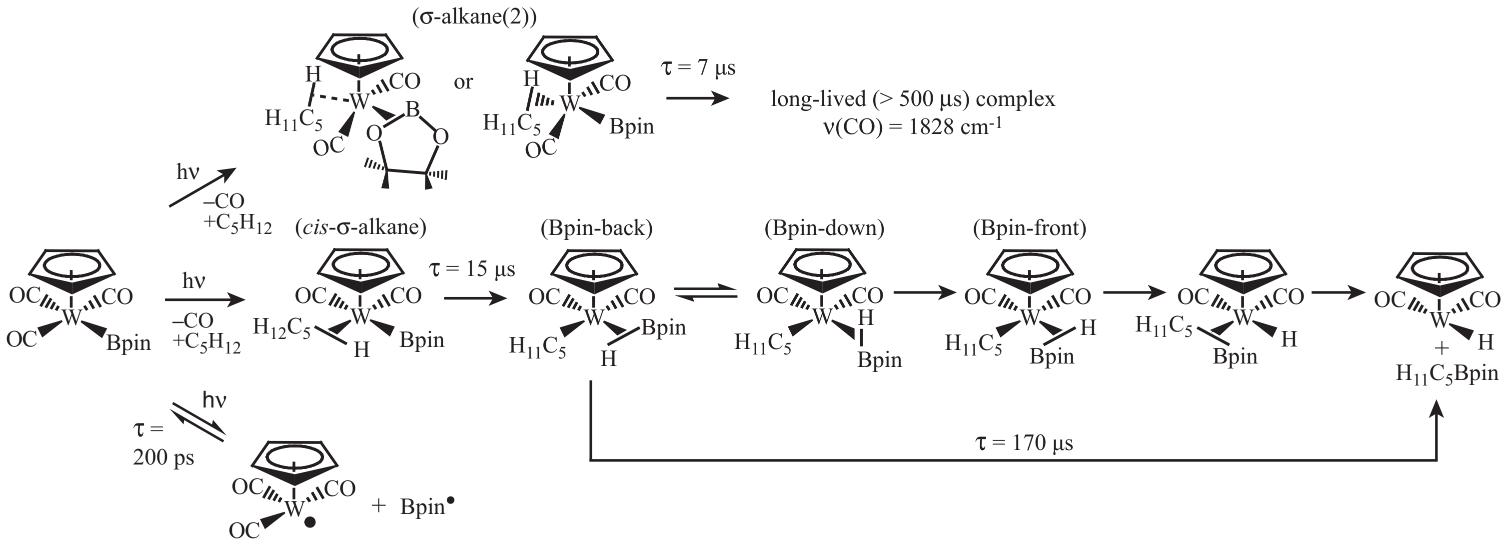

Figure 5.12: Experimentally observed photochemical reactions of Cp*W(CO)$_3$(Bpin) in neat pentane solution.

transition-metal catalysts because in these systems oxidative addition is impossible. [2, 25] The most effective photoactivated transition-metal–boryl catalysts have third-row metal centers, such as tungsten, and thus, initially these compounds were expected to react via oxidative addition. [2, 23, 25, 56] This work shows the first conclusive spectroscopic evidence that tungsten–boryl complexes instead react via a novel $\sigma$-bond metathesis mechanism. Past computational studies have shown that this mechanism is favorable because of the electropositive nature of the boron which provides favorable kinetics for the forming a B–C bond. [25, 148, 149, 171, 172] It is possible that this unusual mechanism is responsible for the extraordinary selectivity of the bond activation reaction. However, the yields for C–H bond activation by iron–boryl complexes are significantly lower than the yields for similar tungsten complexes, and past DFT studies indicate the iron–boryl complexes also favor $\sigma$-bond metathesis. [23–26, 149] Therefore, we expect that other factors are contributing to the efficiency and selectivity of the reaction. Further spectroscopic and computational work is underway to address these remaining questions.

# Chapter 6

# Transient 2D-IR spectroscopic investigations of $Fe(CO)_4$

## 6.1 Introduction

Transient two-dimensional infrared (T2D-IR) spectroscopy (refer to Figure 1.5c) is a new spectroscopic technique that is a combination of UV-pump, IR-probe and two-dimensional infrared (2D-IR) experiments (refer to Figure 1.5a-b). T2D-IR can be used to study vibrational energy flow in photochemical reactions and can, therefore, be used to address some long-standing questions in fundamental photochemical reactions. Because T2D-IR is a new technique, it is also necessary to perform proof-of-principle experiments designed to determine some of the strengths and limitations of multidimensional spectroscopy in the study of chemical reactions.

A recent investigation by Cahoon et al. demonstrated that 2D-IR spectroscopy can be used to investigate chemical reactions in a novel way that provides experimental evidence for the short-lived transition-state and intermediate structures in solution phase that is not accessible from traditional techniques. [28] Figure 6.1 shows an illustration of the transformation vibrational energy through a generic chemical reaction. A molecule has a unique set of vibrations that can be represented by its irreducible representation, $\Gamma$. As the reactant passes over a barrier to the transition state, the reactant vibrational modes are transformed into a linear combination of the vibrational modes in the transition state, and later, the transition-state vibrational modes are transformed into a linear combination of the vibrational modes in the product. In the event that there is an intermediate structure in the reaction, the reactant vibrational modes will be projected through each transition state and each intermediate enroute to the final product so that the mixing of the vibrations becomes much more complex. 2D-IR can be used to directly monitor the time-scale and extent of vibrational energy transfer, and can, therefore, be used to extract information about the geometries of the transition states and the short-lived intermediates in chemical reactions. [28]

This method for using 2D-IR to study the ultrafast molecular rearrangements in chemical reactions was originally demonstrated by Cahoon et al. in the study of the Berry psuedorotation of $Fe(CO)_5$, a fluxional reaction in which the axial and equitorial CO ligands exchange. [28] In fluxional reactions like the Berry psuedorotation, the reactant and the product are identical, and as a result, molecules cross the transition state multiple times. It is possible to determine detailed information about the reaction in fluxional systems, but it is challenging since much of the information about the energy transformation is washed

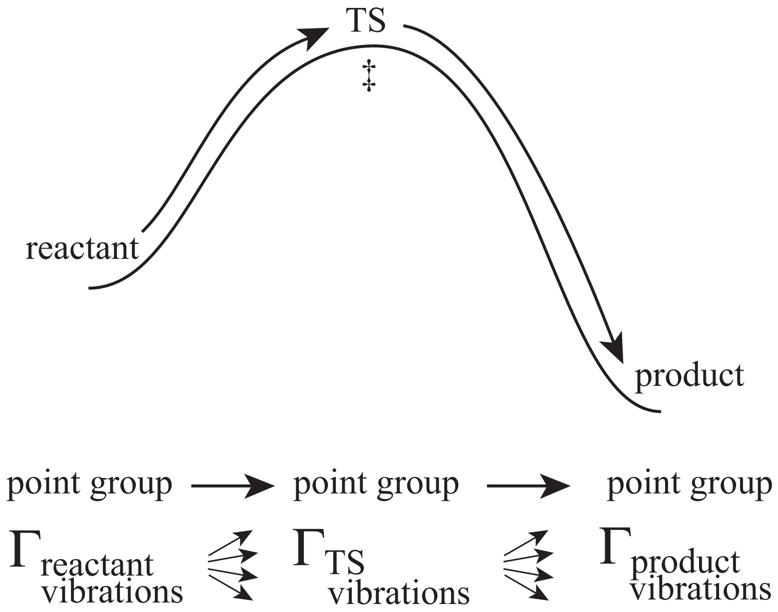

Figure 6.1: Schematic illustration of how vibrational modes transfer, Γ, transfer from a reactant through a transition state and into the final product during the course of a generalized chemical reaction.

out. [28] This problem can be avoided by investigating irreversible reactions, such as CO photodissociation from $Fe(CO)_5$ (Figure 1.1d). I propose to use vibrational labeling T2D-IR (VL T2D-IR) spectroscopy to study this reaction. $Fe(CO)_5$ has long been used as a model system for studying transition-metal chemistry. [2, 107] It is also widely used for the synthesis of iron-containing compounds via standard substitution and decomposition reactions. [173,174] $Fe(CO)_4$ is the key intermediate for most of these reactions, and there are many questions about its formation and reactivity. The VL T2D-IR experiments can be used to answer many of these long-standing questions. [33,38,70,168,175,176] Furthermore, these experiments will reveal the strengths and weaknesses of the application of multidimensional IR spectroscopy to the study of exothermic chemical reactions.

## 6.2 Methods

In order to understand the transfer of vibrational energy that occurs during the course of a chemical reaction (refer to Figure 6.1), I model the energy transfer for a given chemical reaction and compare the simulated results to experiment. A method for modeling energy transfer throughout a chemical reaction is presented by Cahoon et al. and is summarized for a general transition-metal–CO complex here. [28]

### 6.2.1 Modeling energy transfer in chemical reactions for 2D-IR spectroscopy

The first step in these calculations is to determine an intrinsic reaction coordinate by DFT modeling. The DFT calculations for these simulations were performed in similar manner to the calculations presented in Chapter 3. In brief, DFT calculations were performed with the Gaussian03 program [76] at the BP86 level using the basis sets 6-31+g(d) for C and O, 6-31+g(d,p) for H and LANL2DZ for Fe. The LANL2DZ effective core potential was used for iron atoms to account for relativistic effects. [82] Transition states were calculated using the synchronouse transit-guided and quasi-Newton (STQN) method. [83,84] All transition states were verified by following the appropriate eigenvectors, i.e., those eigenvectors corresponding to the imaginary frequency, to their interconnected stationary points.

Starting with the reactant, I assume that the delocalized IR-active CO stretching normal modes of the reactant can be expressed as a linear combination of the localized CO stretching displacements for each individual CO ligand.

$$|n>=\sum_{j=1}^{x}|CO_j><CO_j|n> \tag{6.1}$$

where $|n>$ represents the normal modes composed of the individual CO stretches, $|CO_j>$ and $j = 1...x$ represents the displacement vector of the $j^{th}$ CO ligand. The initial normal modes of the reactant $|n_i>$ before undergoing a reaction can be expressed as a superposition of the normal modes after the reaction.

$$|n_i>= \sum_{j=1}^{x} |n_j> \sum_{j=1}^{x} < n_f|CO_j >< CO_j|n_i > \tag{6.2}$$

where the CO ligands, $|CO_j>$, retain their labels throughout the reaction. The analysis is performed assuming a specific reaction mechanism determined by the internal reaction calculation predicted by DFT, including all transition state and intermediate structures. For simplicity, CO stretching modes $|n>$ of short-lived intermediate structures proposed for photodissociation mechanisms are determined assuming Franck-Codon transitions from the reactant geometry. A specific CO ligand, $|CO_j>$, is removed from the reactant, and the energy and CO normal modes $|n>$ of this CO-loss structure are calculated without performing a geometry optimization calculation. The initial CO modes are then sequentially projected onto all each of these structures and ultimately onto the structure of the final product using the DFT calculated vibrations. The probability that an initial vibration in the reactant will transfer into a specific normal mode in the product is given by equation 6.3.

$$P_{n_i \rightarrow n_f} = \Big| \sum_{j=1}^{x} < n_f|CO_j >< CO_j|n_i > \Big|^2 \tag{6.3}$$

The rate of transferring energy from a mode in the reactant into a mode in the final product is given by equation 6.4, where $k$ is the rate constant for the reaction.

$$k_{n_i \rightarrow n_f} = P_{n_i \rightarrow n_f} * k \tag{6.4}$$

A full simulation of the VL T2D-IR spectrum, similar to the spectra in Figure 1.11, is easily computed on the basis of this analysis and will be compared to the experimental spectra.

## 6.3 Labeling vibrations during photodissociation: CO loss from $Fe(CO)_5$

$Fe(CO)_5$ has five CO ligands arranged in a trigonal bipyramidal geometry and has three IR-active CO stretching modes, two degenerate e' modes and an $a_2$" mode. UV photolysis of this complex leads to the dissociation of a single CO ligand within a few picoseconds to form an $Fe(CO)_4$ fragment which undergoes a structural rearrangements to ultimately form a structure with $C_{2v}$ symmetry. The rearrangement mechanism depends on whether an axial or equatorial CO ligand is photodissociated. The two simplest possible reaction mechanisms for CO photodissociation from $Fe(CO)_5$ are shown in Figure 6.2. In the case that an axial CO ligand is photodissociated (top pathway Figure 6.2), an $Fe(CO)_4$ fragment with a $C_{3v}$ geometry is formed and then undergoes a significant rearrangement of the CO ligands to form the more stable $C_{2v}$ structure. On the other hand, if an equatorial CO ligand is lost (bottom pathway Figure 6.2), the initially formed $Fe(CO)_4$ fragment has a psuedo-$C_{2v}$ geometry and relatively minor structural changes are needed to form the most energetically stable structure.

Photodissociation studies of $Fe(CO)_5$ in the gas-phase [168] and low-temperature matrices [177] suggest that an equitorial CO is dissociated from $Fe(CO)_5$, but there has been no evidence of the molecular rearrangements between photodissociation and the formation of the most stable $Fe(CO)_4$ structure *in solution.* Past UV-pump, IR-probe studies of $Fe(CO)_5$ in neat heptane solution performed by Preston Snee, a former graduate student in the Harris Group, show that the final $C_{2v}$ structure of $Fe(CO)_4$ is formed within a few picoseconds after photolysis. [33] Since the T2D-IR experiments have only one picosecond time resolution, I do not expect to directly observe the dynamics occurring between CO loss and product formation. However, I can gather evidence for those fast rearrangements by studying CO photodissociation from $Fe(CO)_5$ in neat alkane solution with VL T2D-IR (Figure 1.5c). These experiment will provide details about the transformation of vibrational eigenstates from the reactant, $Fe(CO)_5$, through the short-lived intermediates to $Fe(CO)_4$, the final product. As a result, the technique can be used to elucidate information about the structural rearrangement of the CO ligands during the reaction and, thus, to determine which CO ligand, axial or equatorial, is dissociated from $Fe(CO)_5$.

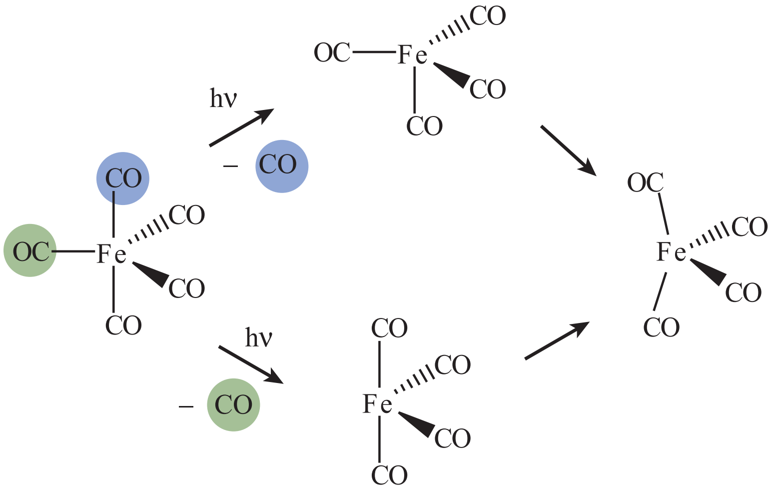

Figure 6.2: Possible reaction mechanisms for axial and equatorial CO loss from $Fe(CO)_4$.

In some ways, I expect that the interpretation of this data will be more straightforward than data for fluxional rearrangements since the system will only rearrange from reactant to product once on the femto- through picosecond time-scale. However, there are many possible ways for the CO ligands in the $Fe(CO)_4$ fragment to rearrange enroute to forming the most stable structure—Figure 6.2 only shows two possibilities. For example, Trushin et al. have investigated the photodissociation mechanism in the gas phase. They propose that the $Fe(CO)_4$ fragment passes through a $T_d$ excited-state conical intersection immediately after photolysis. [168] Clearly, if the $Fe(CO)_4$ fragment rearranges through a $T_d$ intermediate structure before the final $C_{2v}$ structure is formed, the mixing of the vibrational modes will become significantly more complicated. [33, 178] Additionally, $^3Fe(CO)_4$ will eventually be solvated by the alkane bath to form $^1Fe(CO)_4$(alkane), but, as I discuss in section 6.4, the time-scale for this process is still unclear. [70] Therefore, it is possible that the structure that will be interrogated with the IR probe pulse in the VL T2D-IR experiment will correspond to $^1Fe(CO)_4$(alkane), rather than $^3Fe(CO)_4$. Again, if this is the case, the mixing of the vibrational modes will become more complicated. Because the mixing of the CO stretching modes will be unique for each pathway, the simulated VL T2D-IR spectra for each pathways will be different, and I will be able to distinguish between them by comparing the simulated spectra to experiment.

VL T2D-IR uses a pulse sequence in which the UV pump pulse is inserted between the narrowband IR pump and broadband IR probe pulses (Figure 1.5c). The experiment is discussed in detail in section 1.2.3. In brief, the IR pump pulse labels a vibrational mode in $Fe(CO)_5$ by transferring population from the $v = 0$ to the $v = 1$ vibrational levels. The UV pump pulse then dissociates a CO from $Fe(CO)_5$, and the IR probe pulse reads the absorption spectrum. A 2D-IR spectrum is generated by scanning the IR pump frequency and plotting the corresponding IR absorption spectrum along the y-axis to create a contour plot like Figure 1.11. Unlike the standard T2D-IR spectrum, the product peaks now correlate the vibrational modes of the reactant and photoproduct. [55] Because of the time resolution in this experiment, the IR laser fields will only interrogate $Fe(CO)_5$ and $Fe(CO)_4$, but the data provides evidence for the energy exchange from reactant to product, [55] and thus can be used to determine the time-scale, intermediates, transition states and mechanism of the photochemical reaction. [28]

In order to more quantitatively understand the differences in the energy transfer mechanisms for the two pathways shown in Figure 6.2, I used DFT calculations and the vibrational energy transfer model outlined in section 6.2.1 to calculate the splitting of the vibrational modes of $Fe(CO)_5$ after the molecule loses either an axial or equatorial CO and then rearranges to the most stable $Fe(CO)_4$ geometry. In brief, the DFT calculated CO normal modes of $Fe(CO)_5$ are projected onto each of the two intermediates, with $C_{3v}$ and $C_{2v}$ symmetries, and then onto the final structure of $Fe(CO)_4$. [28] In these preliminary calculations, the final $Fe(CO)_4$ geometry is assumed to be the triplet structure shown in Figure 6.4, since it is considered to be the most stable structure by most authors. [70] The results of these calculations are summarized in Figure 6.3, where the states are labeled by their corresponding symmetries. The final distribution of energy is shown on the far right in percentages. It is clear from Figure 6.3 that final distribution of vibrational energy in $Fe(CO)_4$ depends on which CO ligand is dissociated from the starting material. For example, in the case that an equatorial CO is dissociated, the $|a_2'' >$ mode in the $D_{3h}$ structure will exclusively transfer to the $|b_1 >$ mode in the $C_{2v}$ complex. On the other hand, if an axial CO ligand is dissociated, the $|a_2'' >$ mode will mix in a significantly more complicated fashion.

A full simulation of the VL T2D-IR spectra based on this analysis in comparison with experimentally measured spectra will reveal which CO ligand is dissociated from $Fe(CO)_5$ and the nature of the structural rearrangements from the initially formed $Fe(CO)_4$ fragment to the more stable $C_{2v}$ structure. The results from this experiment will not only address key questions in photochemistry that have never before been investigated in solution phase, but will also reveal the power of 2D-IR spectroscopy in studying exothermic reactions in which the system crosses the transition state only once.

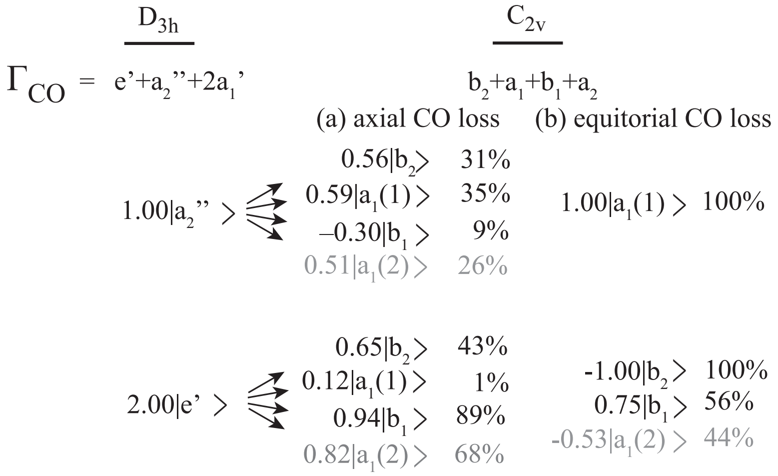

Figure 6.3: The exchange of normal modes for (a) axial and (b) equatorial CO loss from $Fe(CO)_4$. The vibrational modes are labeled by the corresponding symmetry labels for $D_{3h}$ and $C_{2v}$ symmetries.

## 6.4 Structure determination with T2D-IR: $Fe(CO)_4$

An additional benefit in using 2D-IR spectroscopy is that it can be used to monitor molecular structure on the ultrafast time-scale. The cross peaks in 2D-IR spectra show how vibrational modes in a molecule are coupled, and thus, can be used to ascertain the relative orientation of the corresponding transition dipole vectors. Considerable work has been done to determine the molecular structure of proteins and peptides by analyzing the 2D-IR spectra of the amide I bands. Such peptide systems are generally regarded as possessing weakly coupled amide I vibrational modes, and the 2D-IR data can be modeled with dipole-dipole couplings. [42, 43, 54, 179, 180] In order to determine the structure of organometallic complexes with strongly coupled vibrations, however, a local-mode description is necessary. [181] Despite the extensive work done in extracting structural information from 2D-IR spectra, [43, 44, 54, 57, 180–182] the technique has not yet been extended to determine the structure of transient intermediates in chemical reactions that occur on the picosecond time-scale. UV-pump, 2D-IR probe transient 2D-IR spectroscopy (T2D-IR: Figure 1.5c) can be used to monitor molecular structure in solution.

$Fe(CO)_4$ is an ideal system for determining the strength of using 2D-IR spectroscopy for molecular structure determination since there is some ambiguity about its spin state and structure on a picosecond time-scale. Many authors argue that $Fe(CO)_4$ is most stable as a triplet based on molecular orbital descriptions. [70] This assignment is supported by qualitative results from magnetic circular dichroism investigations of matrix isolated $Fe(CO)_4$. [70,173] However, the attempts to experimentally determine the spin state of $Fe(CO)_4$ have failed. [70, 175, 176] Interestingly, I have recently performed DFT calculations that suggest that on the picosecond time-scale $Fe(CO)_4$ is most stable as a solvated singlet. The resulting structures from these DFT calculations are shown in Figure 6.4. Both structures have a truncated trigonal bipyramidal structure that would be expected to form if an equitorial CO ligand was photodissociated from $Fe(CO)_5$. However, the geometries of the two structures are different. In the solvated singlet complex, $^1Fe(CO)_4$(ethane), the CO ligands, labeled CO(1) and CO(2) in Figure 6.4, are at a 180° degress, but the angle between CO(1) and CO(2) is 120° degress in the unsolvated triplet structure, $^3Fe(CO)_4$.

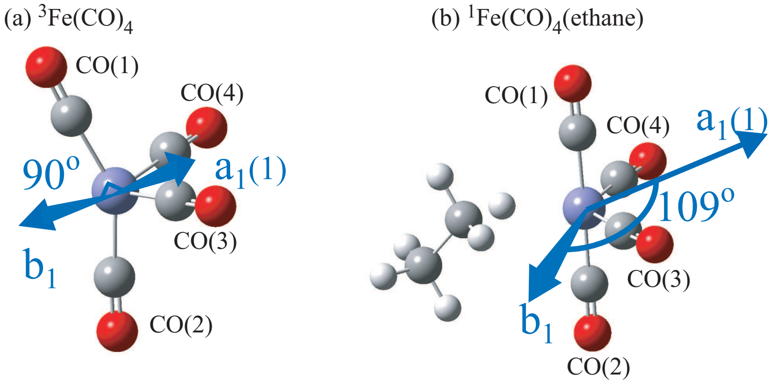

Figure 6.4: DFT calculated structures for the (a) $^3Fe(CO)_4$ and (B) $^1Fe(CO)_4$(ethane). Arrows represent the $b_1$ and $a_1(1)$ transition dipole vectors.

The calculated CO stretching vibrations for these two structures compared to UV-pump, IR-probe experiments of $Fe(CO)_5$ in neat heptane solution are presented in Table 6.1. The experiments [33, 178] indicate that $Fe(CO)_4$ is formed within a few picoseconds after photolysis with CO stretching modes at 1987 and 1967 $cm^{-1}$. DFT calculations of the CO stretching modes of the optimized structures of $^3Fe(CO)_4$ and $^1Fe(CO)_4$(ethane) show that the CO stretching modes of the latter have almost exact agreement with the values measured on the picosecond time-scale. In contrast, the calculated CO stretching modes for the triplet structure are up to 20 $cm^{-1}$ higher in energy than the experimentally observed peaks. However, given the accuracy of DFT calculations, [72] the calculated CO stretching modes for both the triplet and singlet complexes are in reasonable agreement with the experimentally measured values. [33, 178] Since both structures have the same number of CO stretching modes and similar frequencies, there are no simple methods for distinguishing them. It should also be noted that similar experiments performed on a nanosecond time-scale show that the features observed on the picosecond time-scale decay to form a new species with CO stretching modes at 1989, 1973 and 1953 $\text{cm}^{-1}$. [178] The authors of this work assign the initial picosecond photoproduct to $^3\text{Fe(CO)}_4$ which then decays to form $^1\text{Fe(CO)}_4$(ethane) in ca. 13 ns. [178]

| **Exp Freq ($\text{cm}^{-1}$)** | **DFT Freq ($\text{cm}^{-1}$)** | |
|---|---|---|
| | **$^3\text{Fe(CO)}_4$** | **$^1\text{Fe(CO)}_4$(ethane)** |
| 1965 | 1983 (0.58) | 1965 (0.90) |
| | 1985 (1.0) | |
| 1987 | 1993 (0.42) | 1986 (0.25) |
| | | 1989 (1.0) |

Table 6.1: DFT calculated CO stretching modes of $^3\text{Fe(CO)}_4$ and $^1\text{Fe(CO)}_4$(ethane) compared to the results of UV-pump, IR-probe experiments of $\text{Fe(CO)}_5$ in neat heptane solution. [33] Relative intensities of the modes are given in parentheses.

T2D-IR spectroscopy can be used to provide unique evidence for the molecular structure of $\text{Fe(CO)}_4$ on the picosecond time-scale in solution, thus providing evidence for the spin state of the intermediate. The molecular structure of $\text{Fe(CO)}_4$ can be determined by comparing the off-diagonal cross peak amplitudes resulting from T2D-IR data collected with different IR pump polarizations. [55,181,182] T2D-IR experiments use the UV-pump, 2D-IR probe pulse sequence shown in Figure 1.5c. This pulse sequence generates a 2D-IR spectrum of the nonequilibrium ensemble present at the time delay ($\tau_1$) between the UV pump and the 2D-IR probe. Like a standard 2D-IR spectrum, the cross peaks in a T2D-IR spectra result from the interaction of the IR fields with two vibrational eigenstates with unique transition dipole moment vectors. The relative polarization of the IR fields determines the interaction with the transition dipole moment vectors and affects the intensity of the cross peaks. [55,181,182] The polarization of the IR pump field is set to be either parallel or perpendicular to the polarization of the IR probe, and the ratio of the cross peak amplitudes from the two different relative polarizations is

$$\frac{A_\perp}{A_\parallel} = \frac{2 - cos^2\theta}{1 + 2cos^2\theta} \tag{6.5}$$

where $\theta$ is the projection angle between the dipoles of the vibrational eigenstates. [55] Equation 6.5 is plotted as a function of $\theta$ in Figure 6.5.

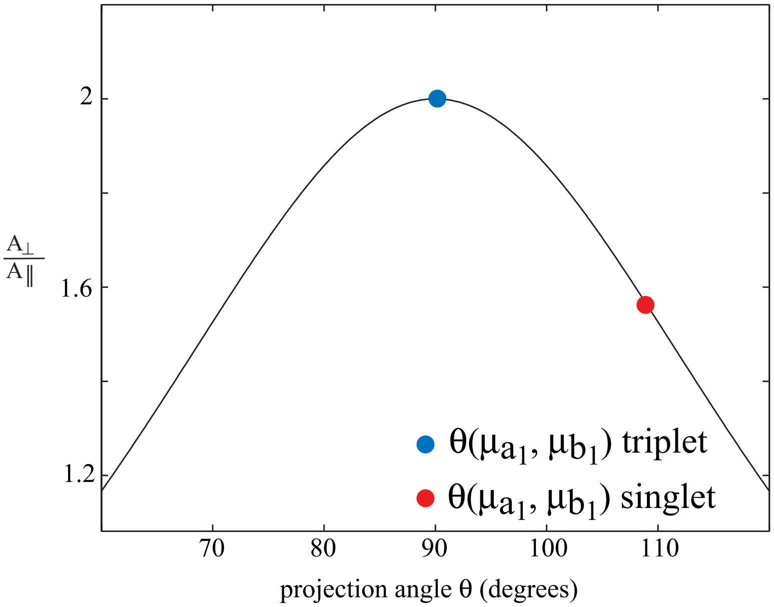

Figure 6.5: Ratio of the off-diagonal peak amplitudes with parallel and perpendicular IR fields as a function of the projection angle $\theta$ between the transition dipole moments for two of the delocalized $b_1$ and $a_1(1)$ IR active CO stretching modes of $^3Fe(CO)_4$ and $^1Fe(CO)_4$(ethane).

I have used DFT calculated projection angle between the transition dipole vectors of the singlet and triplet to determine the viability of this experiment. The cross peak ratios ($\frac{A_\perp}{A_\parallel}$) for all of the modes in both $Fe(CO)_4$ structures were calculated according to equation 6.5 and are plotted in Figure 6.5. [181] As an example, consider the transition dipole vectors for the $b_1$ and $a_1(1)$ vibrations. The singlet and triplet geometries give distinguishably different results for ($\frac{A_\perp}{A_\parallel}$), a ratio of 1.77 for the triplet and 0.98 for the singlet, allowing for unambiguous determination of the structure and spin state of $Fe(CO)_4$. While DFT calculated structures of the singlet and triplet forms of $Fe(CO)_4$ may not capture the true geometry of $Fe(CO)_4$ in solution, the T2D-IR data provides direct experimental evidence for the molecular structure on a picosecond time-scale. A local mode analysis of the vibrational modes will relate T2D-IR data to structural variables such as bond position and orientation, providing the precise structure of $Fe(CO)_4$. [181] T2D-IR represents the first opportunity to experimentally determine of chemically relevant short-lived transient species, such as $Fe(CO)_4$; therefore, it has the potential for widespread application in the study of chemical reaction dynamics.

## 6.5 Conclusion

The Harris group has recently demonstrated that two-dimensional infrared (2D-IR) spectroscopy has enormous potential in determining the details of chemical reactions, such as mechanisms, free energies of activation and transition state structures. [28] However, this experimental technique is still new, and further investigations are needed to determine its strengths and limitations. The preceding sections outline two important proof-of-principle studies of $Fe(CO)_5$ photochemistry that will not only address some key issues with the technique but will also address some long-standing questions in fundamental solution-phase organometallic chemistry.

In section 6.3, I present evidence that vibrational labeling transient 2D-IR spectroscopy (VL T2D-IR) can be used to determine whether an axial or equitorial CO ligand is photodissociated from $Fe(CO)_5$ in solution-phase. There is no other experimental technique that can provide this information because the molecular rearrangements between CO dissociation and the formation of $Fe(CO)_4$ occur on the sub-picosecond time-scale (too quickly to be observed by conventional spectroscopic methods). Interestingly, the time resolution of the VL T2D-IR experiment described above is only 1 ps; however, the cross peaks in the VL T2D-IR spectra provide information about the structures of the transition states and short-lived intermediates connecting the reactant ($Fe(CO)_5$) and the photoproduct ($Fe(CO)_4$). By determining the transition state and intermediate structures in the CO photodissociation reaction of $Fe(CO)_5$, it is possible to determine which CO is lost from the complex.

Transient molecular structure determination is another potential use of T2D-IR spectroscopy in the study of chemical reactions. Currently, no experimental technique exists for measuring the transient molecular structure on the picosecond time-scale. Instead researchers rely heavily on DFT calculations, like the ones outlined in Chapters 3 – 5. These T2D-IR experiments are performed using a UV-pump, 2D-IR probe pulse sequence to measure 2D-IR spectra of the intermediate and product species that are formed as a result of the initial UV pump pulse. The dependence of the T2D-IR cross peaks intensities on the IR pump polarization can be used to determine the projection angle between CO normal modes and a local mode analysis can be used to extract structural information like bond lengths and angles from the data.

Both of these projects demonstrate the potential power of T2D-IR in the study of chemical reactions that exists because the spectra contain detailed information about ultrafast molecular rearrangements and transient molecular structure. This information is masked in the linear IR spectra that are most often used to investigate chemical reaction dynamics, like the UV-pump, IR-probe data presented in the preceding Chapters. In fact, the work presented above exemplifies the limitations of UV-pump, IR-probe spectroscopy. All of the projects have been heavily supplemented with DFT calculations because there is no other way to determine the structures of transient species or the structural changes that take place in the reactions. While the analysis of T2D-IR data still relies on DFT calculations, there is information in the experimental data itself about molecular structure and molecular rearrangements. Thus, these experiments allow us to monitor chemical reaction dynamics at a level of detail that has never before been achieved. The preliminary T2D-IR work delineated here verifies that these experiments are feasible, and I expect that one day 2D-IR and T2D-IR spectroscopies will be common tools used by both physical and synthetic chemists.

# Chapter 7

# Conclusion

A complete understanding of fundamental chemical reactions remains one of the central goals of modern chemistry. Some of the most intriguing systems to investigate are organometallic complexes because their reactivities are determined by the interaction of organic and inorganic moieties. They are novel systems that can be used to gain considerable insight across the chemical sciences. Moreover, organometallic complexes are central to some societally important physical systems, such as biologically relevant enzymes and are homogeneous catalysis reactions. In my doctoral work, I investigated the reactivities of four organometallic complexes in solution phase using time-resolved IR spectroscopy with the goal of determining some key trends in the systems that can be applied to a variety of systems.

The first project, presented in Chapter 3, is the study of the mechanisms for iron-catalyzed alkene isomerization in solution, one of the most important reactions used by synthetic chemists. This work was performed by monitoring the photochemistry of a model system, $Fe(CO)_4(\eta^2$-1-hexene), in neat 1-hexene solution. UV photolysis of this compound leads to the dissociation of a single CO to form $Fe(CO)_3(\eta^2$-1-hexene), in a singlet spin state. This CO loss complex shows a dramatic selectivity to form an allyl hydride, $HFe(CO)_3(\eta^3$-$C_6H_{11})$, via an internal C–H bond-cleavage reaction in 5–25 ns. We find no evidence for the coordination of an alkene molecule from the bath to the CO loss complex but do observe coordination to the allyl hydride, indicating that it is the key intermediate in the isomerization mechanism. Coordination of the alkene ligand to the allyl hydride leads to the formation of the bisalkene isomers, $Fe(CO)_3(\eta^2$-1-hexene)($\eta^2$-2-hexene) and $Fe(CO)_3(\eta^2$-1-hexene$)_2$. Because of the thermodynamic stability of $Fe(CO)_3(\eta^2$-1-hexene)($\eta^2$-2-hexene) over $Fe(CO)_3(\eta^2$-1-hexene$)_2$ (ca. 12 kcal/mol), nearly 100% of the alkene population will ultimately be 2-alkene. These results provide the first direct evidence for this mechanism in solution and suggest modifications to the currently accepted mechanism. [13, 166]

In the second project, discussed in Chapter 4, I present a combined experimental and computational study that provides the first evidence for an excited state transition-metal complex with a bent-NO ligand. Photolysis of transition-metal–NO complexes lead to the formation of a variety of structural isomers that may be used for medical and optical data storage devices. [16–22] Ground state structures with side-on nitrosyl ($\eta^2$-NO) and isonitrosyl (ON) ligands have been observed for a variety of transition metal complexes. [20] In contrast, excited state structures with bent-NO ligands have been proposed for years but never directly observed. [41, 111] I studied the photochemistry of $Co(CO)_3(NO)$, a model transition-metal–NO compound, and surprisingly, I have observed no evidence for ON and $\eta^2$-NO structural isomers but have observed two bent-NO complexes. DFT modeling of the ground and excited state potentials indicates that the bent-NO complexes correspond to triplet excited states. Photolysis of $Co(CO)_3(NO)$ with a 400-nm pump pulse leads to population of a manifold of excited states which decay to form an excited state triplet bent-NO complex within 1 ps. This structure relaxes to the ground triplet state in ca. 350 ps to form a second bent-NO structure. This work provides the first direct experimental observation of excited state bent-NO complexes. However, further experimental and theoretical investigations are suggested to determine the generality of this mechanism and to determine the effect that this pathway has on the photophysical properties of other transition-metal–NO compounds.

In Chapter 5, I present an investigation of novel photoactivated transition-metal–boryl catalysts. Recently, Hartwig and coworkers reported the discovery of these compounds and found that they selectively activate C–H bonds in high yield. [23–27] UV-irradiation of $Cp^*W(CO)_3(Bpin)$ in neat pentane solution primarily results in dissociation of a single CO ligand and solvation of the metal by a pentane molecule from the bath within 2 ps. The resulting complex, *cis*-$Cp^*W(CO)_2(Bpin)$(pentane), undergoes C–H bond activation by a $\sigma$-bond metathesis mechanism on a microsecond time-scale—in 15 $\mu$s, a terminal hydrogen on pentane shifts to the Bpin ligand to form a $\sigma$-borane complex, $Cp^*W(CO)_2(H\text{-}Bpin)(C_5H_{11})$. The borane ligand rotates through two isomers until the boron is directly adjacent to the $C_5H_{11}$ ligand. In this configuration, the B–H $\sigma$-bond is broken in favor of a B–C $\sigma$-bond, forming $Cp^*W(CO)_2(H)(C_5H_{11}\text{–}Bpin)$, a tungsten–hydride complex with a weakly bound alkylboronate ester. The ester is then eliminated to form $Cp^*W(CO)_2(H)$ in approximately 170 $\mu$s. I also identify two side reactions that limit the total yield of bond activation products and explain the 72% yield previously reported for this complex. This work represents the first direct observation of a $\sigma$-bond metathesis mechanism for C–H bond activation by tungsten–boryl complexes. It is possible that this unusual mechanism is responsible for the extraordinary selectivity of the bond activation reaction, but it is unlikely since iron–boryl complexes, which have significantly lower bond activation yield, are expected to react via a similar mechanism. [149] Further spectroscopic and computational work is underway to address these remaining questions.

Finally, in Chapter 6, I describe a novel experiment, transient two-dimensional infrared (T2D-IR) spectroscopy, designed to increase the amount of detail observable in time-resolved IR spectra. In Chapters 3 – 5, I describe UV-pump, IR-probe spectroscopy experimens used to investigate fundamental homogeneous catalysis and spin-forbidden reactions. This is a well-established technique which allows for the determination of free energies of activation and the sequential mechanistic steps in a photochemical reaction, but it has some substantial limitations to the technique. The spectra provide no evidence for molecular structure of the observable intermediates, nor do they provide information about the molecular rearrangements that between reactive steps. As a result, we rely on DFT calculations for structural information. T2D-IR spectra, on the other hand, do provide detailed structural information about chemical reactions since they expand linear IR spectra into a second frequency dimension, displaying evidence for the coupling between vibrational modes in a molecule or between molecules. I describe two proof-of-principle experiments designed to illustrate the strengths and limitations of this technique in the study of chemical reactions. These experiments will also answer long-standing questions about the photochemistry of $Fe(CO)_5$ in solution, a model transition-metal–CO complex. It is reasonable to expect that once these preliminary investigations of T2D-IR spectroscopy are complete, the technique will begin to be established as a common and powerful experimental method in physical chemistry.

All of these studies add to the general understanding of the reactivity trends in organometallic photochemistry. However, it should be noted that in each case there are still follow up questions that can be addressed both experimentally and theoretically. For example, it is important to note that in all cases, there are questions about the generality of the observed mechanisms and the only reasonable way to answer these questions is to perform further experiments. In the metal-assisted alkene isomerization project, it is still unclear why the iron-catalyzed reaction is so much more efficient than the analogous ruthenium-catalyzed system. Elizabeth Glascoe found that the difference is largely due to the reactivity difference between the initially formed coordinatively unsaturated metal complexes. [36] However, she proposed that the difference may be due to a spin-state effects, and my investigation suggests otherwise. In the case of the $Co(CO)_3(NO)$ study, I present the first direct evidence for the existence of an excited state bent-NO–transition-metal complex. However, the quantum yield for the reaction is quite low and it is unclear whether the pathway will be observable in other systems. Furthermore, there are questions about the role of these relatively long-lived bent-NO complexes in biological systems, since there is no evidence for a photoinduced bent-NO complex in a biologically relevant molecule. There are also many existing questions about the reactivity of transition-metal–boryl catalysts. These compounds were only discovered a decade ago, and the details of the system are still largely unknown. While my work has illuminated the bond activation mechanism, it is still unclear what factors lead the extraordinary selectivity observed by Hartwig and coworkers. [23] Hopefully, further work will be done by the Harris group to address these questions. The most promising project that I presented here is the preliminary discussion of T2D-IR studies of chemical reactions dynamics. I have laid out some experiments to be performed using this new and exciting technique, but at this early stage, it is not possible to accurately predict direction that these projects will go. I am curious and excited to see how this technique will be used in the future.

# Bibliography

[1] Cotton, F. A., Wilkinson, G., and Gaus, P. L. *Basic Inorganic Chemistry.* John Wiley and Sons, Toronto, (1995).

[2] Crabtree, R. *The Organometallic Chemistry of Transition Metals.* John Wiley and Sons, New York, NY, (2001).

[3] Grubbs, R. H. *Tetrahedron* **60**, 7117–7140 (2004).

[4] Hill, A. F. *Organotransition Metal Chemistry.* Royal Society of Chemistry, Cambridge, UK, (2002).

[5] McCleverty, J. A. *Chemical Reviews* **104**, 403–418 (2004).

[6] Voet, D. and Voet, J. G. *Biochemistry.* John Wiley and Sons Inc., New York, (1995).

[7] Barrett, A., Barton, D., and Johnson, G. *Journal of the Chemical Society Perkin Transactions* **1**, 1014 (1978).

[8] Fleckner, H., Grevels, F., and Hess, D. *Journal of the American Chemical Society* **106**(7), 2027–2032 (1984).

[9] Gree, R. *Synthesis* **5**, 341 (1989).

[10] Knolker, H., Braier, A., Brocher, D., Cammerer, S., Frohner, W., Gonser, P., Hermann, H., Herzberg, D., Reddy, K., and Rohde, G. *Pure and Applied Chemistry* **73**(7), 1075–1086 (2001).

[11] Pearson, A. J. *Accounts of Chemical Research* **13**, 463 (1980).

[12] Rodreiguez, J., Brun, P., and Waegell, B. *Tetrahedron Letters* **27**, 835 (1986).

[13] Long, G. T. and Weitz, E. *Journal of the American Chemical Society* **122**, 1431 (2000).

[14] Long, G. T., Wenhua, W., and Weitz, E. *Journal of the American Chemical Society* **117**, 12810 (1995).

[15] Hayton, T. W., Legzdins, P., and Sharp, W. B. *Chemical Reviews* **102**, 935–991 (2002).

[16] Culoota, E. and Koshland, D. E. *Science* **259**(1862) (1992).

[17] Schaniel, D., Woike, T., Delley, B., Biner, D., Kramer, K. W., and Gudel, H. U. *Physical Chemistry Chemical Physics* **9**, 5149–5157 (2007).

[18] Stamler, J. S., Singlet, D. J., and Loscalzo, J. *Science* **258**, 1898 (1992).

[19] Atanasov, M. and Schonherr, T. *Journal of Molecular Structure* **592**, 79–93 (2002).

[20] Bitterwolf, T. E. *Coordination Chemistry Reviews* **250**, 1196–1207 (2006).

[21] Boulet, P., Chermette, H., and Weber, J. *Inorganic Chemistry* **40**, 7032–7039 (2001).

[22] Coppens, P., Fomitchev, D. V., Carducci, M. D., and Culp, K. *Journal of the Chemical Society Dalton Transactions* , 865–872 (1998).

[23] Waltz, K. M. and Hartwig, J. F. *Science* **277**, 211–213 (1997).

[24] Waltz, K. M., Muhoro, C. N., and Hartwig, J. F. *Organometallics* **18**, 3383–3393 (1999).

[25] Waltz, K. M. and Hartwig, J. F. *Journal of the American Chemical Society* **122**, 11358–11369 (2000).

[26] Hartwig, J. F., Cook, K. S., Hapke, M., Incarvito, C. D., Fan, Y., Webster, C. E., and Hall, M. B. *Journal of the American Chemical Society* **127**, 1538–2552 (2005).

[27] Chen, H., Schlecht, T. C., and Hartwig, J. F. *Science* **287**, 1995–1997 (2000).

[28] Cahoon, J. F., Sawyer, K. R., Schlegel, J. P., and Harris, C. B. *Science* **319**, 1820–1823 (2008).

[29] Paterson, M., Hunt, P., M.A., R., and Takahashi, O. *Journal of Physical Chemistry A* **106**, 10494–10504 (2002).

[30] Lian, T., Bromberg, S., Aslpund, M., Yang, H., and Harris, C. B. *Journal of the American Chemical Society* **100**, 11994–12001 (1996).

[31] Glascoe, E. A., Kling, M. F., Shanoski, J. E., and Harris, C. B. *Organometallics* **25**, 775–784 (2006).

[32] Shanoski, J. E., Payne, C. K., Kling, M. F., Glascoe, E. A., and Harris, C. B. *Organometallics* **24**(8), 1852–1859 (2005).

[33] Snee, P. T., Payne, C. K., Kotz, K. T., Yang, H., and Harris, C. B. *Journal of the American Chemical Society* **123**, 2255–2264 (2001).

[34] Dougherty, T. P. and Heilweil, E. J. *Journal of Chemical Physics* **100**(5), 4006–4009 (1994).

[35] Shanoski, J. E., Glascoe, E. A., and Harris, C. B. *Journal of Physical Chemistry B* **110**, 996–1005 (2006).

[36] Glascoe, E. A., Sawyer, K., Shanoski, J., and Harris, C. B. *Journal of Physical Chemistry C* **111**(25), 8789–8795 (2007).

[37] Yang, H., Asplund, M. C., Kotz, K. T., Wilken, M. J., Frei, H., and Harris, C. B. *Journal of the American Chemical Society* **120**, 10154–10165 (1998).

[38] Snee, P. T., Payne, C., Mebane, S., Kotz, K. T., and Harris, C. B. *Journal of the American Chemical Society* **123**, 6909 (2001).

[39] Glascoe, E. A., Kling, M. F., Shanoski, J. E., DiStasio Jr., R. A., Payne, C. K., Mork, B. V., Tilley, T. D., and Harris, C. B. *Organometallics* **26**, 1424–1432 (2007).

[40] Vlcek Jr., A. *Coordination Chemistry Reviews* **200**, 933–977 (2000).

[41] Evans, W. and Zink, J. I. *Journal of the American Chemical Society* **103**(10), 2635–2640 (1981).

[42] Bredenbeck, J. and Hamm, P. *Journal of Chemical Physics* **119**, 1569–1578 (2003).

[43] Hamm, P., Lim, M. H., and Hochstrasser, R. M. *Jouranl of Physical Chemistry B* **96**, 2036–2041 (1998).

[44] Woutersen, S. and Hamm, P. *Journal of Physics: Condensed Matter* **14**, R1035–R1062 (2002).

[45] Ganim, Z., Chung, H. S., Smith, A., DeFlores, L. P., Jones, K. C., and Tokmakoff, A. *Accounts of Chemical Research* **41**, 432–441 (2008).

[46] Ishikawa, H., Kim, S., Kwak, K., Wakasugi, K., and Fayer, M. *Proceedings of the National Academy of Sciences of the United States of America* **104**, 19309–19314 (2007).

[47] Loparo, J. J., Robert, S. T., and Tokmakoff, A. *Journal of Chemical Physics* **125**, 194522 (2006).

[48] Strasfeld, D. B., Ling, Y. L., Shim, S. H., and Zanni, M. T. *Journal of the American Chemical Society* **130**, 6698–6699 (2008).

[49] Tokmakoff, A. *Science* **317**, 54–55 (2007).

[50] Cervetto, V., Helbing, J., Bredenbeck, J., and Hamm, P. *Journal of Chemical Physics* **121**, 5935–5942 (2004).

[51] Zheng, J. R., Kwak, K. W., Steinel, T., Asbury, J., Chen, X., Xie, J., and Fayer, M. D. *Science* **309**, 1338 (2005).

[52] Zheng, J. R., Kwak, K. W., Xie, J., and Fayer, M. D. *Science* **313**, 1951 (2007).

[53] Kim, Y. S. and Hochstrasser, R. M. *Proceedings of the National Academy of Sciences of the United States of America* **102**, 11185 (2005).

[54] Woutersen, S., Mu, Y., G., S., and Hamm, P. *Chemical Physics* **266**, 137 (2001).

[55] Bredenbeck, J., Helbing, J., and Hamm, P. *Journal of Chemical Physics* **121**, 5943–5957 (2004).

[56] Niu, S. and Hall, M. *Chemistry Reviews* **100**, 353 (2000).

[57] Hamm, P., Kaindl, R. A., and Stenger, J. *Optics Letters* **25**, 1798 (2000).

[58] Boyd, R. W. *Nonlinear Optics*. Elsevier, San Diego, (2003).

[59] Hecht, E. *Optics*. Addison Weasley, San Francisco, (2002).

[60] Sun, H. and Frei, H. *Journal of Physical Chemistry B* **101**, 205–209 (1997).

[61] Yeom, Y. and Frei, H. *Journal of Physical Chemistry B* **107**(26), 6286–6291 (2003).

[62] Barnhart, T. M., De Felippis, J., and McMahon, R. J. *Angewandte Chemie-International Edition in English* **32**, 1073–1074 (1993).

[63] Barnhart, T. M. and McMahon, R. J. *Journal of the American Chemical Society* **114**, 5434 (1992).

[64] Ellerhorst, G., Gerhartz, W., and Grevels, F. *Inorganic Chemistry* **19**, 67 (1980).

[65] Gravelle, S. J., van de Burgt, L., and Weitz, E. *Journal of Physical Chemistry* **97**, 5272 (1993).

[66] Mitchener, J. C. and Wrighton, M. *Journal of the American Chemical Society* **105**, 1065 (1982).

[67] Wuu, Y., Bentsen, J., Brinkley, C., and Wrighton, M. *Inorganic Chemistry* **26**(4), 530–540 (1987).

[68] Wuu, Y., Zou, C., and Wrighton, M. *Inorganic Chemistry* **27**(17), 3039 – 3044 (1988).

[69] Hayes, D. and Weitz, E. *Journal of Physical Chemistry* **95**, 2723 (1991).

[70] Leadbeater, N. *Coordination Chemistry Reviews* **188**, 35–70 (1999).

[71] Poliakoff, M. and Turner, J. *Journal of the Chemical Society Dalton Transaction* **20**, 2276 (1974).

[72] Scott, A. P. and Radom, L. *Journal of Physical Chemistry* **100**, 16502 (1996).

[73] Schroeder, M. and Wrighton, M. S. *Journal of the American Chemical Society* **98**, 551 (1973).

[74] Snee, P. T., Yang, H., Kotz, K. T., Payne, C. K., and Harris, C. B. *Journal of Physical Chemistry A* **103**, 10426 (1999).

[75] Cedeno, D. L. and Weitz, E. *Organometallics* **22**, 2652 (2003).

[76] Frisch, M. J., Trucks, G. W., Schlegel, H. B., Scuseria, G. E., Robb, M. A., Cheeseman, J. R., Montgomery, Jr., J. A., Vreven, T., Kudin, K. N., Burant, J. C., Millam, J. M., Iyengar, S. S., Tomasi, J., Barone, V., Mennucci, B., Cossi, M., Scalmani, G., Rega, N., Petersson, G. A., Nakatsuji, H., Hada, M., Ehara, M., Toyota, K., Fukuda, R., Hasegawa, J., Ishida, M., Nakajima, T., Honda, Y., Kitao, O., Nakai, H., Klene, M., Li, X., Knox, J. E., Hratchian, H. P., Cross, J. B., Bakken, V., Adamo, C., Jaramillo, J., Gomperts, R., Stratmann, R. E., Yazyev, O., Austin, A. J., Cammi, R., Pomelli, C., Ochterski, J. W., Ayala, P. Y., Morokuma, K., Voth, G. A., Salvador, P., Dannenberg, J. J., Zakrzewski, V. G., Dapprich, S., Daniels, A. D., Strain, M. C.,

Farkas, O., Malick, D. K., Rabuck, A. D., Raghavachari, K., Foresman, J. B., Ortiz, J. V., Cui, Q., Baboul, A. G., Clifford, S., Cioslowski, J., Stefanov, B. B., Liu, G., Liashenko, A., Piskorz, P., Komaromi, I., Martin, R. L., Fox, D. J., Keith, T., Al-Laham, M. A., Peng, C. Y., Nanayakkara, A., Challacombe, M., Gill, P. M. W., Johnson, B., Chen, W., Wong, M. W., Gonzalez, C., and Pople, J. A. *Gaussian 03, Revisions, C.02, Gaussian. Inc.* Wallingford, CT, (2004).

[77] Becke, A. *Physical Review A* **38**, 3098 (1988).

[78] Perdew, J. P. *Physical Review B* **33**, 8822–8824 (1986).

[79] Francl, M., Petro, W. J., Hehre, W., Binkley, J., and Pople, J. A. *Journal of Chemical Physics* **77**, 3654 (1982).

[80] Hariharan, P. and Pople, J. A. *Theoretica Chimica Acta* **28**, 213 (1973).

[81] Hehre, W. J., Ditchfield, R., and Pople, J. A. *Journal of Chemical Physics* **56**, 2257 (1972).

[82] Hay, P. J. and Wadt, W. R. *Journal of Chemical Physics* **82**, 299–310 (1985).

[83] Peng, C. Y., Ayala, P., Schlegel, H., and Frisch, M. *Journal of Computational Chemistry* **17**, 49 (1996).

[84] Peng, C. Y. and Schlegel, H. *Israel Journal of Chemistry* **33**, 449 (1993).

[85] Harvey, J. N. In *Computational Organometallic Chemistry,* Cundari, T. R., editor, volume 1, 291–321. Marcel Dekker Inc., New York, NY (2001).

[86] Lee, C., Yang, W., and Parr, R. G. *Physical Review B* **37**, 785 (1988).

[87] Becke, A. D. *Journal of Chemical Physics* **98**, 5648 (1993).

[88] Stephens, P. J., Devlin, G. J., Chabalowski, C. F., and Frisch, M. M. *Journal of Physical Chemistry* **98**, 11623 (1994).

[89] Ricca, A. and Bauschlicher, C. W., J. *Journal of Physical Chemistry* **98**, 12899 (1994).

[90] Wang, W. and Weitz, E. *Journal of Physical Chemistry A* **101**, 2358 (1997).

[91] Wong, M. W. and Radom, L. *Journal of Physical Chemistry* **99**, 8582 (1995).

[92] Bentsen, J. and Wrighton, M. *Journal of the American Chemical Society* **109**(15), 4518–4530 (1987).

[93] Desrosiers, M., Wink, D., Trautman, R., Friedman, A., and Ford, P. *Journal of the American Chemical Society* **108**, 1917 (1986).

[94] Bogdan, P. L. and Weitz, E. *Journal of the American Chemical Society* **111**(9), 3163–3167 (1989).

[95] Poli, R. and Harvey, J. N. *Chemical Society Reviews* **32**, 1–8 (2003).

[96] Clot, E. and Einstein, O. *Principles and Applications of Density Functional Theory in Inorganic Chemistry II*. Springer, Berlin, Heidelberg, Germany, (2004).

[97] Steinfield, J. I., Francisco, J. S., and Hase, W. L. *Chemical Kinetics and Dynamics*. Prentice-Hall Inc., Upper Saddle River, NJ, (1999).

[98] Ziegler, T. *Inorganic Chemistry* **25**, 2721 (1986).

[99] Richter-Addo, G. and Legzdins, P. *Metal Nitrosyls.* Oxford University Press Inc., New York, (1992).

[100] Ford, P. C. and Lorkovic, I. M. *Chemical Reviews* **102**, 993–1017 (2002).

[101] Laverman, L. E., Wanat, A., Oszajca, J., Stochel, G., Ford, P. C., and van Eldik, R. *Journal of the American Chemical Society* **123**(2), 285–293 (2001).

[102] Lim, M. D., Lorkovic, I. M., and Ford, P. C. *Journal of Inorganic Biochemistry* **99**(1), 151–165 (2005).

[103] Lim, M. D., Lorkovic, I. M., Wedeking, K., Zanella, A. W., Works, C. F., Massick, S. M., and Ford, P. C. *Journal of the American Chemical Society* **124**(33), 9737–9743 (2002).

[104] Snyder, S. H. and Bredt, D. S. *Scientific American* **266**(5), 68 (1992).

[105] Weichsel, A., Andersen, J. F., Roberts, S. A., and Montfort, W. R. *Nature Structural Biology* **7**(7), 551–554 (2000).

[106] Geoffroy, G. L. and Wrighton, M. S. *Organometallic Photochemistry.* Academic Press, New York, (1979).

[107] Huheey, J. E., Keiter, E. A., and Keiter, R. L. *Inorganic Chemistry: Principles of Structure and Reactivity.* Harper Collins College Publishers, New York, (1993).

[108] Shriver, D. and Atkins, P. *Inorganic Chemistry.* W.H. Freeman and Company, New York, NY, (1999).

[109] Buchs, M., Daul, C., Manoharan, P., and Schlapfer, C. *International Journal of Quantum Chemistry* **91**, 418–431 (2003).

[110] Coppens, P., Novozhilova, I. V., and Kovalevky, A. *Chemical Reviews* **102**, 861–883 (2002).

[111] Enemark, J. H. and Feltham, R. D. *Coordination Chemistry Reviews* **13**, 339–406 (1974).

[112] Crichton, O. and Rest, A. J. *Journal of the Chemical Society Dalton Transactions* (6), 536–541 (1977).

[113] Rayner, D. M., Nazran, A. S., Drouin, M., and Hackett, P. A. *Journal of Physical Chemistry* **90**(13), 2882–2888 (1986).

[114] Crichton, O. and Rest, A. *Journal of the Chemical Society Dalton Transactions* **3**, 208–215 (1978).

[115] Thorsteinson, E. M. and Basolo, F. *Journal of the American Chemical Society* **88**(17), 3929–3936 (1966).

[116] Wang, X. F. and Andrews, L. *Journal of Physical Chemistry A* **105**(18), 4403–4409 (2001).

[117] Kohn, W. and Sham, L. J. *Physical Reviews* **140**, A1133 (1965).

[118] Shao, Y., Fusti-Molnar, L., Jung, Y., Kussmann, J., Ochsenfeld, C., Brown, S. T., Gilbert, A. T. B., Slipchenko, L. V., Levchenko, S. V., O'Neill, D. P., Distasio, J. R. A., Lochan, R. C., Wang, T., Beran, G. J. O., Besley, N. A., Herbert, J. M.,

Lin, C. Y., Van Voorhis, T., Chien, S. H., Sodt, A., Steele, R. P., Rassolov, V. A., Maslen, P. E., Korambath, P. P., Adamson, R. D., Austin, B., Baker, J., Byrd, E. F. C., Dachsel, H., Doerksen, R. J., Dreuw, A., Dunietz, B. D., Dutoi, A. D., Furlani, T. R., Gwaltney, S. R., Heyden, A., Hirata, S., Hsu, C.-P., Kedziora, G., Khalliulin, R. Z., Klunzinger, P., Lee, A. M., Lee, M. S., Liang, W., Lotan, I., Nair, N., Peters, B., Proynov, E. I., Pieniazek, P. A., Rhee, Y. M., Ritchie, J., Rosta, E., Sherrill, C. D., Simmonett, A. C., Subotnik, J. E., Woodcock III, H. L., Zhang, W., Bell, A. T., Chakraborty, A. K., Chipman, D. M., Keil, F. J., Warshel, A., Hehre, W. J., Schaefer III, H. F., Kong, J., Krylov, A. I., Gill, P. M. W., and Head-Gordon, M. *Physical Chemistry Chemical Physics* **8**, 3172–3191 (2006).

[119] Clark, T., Chandrasekhar, J., Spitvagel, G. W., and Schleyer, P. *Journal of Computational Chemistry* **4**, 294 (1983).

[120] Sawyer, K. R., Steele, R. P., Glascoe, E. A., Cahoon, J. F., Schlegel, J. P., Head-Gordon, M., and Harris, C. B. *Journal of Physical Chemistry A* **112**, 8505–8514 (2008).

[121] Frisch, M., Pople, J. A., and Binkley, J. *Journal of Chemical Physics* **80**, 3265 (1984).

[122] Krishnan, R., Binkley, J., Seeger, R., and Pople, J. A. *Journal of Chemical Physics* **72**, 650 (1980).

[123] Balabanov, N. B. and Peterson, K. A. *Journal of Chemical Physics* **123**, 064107 (2005).

[124] Dunning, T. J. *Journal of Chemical Physics* **90**, 1007–1023 (1989).

[125] Gill, P., Johnson, B., and Pople, J. A. **209**, 506 (1993).

[126] Casida, M. E. In *Recent Advances in Density Functional Methods, Part I,* Chong, D. P., editor. World Scientific, Singapore (1995).

[127] Gross, E. K. U. and Kohn, W. *Advances in Quantum Chemistry* **21**, 255 (1990).

[128] Petersilka, M., Gossmann, U. J., and Gross, E. K. U. *Physical Review Letters* **76**(1212) (1996).

[129] Runge, E. and Gross, E. K. U. *Physical Review Letters* **52**, 997 (1984).

[130] Hirata, S. and Head-Gordon, M. *Chemical Physics Letters* , 291–299 (1999).

[131] Hanlan, L., Huber, H., Kundig, E. P., McGarvey, B. R., and Ozin, G. A. *Journal of the American Chemical Society* **97**, 7054–7068 (1975).

[132] Grevels, F., Klotzbucher, W., Schrickel, J., and Schaffner, K. *Journal of the American Chemical Society* **116**(14), 6229–6237 (1994).

[133] Vergeer, F., Hartl, F., Matousek, P., Stufkens, D., and Towrie, M. *Chemical Communications* (11), 1220–1221 (2002).

[134] DeKock, R. L. and Gray, H. B. *Chemical Structure and Bonding.* University Science Books, Sausilito, CA, (1989).

[135] Koseki, S., Schmidt, M. W., and Gordon, M. S. *Journal of Physical Chemistry A* **102**, 10430 (1988).

[136] Lengsfield, B. H., Jafri, J. A., and Phillips, D. H. *Journal of Chemical Physics* **74**, 6849 (1981).

[137] Humprey, W., Dalke, A., and Schulten, K. *Journal of Molecular Graphics* **14**, 33–38 (1996).

[138] Yang, H., Snee, P. T., Kotz, K. T., Payne, C. K., and Harris, C. B. *Journal of the American Chemical Society* **123**(18), 4204–4210 (2001).

[139] Allen, W. D., Yamaguchi, Y., Caszar, A. G., Clabo Jr., D. A., Remington, R. B., and Schaefer III, H. F. *Chemical Physics* **1990**, 427–466 (1990).

[140] Novozhilova, I. V., Coppens, P., Lee, J., Richter-Addo, G., and Bagley, K. A. *Journal of the American Chemical Society* **128**, 2093 (2006).

[141] Marcus, R. A. *Journal of Chemical Physics* **24**, 966 (1956).

[142] Koseki, S., Schmidt, M. W., and Gordon, M. S. *Journal of Physical Chemistry* **96**, 10768–10772 (1992).

[143] Walker, T. E. H. and Richards, W. G. *Journal of Chemical Physics* **52**, 1311–1314 (1970).

[144] Grampp, G. *Angewandte Chemie, International Edition in English* **32**, 691–693 (1993).

[145] Marcus, R. A. and Sutin, N. *Biochimica et Biophysica Acta* **811**, 265–322 (1985).

[146] Bromberg, S. E., Yang, H., Asplund, M. C., Lian, T., McNamara, B. K., Kotz, K. T., Yeston, J. S., Wilkens, M., Frei, H., Bergman, R. G., and Harris, C. B. *Science* **278**, 260–263 (1997).

[147] Cowan, A. J., Portius, P., Kawanami, K., Jina, O. S., Grills, D. C., Sun, X., McMaster, J., and George, M. W. *Proceedings of the National Academy of Sciences of the United States of America* **104**(17), 6933–6938 (2007).

[148] Shilov, A. and Shul'pin, G. B. *Chemical Reviews* **97**, 2879–2932 (1997).

[149] Webster, C. E., Fan, Y., Hall, M. B., Kunz, D., and Hartwig, J. F. *Journal of the American Chemical Society* **125**, 858–859 (2003).

[150] Lam, W. H. and Lin, Z. *Organometallics* **22**, 473–480 (2003).

[151] Arndtsen, B. A. and Bergman, R. G. *Science* **270**, 1970–1973 (1995).

[152] Asplund, M. C., Snee, P. T., Yeston, J. S., Wilkens, M. J., Payne, C. K., Yang, H., Kotz, K. T., Frei, H., Bergman, R. G., and Harris, C. B. *Journal of the American Chemical Society* **124**(35), 10605–10612 (2002).

[153] Perdew, J. P. and Zunger, A. *Physical Review B* **23**, 5048–5079 (1981).

[154] Parr, R. G. and Yang, W. *Density Functional Theory of Atoms and Molecules*. Oxford University Press, New York, (1989).

[155] Wadt, W. R. and Hay, P. J. *Journal of Chemical Physics* **82**, 284–298 (1985).

[156] Couty, M. and Hall, M. B. *Journal of Computational Chemistry* **17**, 1359–1370 (1996).

[157] Woon, D. E. and Dunning, T. H. *Journal of Chemical Physics* **100**, 2875–2988 (1994).

[158] Davidson, E. R. *Chemical Physics Letters* **260**, 514–518 (1996).

[159] Dunning, T. and Hay, P. J. *Modern Theoretical Chemistry.* Plenum, New York, (1976).

[160] Dunlap, B. I. *Journal of Chemical Physics* **78**, 3140–3142 (1983).

[161] Dunlap, B. I. *Journal of Molecular Structure (Theochem)* **529**, 37–40 (2000).

[162] Dunlap, B. I., Connolly, J. W. D., and Sabin, J. R. *Chemical Physics* **71**, 3396–3402 (1979).

[163] Dunlap, B. I., Connolly, J. W. D., and Sabin, J. R. *Journal of Chemical Physics* **71**, 4993–4999 (1979).

[164] Blake, A. J., George, M. W., Hall, M. B., McMaster, J., Portius, P., Sun, X. Z., Webster, C. E., Wilson, C., and Zaric, S. D. *Organometallics* **27**, 189–201 (2008).

[165] Cahoon, J. F., Kling, M. F., Schmatz, S., and Harris, C. B. *Journal of the American Chemical Society* **127**(36), 12555–12565 (2005).

[166] Sawyer, K. R., Glascoe, E. A., Cahoon, J. F., Schlegel, J. P., and Harris, C. B. *Organometallics* **27**, 4370–4379 (2008).

[167] Chong, T. S., Li, P., Leong, W. K., and Fan, W. Y. *Journal of Organometallic Chemistry* **690**(4132-4138) (2005).

[168] Trushin, S. A., Fuss, W., Kompa, K. L., and Schmid, W. E. *Journal of Physical Chemistry A* **104**, 1997–2006 (2000).

[169] Joly, A. G. and Nelson, K. A. *Chemical Physics* **152**, 69–82 (1991).

[170] Simon, J. D. and Xie, X. *Journal of Physical Chemistry* **91**, 5538–5540 (1987).

[171] Baker, R. T. and Calabrese, J. C. *Journal of the American Chemical Society* **115**, 4367–4368 (1993).

[172] Baker, R. T., Calabrese, J. C., Westcott, S. A., and Marder, T. B. *Journal of the American Chemical Society* **117**, 8777–8784 (1995).

[173] Poliakoff, M. and Weitz, E. *Accounts of Chemical Research* **20**, 408–414 (1987).

[174] S., W. M. *Chemical Reviews* **74**, 401–430 (1974).

[175] Nayak, S. K., Farrell, G. J., and Burkey, T. J. *Inorganic Chemistry* **33**, 2236–2242 (1994).

[176] Ihee, J., Cao, J. M., and Zewail, A. H. *Angewandte Chemie, International Edition* **40**, 1532–1535 (2001).

[177] K., B. J., Grzybowski, J. M., Poliakoff, M., and Turner, J. J. *Journal of the American Chemical Society* **98**, 5728–5729 (1976).

[178] Portius, P., Yang, J., Sun, W., Grills, D. C., Matousek, P., Parker, A. W., Towrie, M., and George, M. W. *Jouranl of the American Chemical Society* **126**, 10713–10720 (2004).

[179] Hamm, P., Lim, M. H., DeGrado, W. F., and Hochstrasser, R. M. *Journal of Chemical Physics* **112**, 1907–1916 (2000).

[180] Woutersen, S. and Hamm, P. *Journal of Physical Chemistry B* **104**, 11316–11320 (2000).

[181] Golonzka, O., Khalil, M., Demirdoven, N., and Tokmakoff, A. *Journal of Chemical Physics* **115**, 10814–10828 (2001).

[182] Golonzka, O., Khalil, M., Demirdoven, N., and Tokmakoff, A. *Physical Review Letters* **86**, 2154–2157 (2001).

[183] Stratt, R. M. and Maroncelli, M. *Journal of Physical Chemistry* **100**, 12981–12996 (1996).

[184] Owrutsky, J. C., Rafery, D., and Hochstrasser, R. M. *Annual Review of Physical Chemistry* **45**, 519–555 (1994).

[185] King, J. C., Zhang, J. Z., Schwartz, B. J., and Harris, C. B. *Journal of Chemical Physics* **99**(10), 7595–7601 (1993).

[186] Foresman, J. B. and Frisch, A. *Exploring Chemistry with Electronic Structure Methods*. Gaussian Inc., Pittsburgh, PA, (1996).

[187] II, R. D., Keith, T., and Millam, J. Semichem, Inc., Shawnee Mission, KS, 2007.

# Appendix A

# Supplementary Information

## A.1 Chapter 3

### A.1.1 Experimental artifacts

There are small oscillations along the baseline throughout the spectra marked with * in Figure 3.2. The step-scan FTIR spectra from 1800 to 2100 $\text{cm}^{-1}$ of $\text{Fe(CO)}_4(\eta^2\text{-1-hexene})$ in 1-hexene solution are displayed in Figure A.1 to demonstrate that the oscillations observed in the spectra are experimental artifacts.

### A.1.2 Partial optimization calculations of singlet and triplet $\text{Fe(CO)}_3(\eta^2\text{-1-butene})$

In order to locate the crossing points between the ground triplet and singlet potentials ($T_1$ and $S_0$) of $\text{Fe(CO)}_3$(1-butene), I performed partial optimization and energy calculations at successive Fe-$\gamma$H distances in both spin states. Because the calculations

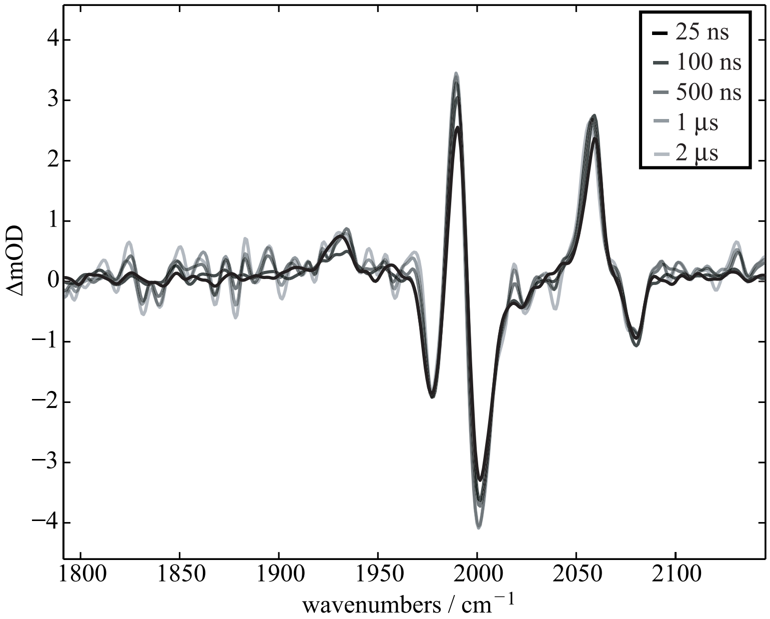

Figure A.1: Transient infrared spectra of Fe(CO)$_4$(1-hexene) in solution with 1-hexene.

do not account for spin-orbit coupling between the $S_0$ and $T_1$ potentials, the surfaces are diabatic and are, therefore, able to cross. In reality I expect that, like most transition metal systems, there is considerable spin-orbit coupling in this complex. Thus, the potentials will only cross at a conical intersection (CI). However, because I do not explicitly account for spin-orbit coupling in the calculations, I cannot observe a CI using this computational method.

The $S_0$ and $T_1$ calculated potentials plotted in the main part of the text (see Figure 3.4) shows that the $S_0$ and $T_1$ surfaces are close in energy in the vicinity of the minimum energy structure of the $^3\mathbf{B}_1$. I have performed similar partial optimization calculations at decreasing Fe-$\gamma$H distance with slightly different starting geometries of $\mathbf{B}_1$ in both spin states in order to locate crossing points between the potentials. The results of these calculations are shown in Figure A.2. The results of these calculations are qualitatively very similar to Figure 3.4; in the potentials plotted in Figure A.2, $T_1$ and $S_0$ cross at Fe-$\gamma$H distances in the range of 2.8–3.1 Å. For all of the structures, this crossing point occurs where there is a sharp drop in energy on the singlet potential that corresponds to a sharp structural change, such as a shift in the location of the alkene moiety relative to the metal center or a change in the geometry of the carbonyl ligands. The structures on the singlet surface at longer Fe-$\gamma$H distances (before the sharp drop) are slightly different from the structures on the triplet surface. This suggests that the crossing points in Figure A.2 are not true crossings of the diabatic surfaces. However, these calculations indicate that regardless of the starting structure, decreasing the Fe-$\gamma$H distance on the singlet potential leads to a decrease in energy that will cause the system to drop below the minimum energy structure on the triplet potential.

Figure A.3 shows the partial optimization calculations of the $S_0$ and $T_1$ potentials calculated using a B3LYP functional. These calculations were performed to determine if using the BP86 functional led to artificially stable singlet states in this system. Regardless of the basis set used, the topology of the $S_0$ and $T_1$ surfaces are identical. The only considerable difference between the calculations is the relative energy of the two states. In the BP86 calculations presented Figure 3.4, the relative energies of the states accurately reflects the experimental results that have shown that the singlet allyl hydride complex (**C**) is more thermodynamically stable than the most thermodynamically stable CO loss product. The B3LYP partial optimization calculations are in poor agreement with the experimental results of this work because they predict that the allyl hydride is less stable

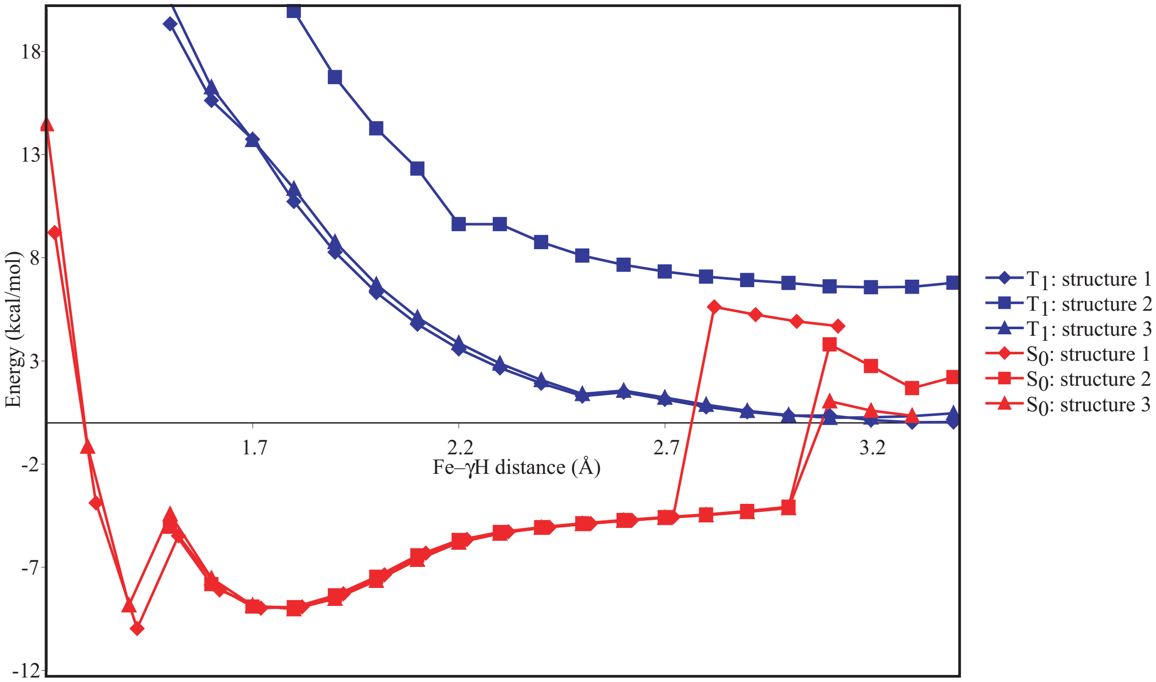

Figure A.2: Results of the DFT calculated one-dimensional potential energy surfaces of the ground singlet and triplet spin states of three different forms of Fe(CO)$_3$($\eta^2$-1-butene) along the Fe-$\gamma$H distance. The curves are generated by performing successive geometry optimizations at fixed values of the Fe-$\gamma$H distance. The lines that connect the data points are guides to the eye.

and that the barrier to forming the allyl hydride from the most stable $\mathbf{B}_1$ structure ($^3\mathbf{B}_1$) is ca. 20 kcal/mol, corresponding to barrier of seconds, nearly 10 orders of magnitude higher than the experimentally observed rate of 5–25 ns.

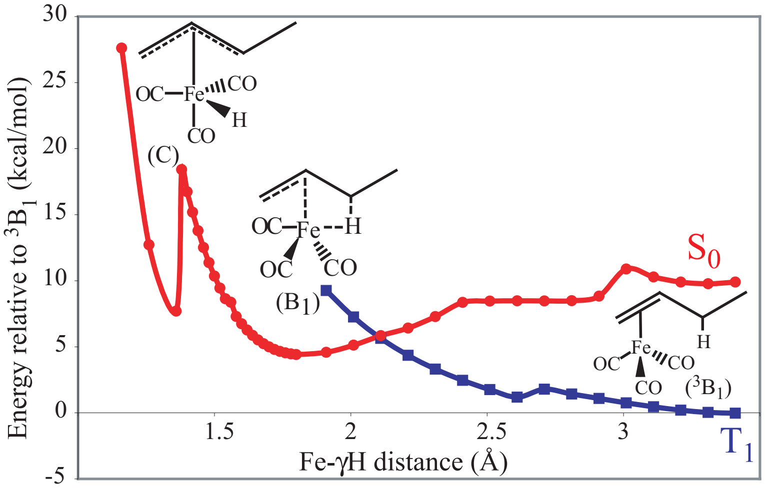

Figure A.3: B3LYP results of the calculated one-dimensional potential energy surfaces of $Fe(CO)_3(\eta^2\text{-1-butene})$ in the $S_0$ and $T_1$ spin states along the Fe-$\gamma$H distance. The curves are generated by performing successive geometry optimizations at fixed values of the Fe-$\gamma$H distance. The lines that connect the data points are guides to the eye.

## A.2 Chapter 4

### A.2.1 Full spectra of $Co(CO)_3(NO)$ in hexane solution

Figures A.4 and A.5 shows visible-pump, IR-probe spectra of dilute solutions of $Co(CO)_3(NO)$ in neat hexane solution. The peaks displayed are photoproducts in the pathways involving the photodissociation of either the carbonyl or nitrosyl ligands resulting in formation of $Co(CO)_2(NO)$ and $Co(CO)_3$, respectively. Peak assignments are based on literature assignments and DFT calculations shown in Table A.1. There is an additional feature in the spectrum displayed in Figure 4.4a marked with a * that appears to be a shoulder for the $\mathbf{B}_{NO}$ peak. The cause of this shoulder is unclear, but a single exponential fit to the feature yields a rise time that is experimentally identical to the rise time of the larger peak at 1684 cm$^{-1}$. It is possible that this feature is the result of a solvent effect that shifts the NO stretching frequency by ca. 10 cm$^{-1}$.

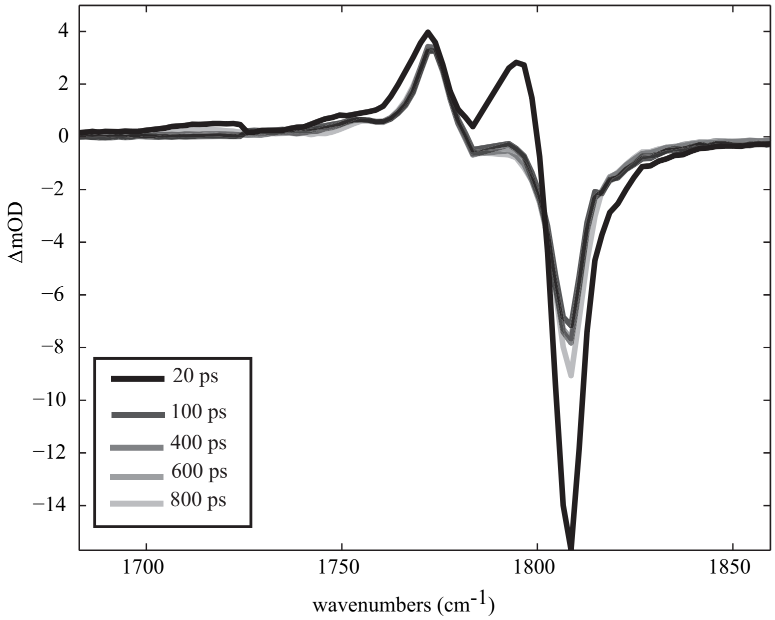

Figure A.4: Ultrafast visible-pump, IR-probe spectra of the NO stretching region of $Co(CO)_3(NO)$ in solution with neat hexane.

### A.2.2 Kinetics for dissociative pathways and vibrational relaxation

Table A.2 shows the dynamics for the features listed in Table A.1. The CO- and NO-loss pathways have been well documented in the literature, and the CO- and NO-loss photoproducts have no dynamics on the picosecond time-scale that are not be attributed to vibrational cooling. Note that the vibrational cooling times for the NO and CO stretches are quite different, ca. 20 ps and ca. 180 ps, respectively. The cooling time-scales are different because the NO stretch is a localized stretch that is better coupled to other modes

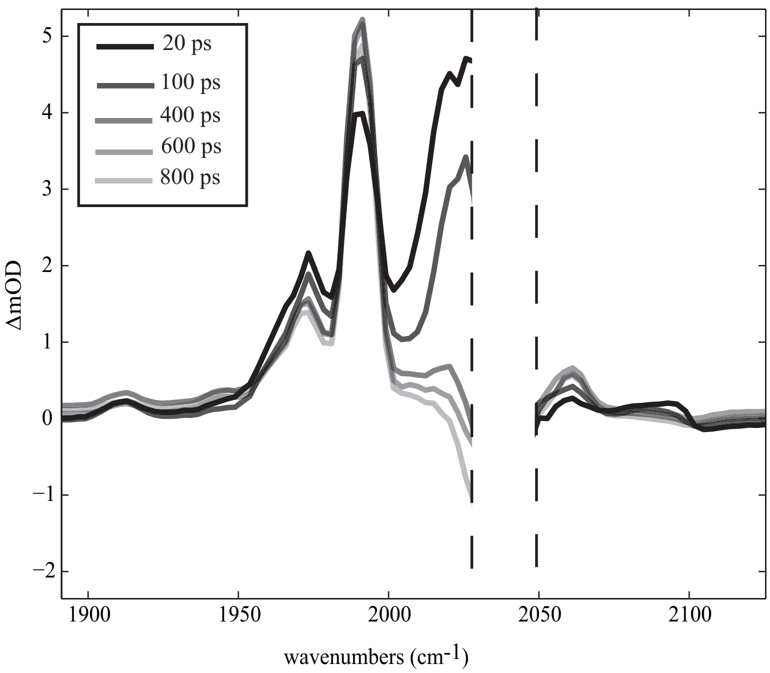

Figure A.5: Ultrafast visible-pump, IR-probe spectra of the CO stretching region of $Co(CO)_3(NO)$ in solution with neat hexane. The space between the dashed lines corresponds to the absorption of the parent bleach at 2037 $cm^{-1}$. This absorption corresponds to the antisymmetric CO stretching modes of $Co(CO)_3(NO)$ and is sufficiently strong that no IR passes through the sample in that spectral region.

| **Assignment** | Lit. Freq ($cm^{-1}$) | Obs. Freq ($cm^{-1}$) | DFT Freq ($cm^{-1}$) |
|---|---|---|---|
| $Co(CO)_3(NO)$ | 1810 | 1807 | 1872 |
| | 2035 | 2037 | 2029(30) |
| | 2103 | 2103 | 2089 |
| $^1Co(CO)_2(NO)(hexane)$ | 1776 | 1775 | 1822 |
| | 1993 | 1992 | 1993 |
| | 2064 | 2064 | 2046 |
| $Co(CO)_3$ | 1982 | 1976 | doublet: 1994(5) |
| | | | quartet: 1972(85) |

Table A.1: Peak assignments for the transient species in the dissociative photochemical pathways of $Co(CO)_3(NO)$. The spin state of $Co(CO)_3$ is unclear from the literature. The DFT calculated frequencies include values for both the doublet and the quartet spin states of $Co(CO)_3$. The DFT calculated frequencies for the quartet agree better with the experimentally observed frequencies, although both are within reasonable errors of DFT frequencies compared to experiment. The quartet structure breaks the symmetry of the CO modes in $Co(CO)_3$ giving rise to 2 peaks. Only one peak is observed in both the experiment and in the literature, suggesting that the doublet is the species that is being observed in experiment.

| Species | Stretch | Peak ($cm^{-1}$) | $\tau$ (ps) | Trend |
|---|---|---|---|---|
| $Co(CO)_3(NO)$ | NO | 1807 | 17±1 | rise |
| | symm CO | 2037 | *Kinetics not resolvable* | |
| | antisymm | 2103 | 3 ± 4 | rise |
| | | | 191 ± 26 | rise |
| vibrationally hot $Co(CO)_3(NO)$ | NO | 1775 | 23 ± 3 | decay |
| | antisymm CO | 2025 | 23 ± 4 | decay |
| | symm CO | 2085 | 4 ± 4 | decay |
| | | | 155 ± 20 | decay |
| $^1Co(CO)_2(NO)(hexane)$ | NO | 1775 | 10 ± 7 | rise |
| | | | 32 ± 20 | decay |
| | antisymm CO | 1992 | 7 ± 2 | decay |
| | | | 162 ± 13 | decay |
| | symm CO | 2062 | 137 ± 20 | decay |
| $Co(CO)_3$ | symm CO | 1973 | 38 ± 15 | decay |

Table A.2: Kinetics for species observed in CO- and NO-loss pathways for the photochemical reaction of $Co(CO)_3(NO)$ in hexane.

in the system, while the CO stretches are strongly coupled to each other. For the CO stretches, vibrational relaxation occurs on two time-scales, a fast time-scale, ca. 20 ps, and a slower time-scale, ca. 180 ps. The faster time-scale agrees within error with the vibrational relaxation times for the NO stretches. This trend in cooling has been observed for NO and CN stretches in another model transition-metal–NO complex, $Na_2[Fe(CN)_5NO]$.

## A.3 Chapter 5

### A.3.1 Minor side-products in the photochemistry of $Cp^*W(CO)_3(Bpin)$ in neat pentane solution

The picosecond UV-pump, IR-probe spectra of $Cp^*W(CO)_3(Bpin)$ in neat pentane solution show three small peaks that are marked with * in Figure 5.2. The feature centered at 1836 cm$^{-1}$ decays on the same time-scale as vibrational cooling for the system and is assigned to the v=1→2 transition of the $\sigma$-alkane structure, Cp*W(CO)$_2$(Bpin)(C$_5$H$_{12}$). The other two peaks (1875 and 1950 cm$^{-1}$), which do not have reactive dynamics on the picosecond time-scale, are assigned to a small population of a different isomer of the $\sigma$-alkane structure. Using DFT calculations, we have identified four different $\sigma$-alkane isomers, shown in Figure A.6, that have slightly different calculated CO stretching frequencies. These peaks are very low in intensity, and as a result, these structures are not expected to contribute significantly to the yield of the bond activation reaction. Additionally, these peaks are not observable on the nano- through microsecond, suggesting that the signal-to-noise is not sufficient to observe them in the step-scan FTIR experiments.

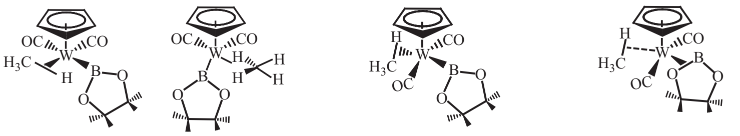
cis-σ-alkane trans-σ-alkane (η2-Bpin)-σ-alkane

Figure A.6: Isomers of Cp*W(CO)$_2$(Bpin)(CH$_4$) identified by DFT calculations

### A.3.2 IR-pump, IR-probe spectra of Cp*W(CO)$_3$(Bpin) in pentane solution

Using the UV-pump, IR-probe spectra alone, we cannot easily determine which of the bleach recovery time constants corresponds to cooling and which correspond to recombination. [183–185] It is reasonable that both processes take place on a time-scale ranging between 5 and 500 ps. Similarly, in the UV-pump, IR-probe spectra there are features red-shifted from the bleach that could be assigned to either vibrationally excited parent molecules or the Cp*W(CO)3$^{\bullet}$ radical species. We have measured IR-pump, IR-probe spectra of Cp*W$(CO)_3$(Bpin) in neat pentane solution at time delays ranging between 1 and 300 ps, so that we can determine the time-scale for vibrational cooling directly and determine the nature of the two bleach recovery processes. The IR-pump, IR-probe spectra of Cp*W$(CO)_3$(Bpin) in neat pentane solution is shown in Figure A.7a. The positive features are identical to the parent bleaches in the UV-pump, IR-probe spectra in the main text, corresponding to the v=0→1 transition, and the negative features (1887 and 1978 $cm^{-1}$) are due to v=1→2 transition. The v=0→1 peaks decay to the baseline on an average time-scale of 34 ± 6 ps, and similarly, the negative v=1→2 features rise to the baseline on an average time-scale of 33 ± 9 ps. The kinetic plots of these peaks are shown in Figure A.7b. The similar decay and rise times of the features indicate that the time-scale for vibrational cooling for this system is ca. 35 ps. Therefore, in the UV-pump, IR-probe spectra in the main text, the fast bleach recovery is due to vibrational cooling and the slow bleach recovery is due to geminate recombination.

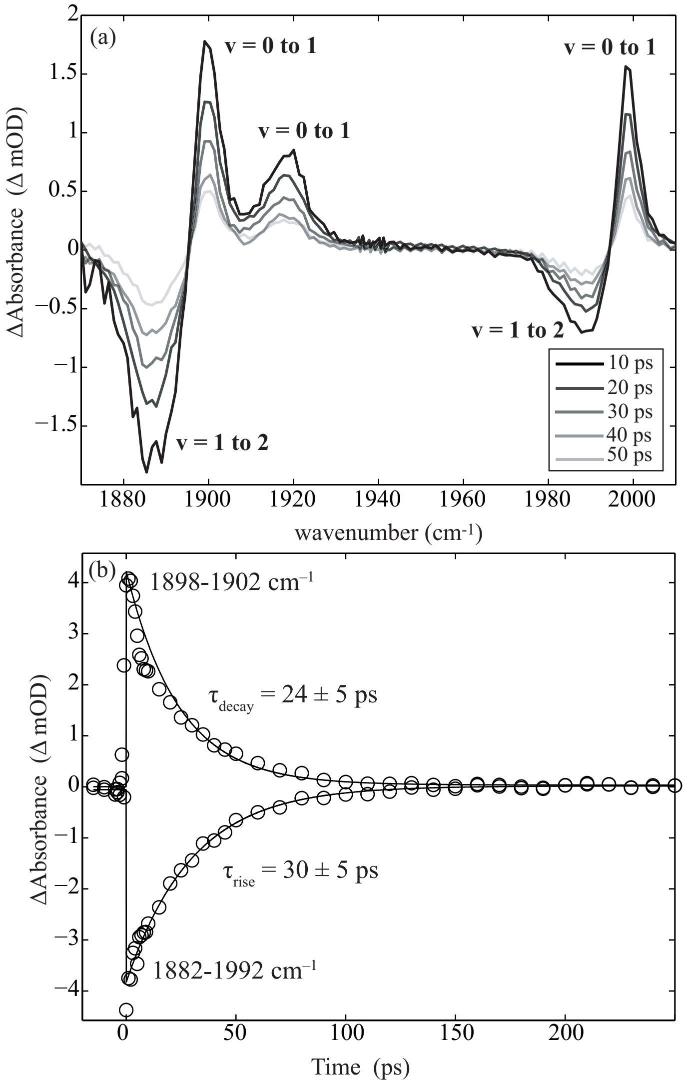

Figure A.7: (a) IR-pump, IR-probe spectra of $Cp^{*}W(CO)_3(Bpin)$ in pentane solution; (b) kinetic plots for the peaks centered at 1887 and 1900 $cm^{-1}$

# Appendix B

# Cartesian coordinates for DFT optimized geometries

| **Atom** | **X** | **Y** | **Z** |
|---|---|---|---|
| Fe | -0.36598 | -0.23033 | -0.1211 |
| O | -0.41402 | -0.44878 | 2.852296 |
| C | -0.39143 | -0.39596 | 1.683533 |
| O | 1.344206 | 2.1988 | -0.24848 |
| C | 0.693342 | 1.226292 | -0.21907 |
| O | -2.94756 | 1.198327 | -0.50923 |
| C | -1.94107 | 0.61807 | -0.37396 |
| C | 1.340449 | -1.60995 | -1.02919 |
| C | 0.037844 | -2.03846 | -1.21634 |
| H | 1.793222 | -0.97125 | -1.80076 |
| H | -0.39376 | -2.81961 | -0.57692 |
| H | -0.50222 | -1.79699 | -2.14116 |
| C | 3.253355 | -1.14505 | 0.631156 |
| H | 3.9773755 | -1.64844 | 1.293459 |
| C | 2.288141 | -2.1686 | 0.006646 |
| H | 1.716101 | -2.6961 | 0.791318 |
| H | 2.887309 | -2.94678 | -0.51312 |
| H | 2.708547 | -0.39541 | 1.227469 |
| H | 3.824854 | -0.60779 | -0.14605 |

Table B.1: Structure of $Fe(CO)_3(\eta^2$-1-butene)

| **Atom** | **X** | **Y** | **Z** |
|---|---|---|---|
| Fe | -0.00122 | 0.00654 | 0.00412 |
| O | -0.01814 | 0.041167 | 2.881842 |
| C | 0.007007 | 0.25875 | 1.709559 |
| O | 2.58859 | -1.43821 | -0.04653 |
| C | 1.559846 | -0.8827 | -0.03192 |
| O | 0.489476 | 2.925684 | -0.16548 |
| C | 0.298795 | 1.77387 | -0.12786 |
| C | -1.45242 | -1.41419 | -0.25315 |
| C | -2.02372 | -0.09993 | -0.25072 |
| H | -1.15985 | -1.82787 | -1.23805 |
| H | -2.63495 | 0.227106 | 0.599152 |
| H | -2.25351 | 0.420049 | -1.19099 |
| C | -0.71926 | -3.55232 | 0.980454 |
| H | 0.196107 | -3.11214 | 1.410127 |
| C | -1.80392 | -2.48533 | 0.766134 |
| H | -2.06668 | -2.00561 | 1.727675 |
| H | -2.73242 | -2.9834 | 0.416532 |
| H | -1.07247 | -4.34288 | 1.664444 |
| H | -0.44126 | -4.0353 | 0.026475 |

Table B.2: Structure of $Fe(CO)_3(\eta^2\text{-1-butene})$

| **Atom** | **X** | **Y** | **Z** |
|---|---|---|---|
| Fe | -0.12794 | 0.086901 | 0.144942 |
| O | 0.106874 | -0.58739 | 3.005856 |
| C | 0.00009 | -0.30305 | 1.874306 |
| O | 0.16239 | -2.44535 | -1.35527 |
| C | 0.006183 | -1.44941 | -0.76205 |
| O | 2.665087 | 0.893547 | 0.230375 |
| C | 1.536931 | 0.575955 | 0.201558 |
| C | -1.00399 | 1.800286 | -0.34985 |
| C | -2.16573 | 1.047209 | 0.198768 |
| H | -0.66603 | 2.732211 | 0.111742 |
| H | -2.99331 | 0.914971 | -0.5238 |
| H | -2.53186 | 1.393276 | 1.1173545 |
| C | 0.577586 | 1.986317 | -2.3883 |
| H | 1.194217 | 1.257651 | -2.94106 |
| C | -0.52152 | 1.308879 | -1.60214 |
| H | -1.22218 | 0.716311 | -2.20613 |
| H | 1.247503 | 2.575489 | -1.74068 |
| H | 0.139755 | 2.67432 | -3.13724 |
| H | -1.89157 | -0.10425 | 0.329644 |

Table B.3: Structure of $Fe(CO)_3(\eta^2\text{-2-butene})$

| **Atom** | **X** | **Y** | **Z** |
|---|---|---|---|
| Fe | 0.001129 | -0.00819 | 0.007742 |
| O | -0.00904 | -0.00041 | 2.916838 |
| C | 0.00692 | -0.00342 | 1.745794 |
| O | -0.52913 | -2.88945 | -0.40742 |
| C | -0.31631 | -1.74918 | -0.26441 |
| O | 2.932187 | 0.331156 | 0.061218 |
| C | 1.767148 | 0.21852 | 0.018775 |
| C | -1.03014 | 1.636161 | -0.38985 |
| C | -1.99793 | 0.671702 | 0.039069 |
| H | -0.80556 | 2.570164 | 0.133348 |
| H | -2.58474 | 0.117044 | -0.70231 |
| H | -2.47535 | 0.774385 | 1.018367 |
| C | 0.526871 | 2.372095 | -2.32162 |
| H | 1.049563 | 1.967242 | -3.20334 |
| C | -0.47345 | 1.368161 | -1.74606 |
| H | 0.036585 | 0.277828 | -1.73397 |
| H | -1.27582 | 1.11374 | -2.46813 |
| H | 1.283231 | 2.654194 | -1.57214 |
| H | -0.00754 | 3.284868 | -2.63599 |

Table B.4: Structure of $Fe(CO)_3(\eta^2$-1-butene)

| **Atom** | **X** | **Y** | **Z** |
|---|---|---|---|
| Fe | -0.04891 | -0.1166 | 0.059654 |
| H | -0.43743 | 0.127349 | 1.506694 |
| C | 2.069262 | -0.9595 | 0.361278 |
| C | 1.738657 | 0.287091 | -0.97777 |
| H | 2.507722 | 0.652125 | 1.027927 |
| H | 1.87663 | 1.331291 | -1.28708 |
| H | 2.357534 | -1.1291 | 0.578479 |
| C | 1.026149 | -0.57363 | -1.83897 |
| H | 1.117328 | -1.65427 | -1.67229 |
| C | 0.568679 | -0.15298 | -3.21456 |
| H | -0.38317 | -0.63388 | -3.49393 |
| O | -0.33073 | 2.850108 | 0.672003 |
| C | -0.18898 | 1.730428 | 0.368502 |
| O | -2.61706 | -0.18342 | -1.34448 |
| C | -1.60508 | -0.10234 | -0.76453 |
| O | -0.24711 | -2.68766 | 1.262715 |
| C | -0.13796 | -1.65687 | 0.723764 |
| H | 1.316461 | -0.45408 | -3.9737 |
| H | -0.433716 | 0.939441 | -3.28191 |

Table B.5: Structure of meridional $HFe(CO)_3(\eta^3\text{-}C_4H_7)$

| **Atom** | **X** | **Y** | **Z** |
|---|---|---|---|
| Fe | 0.002932 | 0.001175 | 0.004711 |
| O | 0.006312 | 0.006169 | 2.968503 |
| C | 0.056413 | 0.003593 | 1.801497 |
| O | -1.72695 | 2.336187 | -0.33534 |
| C | -1.0425 | 1.405717 | -0.16546 |
| O | -1.83455 | -2.24732 | -0.35795 |
| C | -1.10851 | -1.35036 | -0.17634 |
| C | 2.093015 | -0.06696 | -0.00045 |
| C | 1.707163 | 1.18151 | -0.56171 |
| H | 2.534328 | -0.08607 | 1.004719 |
| H | 1.625919 | 1.302188 | -1.64502 |
| H | 1.910762 | 2.095726 | 0.003664 |
| C | 1.983964 | -2.62605 | 0.072223 |
| H | 1.221787 | -3.37901 | -0.18703 |
| C | 1.699471 | -1.29729 | -0.58681 |
| H | -0.21555 | -0.00307 | -1.50131 |
| H | 1.559654 | -1.32017 | -1.67371 |
| H | 2.018068 | -2.53736 | 1.17092 |
| H | 2.959187 | -3.0231 | -0.27107 |

Table B.6: Structure of facial-endo $HFe(CO)_3(\eta^3\text{-}C_4H_7)$

| **Atom** | **X** | **Y** | **Z** |
|---|---|---|---|
| Fe | -0.06031 | 0.027549 | -0.03358 |
| H | -0.18801 | 0.043759 | 1.482167 |
| C | 2.159572 | 0.094418 | 0.022742 |
| C | 1.519216 | 1.190635 | 0.656873 |
| H | 1.571639 | 1.274035 | 1.748958 |
| H | 2.400568 | 0.197322 | -1.04239 |
| C | 0.651854 | 2.05213 | -0.07317 |
| H | 0.860392 | 2.291228 | -1.11998 |
| O | -0.18406 | -2.8368 | 0.563948 |
| C | -0.14085 | -1.69894 | 0.303535 |
| O | -2.84242 | 0.869725 | 0.311107 |
| C | -1.73687 | 0.529788 | 0.150855 |
| O | -0.08502 | -0.20822 | -2.98501 |
| C | -0.04257 | -0.0932 | -1.82407 |
| H | 2.662857 | -0.99996 | 1.833374 |
| C | 2.99808 | -0.90247 | 0.78716 |
| H | 2.965393 | -1.90212 | 0.32338 |
| H | 4.058626 | -0.58393 | 0.793846 |
| H | 0.076634 | 2.804312 | 0.474034 |

Table B.7: Structure of facial-exo $HFe(CO)_3(\eta^3\text{-}C_4H_7)$

| **Atom** | **X** | **Y** | **Z** |
|---|---|---|---|
| Fe | -0.0267 | -0.0437 | 0.00627 |
| C | -0.07346 | -0.15633 | 1.792444 |
| C | 0.159886 | 0.036059 | -1.77351 |
| C | -1.78775 | -0.09743 | -0.13507 |
| O | -0.09195 | -0.27284 | 2.954396 |
| O | 0.287037 | 0.08269 | -2.93304 |
| O | -2.95007 | -0.18568 | -0.2446 |
| H | 1.994711 | 1.40282 | 1.154333 |
| C | 1.490474 | 1.449283 | 0.180689 |
| C | 0.246149 | 2.12256 | 0.068653 |
| H | 2.165046 | 1.371263 | -0.67905 |
| H | -0.04195 | 2.488085 | -0.9282 |
| H | -0.31647 | -2.63798 | 0.7726 |
| C | 0.17399 | -2.17568 | -0.09135 |
| C | 1.459947 | -1.59592 | 7 0.035488 |
| H | -0.17964 | -2.54042 | -1.06213 |
| H | 2.117166 | -1.50581 | -0.83631 |
| H | 1.982983 | -1.6068 | 0.997994 |
| C | -0.36047 | 2.930061 | 1.203051 |
| C | -1.88294 | 3.132331 | 1.136896 |
| H | 0.125982 | 3.930118 | 1.162441 |
| H | -0.07231 | 2.499408 | 2.180785 |
| H | -2.21714 | 3.839422 | 1.91736 |
| H | -2.18748 | 3.545581 | 0.157174 |
| H | -2.42688 | 2.183716 | 1.282926 |

Table B.8: Structure of $Fe(CO)_3(\eta^2\text{-1-butene})_2$

| **Atom** | **X** | **Y** | **Z** |
|---|---|---|---|
| Fe | 0.017546 | -0.02766 | -0.00083 |
| C | 0.130315 | 0.011868 | 1.784855 |
| C | 0.044491 | -0.13437 | -1.78934 |
| C | -1.71941 | -0.34887 | 0.036299 |
| O | 0.225362 | -0.01226 | 2.949077 |
| O | 0.042954 | -0.24487 | -2.95216 |
| O | -2.86998 | -0.56186 | 0.069472 |
| H | 1.557085 | 1.973915 | 1.018956 |
| C | 1.160314 | 1.830778 | 0.00344 |
| C | -0.21904 | 2.116313 | -0.17322 |
| H | -0.54728 | 2.327631 | -1.20159 |
| H | 0.322371 | -2.53705 | 1.011606 |
| C | 0.638624 | -2.07376 | 0.071355 |
| C | 1.78557 | -1.2395 | 0.029088 |
| H | 0.302812 | -2.60204 | -0.82679 |
| H | 2.346593 | -1.12227 | -0.90379 |
| H | 2.371637 | -1.05672 | 0.935589 |
| C | -1.07887 | 2.774844 | 0.887157 |
| H | -1.05432 | 3.874634 | 0.751489 |
| H | -0.71883 | 2.560373 | 1.907477 |
| C | 2.203584 | 2.000254 | -1.08231 |
| H | 3.032228 | 1.279209 | -0.98216 |
| H | 1.776353 | 1.893927 | -2.09341 |
| H | 2.646748 | 3.013853 | -1.0141 |
| H | -2.13493 | 2.463141 | 0.823782 |

Table B.9: Structure of $Fe(CO)_3(\eta^2\text{-2-butene})_2$

| Atom | X | Y | Z |
|---|---|---|---|
| N | -1.75771912 | -.00043299 | .00000000 |
| Co | -.10327657 | .00030589 | .00000000 |
| C | .66339362 | -.80793535 | -1.39959930 |
| C | .66339362 | -.80793535 | 1.39959930 |
| C | .66342868 | 1.61735869 | .00000000 |
| O | 1.11759906 | -1.34001635 | 2.31767913 |
| O | 1.11759906 | -1.34001635 | -2.31767913 |
| O | 1.11268391 | 2.68053828 | .00000000 |
| O | -2.92311708 | -.00102743 | .00000000 |

Table B.10: Structure of ground state Co(CO)$_3$(NO).

| Atom | X | Y | Z |
|---|---|---|---|
| N | -1.77936180 | .66957022 | .00000015 |
| Co | -.11919713 | -.04560680 | .00000126 |
| C | .46931888 | -.85818857 | -1.50910257 |
| C | .46930800 | -.85817353 | 1.50907435 |
| C | .97749503 | 1.40498456 | .00000004 |
| O | .82972254 | -1.37033789 | 2.47580727 |
| O | .82971240 | -1.37032368 | -2.47578048 |
| O | 1.72179466 | 2.28252004 | -.00000004 |
| O | -2.89495624 | .27164936 | -.00000005 |

Table B.11: Structure of T$_1$ state Co(CO)$_3$(NO).

| Atom | X | Y | Z |
|---|---|---|---|
| N | -1.62795276 | 1.00229315 | 0.00000000 |
| Co | -0.12540837 | -0.04195884 | 0.00000000 |
| C | 0.30569689 | -0.92811761 | -1.52444759 |
| C | 0.30569689 | -0.92811761 | 1.52444759 |
| C | 1.18463256 | 1.21782735 | 0.00000000 |
| O | 0.58901179 | -1.46626383 | 2.50259822 |
| O | 0.58901179 | -1.46626383 | -2.50259822 |
| O | 2.06046273 | 1.96470206 | 0.00000000 |
| O | -2.76480777 | 0.66404004 | 0.00000000 |

Table B.12: Structure of S$_1$ state Co(CO)$_3$(NO).

| **Atom** | **X** | **Y** | **Z** |
|---|---|---|---|
| N | 0.00000966 | -0.62452412 | -1.83983647 |
| Co | 0.00000047 | -0.11357686 | -0.13417774 |
| C | 1.47068748 | -0.32629260 | 0.92885150 |
| C | -1.47069830 | -0.32629163 | 0.92883432 |
| C | 0.00000394 | 1.63644792 | -0.46286892 |
| O | -2.43059539 | -0.39640146 | 1.55855733 |
| O | 2.43057738 | -0.39640358 | 1.55858529 |
| O | 0.00000598 | 2.78067578 | -0.59713441 |
| O | 0.00000804 | -1.76173193 | -1.44738179 |

Table B.13: Structure of $Co(CO)_3(\eta^2\text{-}NO)$.

| **Atom** | **X** | **Y** | **Z** |
|---|---|---|---|
| O | -1.86548258 | 0.06088792 | 0.00000000 |
| Co | -0.12205281 | 0.00619132 | 0.00000000 |
| C | 0.60985972 | -0.82944991 | -1.40619969 |
| C | 0.60985972 | -0.82944991 | 1.40619970 |
| C | 0.68929573 | 1.60508660 | 0.00000000 |
| O | 1.11505742 | -1.35968860 | 2.29721196 |
| O | 1.11505742 | -1.35968860 | -2.29721196 |
| O | 1.24367744 | 2.61630596 | 0.00000000 |
| N | -3.02619648 | 0.09581428 | 0.00000000 |

Table B.14: Structure of $Co(CO)_3(ON)$.

| **Atom** | **X** | **Y** | **Z** |
|---|---|---|---|
| Co | 0.00000018 | 0.00033181 | -0.00135048 |
| C | 1.56394018 | 0.00016022 | 0.90310347 |
| C | -1.56393579 | 0.00016015 | 0.90310078 |
| O | 2.56261624 | -0.00024001 | 1.48192631 |
| O | -2.56262078 | -0.00023998 | 1.48192905 |
| C | -0.00000017 | 0.00006355 | -1.80718399 |
| O | 0.00000013 | -0.00023675 | -2.96152715 |

Table B.15: Structure of $Co(CO)_3$.

| Atom | X | Y | Z |
|---|---|---|---|
| N | -1.64181048 | -0.00013273 | -0.03158637 |
| Co | -0.03874309 | -0.00000437 | -0.38064738 |
| C | 0.90504639 | 1.45783927 | 0.01514698 |
| C | 0.90528660 | -1.45769309 | 0.01514839 |
| O | 1.45031962 | 2.39817381 | 0.40502187 |
| O | 1.45071483 | -2.39793792 | 0.40502271 |
| O | -2.69144208 | -0.00021464 | 0.47955687 |

Table B.16: Structure of $^1$Co(CO)$_2$(NO).

| Atom | X | Y | Z |
|---|---|---|---|
| N | -0.67574997 | -1.61005056 | 0.16974426 |
| Co | -0.22409440 | -0.02740197 | 0.02401707 |
| C | -0.19927443 | 0.54955898 | -1.65824506 |
| O | -0.32417015 | 0.86244496 | -2.76487076 |
| O | -1.24442498 | -2.63129765 | 0.12572139 |
| C | -1.27001996 | 1.12607812 | 0.89037103 |
| O | -2.06417398 | 1.80558889 | 1.38475001 |
| C | 3.33379292 | -0.11988263 | 0.29915638 |
| H | 3.84649366 | 0.71068030 | -0.20456667 |
| H | 3.09587623 | -0.87684541 | -0.45932446 |
| H | 4.04165422 | -0.56894802 | 1.00986751 |
| C | 2.07336793 | 0.35672429 | 1.02117373 |
| H | 2.27986108 | 1.12267040 | 1.78017929 |
| H | 1.55990931 | -0.46760531 | 1.53560127 |
| H | 1.40548891 | 0.88983853 | 0.28419212 |

Table B.17: Structure of $^1$Co(CO)$_2$(NO)(ethane).

| **Atom** | **X** | **Y** | **Z** |
|---|---|---|---|
| N | -1.76803026 | -0.00000163 | 0.00031415 |
| Co | -0.06271950 | -0.00000004 | 0.00066480 |
| C | 0.97105982 | -1.47899495 | 0.00038349 |
| C | 0.97105674 | 1.47899653 | 0.00038519 |
| O | 1.63275720 | -2.42422888 | -0.00014214 |
| O | 1.63275216 | 2.42423303 | -0.00014334 |
| O | -2.94459211 | -0.00000319 | -0.00006043 |

Table B.18: Structure of $^3\mathrm{Co(CO)_2(NO)}$.

# Appendix C

# Standard Operating Procedure

## C.1 Instructions for performing UV-pump, IR-probe experiments

1. Follow the procedure for aligning the OPA outlined in section C.3. You will need less than 3% noise for UV-pump, IR-probe experiments.
   (a) To decrease the noise of the IR, adjust the compression out of the Spitfire while monitoring the noise in the Scaling Array Program in Labview. Also try adjusting the first-pass pump timing and the focus of the first-pass seed onto the sapphire. Note that the IR noise increases significantly when the OPA lid is not in place. It is unlikely that you will get below 2% noise in the IR with the lid off.
2. Overlap UV pump and IR probe beams onto the Si or Ge wafer.
   (a) Put the Si and Ge wafers in the sample holder. Note that the Si works with both the 266- and 400-nm beams, but the Ge only works with the 266-nm.

(b) There are two pinholes beside the Si and Ge wafers. Block the IR out of the OPA and align the HeNe beam through the pinholes. Move the position of the sample cell (using the micrometers above and to the side of the cell) so that the HeNe beam passes through the pinhole. Note that this requires that the HeNe is properly aligned with the IR.

(c) Block the HeNe beam and unblock the IR. Look at the sample line on the oscilloscope to monitor how much IR is passing through the pinhole. Adjust the position of the sample cell (again using the micrometers) to maximize the IR intensity passing through the pinhole.

(d) Align the UV beam through the pinhole using the last mirror in the UV line before the sample cell.

    i. Note that after the 266- and 400- nm beams are separated (using the 266 HR after the silica rod), the mirrors are specific to either the 266 or 400 beams. You may have to change out the mirrors depending on which pump wavelength you are using.

(e) Now the UV and IR beams are roughly spatially aligned. You will need to find the temporal overlap between them. To do this, move the sample cell so that the beams are hitting the either Si the or the Ge wafer. It is best to use the HeNe to do this. Now run the kinetic t0 program and look for a response (a significant drop or increase in signal).

(f) You now have a rough idea for the temporal overlap between the beams. Change the timing between the beams to the time with the strongest signal. Now go the

IR-overlap program and use the last mirror before the sample cell to maximize the signal.

   (g) Now that the spatial overlap is improved, go back and run the Kinetic t0 program with higher resolution. Set the t0 to the mid-point of the rise/decay.
   (h) Set the UV-IR time delay to 2 ps and maximize the IR intensity on a fresh part of the Si or Ge wafer. With 266-nm light you should get a response of ca. 50–70 and with 400-nm light you should get a response of 800–1000. If you get a significantly smaller response verify that you have sufficient UV light and that the UV is tightly focused at the sample.

3. Overlap the UV pump and IR probe beams onto the sample.
   (a) Take the Si/Ge wafer out of the sample holder and insert the sample cell.
   (b) Move the spectrograph to the position of a strong bleach in the reactant.
   (c) Move the UV–IR time delay to ca. 100 ps and maximize the IR-overlap signal using the last mirror before the sample in the UV path.

4. Adjust the integration gate so that it read 6–8 in the Scaling Array Program. Note that if you are measuring data below 1800 $\mathrm{cm}^{-1}$, you may not be able to get enough IR to reach 6–8 in the Scaling Array Program. You can take data with a signal as low as 2–3.

5. Use the Cell Control program to move Standa stages back to the zero position. Then manually move the cell so that it is in the upper right corner of the cell.

6. You are now ready to take data. Specify the following values on the front panel of the LabView program. Each of the these are specified in an individual .txt file.

    (a) Kinetics: The UV-IR time delays that you want to measure are specified using a file with the format below. Spectra are measured at each time delay in the order specified and then the delay stage measures the same spectra in the opposite order. So that spectra are measured at each time delay twice.

        time delay(1)
        time delay(2)
        time delay (3) etc.

    (b) Spectrograph positions: The spectrograph positions that you want to measure are listed using a file with the format below. You can also specify a particular integration gate setting for each spectrograph position. If this portion is left blank, the integration gate will not be changing from the original setting. Each entry is separated by *tab* in the .txt file.

        spec. position(1) int. gate(1) spec. position (2) int. gate (2) etc.

    (c) Polarization: The polarization setting that you want for each spectra are specified using a file with the following format.

        polarization (1)
        polarization (2)

## C.2 Instructions for performing T2D-IR experiments

1. Follow the procedure for aligning the OPA outlined in section C.3 section. You will need less than 3% noise for T2D-IR experiments.
2. Follow the instructions laid out in James Cahoon's thesis about how to peform a 2D-IR experiment.
    (a) The only difference here will be that you will use the sample cell from the UV-pump, IR-probe experiments, not the static 2D-IR sample cell.
3. Follow the procedure outlined above for measuring UV-pump, IR-probe spectra.
    (a) The only difference here is that you will need to change the UV chopper frequency to 250 Hz.
        i. Overlap that UV pump and IR probe beams onto the Si or Ge wafer.
        ii. Change the UV chopper frequency to 250 Hz.
        iii. Adjust the UV chopper phase to maximize the overlap intensity.
4. You are now ready to take T2D-IR data. Specify the following values on the front panel of the LabView program. Each of the these are specified in an individual .txt file.
    (a) UV and IR Kinetics: The UV time delays and the IR time delays that you want to measure are specified using two separate files with the same format specified above. The first spectra are measured at UV delay (1) and then spectra are

measured at each IR time delay twice (stage running forwards and backwards). Then the spectra are measured at the UV delay (2) and the each IR delay twice.

(b) Spectrograph positions: The spectrograph positions that you want to measure are listed using a file with the format described above.

(c) Polarization: The polarization setting that you want for each spectra are specified using a file with the following format. In each line the entries are separated by *tab*.

UV polarization (1) IR polarization(1)

UV polarization (2) IR polarization (2)

etc.

(d) Fabry Perot (FP) frequencies: The Fabry Perot frequencies that you want to measure are listed using a file with the format below. In each line the entries are separated by *tab*.

FP frequency(1) FP frequency (2) etc.

## C.3 Trouble-shooting

Listed below is a trouble-shooting guide for the most common problems faced when operating the experimental setup.

### C.3.1 Symptom: There is insufficient mid-IR from the OPA

1. Verify that the OPA crystal angles have been adjusted to match the spectrograph settings.

   (a) Iterate through adjusting the crystal angles to optimize IR intensity and so that the intensity of the spectral profile does not change in the Scaling Array program.

2. Verify that there is white light at the sapphire.

   (a) Adjust the focus of the 800-nm seed onto the sapphire and open the iris that spatially filters the 800-nm beam. Keep track of what you are doing and be able to move it back to approximately where you started.

      i. If these techniques give you white light, adjust the compression out of the Spitfire to improve it. Cycle through these techniques (focus, beam size, compression etc.) until the white light is bright without spots and with a red circle around the perimeter. If this is adjusted properly there will be no jittering in the white light.

      ii. If you do not see white light after adjusting the seed focus and beam size, move the focus and beam size approximately back to where it was originally. Adjust the compression out of the Spitfire to optimize the 400 nm power after the first BBO crystal in the UV pump line.

3. Verify that the first pass pump is spatially and temporally overlapped on the top of the first-pass BBO crystal in the OPA.

   (a) If the beam is not spatially overlapped, use the two mirrors before the BBO crystal in the first-pass pump line to walk the first-pass pump beam to be overlapped with the white light seed before and after the BBO.

   (b) Adjust the focus of the first-pass pump by moving the first-pass pump lens (which is on a translation stage) to create white light at the BBO. Then back the focus off enough so that there is no longer white light.

   (c) Once the beam is spatially overlapped and is properly focused, adjust the timing of the first-pass pump at the BBO crystal to maximize the intensity at the single-element detector. Keep track of the micrometer position on the translation stage BEFORE you change the timing. Always move it back to where it was originally so that you don't completely lose the timing.

   (d) Tweak the overlap, timing and first-pass focus to optimize the first-pass.

4. Assuming that the first-pass is properly aligned and optimized, verify that the second-pass pump is spatially and temporally overlapped onto the bottom of the BBO.

   (a) Adjust the second-pass pump so that it is aligned through the bottom of the BBO and is aligned onto the small gold mirror that directs the beam into the interferometer.

   (b) Once the position of the second-pass pump is set, walk the second-pass seed beam onto the second-pass pump beam before the BBO and after the gold mirror using the curved mirror and the dichroic mirror at the end of the first-pass.

   (c) Once the beams are properly aligned, adjust the temporal overlap of the second-pass seed and pump beams using the translation stage that hold the curved mirror. When the timing is correct, there will be bright green light observable after the small gold mirror.

5. Assuming that the first and second passes through the BBO are properly aligned (i.e.,

you see green light before interferometer), check the alignment of the interferometer.

(a) Align one of the two arms of the interferometer to be straight through the AgGaS crystal.

(b) Overlap the second arm on top of the first.

(c) Once the beams are spatially overlapped, adjust the temporal overlap between the two beams by tweaking the translation stage holding one of the interferometer mirrors. Keep track of the micrometer position on the translation stage BEFORE you change the timing. Always move it back to where it was originally so that you do not completely lose the timing. Do not adjust the AgGaS crystal angle until you get the timing.

(d) In realigning the beams into the AgGaS crystal, you may lose the alignment of the IR into the spectrograph.

   i. You should also open the slits of the spectrograph so that it is less likely that the beam will be blocked at its opening.

   ii. If opening the slits is not sufficient to get the IR to the detector, it may be necessary to put a single element detector after the AgGaS crystal to detect the IR, but do not move the filter after the crystal. That filter is necessary to filter out the near-IR light that will mask the mid-IR that you want to detect.

(e) Once you detect the IR light, tweak the spatial and temporal overlap of the beams in the interferometer and the AGS crystal angle to optimize the intensity of the beam.

### C.3.2 Symptom: No IR is detected

1. The laser is broken.
2. There is not enough IR being generated by the OPA. Refer to section C.3.1 for OPA alignment instructions.
3. Verify that you are looking at the correct channel (signal vs. reference) on the oscilloscope.
4. Verify that the detector is cold. If not, fill it with liquid $N_2$.
5. Verify that the detector is on. If it is not, turn it on.
6. Verify that the Spitfire is lasing and is not blocked.
7. Verify that the integration gate is set properly.
    (a) If not adjust it so that the signal and reference lines are reading between 6 and 8 in the Scaling Array Program.
8. Verify that the mid-IR is not blocked before the detector. If it is, unblock it.
9. Verify that the IR is aligned into the spectrograph.
    (a) Open the slits all the way to see if you can now detect IR.
    (b) Adjust the alignment of the IR (signal and reference lines) into the spectrograph to optimize the IR power.
    (c) Close the slits a bit and realign the IR into the spectrograph. Cycle through this process: align IR, close slits a little more, align IR, close slits etc. until the beam

is properly aligned with the slits at 35–50 $\mu$m.

10. Verify that you have not left the Si or Ge in the sample holder.
11. Verify that you have adjusted the OPA crystal angles to match the spectrograph setting.
12. Verify that the sample is not absorbing too much. Ideally, you will measure OD $\leq$ 0.7 on the FTIR.
13. Verify that the first-pass of the OPA is functioning properly. Make sure that you see green light before the interferometer. If not, put liquid $N_2$ in the single-element detector and adjust the first pass of the OPA to get maximum power (refer to section C.3.1).
14. The laser is broken.

### C.3.3 Symptom: Your data is noisy.

1. Verify that your sample has not decomposed and that there is not photoproduct accumulating on the sample cell windows.
2. Verify that there are no bubbles flowing through your sample.
3. Verify that the detector is cold. If not, fill it with liquid $N_2$.
4. Verify that the IR noise is less than 2% on the Scaling Array program. If it is not, adjust the Spitfire compression, the white-light focus and the timing in the first-pass of the OPA to lower it (refer to section C.3.1).

5. Verify that the integration gate is set properly. If not adjust it so that the signal and reference lines are reading between 6 and 8 in the Scaling Array Program.
6. Verify that the UV and IR pump beams are not being clipped by the chopper blades. For the UV pump, you can check for jitter in the beam. For the IR pump, look at the Fabry-Perot program and adjust the phase of the IR chopper to maximize the intensity.
7. Take some more averages. Bear in mind that depending on the amount of noise in your spectra, this may only marginally improve the situation.

### C.3.4 Symptom: You are measuring spectra, but you do not see peaks.

1. Refer to the preceding section to verify that you are detecting IR.
2. Verify that you have put your sample in.
3. Verify that the UV beam is not blocked before the sample.
4. Verify that the electronic shutter is not blocking the UV beam.
5. Verify that the sample is sufficiently concentrated.
6. Verify that you have overlapped the UV and/or IR pump beams onto the sample. If you cannot get them overlapped onto the sample, make sure that the spectrograph is set at a bleach or peak on the sample. If you still cannot get them overlapped on the sample, try to overlap them onto the Si or Ge.
7. Verify that the Standa stages are properly positioned so that the beams are not blocked on the sample cell or the spacers.

8. Verify that you are at the correct timing.

9. You experiment does not work. Reevaluate goals.

## C.4 Example DFT input files

Included below are sample input files for standard DFT calculations performed using the Gaussian03 program package [76] run on the *Jacquard* 712-CPU Opteron cluster running a Linux operating system at the National Energy Research Scientific Computing Center (NERSC) at the Lawrence Berkeley National Laboratory. [76] For instructions for running Gaussian jobs on NERSC refer to the following website.

http://www.nersc.gov/nusers/resources/software/apps/chemistry/g03/

### C.4.1 Geometry optimization and frequency calculations

Input file for geometry optimization and frequency calculation for $Fe(CO)_4$ is shown in Figure C.1. There are six sections to an input file: link(0)/route, title, z-matrix, variable, connectivity and basis-set/psuedopotential. [186]

In the link(0)/route section, there are five necessary lines. The first line determines the directory for the .chk file. The second and third lines are added in order to run the jobs on *Jacquard*. The second line determines the amount of memory used and the third line determines the number of processors to use. The fourth line called the route line, specifies the details of the job, such as the calculation type (opt and freq in Figure C.1) and functional (BP86). Refer to http://www.gaussian.com/g_ur/keywords.htm for more information of Gaussian03 [76] keywords. This section is terminated by a blank line and followed by the second section, the title line. [186]

The z-matrix, variables and connectivity are given in the third through fifth sections. These values give the structural details for the molecular system and are generated by using the GaussView program package. [187] Once you create an initial molecular structure in GaussView, [187] save the structure as a .com file and go to Windows→ViewFile on the taskbar to open a document specifying the structural parameters for the system. Z-matrices generally use the following format

Element-label, atom 1, bond-length, atom 2, bond-angle, atom 3, dihedral-angle.

The variables section then specifies the values of the variables in the z-matrix. Finally, the connectivity section explicitly specifies the bonding data. This section is optional and only included when you use the geom=connectivity keyword in the route section. All three of the sections are terminated by a blank line. The last section specifies the basis sets for each atom. The non-metals are specified in one line and the metals are on a separate line because they have different basis sets, 6-31+g(d) and LANL2DZ, respectively, in this case. It is only necessary to have multiple lines (separated by ****) for atoms if some have different basis sets. This section is terminated by a blank line. For metal complexes, this section has an additional specification for a psuedopotential that accounts for relativistic effects, LANL2DZ in this case. [186] Add a blank line at the end of the file.

After you have completed a geometry and frequency calculation, verify that you have a minimum energy structure by checking that the frequency calculation does not give any imaginary frequencies (shown as negative values). If you do have a structure with a negative feature, use the GaussView [187] to view the motion associated with the imaginary frequency. Then perturb the structure along that normal mode and run another geometry optimization and frequency calculation. [186]

There are some changes to the input files that are necessary for partial optimization calculations.

1. In the route section, remove the freq keyword.
2. Change the opt keyword to opt=modredundant.
3. Add an additional section before the basis sets.
    (a) For performing a partial optimization calculation in which you perform successive geometry optimizations at varying distances between atoms X and Y add a line with the following format:
    label X, label Y, starting distance, S, number of steps, step size: an example line is: 1 16 3.4 S 23 -0.1 The atom labels can be determined from GaussView taskbar; [187] go to View→Labels.

    You can vary bond distances, bond angles (3 variables) and dihedral angles (4 variables) in partial optimization calculations.

### C.4.2 Transition state calculations

The structure of an input file for a transition state calculation is similar to the structure of an input file for a standard geometry optimization. The general structure of the input file is shown in Figure C.2. For transition state calculations, specify the

```
%chk=/scratch/scratchdirs/karmas/feco4_3.chk
%mem=900MB
%nproclinda=2
#BP86/Gen GFINPUT pseudo=read SCFCYC=5000 opt freq test nosymm geom=connectivity
```

link 0 and route

```
Fe(CO)4 triplet Geometry Optimization and Frequency Calculation
```

title

```
0 3
 Fe
 C        1      B1
 C        1      B2   2      A1
 C        2      B3   3      A2   1      D1
 C        1      B4   2      A3   4      D2
 O        5      B5   1      A4   2      D3
 O        5      B6   1      A5   2      D4
 O        1      B7   2      A6   5      D5
 O        1      B8   2      A7   5      D6
```

z-matrix

```
  B1        1.93012945
  B2        1.93171819
  B3        2.88325361
  B4        1.92875053
  B5        3.74901110
  B6        3.67115847
  B7        3.04404007
  B8        3.04411578
  A1      152.44471888
  A2       48.00791994
  A3       95.18229409
  A4       53.99727939
  A5       55.99598304
  A6       95.20318942
  A7       96.68885381
  D1       56.61481221
  D2      143.83781624
  D3        0.00000000
  D4      153.44780799
  D5       -0.00549535
  D6     -143.83395027
```

variables

```
 1 2 1.0 3 1.0 4 1.0 5 1.0
 2 6 3.0
 3 7 3.0
 4 9 3.0
 5 8 3.0
 6
 7
 8
 9
```

connectivity

```
C O 0
6-31+g(d)
****
Fe 0
LANL2DZ
****

Fe 0
LANL2DZ
```

basis set and
psuedopotential

Figure C.1: Sample input file for running a DFT geometry optimization and frequency calculation for $Fe(CO)_4$ on *Jacquard* at the NERSC facility at LBNL.

keyword opt=QST3. After the route section, there are three distinct sections specifying the structures of the reactant, product and transition state. Note that each section is terminated by a blank line and the preceding section begins with a title line followed by a blank line. The reactant and product z-matrices should be fully optimized structures imported from earlier geometry optimization calculations. [186]

The structure of the transition state should built in GaussView [187] be estimated based on the optimized structures of the reactant and the product. You should always confirm the identity of a transition state by running a frequency calculation to verify that there is only one imaginary frequency. Additionally, you must verify that transition state is connecting the desired reactant and product species. This can be done by performing an internal reaction coordinate (IRC) calculation. [186] The input file is identical to the geometry optimization file, except that the molecule specified is the transition state, the opt keyword is replaced by IRC=(RCFC) and the .chk file for the frequency calculation is listed in the link(0) line. Another option for manually verifying the nature of the transition-state is to perturb the imaginary normal mode in the positive and negative direction to force the system to fall into the associated reactant and product potentials.

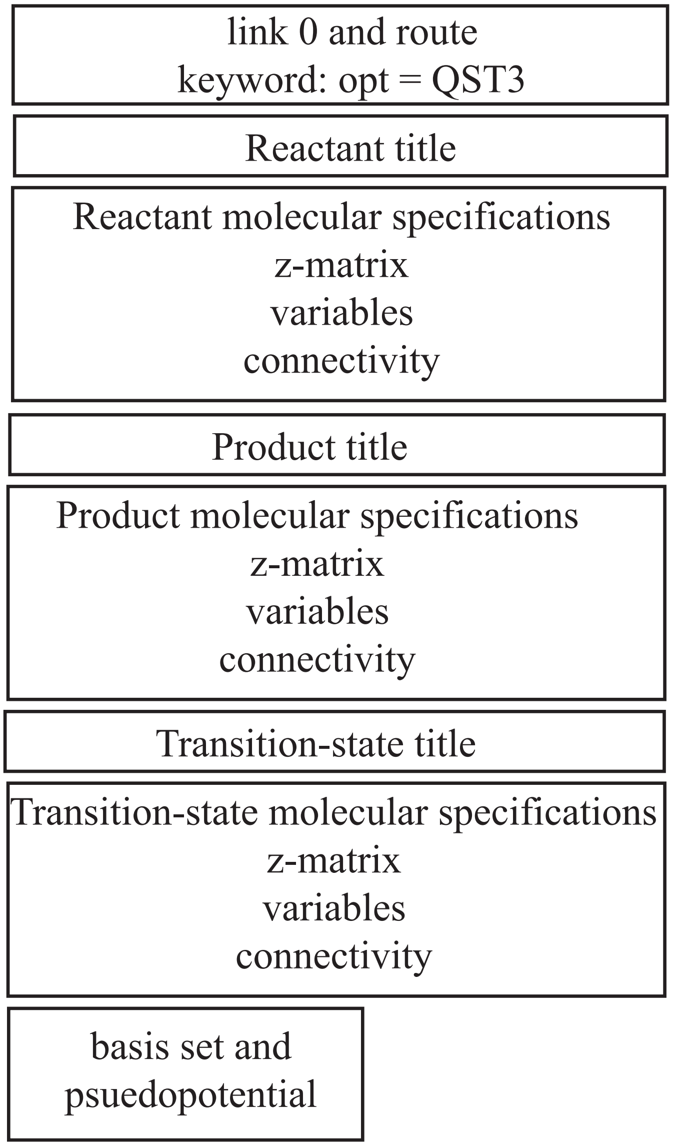

Figure C.2: Structure of an input file for running a transition state calculation.